



**HELLENIC REPUBLIC  
UNIVERSITY OF IOANNINA  
SCHOOL OF ENGINEERING  
DEPARTMENT OF MATERIALS SCIENCE AND ENGINEERING**

**Macromolecular Architecture: Synthesis, Characterization and Properties  
of Linear and Non-Linear Block Copolymers of Polystyrene  
and Poly(dimethylsiloxane) for Nanotechnology Applicationse**

**MANESI MARIA-GKRETI**  
Materials Science Engineer, MSc

PhD THESIS

“The research work was supported by the Hellenic Foundation for Research and Innovation (H.F.R.I.) under the 2nd Call for PhD Fellowship Grands with fellowship number 1651”



**IOANNINA 2022**









**ΕΛΛΗΝΙΚΗ ΔΗΜΟΚΡΑΤΙΑ  
ΠΑΝΕΠΙΣΤΗΜΙΟ ΙΩΑΝΝΙΝΩΝ  
ΠΟΛΥΤΕΧΝΙΚΗ ΣΧΟΛΗ  
ΤΜΗΜΑ ΜΗΧΑΝΙΚΩΝ ΕΠΙΣΤΗΜΗΣ ΥΛΙΚΩΝ**

**Μακρομοριακή Αρχιτεκτονική: Σύνθεση, Χαρακτηρισμός και Ιδιότητες  
Γραμμικών και μη Γραμμικών Συμπολυμερών Πολυστυρενίου  
και Πολυ(διμεθυλοσιλοξάνης) για Εφαρμογές στη Νανοτεχνολογία**

**ΜΑΝΕΣΗ ΜΑΡΙΑ-ΓΚΡΕΤΗ**  
Μηχανικός Επιστήμης Υλικών, MSc

ΔΙΔΑΚΤΟΡΙΚΗ ΔΙΑΤΡΙΒΗ

“Η ερευνητική εργασία υποστηρίχτηκε από το Ελληνικό Ίδρυμα Έρευνας και Καινοτομίας (ΕΛ.ΙΔ.Ε.Κ.) στο πλαίσιο της Δράσης 2η Προκήρυξη Υποτροφιών ΕΛΙΔΕΚ για Υποψήφιους Διδάκτορες με αριθμό υποτροφίας 1651”



**ΙΩΑΝΝΙΝΑ 2022**



*«Η έγκριση της διδακτορικής διατριβής από το Τμήμα Μηχανικών Επιστήμης Υλικών της Πολυτεχνικής Σχολής του Πανεπιστημίου Ιωαννίνων, δεν υποδηλώνει αποδοχή των γνωμών της συγγραφέως (N. 5343/32, άρθρο. 202, παράγραφος 2)»*



**Application date of Mrs. Manesi Maria-Gkreti:** 19-01-2018

**Appointment date for the three-membered advisory committee:** 31-01-2018

**Members of the three-membered advisory committee:**

Supervisor

**Apostolos Avgeropoulos**, Professor at the Department of Materials Science Engineering, School of Engineering, University of Ioannina

Members

**Nikolaos Zafeiropoulos**, Professor at the Department of Materials Science Engineering, School of Engineering, University of Ioannina

**Georgios Sakellariou**, Associate Professor at Chemistry Department, National Kapodistrian University of Athens

**Subject appointment date:** 31-01-2018

*“Macromolecular Architecture: Synthesis, Characterization and Properties of Linear and Non-Linear Block Copolymers of Polystyrene and Poly(dimethylsiloxane) for Nanotechnology Applications”*

**APPOINTMENT DATE FOR THE SEVEN-MEMBERED ADVISORY COMMITTEE:** 24-05-2022

**Apostolos Avgeropoulos**, Professor at the Department of Materials Science Engineering, School of Engineering, University of Ioannina

**Nikolaos Zafeiropoulos**, Professor at the Department of Materials Science Engineering, School of Engineering, University of Ioannina

**Georgios Sakellariou**, Associate Professor at Chemistry Department, National Kapodistrian University of Athens

**Dimitrios Gournis**, Professor at the Department of Materials Science Engineering, School of Engineering, University of Ioannina

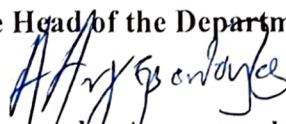
**Dimitrios Bikiaris**, Professor at the Department of Chemistry, School of Science, Aristotle University of Thessaloniki

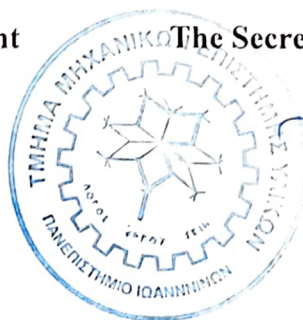
**Rong-Ming Ho**, Professor at Chemical Engineering Department, National Tsing Hua University Hsinchu Taiwan

**Dimitri A. Ivanov**, Professor at Institut de Sciences des Matériaux de Mulhouse-IS2M, CNRS Mulhouse France

The Ph.D thesis was awarded with grade “EXCELLENT” at 20-07-2022

The Head of the Department

  
Apostolos Avgeropoulos  
Professor



The Secretary of the Department

  
Maria Kontou



**Ημερομηνία αίτησης της κ. Μάνεση Μαρίας-Γκρέτη: 19-01-2018**

**Ημερομηνία ορισμού Τριμελούς Συμβουλευτικής Επιτροπής: 31-01-2018**

**Μέλη Τριμελούς Συμβουλευτικής Επιτροπής:**

Επιβλέπων

**Απόστολος Αυγερόπουλος**, Καθηγητής Τμήματος Μηχανικών Επιστήμης Υλικών, Πολυτεχνική Σχολή, Πανεπιστήμιο Ιωαννίνων

Μέλη

**Νικόλαος Ζαφειρόπουλος**, Καθηγητής Τμήματος Μηχανικών Επιστήμης Υλικών, Πολυτεχνική Σχολή, Πανεπιστήμιο Ιωαννίνων

**Γεώργιος Σακελλαρίου**, Αναπληρωτής Καθηγητής Τμήματος Χημείας, Εθνικό Καποδιστριακό Πανεπιστήμιο Αθηνών

**Ημερομηνία ορισμού θέματος: 31-01-2018**

*“Μακρομοριακή Αρχιτεκτονική: Σύνθεση, Χαρακτηρισμός και Ιδιότητες Γραμμικών και μη Γραμμικών Συμπολυμερών Πολυστυρενίου και Πολυ(διμεθυλοσιλοξάνης) για Εφαρμογές στη Νανοτεχνολογία”*

**ΔΙΟΡΙΣΜΟΣ ΕΠΤΑΜΕΛΟΥΣ ΕΞΕΤΑΣΤΙΚΗΣ ΕΠΙΤΡΟΠΗΣ: 24-05-2022**

**Απόστολος Αυγερόπουλος**, Καθηγητής Τμήματος Μηχανικών Επιστήμης Υλικών, Πολυτεχνική Σχολή, Πανεπιστήμιο Ιωαννίνων

**Νικόλαος Ζαφειρόπουλος**, Καθηγητής Τμήματος Μηχανικών Επιστήμης Υλικών, Πολυτεχνική Σχολή, Πανεπιστήμιο Ιωαννίνων

**Γεώργιος Σακελλαρίου**, Αναπληρωτής Καθηγητής Τμήματος Χημείας, Εθνικό Καποδιστριακό Πανεπιστήμιο Αθηνών

**Δημήτριος Γουρνής**, Καθηγητής Τμήματος Μηχανικών Επιστήμης Υλικών, Πολυτεχνική Σχολή, Πανεπιστήμιο Ιωαννίνων

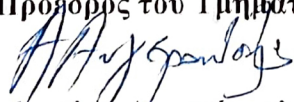
**Δημήτριος Μπικιάρης**, Καθηγητής Τμήματος Χημείας, Σχολή Θετικών Επιστημών, Αριστοτέλειο Πανεπιστήμιο Θεσσαλονίκης

**Rong-Ming Ho**, Professor Chemical Engineering Department, National Tsing Hua University Hsinchu Taiwan

**Dimitri A. Ivanov**, Professor Institut de Sciences des Matériaux de Mulhouse-IS2M, CNRS Mulhouse France

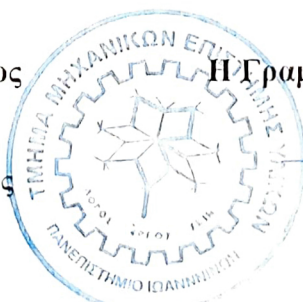
**Έγκριση Διδακτορικής Διατριβής με βαθμό “ΑΡΙΣΤΑ” στις 20-07-2022**

Ο Πρόεδρος του Τμήματος

  
Απόστολος Αυγερόπουλος  
Καθηγητής

Η Γραμματέας του Τμήματος

  
Μαρία Κόντου





*Αφιερωμένο*

*στην οικογένειά μου και τους ανθρώπους που με στήριξαν και συνεχίζουν να με  
στηρίζουν*



## Acknowledgements

I have been an active member of polymers laboratory since April of 2015 when I started my undergraduate diploma thesis. My inclination towards the specific field was evident after the first lecture of “Polymeric Materials” and the first contact with the Polymers Laboratory. I would like to express my deepest gratitude and appreciation to the advisor of my diploma, master and PhD thesis, Professor Apostolos Avgeropoulos. He never stopped trusting me and helping me overcome any difficulty the last seven years. His guidance, the support and invaluable advices throughout the years had a major contribution on my scientific career. Our discussions were always quite interesting and fruitful. Also, I am truly thankful for giving me the opportunity to travel two times in Hsinchu Taiwan, to National Tsing Hua University, to open my mind to new perspectives and to make new collaborations.

I would like to express my deep and sincere gratitude to my co-advisor Professor Rong-Ming Ho from Chemical Engineering Department, National Tsing Hua University, Taiwan for giving me the opportunity to work in his laboratory. He is a distinguished Professor with high ethical principles and his scientific reputation comes before him. My presence in his laboratory and the continuous discussions we had, helped me become familiar with advanced characterization techniques, to gain further insight into polymer physics and finalize a significant part of my thesis. I would like to express my gratitude to PhD candidate Cheng-Yen Chang for all the experiments he had conducted through the years, his advices and his great help inside and outside the laboratory. Words cannot express my gratitude to Dr. Kai-Chieh Yang, Wei-Chen Pan and Dr. Suhail K. Siddique for their unconditional help in every aspect. Also, I would like to thank every member of Professor’s Rong-Ming Ho research group.

I would like to thank Professor Nikolaos Zafeiropoulos from the Department of Materials Science Engineering, School of Engineering, University of Ioannina and Associate Professor Georgios Sakellariou from Department of Chemistry, National Kapodistrian University of Athens for being members of my 3-member Advisor Committee, for their suggestions and the fruitful discussions we had.

I would like to express my gratitude to Professor Dimitri A. Ivanov from Institut de Sciences des Matériaux de Mulhouse-IS2M, CNRS Mulhouse France for his elaborative advices in several scientific works and also thank Professor Dimitrios

Gournis from the Department of Materials Science Engineering, School of Engineering, University of Ioannina and Professor Dimitrios Bikiaris from the Department of Chemistry, School of Science, Aristotle University of Thessaloniki who honored me by accepting the invitation to be members of the 7-member examining committee.

The Nuclear Magnetic Resonance (NMR) Center of the Network of Research Support Laboratories at the University of Ioannina is gratefully acknowledged for allowing me to use their equipment for the measurements.

I would like also to express my gratefulness to every member of the Polymers Laboratory, either to those who have already left or to those who are still there. Firstly, I would like to express my sincere gratitude to my friend and colleague Ioannis Moutsios for the close collaboration and the numerous projects we have accomplished during our presence in the lab. His assistance during the experiments and his support inside and outside of the work place is priceless.

Furthermore, I would like to thank Dr. Miskaki Christina, Dr. Dimitrios Moschovas, Dr. Konstantinos Ntetsikas and Konstantina Tsitoni for their valuable help during the experiments and the characterizations. It has been an honour for me to work with them. I would like to extend my sincere thanks to Dr. Athanasios Katsouras, Dr. Andreas Karydis-Messinis, PhD candidate Georgios Papadopoulos, PhD candidate Konstantinos Artopoiadis, MSc students Spyridon Tsirkas and Achilleas Gianoutsos for their friendship and the great working environment.

I would like to thank the Hellenic Foundation for Research and Innovation (H.F.R.I.) for the complete financial support that allowed me to conduct this thesis.

I would like to express my gratitude to my very beloved persons Pantelis Papanastasiou for his undivided love, patience, understanding and support, Christina Maziani, Christina Mitraka, Aikaterini Xirostylidou and Marios Michael who always stand by my side in good and bad moments and encourage me to never stop trying.

Without the tremendous understanding and encouragement of my family in the past few years, it would be impossible for me to complete my thesis. The biggest thanks from the deepest part of my heart to my parents Angela and Spyros, my brother Ioannis as well as to Maria, Emmeleia and Syla.

Ioannina, July 4<sup>th</sup>, 2022

Gkreti-Maria Manesi

## Contents

Nomenclature .....	4
Abstract .....	7
Keywords.....	8
Περίληψη.....	9
Λέξεις κλειδιά.....	11
CHAPTER 1.....	13
Introduction .....	13
1.1 Basic Concept.....	13
1.2 Motivation and Outline of Thesis.....	14
1.2.1 Linear Diblock Copolymers (PS- <i>b</i> -PDMS).....	15
1.2.2 Linear and Non-Linear Copolymers [(PS- <i>b</i> -PDMS) <sub><i>n</i></sub> where <i>n</i> = 2 or 3 or 4 or 6]	16
1.2.3 Characterization Techniques .....	18
1.2.4 Overview of this Thesis.....	19
CHAPTER 2.....	21
Anionic Polymerization.....	21
2.1 Introduction .....	21
2.2 Block Copolymers.....	25
2.2.1 Linear Diblock Copolymers .....	25
2.2.2 Linear Symmetric Triblock Copolymers.....	27
2.2.3 Star Block Copolymers with Various Functionalities .....	29
CHAPTER 3.....	32
Physical Properties of Linear and Non-Linear Star Block Copolymers.....	32
3.1 Theoretical Background .....	32
3.1.1 Segregation Limit Regimes .....	34
3.2 Conformational Asymmetry .....	37
3.3 Unusual Nanostructures.....	38
3.4 Microphase Separation of Triblock Copolymers.....	41
3.5 Microphase Separation of Star Block Copolymers .....	42
3.5.1 Theory .....	42
3.5.2 Experimental Results Verifying Theory.....	44
3.6 Solid State vs. Thin Film Assembly .....	46
CHAPTER 4.....	50
Block Copolymers in Nanotechnology Applications .....	50
4.1 General Information .....	50
4.2 Silicon-Based Block Copolymers.....	51

4.3 Beyond Block Copolymers.....	53
4.4 The PS- <i>b</i> -PDMS System as a Milestone Copolymer .....	55
4.4.1 Linear Diblock Copolymers Directed Self-Assembly .....	57
4.4.2 Linear and Non-Linear Copolymers Directed Self-Assembly .....	62
4.4.3 Conclusive Remarks .....	66
CHAPTER 5.....	68
Experimental Section .....	68
5.1 High Vacuum Technique.....	68
5.2 Purification of Reagents .....	71
5.3 Synthetic Protocols.....	76
5.3.1 Synthesis of Linear Diblock Copolymers.....	76
5.3.2 Synthesis of Linear Triblock Copolymers.....	80
5.3.3 Synthesis of Three-Arm Star Block Copolymers .....	81
5.3.4 Synthesis of Four-Arm Star Block Copolymers.....	82
5.3.5 Synthesis of Six-Arm Star Block Copolymers .....	82
5.3.6 Fractionation.....	83
5.3.7 Additional Synthesis Information.....	84
5.4 Molecular Characterization .....	86
5.4.1 Size Exclusion Chromatography (SEC) .....	86
5.4.2 Membrane and Vapor Pressure Osmometry.....	87
5.4.3 Proton Nuclear Magnetic Resonance ( <sup>1</sup> H-NMR) Spectroscopy.....	87
5.5 Thermal Analysis .....	87
5.5.1 Differential Scanning Calorimetry (DSC).....	87
5.6 Morphological Characterization .....	88
5.6.1 Sample Preparation.....	88
5.6.2 Transmission Electron Microscopy (TEM).....	88
5.6.3 Electron Tomography (3D TEM).....	89
5.6.4 Small Angle X-Ray Scattering .....	90
5.6.5 Additional Characterization Techniques .....	90
CHAPTER 6.....	92
Experimental Results-Discussion .....	92
6.1 Synthesis Discussion .....	92
6.2 Molecular Characterization Results of Linear PS- <i>b</i> -PDMS Diblock Copolymers.....	93
6.3 Thermal Characterization Results of Linear PS- <i>b</i> -PDMS Diblock Copolymers .....	101
6.4 Morphological Characterization Results of Linear PS- <i>b</i> -PDMS Diblock Copolymers....	104
6.5 Utilizing Linear Block Copolymers for Superior Mechanical Properties <sup>187</sup> .....	120

6.6 Molecular Characterization Results of Linear and Non-Linear (PS- <i>b</i> -PDMS) <sub><i>n</i></sub> Block Copolymers (Where <i>n</i> = 1 or 2 or 3 or 4 or 6).....	125
6.7 Thermal Characterization Results of Linear and Non-Linear (PS- <i>b</i> -PDMS) <sub><i>n</i></sub> Block Copolymers (Where <i>n</i> = 1 or 2 or 3 or 4 or 6).....	140
6.8 Morphological Characterization Results of Linear and Non-Linear (PS- <i>b</i> -PDMS) <sub><i>n</i></sub> Block Copolymers (Where <i>n</i> = 1 or 2 or 3 or 4 or 6).....	150
6.9 Topological Effect on Order-Disorder Transition.....	183
6.10 Morphological Characterization of Block Copolymers in Thin Film State.....	187
CHAPTER 7.....	189
Conclusions-Future Work .....	189
7.1 Conclusions .....	189
7.2 Future Work .....	195
References .....	197

## Nomenclature

PS	Polystyrene
PDMS	Poly(dimethylsiloxane)
$\chi$	Flory-Huggins interaction parameter
- <i>b</i> -	Block
SEC	Size exclusion chromatography
VPO	Vapor pressure osmometry
MO	Membrane osmometry
$\bar{D}$	Dispersity
$\bar{M}_n$	Number average molecular weight
<sup>1</sup> H-NMR	Proton nuclear magnetic resonance spectroscopy
DSC	Differential scanning calorimetry
TEM	Transmission electron microscopy
SAXS	Small angle X-ray scattering
FESEM	Field emission scanning electron microscopy
SPM	Scanning Probe Microscopy
3D TEM	Three dimensional transmission electron microscopy
BCPs	Block copolymers
N	Total degree of polymerization
ODT	Order-disorder transition
T	Temperature
T <sub>g</sub>	Glass transition temperature
IMDS	Inter material dividing surface
D <sub>3</sub>	Hexamethylcyclotrisiloxane
<i>sec</i> -Buli	Secondary butyllithium
<i>n</i> -Buli	<i>n</i> -butyllithium
$\phi$	Volume fraction
$\alpha$	Constant expressing the enthalpic excess free energy of mixing
$\beta$	Constant expressing the entropic excess free energy of mixing
WSL	Weak segregation limit
SSL	Strong segregation limit
SCFT	Self-consistent field theory
HCP or HEX or CYL	Hexagonally closed packed cylinders
PI	Poly(isoprene)
SPH or BCC	Body centered cubic spheres
LAM	Alternating lamellae
PL	Perforated lamellae
GYR or DG	Double gyroid
ISL	Intermediate segregation limit
DD or OBDD	Double diamond
DP	Double primitive
PMMA	Poly(methyl methacrylate)
P2VP	Poly(2-vinyl pyridine)
P4VP	Poly(4-vinyl pyridine)
PLA	Poly(lactic acid)
P3HS	Poly(3 hydroxystyrene)
PEO	Poly(ethylene oxide)
DSA	Directed self-assembly
RIE	Reactive ion etching
GISAXS	Grazing-incidence small-angle x-ray scattering
Q <sup>230</sup>	Double gyroid
O <sup>70</sup>	Orthorombic morphology

LaB <sub>6</sub>	Hexafluoro lanthanum
$\sigma$	Spherical morphology
C14	Frank–Kasper phase
C15	Frank–Kasper phase
f	Mass fraction
T <sub>m</sub>	Melting temperature
T <sub>c</sub>	Crystallization temperature
FCC	Face-centered cubic
Er	Reduced elastic or indentation modulus
S	Stiffness
At	Projected contact area
d	Domain spacing



## Abstract

Linear and non-linear copolymers consisting of polystyrene (PS) and poly(dimethylsiloxane) (PDMS) demonstrate significant scientific and technological interest. These systems showcase high Flory-Huggins interaction parameter ( $\chi$ ), leading to enhanced microphase separation, even for low average molecular weights (able to approach the molecular weight values in which entanglements are formed). Furthermore, the polysiloxane segment renders the materials quite promising for nanotechnology applications due to the etch contrast capability.

The selection of the  $(\text{PS-}b\text{-PDMS})_n$  system where  $n = 1$  or  $2$  or  $3$  or  $4$  or  $6$  is attributed to several factors. Specifically, the high molecular and compositional homogeneity of the copolymers imparts exquisite properties. The well-defined macromolecular architecture and the desired molecular characteristics are allocated to the synthetic protocol followed, and in particular to anionic polymerization and chlorosilane chemistry. In addition, the microphase separation in bulk state constitutes an important tool for the fabrication of nanostructures without the implementation of sophisticated processing steps. It should be mentioned that, tuning the environmental conditions (pressure and temperature) for the linear diblock copolymers or changing the overall entropy of the system for the triblock and/or the star block copolymers during thin films studies, the perpendicular orientation of the nanodomains can be adopted.

The above-mentioned considerations led to the synthesis of: twenty three (23) linear diblock copolymers of the  $\text{PS-}b\text{-PDMS}$  type, six (6) triblock copolymers or  $(\text{PS-}b\text{-PDMS})_2$ , nine (9) three-arm star block copolymers or  $(\text{PS-}b\text{-PDMS})_3$ , six (6) four-arm star block copolymers or  $(\text{PS-}b\text{-PDMS})_4$  and five (5) six-arm star block copolymers or  $(\text{PS-}b\text{-PDMS})_6$ . The synthesis was realized through anionic polymerization and sequential addition of the two monomers under high vacuum conditions. The synthesis of linear and non-linear copolymers was conducted through chlorosilane chemistry using the appropriate coupling agent including dichlorodimethylsilane, trichloromethylsilane, silicon tetrachloride and 1,2-bis(trichlorosilyl)ethane) respectively. The process involves the reaction of the living copolymer chain ends ( $\text{PS-}b\text{-PDMSLi}^+$ ) with the proper chlorosilane and therefore fifteen (15) linear diblock copolymers were used as precursors for the synthesis of the complex architecture copolymers.

The molecular characterization of the samples in this PhD thesis was carried out through size exclusion chromatography (SEC), vapor pressure and membrane osmometry (VPO, MO) to determine the dispersity indices ( $\mathfrak{D}$ ) and the number average molecular weights ( $\bar{M}_n$ ), respectively. The mass composition in all samples was calculated through proton nuclear magnetic resonance spectroscopy ( $^1\text{H-NMR}$ ) and appropriate equation was used for the calculation of the volume fraction. The thermal characterization for the determination of the thermal transitions was conducted through differential scanning calorimetry (DSC).

The structure/property relationship in bulk state was carried out through transmission electron microscopy (TEM) and small angle X-ray scattering (SAXS) for all copolymer sequences (linear and non-linear architectures). Some linear diblock copolymers were studied through field emission scanning electron microscopy (FESEM) and three dimensional TEM (3D TEM). The order-disorder transition of specific linear and non-linear copolymers was estimated through in-situ SAXS experiments. The surface morphology in specific copolymers was determined through scanning probe microscopy (SPM).

The majority of the morphological characterizations was conducted through the collaboration with the research group of Professor Rong-Ming Ho (Chemical Engineering Department at National Tsing Hua University, Hsinchu, Taiwan) leading to quite significant results.

**Keywords:** Linear diblock and triblock copolymers, star block copolymers, high interaction parameter  $\chi$ , topological effects, novel phases, enhanced mechanical properties, linear vs. non-linear self-assembly, order disorder transition temperature.

## Περίληψη

Τα γραμμικά και μη γραμμικά συμπολυμερή που αποτελούνται από πολυστυρένιο (PS) και πολυ(διμεθυλοσιλοξάνη) (PDMS) παρουσιάζουν τεράστιο επιστημονικό και τεχνολογικό ενδιαφέρον. Τα συστήματα αυτά εμφανίζουν υψηλή παράμετρο αλληλεπίδρασης Flory-Huggins ( $\chi$ ), γεγονός που οδηγεί σε μικροφασικό διαχωρισμό μεταξύ των δύο συστάδων ακόμα και σε περιπτώσεις μικρών μέσων μοριακών βαρών (που δύναται να προσεγγίζουν και τις τιμές μοριακών βαρών που σχηματίζονται οι ενδοεμπλοκές μεταξύ των μακρομοριακών αλυσίδων). Επιπλέον η πολυσιλοξανική συστάδα τα καθιστά αρκετά υποσχόμενα υλικά για νανοτεχνολογικές εφαρμογές λόγω της αντοχής στην εγχάραξη που εμφανίζει.

Η επιλογή του συστήματος (PS-*b*-PDMS)<sub>n</sub> όπου n = 1 ή 2 ή 3 ή 4 ή 6 αποδίδεται σε αρκετές παραμέτρους. Συγκεκριμένα, η υψηλή ομοιογένεια ως προς τη σύσταση και το μοριακό βάρος που εμφανίζουν τα συμπολυμερή τους προσδίδει σημαντικές ιδιότητες. Η αυστηρά καθορισμένη μακρομοριακή αρχιτεκτονική και τα επιθυμητά μοριακά χαρακτηριστικά απορρέουν από τη συνθετική πορεία που ακολουθείται και συγκεκριμένα λόγω του ανιοντικού πολυμερισμού και της χημείας χλωροσιλανίων. Επιπλέον, ο διαχωρισμός μικροφάσεων σε κατάσταση τήγματος (bulk) αποτελεί σημαντικό μέσο για την κατασκευή νανοδομών χωρίς την εφαρμογή πολύπλοκων σταδίων επεξεργασίας για τα συγκεκριμένα υλικά. Αξιοσημείωτο είναι να αναφερθεί ότι ελέγχοντας περιβαλλοντολογικές συνθήκες (πίεση και θερμοκρασία) για τα γραμμικά δισυσταδικά συμπολυμερή ή μεταβάλλοντας τη συνολική εντροπία του συστήματος για τα τρισυσταδικά ή/και αστεροειδή συμπολυμερή κατά τη μελέτη τους υπό μορφή λεπτών υμενίων (thin films), ο κάθετος προσανατολισμός των νανοδομών δύναται να υιοθετηθεί.

Οι παραπάνω λόγοι οδήγησαν στη σύνθεση: εικοσιτριών (23) γραμμικών δισυσταδικών συμπολυμερών του τύπου PS-*b*-PDMS, έξι (6) τρισυσταδικών συμπολυμερών ή (PS-*b*-PDMS)<sub>2</sub>, εννέα (9) αστεροειδών συμπολυμερών με τρεις κλάδους ή (PS-*b*-PDMS)<sub>3</sub>, έξι (6) αστεροειδών συμπολυμερών με τέσσερις κλάδους ή (PS-*b*-PDMS)<sub>4</sub> και πέντε (5) αστεροειδών συμπολυμερών με έξι κλάδους ή (PS-*b*-PDMS)<sub>6</sub>. Η σύνθεση πραγματοποιήθηκε μέσω του ανιοντικού πολυμερισμού και της διαδοχικής προσθήκης μονομερών σε συνθήκες υψηλού κενού. Η σύνθεση των γραμμικών και μη γραμμικών συμπολυμερών πραγματοποιήθηκε μέσω της χημείας των χλωροσιλανίων και των κατάλληλων αντιδραστηρίων σύζευξης τα οποία

περιλαμβάνουν το διχλωροδιμεθυλοσιλάνιο, το τριχλωρομεθυλοσιλάνιο, το τετραχλωροσιλάνιο και το 1,2-δις(τριχλωροσιλυλο)αιθάνιο. Η διαδικασία περιλαμβάνει την αντίδραση των ενεργών αλυσίδων του συμπολυμερούς (PS-*b*-PDMSLi<sup>+</sup>) με το εκάστοτε αντιδραστήριο και για το λόγο αυτό δεκαπέντε (15) από τα δισυσταδικά συμπολυμερή χρησιμοποιήθηκαν ως πρόδρομα υλικά για τη σύνθεση των πολύπλοκης αρχιτεκτονικής δειγμάτων.

Ο μοριακός χαρακτηρισμός των δειγμάτων της παρούσας διατριβής πραγματοποιήθηκε μέσω χρωματογραφίας αποκλεισμού μεγεθών (SEC), οσμωμετρίας τάσης ατμών ή μεμβράνης (VPO, MO) για να προσδιοριστούν η κατανομή μέσω μοριακών βαρών ( $\bar{M}$ ) και τα μέσα μοριακά βάρη κατ' αριθμό ( $\bar{M}_n$ ) αντίστοιχα. Η κατά βάρος και κατ' όγκο σύσταση σε όλα τα δείγματα υπολογίστηκε μέσω φασματοσκοπίας πυρηνικού μαγνητικού συντονισμού πρωτονίου (<sup>1</sup>H-NMR). Ο θερμικός χαρακτηρισμός έλαβε χώρα για τον προσδιορισμό των θερμικών μεταπτώσεων των συστημάτων και διεξήχθει μέσω της διαφορικής θερμιδομετρίας σάρωσης (DSC).

Η μελέτη της σχέσης δομής/ιδιοτήτων σε κατάσταση τήγματος για όλες τις αλληλουχίες δειγμάτων (γραμμικά και μη γραμμικά συμπολυμερή) πραγματοποιήθηκε μέσω ηλεκτρονικής μικροσκοπίας διέλευσης (TEM) και σκέδασης ακτίνων-X υπό μικρές γωνίες (SAXS). Μερικά εκ των συντεθειμένων γραμμικών συμπολυμερών μελετήθηκαν μέσω ηλεκτρονικής μικροσκοπίας σάρωσης πεδίου (FESEM) και μέσω ηλεκτρονικής μικροσκοπίας διέλευσης τριών διαστάσεων (3D TEM). Η μελέτη της θερμοκρασίας μετάπτωσης από την τάξη στην αταξία μερικών γραμμικών και μη γραμμικών συμπολυμερών κατέστη δυνατή μέσω *in-situ* πειραμάτων σκέδασης ακτίνων-X υπό μικρές γωνίες. Η μελέτη επιφάνειας ορισμένων δειγμάτων πραγματοποιήθηκε μέσω μικροσκοπίας σάρωσης με ακίδα (SPM).

Η πλειοψηφία των μετρήσεων του μορφολογικού χαρακτηρισμού πραγματοποιήθηκε μέσω της συνεργασίας με την ερευνητική ομάδα του Καθηγητή Rong-Ming Ho (Chemical Engineering Department at National Tsing Hua University, Hsinchu, Taiwan) οδηγώντας σε ενδιαφέροντα αποτελέσματα.

**Λέξεις κλειδιά:** Γραμμικά δισυσταδικά και τρισυσταδικά συμπολυμερή, αστεροειδή συμπολυμερή, υψηλή παράμετρος αλληλεπίδρασης  $\chi$ , επίδραση αρχιτεκτονικής, καινοτόμες φάσεις, βελτιωμένες μηχανικές ιδιότητες, σύγκριση μικροφασικού διαχωρισμού σε γραμμικά και μη γραμμικά συστήματα, θερμοκρασία μετάβασης από την τάξη στην αταξία.



# CHAPTER 1

## Introduction

### 1.1 Basic Concept

The unique ability of block copolymers (BCPs) to hierarchically self-assemble into chemically distinct nanodomains in bulk or in thin films has led to many potential applications for advanced technologies, such as: next-generation nanolithography, electronics and optics.<sup>1-3</sup> The immiscibility between the chemically different segments induces microphase separation on a scale which is strongly related to the molecular characteristics of the individual polymer blocks. Notably, the segregation strength is determined by the  $\chi N$  value where  $\chi$  corresponds to the Flory-Huggins interaction parameter and  $N$  to the total degree of polymerization of the copolymer studied.<sup>4-5</sup> The  $\chi$  value accounts for the enthalpy constraints, while  $N$  is influenced by entropy factors, with respect to the total free energy. In symmetric diblock copolymers, microphase separation takes place above a critical  $\chi N$  value and specifically when the product is equal or greater than 10.5. At fixed  $\chi$ , hence, there is a minimum  $N$  value necessary to lead to self-assembly.<sup>4-5</sup> The manipulation of BCPs volumetric composition, molecular weight, incompatibility and architecture allows the formation of diverse structures with size and periodicity ranging from 3 up to 100 nm or higher.<sup>2,6</sup>

To obtain well-defined BCPs with long-range order and predetermined feature sizes, living polymerization techniques are required. Anionic polymerization holds a key role in the designing of linear copolymers with structural homogeneity and predetermined characteristics.<sup>7</sup> In addition, anionic polymerization followed by chlorosilane linking chemistry has enabled the synthesis of linear and non-linear complex architecture copolymers with precise functionality (arm number) and narrow dispersity indices.

Star block copolymers constitute a representative case of complex architecture polymers. The linear diblock copolymer arms with identical chemical compositions are anchored to a central junction point forming linear and non-linear star block copolymers [(A-*b*-B)<sub>*n*</sub> (where  $n = 2, 3, 4, 6, \text{etc.}$ , B blocks are the inner segments which are connected together and A blocks are the outer blocks)].<sup>8</sup> The outstanding properties related to these materials [minimized defects/dislocations, increased order of self-assembly, lower  $\chi N_{\text{ODT}}$  (where ODT corresponds to order-disorder transition), enlarged phase boundaries] have attracted considerable interest recently.<sup>2,9</sup>

A significant class of materials synthesized by anionic polymerization is polystyrene-*b*-poly(dimethylsiloxane) or PS-*b*-PDMS diblock copolymers.<sup>10</sup> Silicon containing BCPs are highly applicable from both academic and industrial potential. Various intriguing properties such as extremely low glass transition temperature ( $T_g$ ), high thermal stability and exceptional etch contrast, are attributed to the Si-O-Si bonds located on the PDMS backbone. Also, the PS-*b*-PDMS system showcases a high  $\chi$  value ( $\sim 0.26$ ) enabling periodicities lower than 10 nm and undoubtedly belongs to the high  $\chi$ /low  $N$  block copolymers category for the decrease of feature sizes.<sup>2</sup>

From nanotechnology point of view, PS-*b*-PDMS seems as an ideal candidate for nanopatterning. However, due to the low surface energy of the elastomeric segments, PDMS segregates to the top (air/polymer) during thermal annealing, causing parallel orientation of the domains which is not always favorable.<sup>2,11-14</sup> Furthermore, high  $\chi$  materials in thin-film state display extremely slow assembly kinetics due to the lower inter-diffusivity of BCPs, leading to low pattern quality (e.g. defects and dislocations). This kinetic barrier is usually handled by using solvent vapor annealing or longer thermal annealing time or thermal annealing at significantly elevated temperatures for short time periods (well above the  $T_g$  of the segment with the highest glass transition temperature).<sup>15</sup>

Star block (PS-*b*-PDMS) <sub>$n=2, 3, 4, 6$</sub>  copolymers can be exploited as an innovative tool for the induction of perpendicular to the substrate nanodomains and even smaller dimensions.<sup>2,16-18</sup> Conformational asymmetry and overcrowding effect due to the existence of multiple chains, lead to entropic penalties. As a result, highly improved ordering degree can be achieved while the defects and dislocations are limited. The repulsive energy between the identical segments leads to chain stretching parallel to the interface further facilitating long range order and minimization of nanofeatures.<sup>2,16-18</sup>

## 1.2 Motivation and Outline of Thesis

The scope of this doctorate thesis was the synthesis of linear and non-linear diblock copolymers constituted by polystyrene and poly(dimethylsiloxane) through anionic polymerization under high vacuum techniques.<sup>10,19</sup> The PS-*b*-PDMS system was chosen due to the fact that the specific segments exhibit significant properties for targeted applications. Principally, the high  $\chi$  value and the inherent properties of PDMS, render the system a possible candidate for nanotechnology.

In total five (5) series of samples with different molecular characteristics were synthesized and characterized. In particular, sequential monomer addition led to the synthesis of linear diblock copolymers of the PS-*b*-PDMS type, while chlorosilane linking chemistry to the preparation of linear triblock copolymers of the PS-*b*-PDMS-*b*-PS or (PS-*b*-PDMS)<sub>2</sub> types as well as to non-linear (PS-*b*-PDMS)<sub>3 or 4 or 6</sub> star block copolymers. All samples prepared in the context of this dissertation are divided in five categories as follows:

1. *Linear diblock copolymers (PS-*b*-PDMS)*
2. *Linear triblock copolymers [PS-*b*-PDMS-*b*-PS or (PS-*b*-PDMS)<sub>2</sub>]*
3. *Non-linear three arm star block copolymers (PS-*b*-PDMS)<sub>3</sub>*
4. *Non-linear four arm star block copolymers (PS-*b*-PDMS)<sub>4</sub>*
5. *Non-linear six arm star block copolymers (PS-*b*-PDMS)<sub>6</sub>*

A schematic representation of the various copolymer architectures synthesized in this thesis is given in Figure 1.1, where the respective linking agent is given as well in order to understand the differences between the final materials.

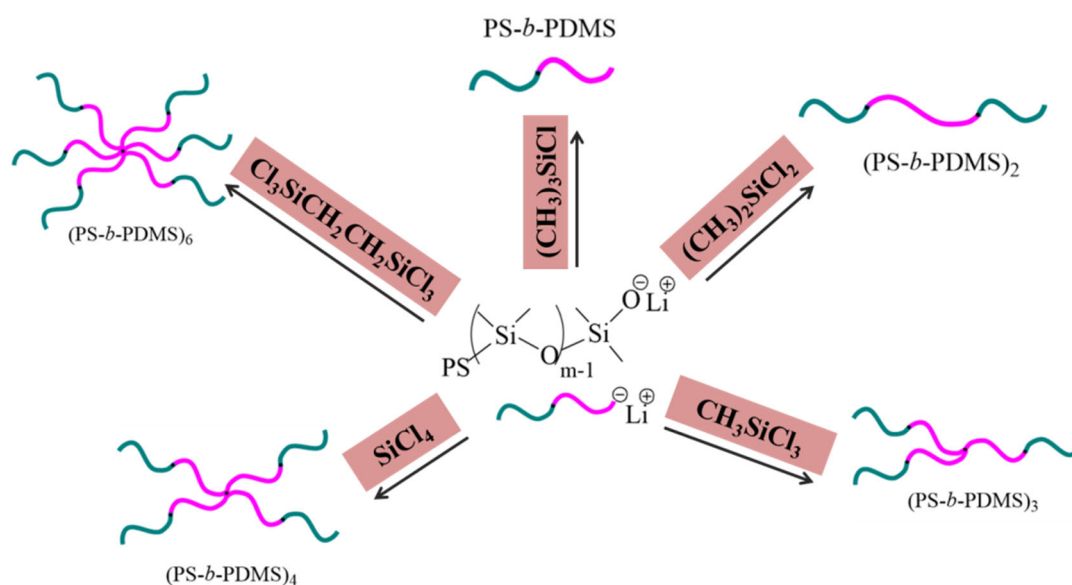


**Figure 1.1:** Schematic with respect to the different architectures synthesized in this thesis.

### 1.2.1 Linear Diblock Copolymers (PS-*b*-PDMS)

Anionic polymerization and sequential addition of styrene and hexamethylcyclotrisiloxane led to the synthesis of twenty three (23) linear diblock copolymers. Specifically, eight (8) out of the twenty three samples, with varying

molecular characteristics (various total number average molecular weights ranging from 20,000 g/mol to 130,000 g/mol and different volume fractions of the PDMS block) were synthesized to study the molecular, thermal and solid state properties.

Emphasis was given to the design of copolymers with the PDMS volume fraction being approximately 0.40 to enable the formation of network phases using solvents with different selectivity (solvent effect) towards the chemically different segments (PS and PDMS). A series of cubic network phases including double gyroid, double diamond and double primitive were obtained using selective solvents for the PS domains during solution casting and subsequent in-situ thermal annealing. ***It should be mentioned that the formation of a double primitive phase in a pure BCP (without homopolymer or any kind of additive) constitutes a novel finding in polymer physics studies. In addition, the BCP that adopted either gyroid or diamond structures (depending on the casting solvent) were implemented as a template for the fabrication of modified nanonetwork epoxy resins for enhanced energy dissipation.***

### **1.2.2 Linear and Non-Linear Copolymers [(PS-*b*-PDMS)<sub>*n*</sub> where *n* = 2 or 3 or 4 or 6]**

The remaining fifteen (15) diblock copolymer samples of the PS-*b*-PDMS type were used as precursors for the preparation of star block copolymers with different arm number (varied from 2 to 3 to 4 and 6, respectively). In this case, the living copolymer chains were coupled with an appropriate chlorosilane agent [dichlorodimethylsilane, trichloromethylsilane, silicon tetrachloride and 1,2-bis(trichlorosilyl)ethane) leading to the desired 2 arms, 3 arms, 4 arms and 6 arms, respectively] giving the desired linear and non-linear copolymers.

Even though, chlorosilane chemistry requires in-depth manipulations, time consuming reactions as well as additional purification procedures, it also provides the ability to obtain materials with precise functionality as well as molecular and compositional homogeneity. Through this synthetic strategy six (6) triblock copolymers [(PS-*b*-PDMS)<sub>2</sub>], nine (9) three arm star [(PS-*b*-PDMS)<sub>3</sub>], six (6) four arm star [(PS-*b*-PDMS)<sub>4</sub>] and five (5) six arm star [(PS-*b*-PDMS)<sub>6</sub>] block copolymers were synthesized.

***Interestingly enough, the synthesis and bulk properties of the non-linear six arm star block copolymers (PS-b-PDMS)<sub>6</sub> have not been reported in the literature yet and are studied for the first time in the research framework of this thesis.***

In all copolymers, the flexible PDMS segments comprised the inner chains while the stiffer PS domains were the peripheral macromolecules. Thorough characterization has been carried out to all the diblock precursors, to understand the origins of the self-assembly mechanism as the architecture alters from linear to non-linear structures. The linear precursors exhibited low (<10,000 g/mol) and average (<40,000 g/mol) molecular weight values and different volume fraction ratios to induce diverse structures during the study of microphase separation. The linear triblock and non-linear star block copolymers demonstrated molecular weight values which are equal to that of the diblock precursor multiplied with their functionality but as expected the volume fraction ratio remained similar to that of the initial precursor. Therefore, depending on the number of arms ( $n = 2$  or  $3$  or  $4$  or  $6$ ), the molecular weight values increased correspondingly. It should be noted that, most of the aforementioned complex architecture samples were synthesized using the same diblock precursor to compare the structure/properties relationship as the number of arms increases while the molecular characteristics of the chemically different blocks (PS and PDMS) remained identical.

Significant studies have been conducted on low molecular weight star block copolymers in conjunction with their linear precursors leading to novel findings in bulk. ***Specifically, an interesting wet-brush-like lamellar phase with an interdigitating structure was discovered irrespective of the arm number. In addition, a unique superlattice structure was evidenced and its transformation from superlattice with chain interdigitation to typical lamellae with bilayer texture was identified. Also, the architecture effect on the superlattice structure formation was explored.*** The topological effect of star-shaped architecture on the self-assembly mechanism was also investigated. Emphasis was given in the determination of order-disorder transition of linear and non-linear copolymer melts as well as the calculation of  $\chi$  value. Furthermore, the study with respect to the solid state properties of six-arm star block copolymers showcased quite intriguing results as will be thoroughly discussed in the relative chapter of this dissertation.

A general perspective of the PhD thesis is illustrated in Figure 1.2.

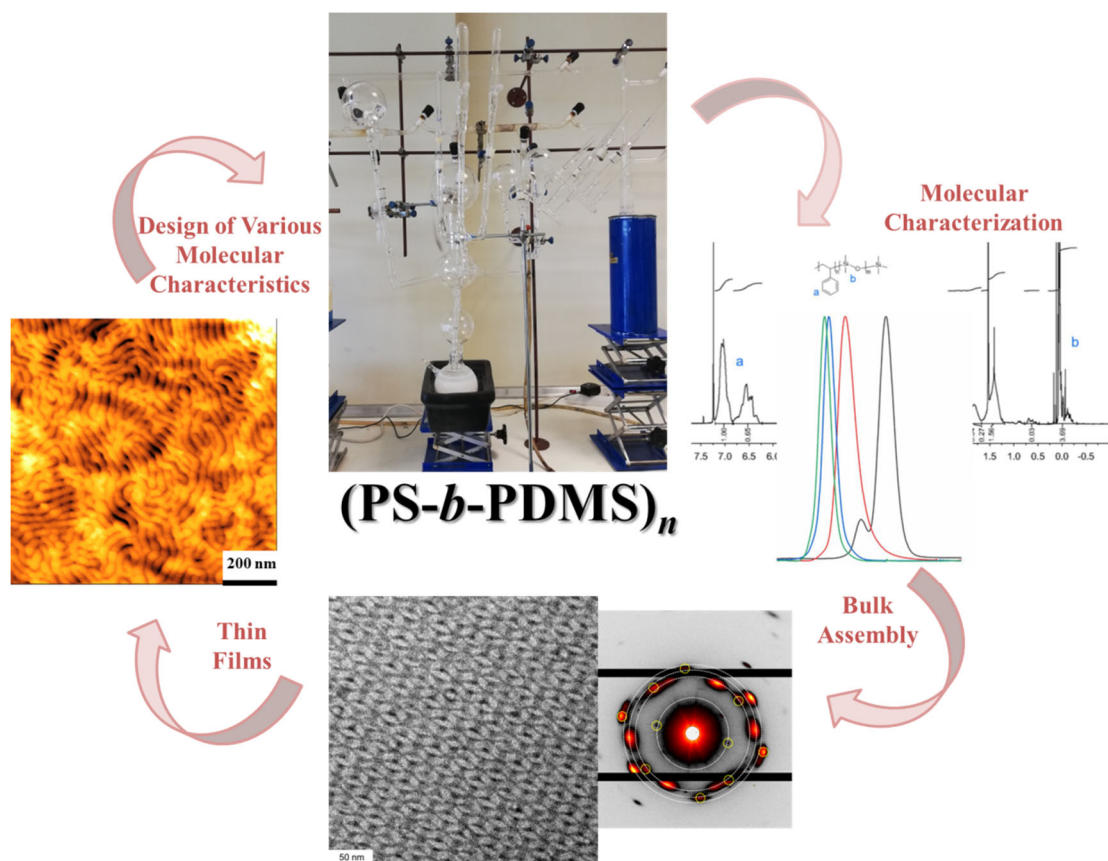


**Figure 1.2:** In the schematic the objectives of this thesis are presented. Following the synthesis of the different copolymer sequences, meticulous characterization in solution takes place to determine the molecular characteristics of the components. Bulk and thin film studies are conducted to study the self-assembly properties of the materials. Depending on the application, the design of different architecture copolymers with diverse molecular characteristics is carried out. The extensive use of the PS-*b*-PDMS copolymers with various arm numbers is attributed to anionic polymerization that enables the synthesis of well-defined materials with exquisite inherent features.

### 1.2.3 Characterization Techniques

The molecular characterization of all synthesized samples has been performed with various techniques such as: size exclusion chromatography (SEC), to determine the dispersity indices, membrane and/or vapour pressure osmometry (MO/VPO) to calculate the number average molecular weights ( $\bar{M}_n$ ) and proton nuclear magnetic resonance spectroscopy ( $^1\text{H-NMR}$ ) to verify the successful synthesis as well as to identify the composition of each segment in the linear and non-linear copolymers. Thermal transitions, the glass transition temperature and melting point variations as well as their dependence from the molecular weight and from the complexity of the system were confirmed through differential scanning calorimetry (DSC). The study of structure/ property relationship has been performed through bright field transmission

electron microscopy (TEM), small angle X-ray scattering (SAXS) and in some cases *via* field emission scanning electron microscopy and three-dimensional tomography (3D TEM). The surface morphology in thin films state was studied with scanning probe microscopy (SPM) for specific copolymer sequences. ***Interesting phenomena regarding the rheological properties of the synthesized materials were observed through in-situ SAXS experiments.***

Most of the above-mentioned morphological characterization methods (TEM, SAXS, 3D-tomography TEM, FESEM, in-situ SAXS) were conducted in the Chemical Engineering Department at National Tsing Hua University located in Hsinchu, Taiwan, through the collaboration with Professor Rong-Ming Ho and his research group, leading to novel experimental considerations for the self-assembly behavior of block copolymers. This collaboration has led to the publication of seven (7) manuscripts in high impact factor journals [ACS Applied Polymer Materials, Molecules-MDPI, PNAS, Polymers-MDPI, Macromolecules (2 articles), ACS Nano].

Slice and view SEM experiments on a specific copolymer sequence were carried out in the Department of Materials Science and Engineering, Texas A&M University, College Station, Texas, USA, through the collaboration with Professor Edwin L. Thomas leading to the submission of an additional publication in Science Advances.

#### **1.2.4 Overview of this Thesis**

**Chapter 2** provides all the necessary information regarding the fundamental principles of anionic polymerization. The synthetic routes involved in the copolymerization of styrene and hexamethylcyclotrisiloxane (or D<sub>3</sub>) monomers as well as the specific limitations due to the siloxane segment are analysed. The basic concept with respect to the chlorosilane chemistry is also reported to further contribute to the understanding of the star block copolymers synthesis.

**Chapter 3** summarizes the origins of self-assembly of diblock copolymers and a precise description regarding non-classical phases is given. Also the theoretical and experimental observations with respect to microphase separation of star-block copolymers are elaborated. Finally, the impact of processing procedures both in bulk and thin films on self-assembly kinetics is described.

In **Chapter 4** basic concepts related to the implementation of block copolymers in nanotechnology are discussed. The great importance of silicon-containing block copolymers is described and the high potential of the linear PS-*b*-PDMS and non-linear (PS-*b*-PDMS)<sub>n</sub> systems with respect to specific recent advances using these copolymers is also analysed. A direct answer to whether these copolymers constitute a very significant material is given.

**Chapter 5** provides all the necessary information regarding the experimental procedures adopted for the synthesis of the linear diblock and triblock copolymers as well as the non-linear star block copolymers of the PS-*b*-PDMS, (PS-*b*-PDMS)<sub>2</sub>, (PS-*b*-PDMS)<sub>3</sub>, (PS-*b*-PDMS)<sub>4</sub> and (PS-*b*-PDMS)<sub>6</sub> types respectively. Furthermore, a description of the purification procedures followed to minimize the traces from unwanted reagents prior to the reactions, as well as the instrumentation employed in the characterization of all samples synthesized for this thesis is thoroughly reported.

**Chapter 6** includes the molecular, thermal and morphological characterization results of all synthesized samples. Thorough analysis and discussion of the obtained results is performed to verify the successful synthesis of the linear and non-linear silicon-based copolymers, as well as to study and compare the structure/property relationship as the architecture changes and conformational asymmetry phenomena are arising.

**Chapter 7** summarizes the conclusions and future work.

Complete financial support during the framework of the research activities for this PhD thesis was given by the Hellenic Foundation of Research and Innovation (H.F.R.I.) under the 2<sup>nd</sup> Call for PhD Fellowship Grands with fellowship number 1651 and title: «Macromolecular Architecture: Synthesis, Characterization and Properties of Linear and Non-Linear Copolymers of Polystyrene and Poly(dimethylsiloxane) for Nanotechnology Applications (30 months, 2/10/2019-31/03/2022).

## CHAPTER 2

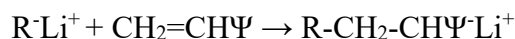
### Anionic Polymerization

#### 2.1 Introduction

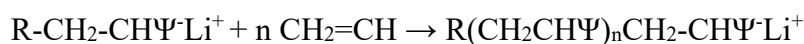
Living polymerization methods have enabled the synthesis of various well-defined linear and non-linear polymers presenting structural and compositional homogeneity.<sup>7,8</sup> The ability to design polymers (homopolymers, copolymers, terpolymers etc.) with absolute control over the molecular characteristics motivated numerous studies related to synthesis,<sup>7,8</sup> polymer physics<sup>4,5</sup> and their potential applications.<sup>1,3,20</sup> Since its first analytical reference by Szwarc<sup>21</sup> in 1956, anionic polymerization is undoubtedly considered the most well-known living polymerization to lead to low dispersity indices and has contributed to the advent of several living-like type polymerizations. The general concept involves the reaction between monomer and initiator in purified glass apparatuses with the constraint that all reagents are as well of extreme purity. In this case the enthalpy gain of the conversion of the double carbon bonds of the initial vinyl-type monomers to single or the ring strain relief in cyclic monomers carrying polar substituents outmatches the entropic penalty, while each chain grows at the same rate until all monomer has been consumed,<sup>7</sup> leading to polymers with dispersity indices well below 1.1.

The absolute control of termination and/or chain transfer reactions, render the negatively charged active chain-ends bearing positively charged metallic counterions (usually Li<sup>+</sup>) able to remain highly reactive but stable for adequate time, prior to the addition of a second monomer or a linking reagent.<sup>7,8,22</sup> The general synthetic route in anionic polymerization involves the following two most prominent reaction steps:

**Initiation:**



**Propagation:**

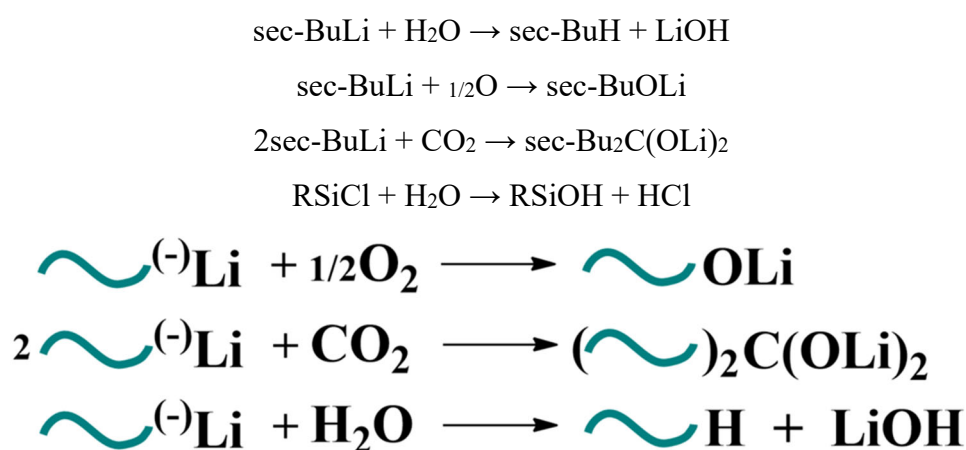


**Scheme 2.1:** *General initiation and propagation reactions for living anionic polymerization.*

In most cases, the termination of the living chains takes place after the introduction of a proper electrophilic agent such as methanol or trimethylchlorosilane.<sup>23</sup>

To avoid any termination of the active sites or deactivation of the coupling agents, high vacuum techniques are employed. The introduction of atmospheric traces

in the reactions such as humidity, carbon dioxide, oxygen or impurities from the insufficient purification of the reagents involved in the polymerization procedure lead to premature termination and undesired molecular characteristics. The reactions between the most commonly utilized anionic polymerization initiator (secondary butyllithium, *sec*-BuLi) with water, oxygen and carbon dioxide as well as the deactivation of linking chlorosilane agents due to water are presented in Scheme 2.2. The termination reactions of the living macroanion sites with O<sub>2</sub>, CO<sub>2</sub> and H<sub>2</sub>O are also illustrated.



**Scheme 2.2:** Termination reactions of *sec*-BuLi with water, oxygen and carbon dioxide as well as deactivation reaction of chlorosilane agent in the presence of water. Termination reactions of the living macroanions with O<sub>2</sub>, CO<sub>2</sub> and H<sub>2</sub>O.

Therefore, to conduct any anionic polymerization reaction the existence of inert atmosphere or high vacuum conditions (10<sup>-6</sup>-10<sup>-7</sup> mmHg) in conjunction with thoroughly purified reagents is a necessity. High vacuum techniques are quite challenging and require specific manipulations as well as specialized scientific glass blowing techniques. The time consuming procedures together with the limited quantity of the final material (especially when complex architectures are synthesized) can be compensated by the high quality of the synthesized polymers.

An outstanding feature of anionic polymerization is the extremely narrow dispersity indices ( $\bar{D} < 1.1$ ) exhibited in the final products, attributed to the higher initiation ( $R_i$ ) compared to the propagation rate ( $R_p$ ), while the monomer addition occurs irreversibly.<sup>7,24</sup> The dispersity holds a central role in the self-assembly properties, since high ordering degree can be achieved using narrow-dispersed polymers.<sup>25,26</sup> To ensure low  $\bar{D}$  values some distinctive parameters such as the

appropriate choice of initiator-solvent-monomer system in combination with the higher  $R_i$  to  $R_p$  at a specified temperature should be taken into consideration. The polymerization of all monomeric units proceeds simultaneously, while the number of monomeric units added to the living chains remains almost similar until all monomer quantity is consumed.<sup>27</sup>

From the above, it is easily understood that the polymerization reaction will be completed when all monomer quantity has reacted during the propagation reaction leading to 100% yield in most cases. Consequently, the total number average molecular weight ( $\bar{M}_n$ ) of the final polymer can be sufficiently determined by the known quantity of the monomer and the concentration of the initiator,<sup>22</sup> using the following equation (2.1):

$$\bar{M}_n = \frac{g_{monomer}}{moles_{initiator}} \quad (2.1)$$

The molecular weight constitutes another variable affecting the polymer properties. The synthesis of polymers with predetermined molecular characteristics is of major importance for different applications ranging from low-molecular weight nanotechnology-related ones<sup>1-3,6</sup> to high-molecular weight materials targeting to photonics performances.<sup>28,29</sup>

Several organometallic compounds have been utilized as anionic initiators but the most prominent are the alkyllithium compounds, which are commercially available or can be synthesized by the reaction of alkyl chloride with lithium (Li) metal.<sup>23,30</sup> Various features related to the alkyllithiums in combination with their solubility in hydrocarbon solvents render them as best initiators of choice. The smallest radius, the highest electronegativity as well as the highest ionization potential of lithium among other alkali metals<sup>30,31</sup> suggest that C-Li bond exhibits both covalent and ionic properties.<sup>30,32,33</sup> The formation of aggregates is also a characteristic property of organolithium compounds.<sup>27,30</sup> The organic moiety structures, the solvent's nature, the solution concentration and the temperature have a severe impact on the extent of aggregation.<sup>27,30</sup> Principally, the lower the degree of association the higher the reactivity of the initiator will be during the reaction.<sup>34</sup> Decreased concentration, increased temperature, strongly solvating solvents and the presence of organic groups are the contributing factors to the enhanced reactivity of the alkyllithium initiators.<sup>27,30</sup> The relative reactivity of multiple alkyllithium reagents

in hydrocarbon solvents for the polymerization of styrene as well as dienes (isoprene and butadiene) and the respective degree of aggregation (in parentheses) are presented below<sup>35</sup>:

Methylolithium (2) > secondary butyllithium (*sec*-BuLi) (4) > isopropyllithium (*i*-PrLi) (4-6) > tertiary butyllithium (*tert*-BuLi) (4) > normal butyllithium (*n*-BuLi) (6)

In the propagation step the negatively charged macromolecular chains with the lithium counterion are able also to aggregate. In the case of living (polystyryl)lithium [PS<sup>(-)</sup>Li<sup>(+)</sup>] chains in aromatic and aliphatic hydrocarbon solvents, the aggregation rate has been found equal to 2.<sup>27,35</sup> Several kinetic studies indicate that the aggregation rate of initiators and macromolecular chains in polar environments is further decreased.<sup>27,34</sup> Specifically, the degree of association of PS<sup>(-)</sup>Li<sup>(+)</sup> in tetrahydrofuran (THF) has been calculated equal to 1, due to the shifted equilibrium between the aggregated and non-aggregated polymer chains towards the non-aggregated ionic pairs PS<sup>(-)</sup>Li<sup>(+)</sup>, resulting in decreased solution viscosity and enhanced reaction kinetics.<sup>36,37</sup> All ionic pairs evident in Scheme 2.3 are regarded as a living centre enabling the polymerization. Free ions, even at lower concentrations, are highly functional and accountable for the substantially increased propagation rate. Accordingly, the relative enhancement on the concentration of free ions leads to higher propagation rate in polar solvents.

**Aggregated:** (PS<sup>-</sup>Li<sup>+</sup>)<sub>2</sub> ↔ **Non-aggregated:** 2(PS<sup>-</sup>Li<sup>+</sup>) ↔ **In contact:** PS<sup>-</sup>,Li<sup>+</sup> ↔ **In distance:** PS<sup>-</sup> || Li<sup>+</sup> ↔ **Free ions:** PS<sup>-</sup> Li<sup>+</sup>

**Scheme 2.3:** Aggregated and non-aggregated ionic pair structure of (polystyryl)lithium in the presence of polar environments.

The monomers that are susceptible to anionic polymerization should form stable reactive sites at given polymerization conditions. Various monomers including vinyl such as styrene and its derivatives (a-methyl styrene, p-methyl styrene),<sup>38-40</sup> (meth)acrylates<sup>41-43</sup> as well as vinylpyridines (2- and 4-vinylpyridine),<sup>44</sup> alkadienes (isoprene, 1,3-butadiene, 2-methyl-1,3-pentadiene, 1,3-cyclohexadiene)<sup>45-48</sup> and cyclic (ethylene oxide, hexamethylcyclotrisiloxane and ε-caprolactone)<sup>10,49,50</sup> have been utilized in anionic polymerization, due to their ability to stabilize the propagating negative charge. Each monomer should be polymerized under specified reaction conditions<sup>30</sup> (e.g. bulky initiators, low temperature, etc.) to obtain polymers with the desired properties, macromolecular architecture, structural and molecular homogeneity.

## 2.2 Block Copolymers

Block copolymers are classified amongst the most prominent class of materials for many applications<sup>1-3,20,28,29</sup> due to the chemical immiscibility between the two chemically different but covalently bonded segments leading to exceptional properties. In addition, the final materials combine both chemical and physical features of both homopolymer subunits. Furthermore, the two chemically divergent blocks are able to microphase separate in various well-ordered nanostructures both in bulk<sup>4,5</sup> and in thin film states,<sup>6</sup> further expanding their potential uses and applications.

Recently developed living polymerization methods and post-polymerization chemical modification reactions have a critical role in the development of several copolymer combinations, but anionic polymerization remains ideal for intended applications. When particular prerequisites are fulfilled, such as complete absence of impurities and existence of high vacuum conditions, excellent control over the molecular characteristics (molecular weight and composition), architecture and functionality, compared to other controlled polymerization techniques, is achieved. In addition, complex architecture copolymers such as miktoarm or star block,<sup>8</sup> graft<sup>51</sup> and dendritic<sup>52</sup> can be synthesized combining anionic polymerization and the appropriate linking agents.

### 2.2.1 Linear Diblock Copolymers

Diblock copolymers are consisting from chemically immiscible monomeric units grouped in two separate segments linked together with covalent bonds.<sup>53</sup> The most commonly encountered method of synthesizing linear diblock copolymers involves the sequential addition of two monomers (A and B), where after the complete polymerization of A, the B monomer is introduced and polymerized, until its absolute consumption, due to the living macroanions of the first block. After the complete consumption of the second monomer's quantity, a terminating agent is added to deactivate the living ends under high vacuum.

It should be noted that, sequential monomer addition is strongly dependant on the nucleophilicity of the macroanions. As a general rule, the polymerization of the second monomer takes place only when the nucleophilicity of the macroanions is sufficiently higher than the one obtained from the second monomer. The increased electron affinity determines the order in which monomers are added during sequential addition as follows: styrene < butadiene~isoprene < vinyl pyridine < methyl acrylate

< ethylene oxide < hexamethylcyclotrisiloxane.<sup>20</sup> Slight alternations in the reactivity order are possible, but only limited studies related to such exemptions are found in the literature.<sup>54-56</sup> Even though, the electron affinity of some monomers is indeed higher than others (e.g. methyl acrylate) they are not able to act as macromolecular initiators, making the polymerization of the second monomer unattainable (e.g. hexamethylcyclotrisiloxane or D<sub>3</sub>) through sequential monomer addition. Furthermore, in almost all cases PDMS<sup>-</sup>Li<sup>+</sup> macroanions are weak nucleophiles rendering them unable to initiate the polymerization of any other monomer.

As a second required condition, the initiation rate for the polymerization of the B monomer by the macroanions of the A should be higher than the propagation rate during the polymerization of the B monomer to obtain well-defined BCPs exhibiting molecular and compositional homogeneity. The high purification degree of all compounds involved in the polymerization from monomer, initiator, solvent, linking agent to termination reagent is an inevitable precondition for the successful outcome of all reactions.

The synthesis of BCPs through anionic polymerization and sequential monomer addition has been reported in the literature for diverse combinations of copolymers.<sup>23 pp541-623</sup> A significant class of materials containing polysiloxane segments has attracted tremendous interest in both scientific and industrial community due to their exploitation in the field of nanotechnology and specifically in nanostructuring and nanofabrication.<sup>2,11-14,16-18</sup> An extensive report on their potential uses will be given in a following chapter of this dissertation (Chapter 4).

Regarding the synthesis of silicon-containing BCPs, anionic polymerization of styrene<sup>10,57</sup> or alkadienes<sup>58-60</sup> as first blocks followed by the addition of siloxane monomers has led to the preparation of model copolymers with various molecular characteristics. PDMS-based BCPs require specific experimental conditions to ensure high quality products. In addition to the insufficient nucleophilicity that binds the utilization of the specific monomer hexamethylcyclotrisiloxane or D<sub>3</sub> as the last segment, side reactions<sup>61-63</sup> displayed during the propagation step lead to broader dispersity indices. They can be categorized as back-biting or decomposition, where a nucleophilic addition of the silanol anion in a distant Si atom occurs, resulting in cyclic species, and inter-chain (redistribution) reactions (Figure 2.1). To eliminate the aforementioned side reactions specified experimental conditions are applied.<sup>10,64</sup> The addition of a polar solvent contributes to the higher propagation rate in which the

lithium counterion interacts preferentially with polar additives rather than the active poly(siloxane) propagating chain end. When the concentration of the D<sub>3</sub> monomer is substantially decreased during the polymerization, especially in the cases of higher molecular weight, the contribution of side reactions is enhanced. For this reason, to avoid such unwanted reactions a terminating agent was introduced to the solution prior to the quantitative conversion of D<sub>3</sub>.<sup>57</sup> The addition of two fold excess of the D<sub>3</sub> monomer to enhance the polymerization kinetics and to eliminate the side reactions has also been reported.<sup>57,65</sup> Recently, the most dominant synthetic route involves the use of low temperature (-20 °C) for the polymerization of the remaining monomer quantity (at least 50%) without the appearance of any side reactions as verified by the subsequent molecular characterization techniques.<sup>10</sup>

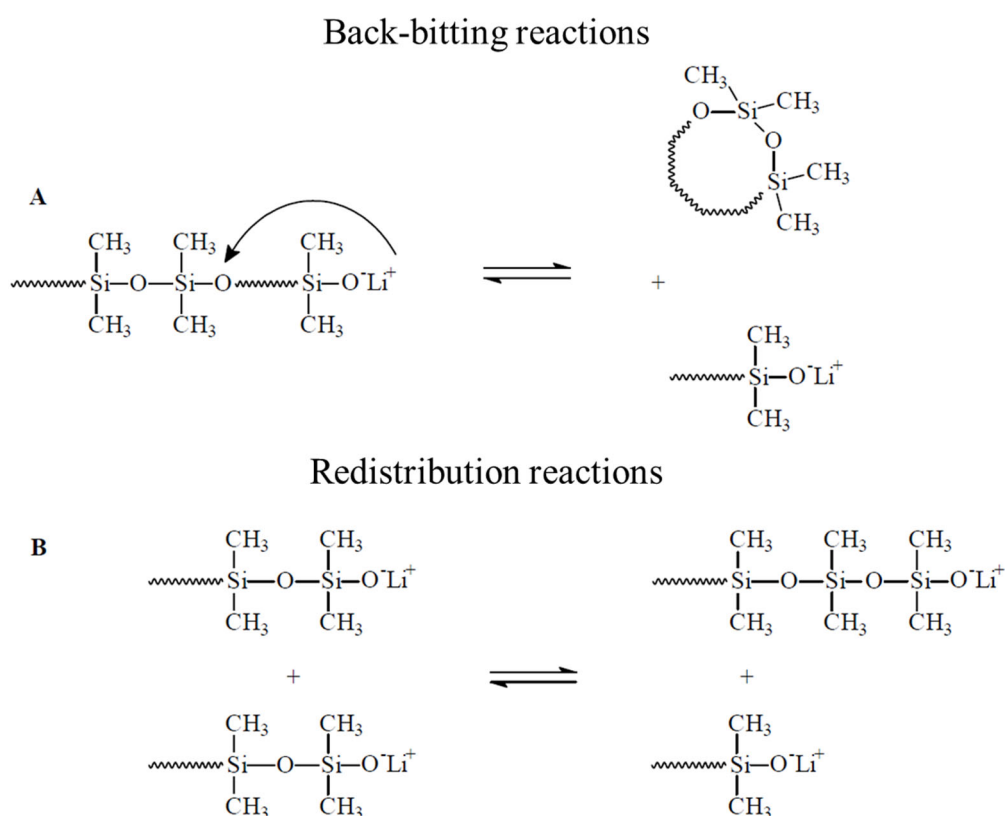


**Figure 2.1:** Side reactions (back-biting and redistribution) during PDMS synthesis.

### 2.2.2 Linear Symmetric Triblock Copolymers

Triblock copolymers and especially silicon-containing ones have a significant role in various nanotechnology applications due to their major processing window and the ability to adopt smaller dimensions for comparable molecular weights to the analogous diblock copolymers.<sup>66-69</sup> In addition, the thin-film assembly of ABA

copolymers exhibits a unique benefit based on theoretical and experimental studies, where perpendicular orientation of the nanodomains is more easily achievable than in diblock copolymers.<sup>67-69</sup> Anionic polymerization offers an absolute control during the synthesis and yields well-defined triblock copolymers with the desired molecular and compositional characteristics.

Linear symmetric triblock copolymers consist of two different segments, where the outer blocks have identical chemical nature and molecular characteristics, while the second (middle) block has different chemical structure. Several synthetic strategies have been employed for the preparation of well-defined *A-b-B-b-A* triblock copolymers in terms of molecular weight and dispersity. An *A-b-B-b-A* copolymer can be prepared by adding specific amount of A monomer to the living  $A-b-B^{(-)}Li^{(+)}$  chains in a process known as sequential addition of monomers or by coupling the living copolymer  $[A-b-B/2^{(-)}Li^{(+)}]$  species with an appropriate coupling agent. In this case the A blocks have exactly identical molecular characteristics and the B active chains have half the molecular weight needed in the final triblock copolymer after the linking reaction with the appropriate linking reagent. The use of difunctional initiators has also been reported in the literature, where the synthesis starts off from the difunctional living sites of B chains and then the appropriate quantity of the other monomer is added.<sup>23pp</sup>

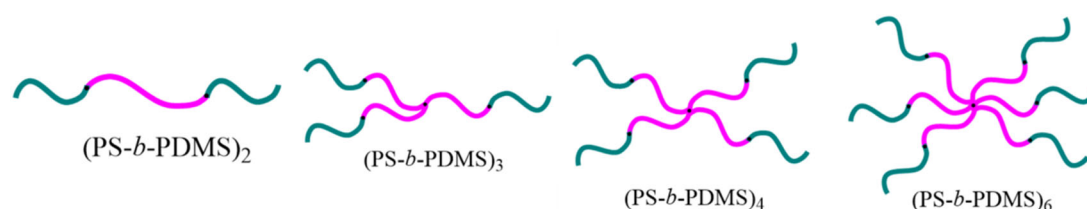
Sequential monomer addition is possible to lead to non-perfectly symmetric materials since the amount of A monomer used in the first and third step will be different, leading to non-identical molecular characteristics.

The use of chlorosilane linking chemistry allows the synthesis of perfectly symmetric ABA copolymers in a two-step procedure. Initially, a living diblock copolymer precursor AB is synthesized through sequential monomer addition (the B block has only half the molecular weight compared to the desired one) and then the linking reaction takes place.<sup>70</sup> Specifically, a linking agent (e.g. dichlorodimethylsilane) bearing two functional groups reacts with the living diblock chains to the formation of covalent bonds. Moreover, the stoichiometry of the reaction is difficult to control, therefore the use of a small excess of the living diblock copolymer (approximately 10% excess) is needed to ensure complete linking necessary. After completion of the linking reaction (2-3 weeks at least) the excess diblock copolymer is removed by fractionation (a technique which will be explained in Chapter 5 of this dissertation).

The key parameters for the successful synthesis using this method will be thoroughly elaborated as follows, in which a comprehensive analysis of chlorosilane chemistry for the preparation of star block copolymers with different functionalities will be provided.

### 2.2.3 Star Block Copolymers with Various Functionalities

Star block copolymers are comprised by various linear diblock copolymer chains (arms) connected to a central junction point (core).<sup>8</sup> All arms display identical chemical composition and molecular weight.<sup>16-19</sup> A schematic illustration of the star block copolymers synthesized in the framework of this thesis is presented in Scheme 2.3.



**Scheme 2.4:** Schematic illustrations of the synthesized star block copolymers.

The intriguing properties are induced by the complex architecture due to the conformational asymmetry leading to high scientific interest. Star block copolymers self-assembly provides enhanced benefits directly related to orientation, order, feature sizes and are potential low cost candidates for next-generation patterning.<sup>2</sup> Nanopatterning relates on perfectly controlling the behavior and structure of the surface at a nanoscale level, therefore, well-defined star block copolymers devoid of any impurities are of paramount importance.

Anionic polymerization in combination with chlorosilane chemistry is the method of choice for the synthesis of star block copolymers with various functionalities.<sup>19,68,71</sup> The prevalence of chlorosilane coupling agents towards other multifunctional electrophilic coupling agents such as chloromethylated benzene derivatives lays upon the efficient and complete coupling of the polymeric chains. In cases of increased functionality and high molecular weight, chloromethylated benzene derivatives lead to insufficient reactions and uncontrolled number of arms.<sup>70,72</sup>

The linking efficiency of chlorosilane compounds is severely influenced by the chemical nature of each monomeric unit. The minimization of steric factors

contributes to the complete reaction of living chain ends with a stoichiometric quantity of linking agents. The electrophilic substitution rate decreases in the order: polybutadienyl > polyisoprenyl > polystyryl. Furthermore, the successful reaction outcome is determined by the stereochemistry of linking agents. Steric hindrance phenomena are evident when the multifunctional reagent bears at least four chlorine atoms. Star block copolymers with higher than four arms, demand the use of reagents in which the number of chlorine atoms per silicon should be less than three and silicon atoms should be separated with ethylene spacers.<sup>70,72</sup> It should be noted here that the linking agents of the  $(\text{CH}_3)_2\text{SiCl}_2$ ,  $\text{CH}_3\text{SiCl}_3$  and  $\text{SiCl}_4$  types are volatile compounds whereas the reagents in which the number of chlorine atoms per silicon is less than three and the silicon atoms are separated with ethylene spacers are high boiling point compounds.

Note that, chlorosilane related linking reactions is a time consuming process, since the coupling of the living chains requires longer reaction time and high vacuum conditions to avoid the linking agents' deactivation which would eventually lead to stars with lower than the desired functionality. Additional caution should be given on the stoichiometry of the coupling reaction. Principally, an excess of reacting chains to the linking sites is used to ensure that all chlorine atoms of the coupling agent have reacted completely. It has been reported in the literature that, to prepare poly(butadiene) stars with increased functionality (number of arms > 64) the excess of living ends over Si-Cl should exceed 100%.<sup>70,72</sup>

One final demanding step of coupling reactions is the elimination of the unlinked products (e.g. unwanted diblock of the A-*b*-B type from the desired A-*b*-B-*b*-A triblock copolymer) which takes place by employing a fractionation procedure to the final material which is based on solvent/non-solvent condition system. Specifically, the elimination of the excess of the unreacted species takes place with the use of a solvent/non solvent pair by partitioning the different polymer species between two liquid phases based upon their molecular characteristics (molecular weight and composition).

In general, star block polymers have a significant role in the development of polymer chemistry and physics. They may provide a different alternative to the high  $\chi$ /low *N* approach to obtain low feature sizes that will be elaborated in Chapter 4 of this dissertation. The synthesis of silicon-containing star block copolymers of polystyrene and poly(dimethylsiloxane) using several chlorosilanes as linking agents

has been mentioned in the literature and has led to fascinating discoveries both in bulk<sup>19,73</sup> and thin film states.<sup>16-18,68</sup> In this reports the living diblock copolymer chains of the PS-*b*-PDMSLi<sup>+</sup> type were synthesized through sequential addition between the two monomers and then were reacted with an excess of several linking agents for the preparation of linear symmetric two- and non-linear symmetric three- and four- arm stars.

## CHAPTER 3

### Physical Properties of Linear and Non-Linear Star Block Copolymers

#### 3.1 Theoretical Background

Linear diblock copolymers (A-*b*-B) are constituted, in most cases, by immiscible A, B chains covalently attached to each other (this covalent bond is referred to as junction point) and represent a significant class of materials in the contemporary polymer science. In principal, microphase separation is driven by entropy and enthalpy contributions.<sup>4,5</sup> The ability of such copolymers to spontaneously microphase separate in various nanostructures in bulk and in thin film states has intrigued many theoretical<sup>9</sup> and experimental studies.<sup>2</sup> Their implementation in nanotechnology is attributed to their self-assembly potential that leads to distinct periodic nanopatterns with long range order.

The origin of self-assembly is strongly related to the free energy of mixing. Slight chemical or structural differences between the two covalently bonded segments produce free energy contributions that are unfavorable to mixing. In the simplest case, the value of Gibbs free energy ( $\Delta G_M$ ) of mixing between two different homopolymers is described by the following equation (3.1), where  $\Delta H_M$  and  $T\Delta S_M$  stand for the mixing enthalpy and entropy variations, respectively:

$$\Delta G_M = \Delta H_M - T\Delta S_M \quad (3.1)$$

In the case of linear diblock copolymers the final free energy (F) is given by a more complex equation (3.2):

$$\frac{F}{KT} = \chi_{AB}\varphi_A\varphi_B + \left(\frac{\varphi_A}{N_A}\right)\ln(\varphi_A) + \left(\frac{\varphi_B}{N_B}\right)\ln(\varphi_B) \quad (3.2)$$

where  $\varphi_A$ ,  $\varphi_B$  correspond to the volume fraction and  $N_A$ ,  $N_B$  to the degree of polymerization of A and B segments respectively. The composition (or volume fraction  $\varphi$ ) as well as the  $N$  values, which are directly associated with the number average molecular weight of both blocks, represent the entropy of mixing, while  $\chi$  is the Flory-Huggins interaction parameter that shows the repulsion between the constituents and is related to enthalpic contributions. From equation (3.2) it is straightforward that microphase separation depends on the product  $\chi N$ , since  $\chi \ll N$ . The  $\chi$  value demonstrates an inversely proportional dependence on temperature (T) based on the following expression<sup>4</sup> (3.3):

$$\chi = \frac{a}{T} + \beta \quad (3.3)$$

where  $\alpha$ ,  $\beta$  are dimensionless constants<sup>74</sup> that account for the enthalpic contributions to the Gibbs free energy of mixing (a) and excess entropy of mixing (b) respectively, according to the Gibbs free energy theory related to polymer-polymer interaction parameter and both constants are varying depending on the studied segments.<sup>74,75</sup> Consequently, the mixing is promoted as the temperature increases.

In equilibrium state the polymer chains tend to maintain their unperturbed dimensions to minimize the free energy. An increased  $\chi$  value, when the system is studied at low temperature or due to high incompatibility between A and B blocks, leads to strong segregation, favoring the formation of microdomains without any mixing between the A, B domains which are separated from each other by narrow interfaces with minimal or zero thickness. In addition, when  $N$  value is sufficiently high, the chains do not maintain their unperturbed dimensions and the loss in configurational entropy results in a local ordering which is referred as microphase separation. Disordered phases are evident when entropic factors dominate and specifically when the  $\chi$  and/or  $N$  values are substantially decreased. In cases of low segment-segment interaction parameter or high temperature (related to  $\chi$ ) or very low molecular weights (related to  $N$ ) for the systems under consideration, a phenomenon called order-disorder transition (ODT) takes place while the temperature where the transition occurs is known as microphase separation temperature or order-disorder temperature ( $T_{ODT}$ ). For a diblock copolymer exhibiting symmetric segments, meaning  $\phi_A = \phi_B = 0.5$ , the order-disorder transition is observed when  $\chi N \sim 10.5$ .<sup>4,5</sup>

A system goes through the ODT to the weak segregation limit (WSL) when  $\chi N \sim 10.5$  and the diblock copolymers demonstrating this behavior incorporate their junction points on interfaces with enhanced thickness due to phase mixing, since the macromolecular conformations are similar to the unperturbed dimensions. When the chain conformations are rather perturbed ( $\chi N \gg 10.5$ ), pure A and B domains are formed and the interface between the microdomains is quite narrow (minimal or no thickness evident). This regime is called strong segregation limit (SSL). The complete absence of mixing is attributed to the stretched conformation that forces the dissimilar chains to expand away from the interface as far as possible. In this case the  $\chi$  value is related only to the interface area where the junction points between the two different segments are located.<sup>4,5</sup>

### 3.1.1 Segregation Limit Regimes

Various theoretical studies have been developed to describe the phase behavior of the block copolymers and self-consistent field theory (SCFT)<sup>76</sup> is amongst the most dominant theoretical approaches. In SCFT the polymers are characterized as random walks having a monomer statistical segment length,  $\alpha$ , that is equal for both blocks ( $\alpha_A=\alpha_B$ ) and the interaction between them, which accounts for the free energy cost, is described by the  $\chi$  value. The excess free energy per chain is designated by a dimensionless constant ( $g$ ). The theory predicts that a free energy  $g$  for each phase is related with the product  $\chi N$  and the composition  $\varphi_A$ .<sup>76,77</sup>

Consequently, the microphase separated structures can be denoted as phase diagrams by plotting  $\chi N$  as a function of volume fraction and when  $(\chi N)_{ODT}=10.495$  for a symmetric copolymer ( $\varphi_A=0.5$ ) a second order transition from a disordered to an ordered lamellar phase takes place.

The volume fraction can be calculated according to the following equation (3.4), where  $\varphi_A$  corresponds to the volume fraction of A block.  $d_A, d_B$  to the densities and  $f_A, f_B$  to the mass fraction values of A and B blocks respectively.

$$\varphi_A = \frac{f_A d_A}{f_A d_B + f_B d_A} \quad (3.4)$$

The mass fraction of A block can be directly estimated as follows (equation 3.5):

$$f_A = \frac{\bar{M}_{n,A}}{\bar{M}_{n,A} + \bar{M}_{n,B}} \quad (3.5)$$

In the phase diagram the limits are more curved with varying volume fraction values as the segregation becomes weaker. Leibler theory<sup>76</sup> also predicted that with different compositions and  $\chi N$  values higher than 10.5, the system undergoes a first order transition from the disorder phase to a body centered cubic (BCC) sphere phase due to the large asymmetry between the segments. As the  $\chi N$  increases the system undergoes a transition to hexagonally packed cylinders (HPC) and then to the lamellar phase. All the above are illustrated in Figure 3.1.

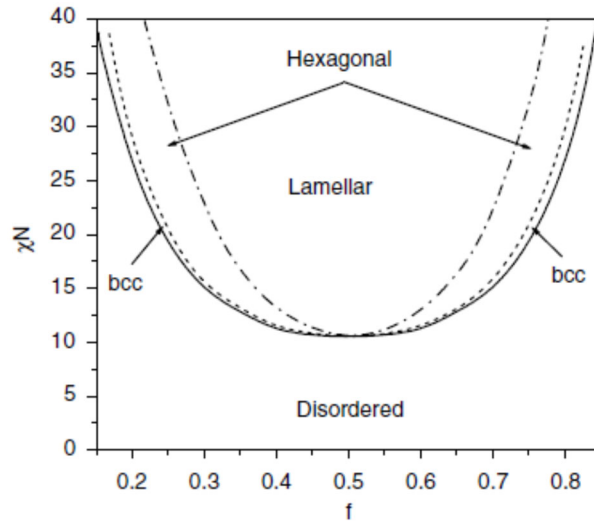


**Figure 3.1:** Theoretical phase diagram for linear diblock copolymers within the mean-field theory assuming equal monomer volumes and statistical segment lengths for the two blocks. On this phase diagram,  $f$  corresponds to the volume fraction.<sup>76</sup>

For the strong segregation limit ( $\chi N > 100$ ) the minimized interface width allows better organization of the structures, meaning 2D surfaces bear the junction points and have both macromolecular chains completely distinct in the case of the simpler diblock copolymers. Helfand and Wasserman<sup>78-80</sup> introduced a post-SCFT model taking into consideration three contributing parameters to the free energy and specifically:

1. the contact enthalpy at the interface between the A and B domains,
2. minimization of entropy due to stretching of chains and
3. confinement entropy due to localization of the junction points at the interface.

The microdomain thickness is predicted using the following equation, where  $\delta \sim 9/14$ ,  $\nu = 1/7$  and  $\alpha$  corresponds to the statistical segment length:

$$d \sim \alpha N^\delta \chi^\nu \quad (3.6)$$

Semenov<sup>81</sup> developed a theoretical study in which the free energy in the asymptotic limit, given in the equation 3.7, suggests that polymer chains are strongly stretched. The equation expresses a great dependence on  $N$  and a weaker one on  $\chi$ .

$$d \sim \alpha N^{2/3} \chi^{1/6} \quad (3.7)$$

It is already well-established that three parameters namely  $\chi$ ,  $N$  and  $\phi$  hold a decisive role in the self-assembly behavior. The chain packing and conformation between the chemically different blocks at the interfaces strongly affect the adopted

morphologies.<sup>4</sup> Manipulating each segment composition leads to various nanostructures. Weaker effect of interfacial curvature energy than stretching of chains favors lamellar (LAM) structures. The higher contribution of the interfacial curvature energy allows the formation of ordered phases with curved interfaces such as bi-continuous double gyroid (DG), hexagonally packed cylinders (HEX) and body-centered cubic (BCC) lattice.<sup>82-86</sup>

Employing a polystyrene-*b*-poly(isoprene) (PS-*b*-PI) system led to the experimental conformation of these ordered phases.<sup>83</sup> Using SCFT and PS-*b*-PI diblock copolymers both theoretical and experimental equilibrium phase diagrams, including the various ordered phases were constructed. In Figure 3.2a the self-assembly of a symmetric A-*b*-B diblock copolymer with lamellar morphology and domain spacing ( $d$ ) and the mean-field phase diagram (Figure 3.2b) showing all the additional stable morphologies in BCPs as a function of volume fraction of A block ( $f_1$ ) are presented.<sup>82,87,88</sup>

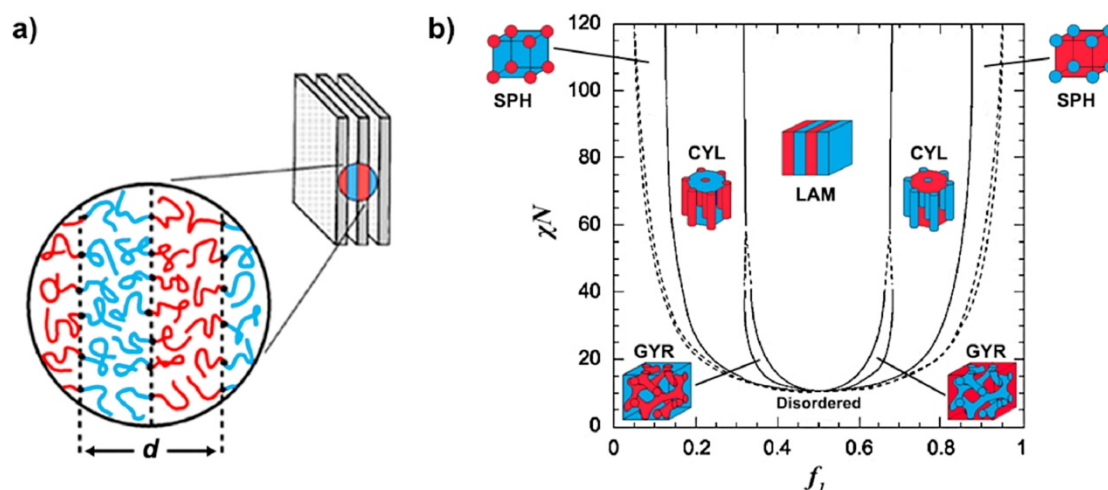


**Figure 3.2:** (a) Schematic illustration of ordered lamellar phase. The view of the LAM phase demonstrates the individual molecules self-assembly within the morphology<sup>87,88</sup>. (b) mean-field phase diagram exhibiting SPH (spheres), CYL (cylinders), LAM (lamellae) and GYR (gyroid) phases.<sup>82,88</sup>

The direct association of stretched chain conformation from the molecular weight dependence of the periodic lattice spacing and domain dimensions are indicated by the  $d \sim N^\delta$  where  $\delta \approx 2/3$  in the SSL, while the structure periodicity in the WSL is an analogue of  $N^{1/2}$ .

Also, a third narrow regime for the  $\chi N$  product ranging from 30 to 100 known as intermediate segregation limit (ISL) has been established to predict more complex phases.<sup>82,89</sup> A prominent morphology evident in the ISL is DG phase which requires a maximum  $\chi N$  value equal to 60 at specified volume fraction region in order to be adopted (Figure 3.2b). It should be noted that, for the PS-*b*-PDMS system, gyroid phases with  $\chi N$  values higher than 100 have been reported.<sup>90</sup> The perforated-lamellar (PL) and ordered bicontinuous double-diamond (DD) were also considered unstable and/or metastable phases in SSL.<sup>91</sup>

### 3.2 Conformational Asymmetry

A parameter significantly affecting the order-order and less the order-disorder phase boundaries, namely conformational asymmetry has been reported by Matsen and Bates.<sup>92</sup> More recent theoretical and experimental results revealed that, to stabilize non classical phases, BCPs with conformational asymmetry are required.<sup>93,94</sup> In cases where  $\alpha_A/\alpha_B=2$  or  $\alpha_A/\alpha_B=1.5$  ( $\alpha$  is the statistical segment length) new phase diagrams were made. Conformational asymmetry plays a crucial role in shifting the phase boundaries towards compositions richer in segments with higher asymmetry. Different monomer volume and chain rigidity contrast (chain flexibility) induce conformational asymmetry ( $\zeta$ ) as described by the following equation:

$$\zeta = \frac{\alpha_A^2/6u_A}{\alpha_B^2/6u_B} \quad (3.8)$$

where  $u$  corresponds to the statistical segment volume and  $\alpha$  the statistical segment length.

From Figure 3.3 it is easily understood that the larger shifts in the OOT (order-order transition) when the asymmetry increases from 1 to 1.5 to 2, are induced by the ability of A segments to stretch more easily than the B blocks. The interface curves towards the A blocks, while B blocks are allowed to relax at the expense of A segments, minimizing their intermolecular interactions to achieve thermodynamic equilibrium. Except for the differences on the phase boundaries, conformational asymmetry has an impact on the relative domain spacing between structures along their boundaries, affecting the kinetics of the corresponding order-order transitions.

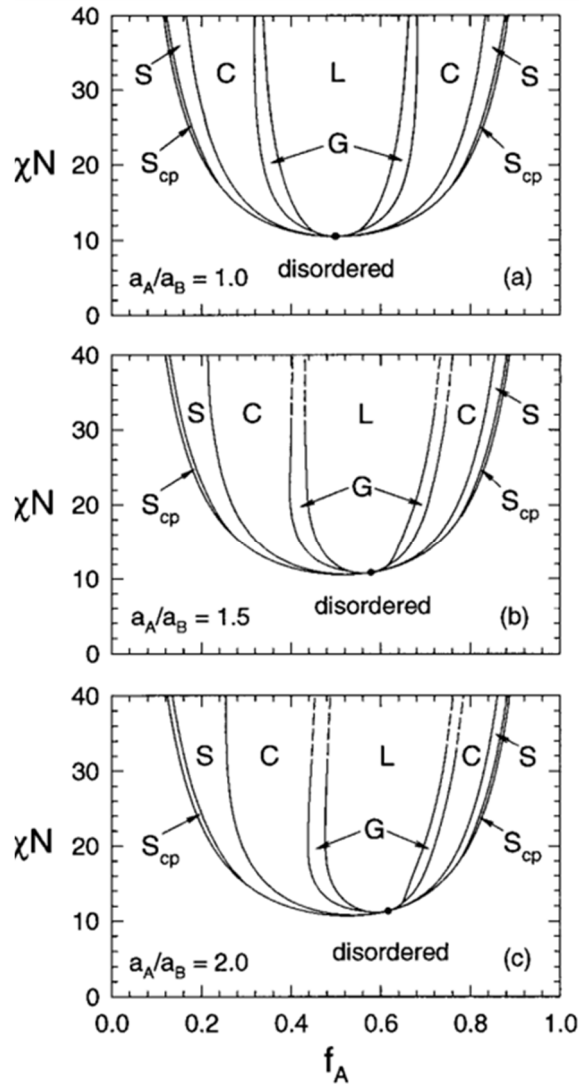


**Figure 3.3:** Mean field phase diagrams for BCPs with varying conformational asymmetry degree. The arrangement of the classical phases remains unaffected as the asymmetry increases but the phase boundaries experience an obvious effect.<sup>92</sup>

### 3.3 Unusual Nanostructures

Besides the equilibrium ordered phases found in BCPs, non-equilibrium ones including perforated-lamellar phase, where hexagonally packed channels of the majority component extend through the minority layers to form a monocontinuous structure and ordered bicontinuous double-diamond have also been experimentally observed (using external stimuli<sup>95,96</sup> or adjusting processing parameters<sup>97</sup>), leading to the development of new theoretical models to predict the principles of the kinetic pathways.

Multiple novel phases anticipated from theory or experimentally observed have been reported in the literature for various copolymers combinations even though it is originally believed that these phases could only be stabilized in complex architecture copolymers.<sup>98-100</sup> The double primitive structure,<sup>97</sup> the Fddd network phase,<sup>101</sup> the Frank-Kasper  $\sigma$ <sup>102-104</sup> as well as A15<sup>105</sup> phases and a dodecagonal quasicrystal<sup>106</sup> are some of the complex ordered phases (Figure 3.4) that have a leading role to the contemporary soft matter theory.

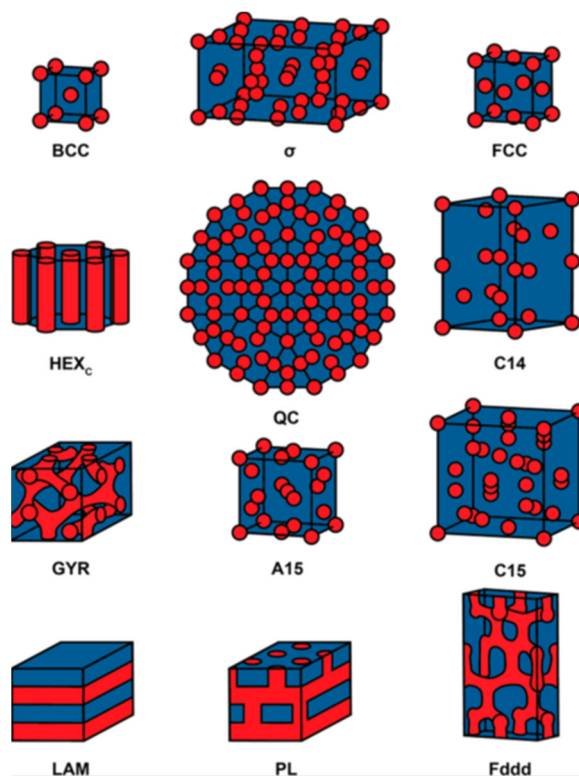


**Figure 3.4:** Nanostructures reported for linear *A-b-B* diblock copolymers. BCC: body-centered cubic;  $\sigma$ : Frank-Kasper sigma phase; FCC: face-centered cubic; HEX<sub>c</sub>: hexagonally packed cylinders; QC: dodecagonal quasi-crystal; C14: Frank-Kasper AB<sub>2</sub> Laves phase; GYR: double gyroid; A15: Frank-Kasper AB<sub>3</sub> phase; C15: Frank-Kasper AB<sub>2</sub> Laves phase; LAM: lamellae; PL: perforated lamellae; Fddd:  $O^{70}$  network.<sup>107</sup>

Molecular geometry induced by conformational asymmetry is strangely linked to the formation and even stabilization of the unusual phases as demonstrated by many experimental studies which support recent theoretical assumptions. Note that, in depth analysis of the observed experimental data (usually through transmission electron microscopy and small angle X-ray scattering) is required to shed light on the adopted morphologies in each case. Furthermore, local segregation of dissimilar copolymers in diblock copolymers blends and different architectures enable the

formation of the uncommon complex ordered phases.<sup>92,98-100</sup> In a following subchapter of this dissertation the effect of thermal processing and the use of selective solvents on the self-assembly behavior will be also discussed.

Bates and co-workers identified a novel network structure called O<sup>70</sup>, which stands for the orthorhombic with space group *70* or *Fddd* phase.<sup>101</sup> The morphology exhibits threefold connected struts of a minority component. Notably, the current SCFT phase diagram of linear BCPs<sup>9</sup> identifies and includes the specific phase since it was not only predicted theoretically but also found experimentally.

The complex Frank-Kasper (FK) phases ( $\sigma$ , A15, C14, and C15)<sup>102-106</sup> are sphere-packing structures initially discovered in hard materials. In cases of increased compositional asymmetry such as in poly(dimethylsiloxane)-*b*-poly(2,2,2-trifluoroethyl acrylate)s,<sup>108-109</sup> poly(isoprene)-*b*-poly(lactic acid)<sup>110</sup> and poly(dodecyl acrylate)-*b*-poly(lactic acid)<sup>105</sup> FK phases have been reported. These phases usually appear in the ISL ( $20 < \chi N < 40$ ) at compositions ranging between BCC and HEX based on the mean-field analysis.<sup>106</sup>

Network phases are of particular interest for technological applications. This is attributed not only to the great exploitation in applications such as photonics and nanoporous materials but also to the fact that the three dimensional network in the nanometer scale cannot be obtained using common processing techniques.<sup>111</sup> The DD structure with space group  $Pn\bar{3}m$  consists of two interpenetrating but non intersecting diamond networks with tetrahedral nodes while DG is characterized by tripod domains interconnected with  $Ia\bar{3}d$  space group symmetry.<sup>97,112,113</sup> The large degree of packing frustration, attributed to the non-uniform stretching of the chains, outmatches the interfacial energy and impedes the formation of DD in copolymer melts.<sup>112</sup> To verify whether the observed morphology corresponds to the DD or DG structure much attention should be paid during the data analysis. Specifically, two dimensional projection in the TEM images is quite similar for both structures and the first pair of allowed reflections at SAXS plots gives close ratio values (OBDD:  $\sqrt{3}/\sqrt{2} = 1.23$  vs DG:  $\sqrt{8}/\sqrt{6} = 1.15$ )<sup>112</sup> but it is widely used to distinguish the two phases in conjunction with other characterization methods such as electron tomography or fast Fourier transform patterns.<sup>97</sup> Electron tomography is a powerful tool for the appropriate analysis of network phases, or in general, porous materials due to the ability to construct 3D images. An innovative newly established technique, namely focused ion

beam SEM is of particular interest to explore structures with 3D architecture. The use of thick films ( $>100$  nm) enables the reconstruction of selective regions with high resolution. It should be noted that, the specific technique was utilized to study a deformed triclinic DG phase. It was evidenced that the slower chain dynamics than the de-swelling rates induce a symmetry-breaking of non-cubic gyroid structures which is attributed to the distortion upon z-directional.<sup>114</sup>

The use of solvent- or thermal-assisted assembly has contributed significantly to the formation of network phases. A characteristic paradigm is the metastable double-primitive phase (DP) with space group of  $Im\bar{3}m$ , recently observed for a PS-*b*-PDMS diblock copolymer by the Ho and Avgeropoulos groups. The discovery is considered very important since the packing frustration is further increased in a node of DP and the minority chains need to be more stretched to fill the space in the hexapod as compared with the tetrapod in DD and the tripod in DG phases as evident from 3D tomography (Figure 3.5).<sup>97</sup>

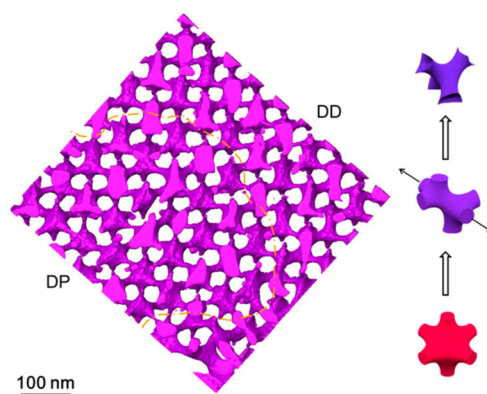


**Figure 3.5:** Three-dimensional tomography of self-assembled PS-*b*-PDMS/SiO<sub>2</sub> from fast solvent evaporation. The identified DP phase appears in the central area (projected along  $[111]$ ) that is surrounded by the DD phase (projected along  $[110]$ ). Rhombohedral distortion (as illustrated in purple) for continuous transition path within the transition zone from DP phase to DD phase with epitaxial relationship between  $[111]_{DP}$  and  $[110]_{DD}$  could be clearly identified. The boundary between the DP and DD phases is marked by the red dashed line.<sup>97</sup>

### 3.4 Microphase Separation of Triblock Copolymers

The self-assembly origins of symmetric triblock copolymers are determined by the Flory-Huggins interaction parameter between the two chemically different chains, degree of polymerization and composition as in the case of diblock copolymers. The principal difference is located in the additional junction point that induces a divergent behavior. Whether the middle block in the A-*b*-B-*b*-A sequence would perform loop or bridge configurations has also an impact not only on the

obtained morphologies but also on the mechanical properties. Both ends in the middle block B occupy the same interface in a looped configuration, while the two ends are placed on different interfaces in a bridged configuration. Estimations indicated that even though triblock copolymers adopt both configurations, when the composition is equal to 1:1:1 bridging is more preferred, while in 1:2:1 looping is suggested.<sup>115</sup>

Mayes<sup>116</sup> used mean-field theory to predict the phase diagrams for such A-*b*-B-*b*-A triblock copolymers. In the WSL the phase boundaries were calculated to be asymmetric a fact that is attributed to the entropic constraints. To confine the two side blocks (A) in a domain compared to a single B block, is considered more difficult since the middle B block has to exhibit higher deformation to accommodate the outer A blocks in A domains.

In the SCFT study conducted by Matsen and Thompson, who compared the triblock with the corresponding diblock copolymer, the triblock showcased enhanced segregation strength, meaning higher  $T_{ODT}$ , due to less number of free ends.<sup>117</sup> The interfaces were also predicted to be more narrow due to the higher segregation strength. Furthermore, the authors defined the percentage of B chains that adopt the bridging conformations for various morphologies (lamellae: 40-45%, cylinders: 60-65%, spheres: 75-80%). The fractions have not demonstrated any significant change due to segregation strength but they were highly affected by the morphology.

The similar free segments energy between diblock and triblock copolymers is accountable for the phase diagrams resemblance. Note that, the  $O^{70}$  phase is stabilized in larger regions but the close-packed spherical phase extends in narrower regions in the triblock copolymers phase diagram.

### **3.5 Microphase Separation of Star Block Copolymers**

#### **3.5.1 Theory**

The effect of macromolecular architecture of star block copolymers on microphase separation has been predicted using SCFT simulations.<sup>118</sup> Olvera de la Cruz and Sanchez<sup>119</sup> were the first researchers to report theoretical calculations concerning the phase separation of  $(A-b-B)_n$  star block copolymers. In Figure 3.6 the dependence of  $\chi N_{ODT}$  on the arm numbers is observed. In principal,  $\chi N_{ODT}$  is predicted to be lower in star blocks compared to diblock copolymer precursors and significantly decreased when the number of arms increases.

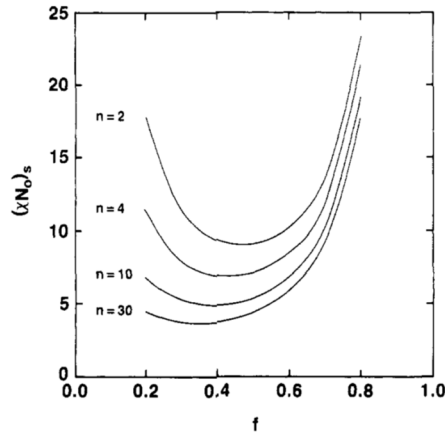


**Figure 3.6:** Variation of  $(\chi N)_s$  with volume fraction for  $(A-b-B)_n$  with various  $n$  when  $A$  constitutes the inner block and has composition  $(f)$ .<sup>119</sup>

Theoretical studies also indicate higher  $T_{ODT}$  values and higher segregation strength for star block copolymers. The lower  $\chi N_{ODT}$  value is attributed to entropic penalties due to configurational constraints imposed by the various chains anchoring from the same junction point. In addition, the overcrowding effect leads to similar chain stretching almost parallel to the interface, allowing a limitation on defects/dislocations, increased order and minimization of the feature sizes. The size of the nanodomains in star block copolymers is almost identical to the one obtained from the block copolymer precursor comprising the arms.<sup>19,71,73,120</sup>

Furthermore, complex architecture affects the phase boundaries as can be clearly evidenced in Figure 3.7. Taking into consideration the theoretical phase diagrams presented in a relatively new study by Matsen,<sup>9</sup> is suggested that for star-block copolymers, the DG morphology may be adopted in a wider range of volume fractions as well as the occurrence of  $O^{70}$  phase is also more pronounced as the number of arms increases. Alterations on the stability of structures in the phase diagram are very important, when, nanoporous materials are required.<sup>9</sup>

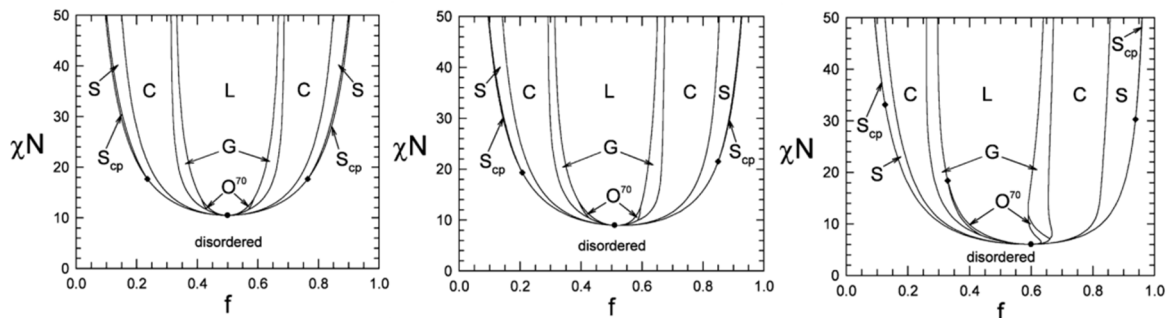


**Figure 3.7:** Phase diagrams: for melts of AB diblock copolymers (left), symmetric ABA triblock copolymers (middle) and 9-arm star block copolymers where each molecule is formed by joining 9 diblocks together by their B-ends.<sup>9</sup>

### 3.5.2 Experimental Results Verifying Theory

A significant contribution to the phase behavior of star block copolymers has been conducted by Thomas and co-workers who studied several  $(PI-b-PS)_n$  (where  $n=18$ ) using PI as the inner block. Employing various volume fraction values for the PS block, spheres, cylinders and DG structures of the PS minority component were obtained. Further increase on volume fraction led to the formation of lamellar morphology and cylinders as well as spheres of the PI minority block.<sup>121</sup> Interestingly, at a fixed PS composition ( $\phi_{PS}=0.27$ ) using the rigid segment as the outer chains gave rise to DG morphology, but inverting the sequence (PS inner block) led to the formation of a cylindrical structure. It was also shown that, when the PI constituted the outer chains and the elastomeric segment had a volume fraction equal to 0.27 a DG phase was also observed (Figure 3.8).

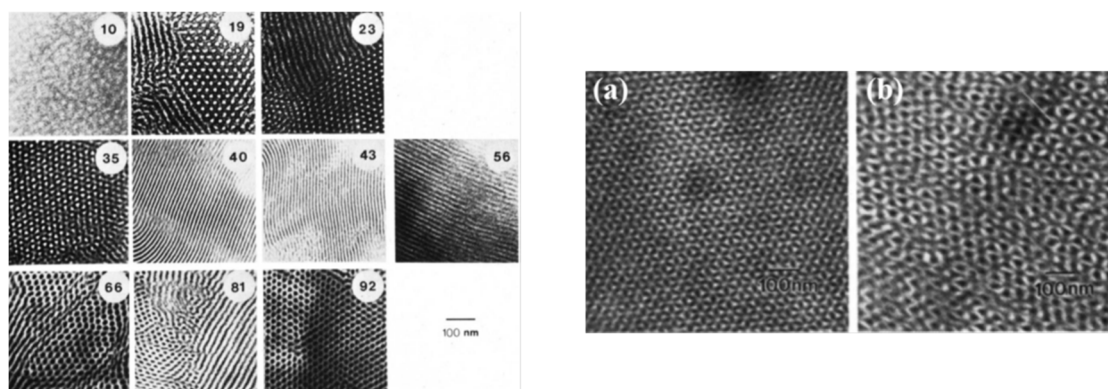


**Figure 3.8:** (Left) TEM images of  $(PI-b-PS)_{18}$  labelled by  $\phi_{PS}$  (PS outer block). (Right) TEM images of (a)  $(PI-b-PS)_{18}$   $\phi_{PS}=0.27$  (PS outer block), (b)  $(PS-b-PI)_{18}$   $\phi_{PI}=0.27$  (PI outer block).<sup>121</sup>

The same group has also explored the impact of molecular weight and arm number ( $n$ ) on the obtained morphology, for  $\phi_{PS}=0.27$  when the PS comprised the outer block. The basic concept of the study was to keep the molecular weights of the constituent arms identical while the arm number increased ( $n=2,4,8,12,18$ ) and to observe whether the morphology alters. By increasing  $n$  or molecular weight the cylindrical phases were transformed to DG. For the lowest molecular weight of the blocks the transition took place for the star with the highest arm number ( $n=18$ ). When the molecular weight of the arms was increased, the DG morphology was evident in 8-, 12- and 18- arm stars. Finally the higher molecular weight value resulted in DG structure at  $n$  larger than 6. The study indicated the influence of multiple arms and the conformational restrictions of the inner chains as the  $n$  increased.

Matsushita and coworkers<sup>122</sup> prepared different molecular weights for two series of star block copolymers of the  $(PI-b-PS)_n$  type where  $n=4$  or  $12$ . In this research a direct comparison between the diblock copolymer precursors and the star-shaped materials was reported. Identical morphologies and equal domain spacing values were observed for all samples. These results indicated that conformational entropy loss induced by the complex molecular architecture may not be capable of affecting the morphology when the arm number is lower than  $12$ .

Jang et al<sup>123</sup> synthesized various star block copolymers of the  $(PS-b-PMMA)_{18}$  with PMMA being the outer block. The phase behavior of the synthesized copolymers was investigated with SAXS and TEM studies. By increasing the  $\phi_{PMMA}$  from  $0.3$  to  $0.8$  various nanodomains such as BCC, HEX, PL and LAM were observed. Highly asymmetric lamellar microdomains were obtained when the outer blocks comprised the majority component ( $\phi_{PMMA}=0.77$ ), while the corresponding linear copolymer did not adopt similar morphology, further suggesting the high effect of the macromolecular architecture. It should be noted that, in the specific study the star samples contained  $75\%$   $PS-b-PMMA$  and  $25\%$  of PS homopolymer, a fact that had severe impact on the obtained morphologies.

Kim and coworkers<sup>124</sup> in a subsequent study synthesized  $(PS-b-PMMA)_{18}$  stars exhibiting  $100\%$  purity without any homopolymer PS present. It was found that, for  $\phi_{PMMA}=0.77$ , BCC PS spherical microdomains were formed instead of asymmetric lamellar domains. Furthermore, the newly synthesized star, devoid of any homopolymer, at a fixed  $\phi_{PMMA}$  equal to  $0.40$  showcased a DG phase, while PL microdomains were formed for the one blended with  $25\%$  of PS homopolymer.

Avgeropoulos and Ho groups reported the synthesis of silicon-based star block copolymers with various arm numbers and PDMS segment being the core in  $(PS-b-PDMS)_n$  type star block copolymers. Coherent results regarding the morphologies and the domain periodicity were obtained, except for a zigzag pattern (chevron texture) in a  $(PS-b-PDMS)_n$  with  $n = 3$ , while straight lamellae were acquired for  $n = 1, 2$ , and  $4$ .<sup>19</sup>

Russell and coworkers<sup>125</sup> prepared  $(PS-b-P2VP)_n$  salt-doped star copolymers (where  $n=2, 3, 4$ ) to generate nanofeatures in the sub- $10$  nm regime. To induce unfavorable interactions between the two constituents salts binding to the P2VP were incorporated leading to an increase in the effective  $\chi$  value. The SAXS profiles confirmed that the domain spacing of the star BCPs is not affected by the number of

arms. In accordance to the previous studies the domain spacing of star-shaped materials is similar to the one obtained for a diblock copolymer with equivalent molecular characteristics. This research is directly linked to the contemporary idea for minimizing the domain spacing through the manipulation of molecular weight to take advantage of the lower critical order-disorder transition point evident in star block copolymers, without compromising the order.

Several star block copolymers consisting of poly( $\epsilon$ -caprolactone) (PCL) and maltotriose (MT) with varying arm numbers ( $n=3, 4, 6$ ) and different PCL length were synthesized recently by Isono et al.<sup>126</sup> The systems adopted HEX phases with well-ordered domains due to the relatively high  $N$  values in star block copolymers and periodicities less than 10 nm.

### 3.6 Solid State vs. Thin Film Assembly

The fundamentals of self-assembly provide information regarding the thermodynamics of each system and the microphase separation origins. The preparation of samples holds a key role for their morphological study. Whether the obtained morphology is equilibrium can be determined by multiple contributing factors such as: molecular weight, composition, dispersity, architecture, amorphous or crystalline chains, solvent used (selective or non-selective), casting procedure, annealing temperature and duration, cooling process, sectioning and staining procedures (in cases of inadequate mass contrast thickness). The importance of processing procedures is reflected in the relative publications in which an analytical description of experimental approaches is always required. BCPs in the SSL or highly segregated copolymers due to the increased repulsion between the chemically different blocks have the ability to be processed with multiple ways, leading to various phases using the same parent material.<sup>97,108-110</sup>

A representative example of such behavior is the published research of Avgeropoulos and Ho<sup>127</sup> groups who exploited one single composition lamellae forming PS-*b*-PDMS diblock copolymer and obtained diverse structures simply by changing the solvent used during casting procedure. Tuning the selectivity of the solvent in accordance with the high segregation strength of the silicon-containing BCPs enabled the formation of phases such as sphere, cylinder, gyroid, lamellar and even inverted ones (Figure 3.9). This multilateral solid state behavior allows the

development of various well-ordered nanostructures. The significance of the reported research is quite high since a direct relationship between the used solvent and the adopted morphology at fixed composition for a silicon-based copolymer has been established.

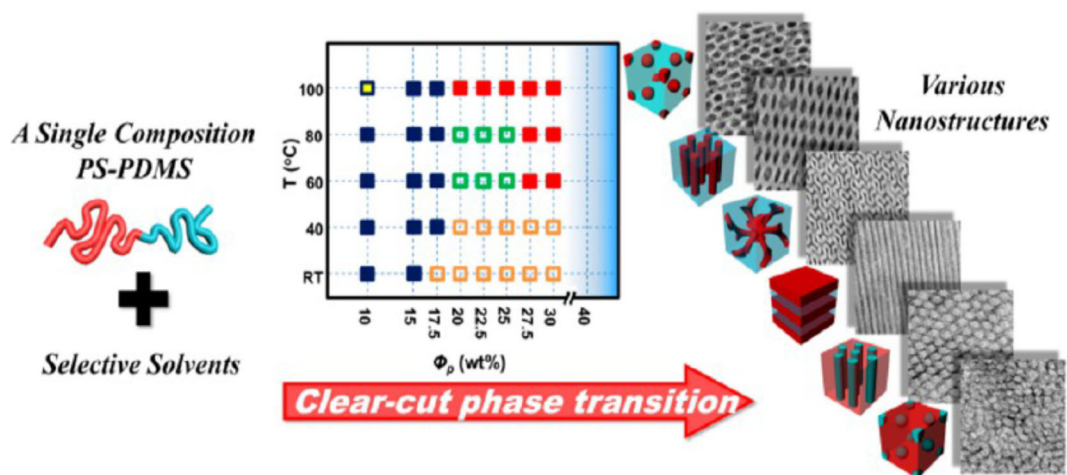


**Figure 3.9:** Phase transitions of PS-*b*-PDMS diblock copolymer using selective solvents.<sup>127</sup>

Another important observation regarding the ordering kinetics of a PI-*b*-PLA system as a function of time following rapid cooling from above the  $T_{ODT}$ , has been reported by Gillard et al.<sup>110</sup> The rapid quenching from the disordered state to temperatures between 25 °C and 45 °C led to the formation of a metastable two-dimensional dodecagonal quasicrystal that transformed into a three-dimensional Frank-Kasper  $\sigma$  phase after a time period. The importance of the work leads to the fact that unusual phases can be obtained utilizing different processing parameters.

Notably, the preparation of samples is not always targeting to the formation of novel structures (stable or metastable). Several studies such as the determination of the  $T_{ODT}$  or the estimation of  $\chi$  require the use of a neutral solvent to promote the equilibrium phases without interfering to the effective volume fraction of the segments due to the preferential swelling of the one component.

In thin films directed self-assembly (DSA) there are additional factors that affect the ordering kinetics and the formation of structures, despite the direct dependence on  $\chi$ ,  $N$  and  $\phi$ . Parameters including periodicity, critical dimension size, interfacial width, surface tension and film thickness determine the shape and quality of the adopted morphology.<sup>1,2,11,14,128-131</sup> Various techniques have been developed to govern the self-assembly of block copolymers in thin films and to provide a

comprehensive understanding with respect to the order, orientation as well as defectivity. Thermal and solvent vapor annealing (SVA),<sup>15</sup> have drawn significant attention and are commonly used to facilitate the self-assembly by offering energy to the system augmenting the mobility of chains in order to diffuse or rearrange. To improve the diffusivity, requires high annealing temperatures, usually just below the  $T_{ODT}$  or the use of solvent vapor annealing that induces enhanced order due to the plasticizing effect of polymers after incorporating solvent molecules. In the case of SVA the vapors lead to a swollen and mobile film while the temperature is well below the  $T_{ODT}$  inducing ordered topologies.

Preferable interactions generating from air and/or substrate surface have a significant role in films orientation and are greatly dependant on the chemical nature of each segment.<sup>2,7,11-14</sup> Therefore, mixed orientations originate from components with different surface tension, in contrast to bulk self-assembly where this effect is absent. Components with similar surface tensions exhibit no surface preferentiality leading to better orientation control. BCPs comprising of components with different surface tensions require various manipulations to achieve perpendicular orientation due to the preferential segregation at the surface of the block with the lower surface tension, inducing parallel orientation.<sup>2,67</sup>

Furthermore, the film formation promotes the microphase separation during the solution casting methods. Dip- and spin-coating are widely used for the preparation of films with different thicknesses and roughness.<sup>130</sup> Spin-coating constitutes the method of choice in numerous studies and processing factors such as spinning velocity, concentration and solvent's volatility affect both thickness and uniformity of the film.

The film thickness plays a pivotal role in BCP self-assembly. Knoll et al.<sup>131</sup> suggested this phenomenon when they observed that a well-defined cylinder forming (bulk) polystyrene-*b*-polybutadiene-*b*-polystyrene (SBS) triblock copolymer showcased a completely different thin film phase behavior. With increasing film thickness, a disordered phase (minimum film thickness) transformed to short cylinders, parallel cylinders, perforated lamellae, parallel cylinders with an elongated cross section and necks, perpendicular cylinders and finally for the highest film thickness two layered parallel cylinders were observed as verified both in experiments and in simulations.

A recent study conducted by Brassat et al.<sup>132</sup> highlights the thickness dependence on domain orientation of one cylinder-forming PS-*b*-PMMA using pre-patterned surfaces. In Figure 3.10, with increasing polymer film thickness (from left to right) various domain orientations with respect to the substrate are formed. Low film thickness (smaller than structure periodicity) led to featureless domains while a slight increase induced microphase separated textures. For larger thicknesses, parallel to the surface cylinders occurred that subsequently evolved to perpendicular ones with limited order. Following the mixed phase, at higher film thicknesses span-through perpendicular cylinders with hexagonal order were obtained.

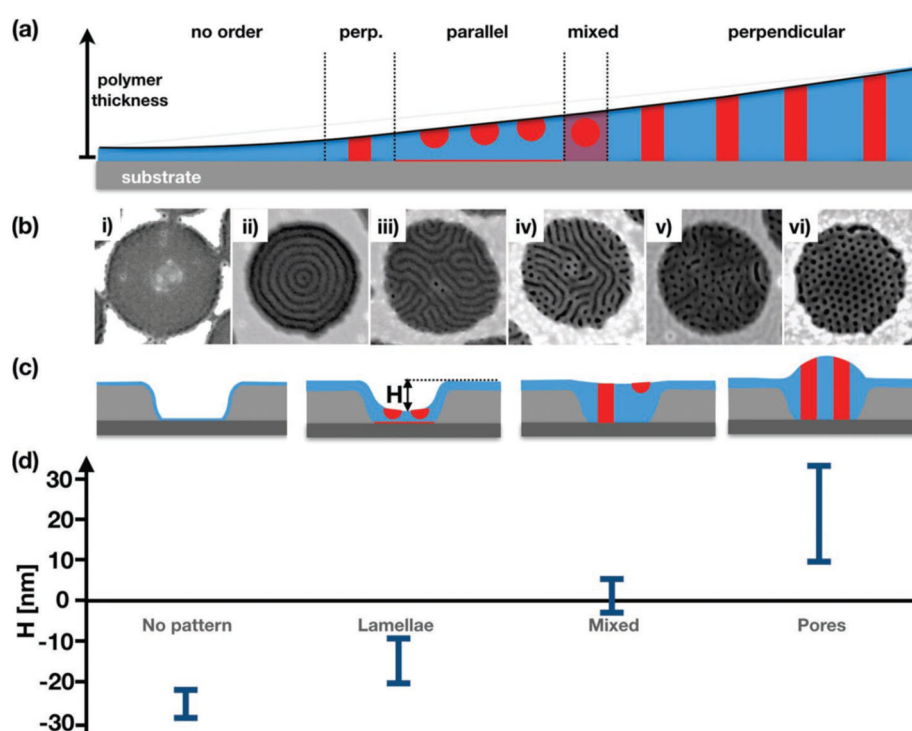


**Figure 3.10:** a) Cross-section of PS (blue) and PMMA (red) on a planar surface demonstrating the variation on cylinders (PMMA) orientation as a function of thickness. b) SEM images of self-assembled domains inside pre-patterned individual nanoholes in Au films. Images are sorted by increasing thickness from i) to vi). c) Schematics of different hierarchical nanostructures from cross-sectional view. d) Height difference ( $H$ ) regimes between mesas and polymer level inside ( $H < 0$ ) or above ( $H > 0$ ) nanohole patterns measured by AFM.<sup>132</sup>

## CHAPTER 4

### Block Copolymers in Nanotechnology Applications

#### 4.1 General Information

The ability of the covalently bonded chemically different homopolymers or block copolymers (BCPs) to microphase separate into a great variety of nanostructures with characteristic features sizes ranging from few to hundreds of nanometers offers a promising alternative to patterning technologies. Conventional or advanced lithographic processes are used in microelectronic fabrication for the development of nanopatterns.<sup>3,133,134</sup> In principal, *top-down* approaches involve the size reduction of larger scale materials down to nanoscale length scales, utilizing optical lithography (photons), e-beam lithography (electrons) and ion beam lithography (ions) for the selective and controlled removal of the substrate. These techniques employ relatively expensive approaches, showcase specific length limits and the formation of irremovable defects is possible.<sup>3,133,134</sup> Cost-effective alternatives<sup>133</sup> with few defects are deriving from another manufacturing technique, namely *bottom-up*, which takes advantage of the self-assembled nanodomains of BCPs. Controlling the BCPs total number average molecular weight, volume fraction, architecture and dispersity, a variety of nanostructures beyond the limits of other fabrication techniques are obtained.<sup>129</sup> The diversity of nanodomains in combination with the precise control over the molecular characteristics which are responsible for the characteristic size of dimensions enables the use of BCPs in numerous applications.<sup>135</sup> In Figure 4.1 some of the possible applications of BCPs such as nanotemplates, nanodots, nanowires, nanomeshes, integrated circuit, nanoporous membranes, ion-conducting membranes and photonic crystals are presented.<sup>129</sup>

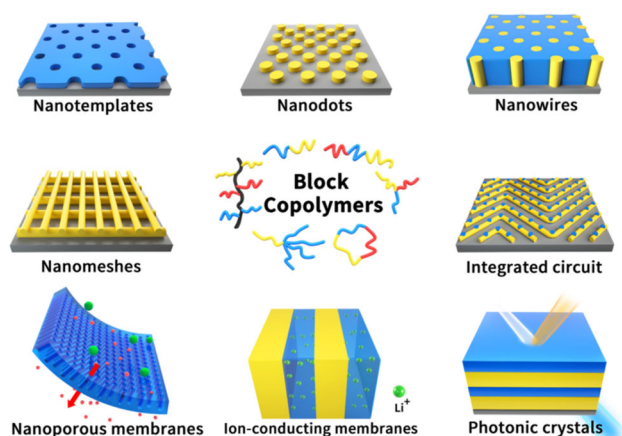


Figure 4.1: Different applications of BCPs in nanotechnology.<sup>129</sup>

Among most appealing applications regarding nanostructured thin films from BCPs self-assembly is the preparation of masks for lithographic applications.<sup>1,2,136</sup> Therefore, the directed self-assembly of BCPs enables the development of next-generation microelectronic devices. A great number of lithographic applications dictate the formation of oriented thin-film nanostructures with ideally perpendicular orientation. The out of plane to the substrate orientation requires non preferential interfaces which can be achieved after substrate surface modification or using copolymers with similar surface energies.<sup>137,138</sup> BCPs nanopatterns are then transferred to other functional materials by the selective removal of one block to achieve high aspect ratio features.

To exploit the technological potential of BCPs, well-defined, defect-free nanodomains with long range order are requested. Tailoring the self-assembly behavior is rather challenging due to misalignment and poor ordering issues and usually external stimuli or pre-patterned surfaces are used.<sup>1,2,129,136-138</sup> External stimuli such as magnetic, shear or electric field alignment techniques, zone, thermal as well as solvent vapor annealing, grapho- and chemo- epitaxy have been implemented to facilitate the development of aligned domains.<sup>134</sup> The use of BCPs in industrial level requires large scale defect-free and perfectly oriented domains; as a result many alignment techniques with the desired characteristics (low cost, universally applied and compatible with current industrial processes) are constantly being developed.

## 4.2 Silicon-Based Block Copolymers

The resolution limitations imposed by commonly utilized BCPs (e.g. PS-*b*-PMMA) have restrained their applicability in nanomanufacturing applications. This impractical behavior is due to the extremely low segment-segment interaction parameter.<sup>139,140</sup> Patterning in the sub-10nm regime requires high interblock repulsion. Based on the SSL relationship  $d \sim N^{2/3} \chi^{1/6}$ , a decrease in the domain size can be effectively conducted by lowering the  $N$  value, while  $\chi$  is substantially increased to maintain the  $\chi N$  product relatively large. This concept led to the development of high  $\chi$ / low  $N$  BCPs for nanotechnology applications.<sup>6</sup>

Regarding high- $\chi$  fully organic BCPs domains as small as 10nm can be formed, but they showcase low etch contrast which is considered a significant drawback. Copolymers containing segments with inorganic molecules, such as silicon

(Si) and oxygen bonded together, have been developed because of their exceptional etch resistant capability in conjunction with the high- $\chi$  values they demonstrate.<sup>7,11,12,14</sup>

PDMS-based<sup>11-14,141-144</sup> copolymers have a leading role in DSA studies but other inorganic segments such as poly(trimethylsilylstyrene) or PTMSS<sup>145</sup> and polyhedral oligomeric silsesquioxanes or POSS<sup>146</sup> have also been reported. Siloxane polymers showcase significant inherent properties due to the flexible Si-O-Si bonds. Low surface energy, low  $T_g$ , high thermal stability, good etching selectivity are some of the appealing properties of PDMS-based systems. The aforementioned copolymers meet both the resolution and throughput challenges but a major drawback related with the low surface energy leads to wetting layer formation during thermal annealing. Preferentially, wetting (on the substrate and/or air interfaces) enables parallel orientation which inhibits the construction of masks for lithographic applications due to the inability to transfer the horizontal structure into a substrate, especially in lamellar phases.<sup>2,11-14,141-144</sup> Additional processing steps to tune the interfacial interactions and to induce normal to the substrate orientation have been evolved. Grafting of polymer brushes onto the substrate or using top coat materials that act as a neutral top surface have been extensively studied in the case of PDMS-based copolymers.<sup>2,13</sup>

**Table 4.1:** PDMS-based BCPs together with their  $\chi$  values and some distinctive properties in thin film state obtained from the relative references. n.s. stands for not specified.

BCP sequence	$\chi$ (25 °C)	Function (F) Remarks (R)	References
PS- <i>b</i> -PDMS	0.26	(F) Film fabrication, multiple processing methods (R) Periodic phases, in plane and out of plane orientation, below 10 nm feature sizes	2,11,13,14,147
PDMS- <i>b</i> -P2VP	n.s.	(F) Film fabrication (R) Highly tunable self-assembly process and patterns with different geometries and sizes	141
PDMS- <i>b</i> -P4VP	n.s.	(F) Film fabrication (R) Extremely low line edge roughness and rapid assembly kinetics	142
PDMS- <i>b</i> -PLA	1.4	(F) Film fabrication (R) Large scale quantity, 10 nm sized thin films	143
PDMS- <i>b</i> -PMMA	0.23	(F) Film fabrication (R) Solvent-dependent morphology, 12 nm sized thin films	144
P3HS- <i>b</i> -PDMS	0.42	Only bulk studies	148
PDMS- <i>b</i> -PEO & PDMS- <i>b</i> -PEOLTA	0.22 & 0.36-0.43	Only bulk studies	149

Taking into consideration the data presented in Table 4.1, the high technological potential of PDMS-based materials is clearly understood. The necessity for high immiscibility between the relative blocks is also obvious, since it comprises an alternative to making pitch sizes as small as possible. The processability as well as the formation of multiple nanostructures simply by manipulating the same parent material indicates the solvent-dependent morphology of these copolymers. Although, the low surface energy related issues of PDMS cannot be overlooked since additional procedures are needed to provide the desired orientation control.

### 4.3 Beyond Block Copolymers

The determinant factor for the BCPs thin film behavior with respect to the orientation is the preferential wetting of the chemically different segments with the top and/or bottom surfaces which is attributed to the different surface energies between them. A new contributing factor, the conformational penalty, is added when the architecture changes from linear BCP to linear triblock copolymer and finally to star block copolymers with various arm numbers. The entropic role in the nanodomains self-assembly is quite prevalent and strongly dependent on the penalty that star-block copolymers have to pay for the preferential wetting on an interface.<sup>16-18,67-69</sup>

*A-b-B-b-A* triblock copolymers demonstrate an advantageous thin-film behavior because of their greater tendency to form perpendicular nanostructures as experimentally<sup>67</sup> and theoretically<sup>150</sup> evidenced and have larger processing window.<sup>68,69,151</sup> Perpendicular orientation is usually induced when the middle block (B) has lower surface energy than A segment and the discrepancy of the surface energies between A and B is not substantial. This tendency is attributed to the wetting layer formation of B blocks at the air interface, that prompt the A blocks to migrate to the air interface due to entropic constrains.<sup>67</sup> Smaller feature sizes of the self-assembled structures than the analogous diblock copolymers and enhanced mechanical properties have also been reported for such triblock materials.<sup>47,67,68,152</sup>

A different approach to the so-called high  $\chi$ /low  $N$  BCPs for nanotechnology applications makes use of star block copolymers<sup>16-18,123-126</sup> [(A-*b*-B)<sub>*n*</sub> where *n* = 3, 4, etc.]. The role of star block copolymers in the self-assembly is dual. The lower  $\chi N_{ODT}$  values allow for the dimensions to become the smallest possible. Not only do the

systems exhibit improved order due to the significantly higher  $N$  values (compared to the ones evident in the diblock copolymer precursors) but also the overcrowding effect facilitates the elimination of defects. Furthermore, the number of arms and the difference on surface energies have an impact on the entropic effect and therefore induce this critical parameter on the orientation control.

Theoretical studies further supported the experimental results regarding the ability of silicon related star shaped copolymers to adopt vertical orientation.<sup>2,16</sup> The comparison of vertical and parallel orientation in cylinder-forming copolymers was studied through SCFT calculations. The discrepancy in the free energy between the differently oriented phases ( $\Delta fE$ ) as a function of  $\Delta\chi$  for various copolymer arms ( $n= 1, 2, 3, 4$ ) is given in Figure 4.2a, where a clear-cut transition from parallel to perpendicular orientation occurs at higher  $\Delta\chi$  values for star block copolymers with higher arm number. The theoretical results strongly suggest that the entropic penalty for reorienting the star block copolymers to parallel morphologies is increased as the number of arms increases. In Figure 4.2b the 3-D density profiles as a function of  $\Delta\chi$  for all copolymers is presented ( $n= 1, 2, 3, 4$ ). When  $\Delta\chi$  ( $\chi_{\text{Bair}} - \chi_{\text{Air}}$ )=0 the microdomains are oriented from the substrate surface to the air interface. Higher  $\Delta\chi$  values induce a wetting layer at the air interface as a result parallel cylinders only for diblock and triblock copolymers are formed. This theoretic model supports the entropy-driven effect but experimentally the formation of wetting layer even for higher number of arms is inevitable when the surface energy deviation between the two blocks is considerable.

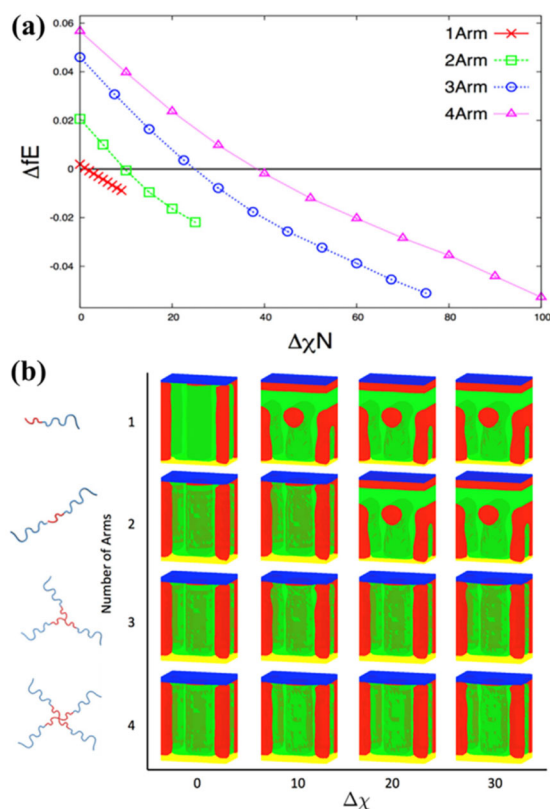


**Figure 4.2:** (a) The free energy discrepancy between the parallel and perpendicular structure for cylinder forming thin films with  $h = 2d_0$  of copolymers with various arm numbers.  $\Delta f = f_{\text{parallel}} - f_{\text{perpendicular}}$  plotted as a function of  $\Delta\chi$  ( $\chi_{\text{Bair}} - \chi_{\text{Aair}}$ ). (b) 3-D density profiles for linear and star-block copolymers with cylindrical structure as a function of  $\Delta\chi$ .<sup>2,16</sup>

#### 4.4 The PS-*b*-PDMS System as a Milestone Copolymer

The advent of several advanced polymerization methods making the combination of dissimilar blocks feasible has been reported in the literature. In addition, post polymerization modification reactions allow the formation of copolymers with desired properties. Furthermore, the advanced polymerization techniques enable the synthesis of various architecture copolymers. It is already well-established that nanotechnology-based applications require materials that can be easily processed with many techniques, demonstrate specific orientation with respect to the substrate and well-defined nanostructures with the desired dimensions as well as high etch selectivity. Two additional parameters are also very significant for advanced applications including the reproducibility and the scale-up potential.

The PS-*b*-PDMS system constitutes a reference material enabling periodic structures with minimum feature sizes approximately 8 nm<sup>6,153</sup> due to the high  $\chi$  value that also leads to a thinner IMDS and low pattern edge roughness.<sup>11</sup> A remarkable amount of publications using various PS/PDMS systems has been reported. The

significance of these studies is important in many ways, providing useful information with respect to the synthesis, the bulk microphase separation and methods to tune the morphology and aspect ratio during thin films assembly. Even though, the BCP is commercially available, meticulously described synthetic protocols have shed light on how to synthesize well-defined linear diblock<sup>10,14,19,73,90</sup> and triblock<sup>10,19,68</sup> copolymers, star block copolymers<sup>16-19,90</sup> with various arm numbers, miktoarm star copolymers<sup>10</sup> of the PS(PDMS)<sub>n=2 or 3</sub> as well as of the inversed sequence, meaning PDMS(PS)<sub>n=2 or 3</sub>,<sup>154</sup> and Janus bottlebrush block copolymers comprising of PS and PDMS.<sup>155,156</sup> Apart from the PS-*branch*-PDMS bottlebrush copolymers, all other sequences require the use of anionic polymerization which affords copolymers with compositional and structural homogeneity, specific architecture and the quantity of the synthesized materials is rather significant. The well-elaborated anionic techniques allow for high reproducibility regarding the molecular characteristics but the synthesis is severely restricted to institutions or industries that are able to perform the specific polymerization technique.

The surface tension discrepancy between the segments ( $\gamma_{\text{PDMS}}=19.9$  mN/m and  $\gamma_{\text{PS}}=40.7$  mN/m), causes the preferential segregation of PDMS at the air/polymer interface.<sup>11</sup>

Plasma etching (dry etching) is, in most cases, the method of choice for anisotropic etching, meaning that etching takes place in vertical direction with no or little lateral etching contrary to the isotropic (wet etching) that etches also in horizontal direction and lacks control as the feature sizes are considerably decreased.<sup>157</sup> Fluorine chemistry is employed to etch the silica-like structures or other halogen atom-based etchants (Cl, Br) are preferred for silicon etching. On the contrary the organic polymers are usually removed with O<sub>2</sub> plasma.

The carbon to fluorine ratio of the gas has an important role on the produced plasma. The free radicals lead to a fluorocarbon film formation on the substrate while the fluorine atoms contribute to the substrate etching. The higher the C/F ratio is, the higher are the amounts of formed free radicals, giving eventually rise to polymerization reactions instead of etching. To restrain this phenomenon the fluorocarbon containing gases are mixed with O<sub>2</sub> plasma since oxygen is an effective free radical scavenger allowing the production of atomic fluorine that favors the etching treatment.<sup>2</sup>

Consequently, to examine the surface morphology under the PDMS thin layer, the air surfaces of the samples are shortly treated with mixed CF<sub>4</sub>/O<sub>2</sub> gases to remove

the top PDMS layer. Afterwards, the PS segment in a PS-*b*-PDMS system, can be easily etched away upon exposure to oxygen plasma, while the silicon segment is transformed to SiO<sub>2</sub> forming a robust hard mask material for subsequent pattern transfer into the underlying substrate.<sup>2,14</sup>

#### 4.4.1 Linear Diblock Copolymers Directed Self-Assembly

A facile method to obtain topographic patterns of polymeric materials has been reported, in which well-ordered perpendicularly oriented nanochannels with dimension as low as 16 nm were used as templates. The PDMS segments (majority component) were oxidized as silicon oxy carbide domains, while the PS blocks were removed using one step oxygen plasma treatment. The freestanding silicon oxy carbide thin films with nanochannels exhibiting hexagonal ordered were subsequently constructed and implemented as masks for pattern transfer to underlying polymeric materials by oxygen reaction ion etching.<sup>65</sup>

In a study conducted by the same group<sup>14</sup> silicon oxy carbide nanoring arrays from the PS-*b*-PDMS (PDMS minority component) thin films were prepared. The sample was spin-coated on the substrate and solvent vapor annealing induced the formation of perpendicular PDMS cylinders. The core-shell cylindrical nanostructures were developed through surface reconstruction. Using oxygen plasma treatment the PDMS core-shell cylinders were oxidized, enabling the formation of silicon oxy carbide nanoring arrays. The findings suggested that the induction of carbon in the SiO<sub>2</sub> network lead to superior thermal, mechanical and anti-corrosion properties due to the tetravalent nature of carbon that reinforces the molecular structure. The above are illustrated schematically in Figure 4.3.

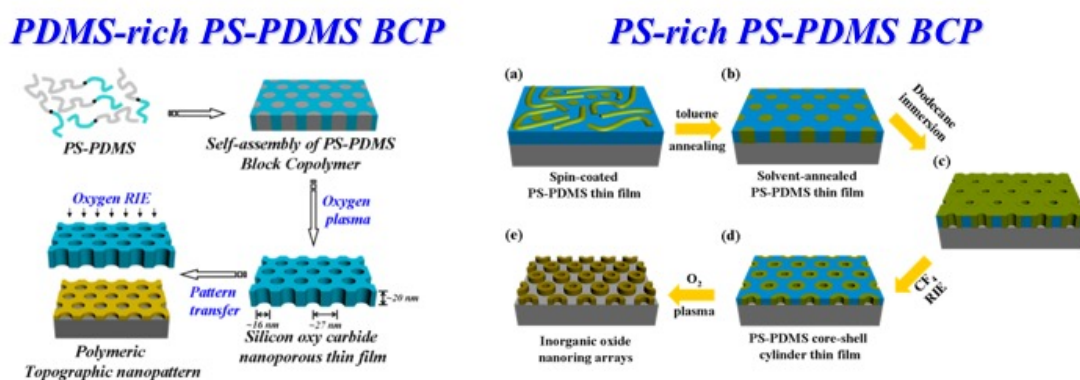


**Figure 4.3:** Schematics with respect to: topographic nanopatterns obtained from the self-assembly of PS-*b*-PDMS thin films (left) and the fabrication of silicon oxy carbide nanoring arrays from PS-*b*-PDMS thin films: (right).<sup>14,65</sup>

Ross and co-workers using cylinder-forming PS-*b*-PDMS copolymers (PDMS minority block) reported the formation of well-defined linear patterns with low defects degree through a synergistic effect of SVA and templating methods. The b and c insets in Figure 4.4 correspond to SEM images with various magnifications of an etched film on a substrate patterned with 10  $\mu\text{m}$  wide trenches.

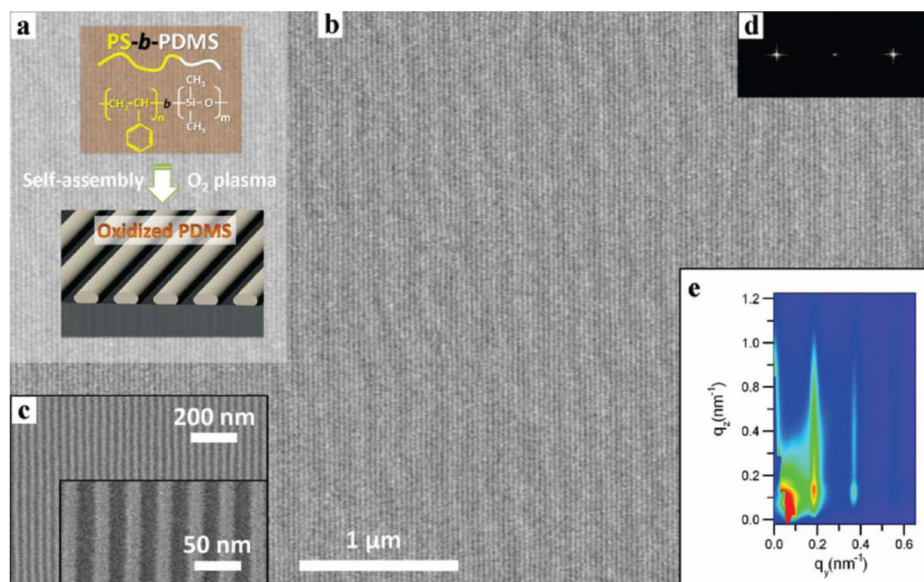


**Figure 4.4:** (a) The PS-PDMS structure and the schematic with respect to the oxidized PDMS cylinders after oxygen etching. (b) SEM image of an oxidized PDMS line pattern from a cylinder-forming PS-PDMS showcasing excellent long-range ordering. The image size is  $5.5 \mu\text{m} \times 3.6 \mu\text{m}$ , and the BCP film was guided by  $10\text{-}\mu\text{m}$ -wide trench patterns (not visible). (c) Magnified images of smaller areas of the array. (d) A fast Fourier transform of the low-magnification image. (e) The GISAXS pattern of the oxidized PDMS line pattern collected from a  $\text{cm}^2$  area.<sup>158</sup>

The exceptional order along the trench walls and the defect free domains over a large area (at least  $6 \mu\text{m}$ ), was clearly demonstrated in Figure 4.4b. The uniform linear periodicity was also revealed by the FFT measurement, in the form of two intense spots away from the center. Coherent results were suggested by the GISAXS studies which showcased sharp diffraction patterns with well-resolved high-order reflections. The conclusion from this research was that the well-ordered defect free domains are the outcome of the high  $\chi$  value between the chemically different segments inducing high interfacial energy and a high penalty for forming defects. The low molecular weight copolymer gave rise to  $17 \text{ nm}$  periodicities that were transferred into a tungsten film to fabricate nanowire arrays with line width equal to  $9 \text{ nm}$ .<sup>158</sup>

In a following study conducted by the same research group, the fabrication of metallic nanowires from a PS-*b*-PDMS BCP (PDMS minority block) and the subsequent pattern transfer took place. The sample was spin coated and submitted to solvent vapor annealing for the formation of a monolayer with parallel cylinders, followed by a two-step RIE treatment to remove the thin PDMS layer and then to oxidize the PDMS cylinders. After the deposition of many metallic films, CF<sub>4</sub> etching treatment was employed leaving different metallic nanowires (Ti, W, Pt, Co, Ni, Ta, Au, and Al) with the desired magnetic and electrical properties.<sup>159</sup>

A gyroid-forming BCP in bulk was used to produce spheres, cylinders, perforated lamellae, or gyroid morphologies by tuning the thin film thickness and solvent annealing conditions (e.g. solvent vapor pressure as well as composition, annealing time and drying process). The utilization of selective solvents led to a change in the effective volume and therefore in the  $\chi_{\text{effective}}$  value. Cylinders formed in 5:1 (toluene:heptane) with period 63 nm and PDMS line-width 35 nm. Changing the ratio between the solvents resulted in a variation on the swelling ratio, allowing the formation of coexistent spheres and lamellae or wetting layer in pure toluene, spheres (from 10:1 toluene:heptane) with period 66 nm, coexistent cylinders and perforated lamellae, perforated lamellae with period 92 nm and hole size 75 nm (3:1 toluene:heptane mixture vapor), coexistence of cylinders and lamellae, coexistence of perforated lamellae and lamellae.<sup>160</sup>

The film thickness effect of the PS-*b*-PDMS was demonstrated also in a different study. It is straightforward that, the thickness should be defined in an optimal range to achieve ordered and defect free films and that is strongly dependant on the annealing technique and the substrate chemistry based on the obtained results. The solvent annealing caused an expansion of the film and the chemistry of substrate strongly determined the preferential wetting of the substrate by PS or PDMS. The periodicity of the films varied with respect to the morphology and confinement effects (Figure 4.5).<sup>161</sup>

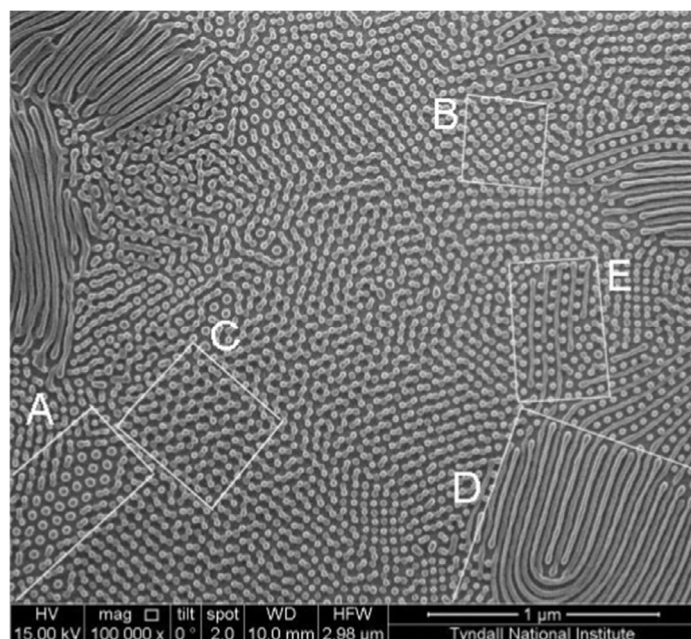


**Figure 4.5:** Various structures corresponding to a solvent-annealed  $PS_{53}$ - $b$ - $PDMS_{17}$  thick film on a PS functionalized substrate (film thickness = 52.2 nm) (A) monolayer spheres, (B) body centered cubic packed spheres, (C) hexagonally packed spheres, (D) hexagonally packed cylinders, and (E) mixed cylinders and spheres.<sup>161</sup>

Son et al. using SVA in acetone and slow drying of BCP films induced the formation of perpendicularly oriented PDMS cylinders and lamellae. The surface energy discrepancy led to the formation of in plane domains at the air interface which subsequently removed with  $CF_4/O_2$  gases.<sup>162</sup>

A procedure to fabricate 5 Tb/in<sup>2</sup> bit patterns from the self-assembly of a low molecular  $PS$ - $b$ - $PDMS$  copolymer was reported by Russell research group.<sup>163</sup> Hydroxyl-terminated PS brushes were first spin coated on Si substrates, followed by deposition of the BCP solution to generate films with the desired thickness prior to solvent vapor annealing at a closed system. It should be noted that, due to the low  $N$  value of the copolymer, it was blended with PS homopolymer (10:1) to stabilize the spherical morphology. The  $SiO_2$  nanodots were then yielded using a two-step RIE treatment ( $CF_4$  and then  $O_2$  plasma).<sup>163</sup>

Kim et al. utilized partially hydrolysed polyvinyl alcohol (PVA) top coats with solvent annealing process in acetone to tune the difference in the surface energy between the constituents and to induce vertical orientation. The PVA topcoat under a controlled solvent vapor atmosphere is capable of reducing the immiscibility between the segments allowing the formation of PDMS cylinders with perpendicular orientation after the removal of the top layer.<sup>164</sup> Mixed highly ordered cylindrical

microdomains with 10nm width were obtained using polyvinyl acetate topcoat that exhibits increased hydrophobicity compared to PVA, in acetone vapors. The combined parallel and perpendicular cylinders were attributed to the dewetted/wetted area of the top coat. The dewetting process introduced a shear-force to the underlying regions of the copolymer aligning the cylinders to the shear direction (parallel), while the substantially decreased interfacial energy during solvent evaporation enabled the formation of highly ordered vertical cylinders.<sup>165</sup>

A remarkable study from Zellsman, Avgeropoulos and Morris groups<sup>166</sup> made use of POSS (polyhedral oligomeric silsequioxane derivatives) substrates to control the orientation and alignment of the pattern in order to produce silicon nanowires, taking advantage of graphoepitaxial DSA of a cylinder-forming PS-*b*-PDMS BCP. The research groups demonstrated that the use of the conventional PDMS hydroxyl terminated polymer brush to modify the substrate led to severe inconsistencies (multilayer pattern formation, lower cylinders correlation length, disclinations and dislocations). The use of POSS to tune the surface chemistry provided a promising platform for the fabrication of patterns in various substrates utilizing nanoimprint or even the conventional 193 nm UV lithography in combination with the DSA potential of BCPs.

Despite the conventional annealing procedures, next generation methods have been developed to promote the self-assembly kinetics and to favor the lateral or perpendicular order including rapid thermal processing,<sup>167</sup> fast microwave-assisted solvothermal process,<sup>168</sup> warm spin-casting method,<sup>169</sup> the use of solvent-saturated polymer gel pad<sup>170</sup> as well as accelerated ion bombardment and vacuum ultraviolet/ultraviolet (VUV/UV) irradiation in plasma.<sup>171</sup>

The potential technological aspects of the PS-*b*-PDMS system were further verified by two very interesting publications. In one case the copolymer was utilized as a porous insulating layer to improve the performance of memory devices. The results implicitly implied a considerable power reduction by taking advantage of BCP DSA and not high-cost lithographic tools.<sup>172</sup> Another research work dealt with the use of a BCP-generated SiO<sub>x</sub> layer in a resistive random access memory device between a Pt (platinum) top electrode and a Ni (nickel) filament layer inducing a reduction in set/reset voltage while minimizing the large variation of high resistance state of the initial device (Figure 4.6).<sup>173</sup>

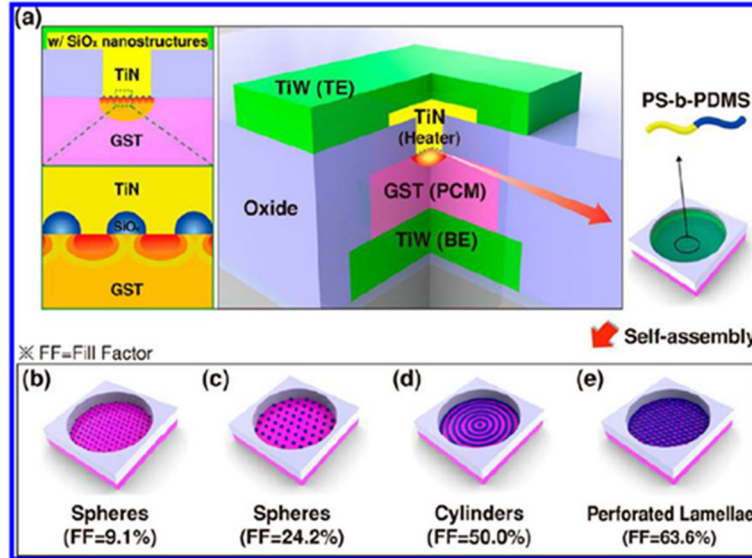


**Figure 4.6:** Phase change memory devices and current-blocking SiO<sub>x</sub> nanostructures. The morphologies as well as fill factors (FF) of the structures were controlled by the self-assembly of PS-*b*-PDMS BCPs. (a) PCM device structure scheme. (b) Various self-assembled nanostructures between GST and TiN. (b) Small spheres (FF =9.1%). (c) Large spheres (FF=24.2%). (d) Cylinders (FF=50.0%). (e) Hexagonally perforated lamellae (HPL) (FF=63.6%).<sup>173</sup>

#### 4.4.2 Linear and Non-Linear Copolymers Directed Self-Assembly

The impact of film thickness and the mixed solvent vapors (simultaneously flow of toluene and heptane at different ratios) on the self-assembled structures of the PS-*b*-PDMS-*b*-PS triblock copolymer thin films has been recently reported.<sup>68</sup> The experimental observations were in a good agreement with the SCFT theoretical predictions further verifying the higher processing window in triblock copolymers. Notably, under specified conditions not only has the formation of double layer of perforated lamellae taken place but also it has been concluded to be a stable morphology. On the basis of the experimental results, phase transitions from lamellae to perforated lamellae to cylinders occurred as the fraction of toluene in the mixed vapors increased inducing also an increase on the  $\chi_{\text{effective}}$ . In addition, the thin film periodicity (~15 nm) proved that lower molecular weight triblock copolymers could induce the formation of sub-10nm spacing, which is unattainable from BCPs with the same molecular characteristics. The stability of the phases theoretically predicted as a function of film thickness and composition indicating a coherent phase transition as the composition increased.

In the linear diblock copolymer the enthalpic contribution of PDMS segment due to the low surface tension is significant leading to parallel orientation. To induce perpendicular cylindrical or lamellar nanodomains, Avgeropoulos and Ho groups<sup>16</sup> studied the architecture effect on PDMS-based star block copolymers. The topological effect gives rise to additional entropic contribution to compensate for the enthalpic one enabling the spontaneous formation of vertical nanostructures. A schematic illustration of various architectures linear and non-linear based on enthalpy- or entropy-driven orientation is given in Figure 4.7. To experimentally demonstrate the architecture effect, a three arm star block copolymer and the equivalent linear diblock copolymer precursor were prepared using the same processing conditions (identical film thicknesses and thermal annealing at 280 ° C for 30 minutes). The preference of PDMS segment to segregate in the air/polymer interface caused the formation of parallel cylinders in the linear copolymer. On the contrary, the TEM studies on the thin films of the three arm star shaped material suggested the formation of hexagonally packed perpendicularly oriented cylinders due to the complexity of the architecture.

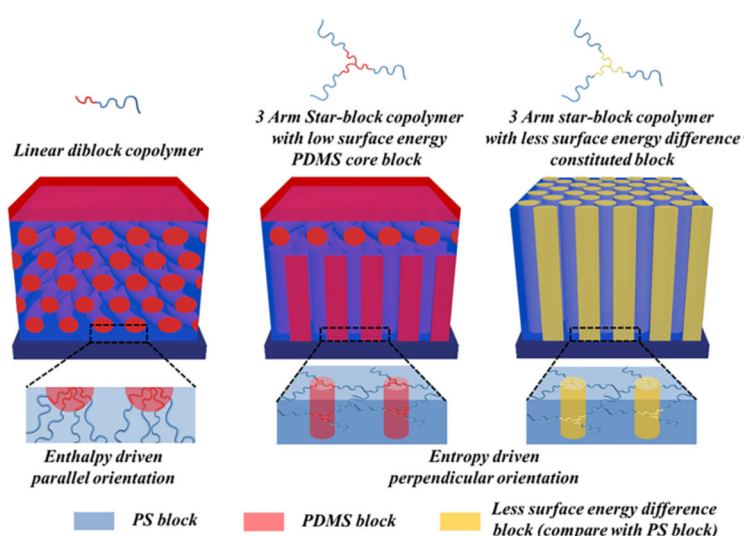


**Figure 4.7:** Schematic representation with respect to the enthalpy- and entropy-driven orientation in linear diblock, star block  $(PS-b-PDMS)_3$  and star block  $(A-b-B)_3$  thin films with less surface energy difference between the chemically different blocks. The formation of surface wetting layer with parallel orientation in the  $(PS-b-PDMS)_3$  and the absence of the wetting layer for  $(A-b-B)_3$  is straightforward.<sup>16</sup>

To further investigate the obtained results FESEM experiments on the top and bottom views were conducted. The top-view FESEM experiments on the star block copolymer revealed the formation of parallel cylinders due to PDMS wetting, while

the bottom view confirmed the formation of well-aligned vertical cylinders. The formation of parallel cylinders from the top and vertical from the bottom was perfectly imprinted in the representative cross-sectional TEM image, in which it is understood that the entropic penalty overran the orientation from the top but the cylinders in the bottom could not propagate to the entire film. Finally, the results were verified by GISAXS measurements. The results from FSEM, cross-sectional TEM and GISAXS are observed in Figure 4.8. The absence of semi-circular lines in combination with the many diffraction spots indicated the formation of parallel cylinders. In the three arm-star block copolymer existence of the Bragg rods confirmed the development of well-ordered hexagonally packed cylinders.<sup>16</sup>

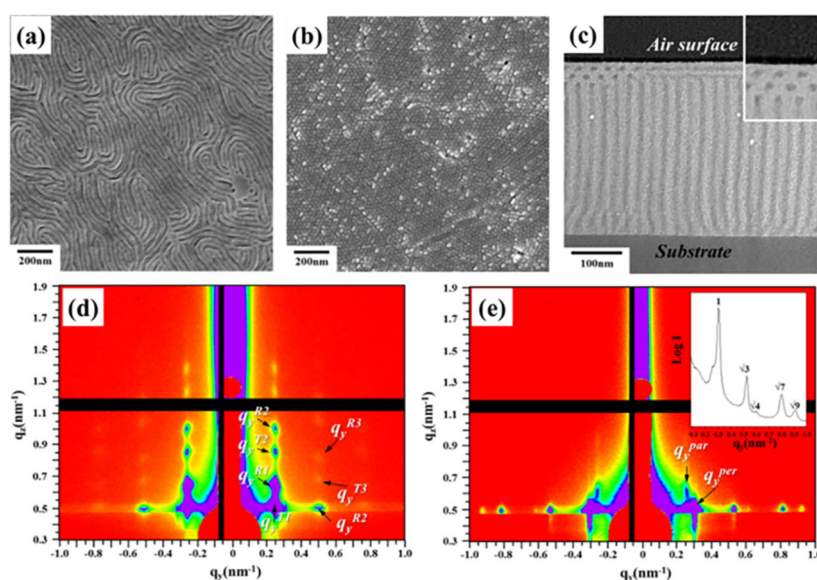


**Figure 4.8:** FESEM of  $(PS-b-PDMS)_3$  thin films (340 nm thickness) (a) top-view and (b) bottom-view (c) Cross-sectional TEM micrograph. 2D GISAXS pattern of (d) linear and (e) 3-arm star block copolymer thin film samples with identical thickness.<sup>16</sup>

To mitigate the enthalpy concerns related to the silicon-based copolymers a new method for the perpendicular orientation of cylinders in a three-arm star block copolymer has been developed. A low voltage-small current air plasma treatment was applied to the spin-coated sample before thermal annealing to provide a neutral “top coat” surface, capable of eliminating the interfacial energy discrepancy due to the formation of an oxidative top mat. Notably, the combination of architecture effect (entropy contribution) and the neutral air surface (enthalpic contribution) gave rise to span-through perpendicular cylinders extending to the whole film as verified by combined cross-section TEM images and scattering results.<sup>17</sup>

Furthermore, to clarify the alignment kinetics, surface studies were conducted. The results indicated that the hydrophobic PDMS wetting layer surface has been transformed to a hydrophilic cross-linked one due to the formed hydrophilic groups (hydroxyl or -OH, carboxyl -COOH) induced during the oxidation. The ionization of oxygen under reduced pressure resulted in the formation of  $O_3^*$ ,  $O^*$ ,  $O_2^*$  radicals which reacted with the copolymer in the top surface and also radical recombination due to the instability of free radical after the treatment contributed to the formation of a robust, hydrophilic, cross-linked surface. Interestingly, the same procedure has been employed for the linear copolymer precursor. The results demonstrated that the enthalpy effect was evident also in the BCP surface but the absence of entropy effect led to the formation of parallel cylinders at the bottom of the film (Figure 4.9).<sup>17</sup>

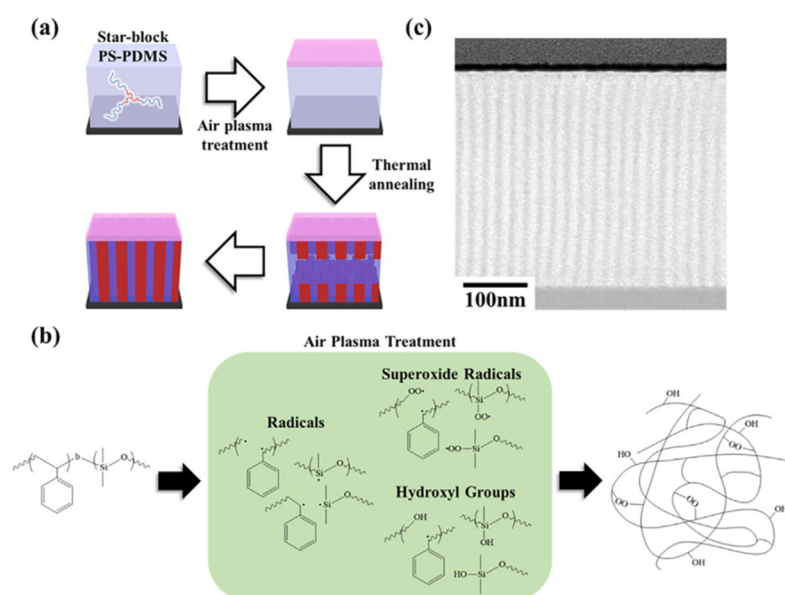


**Figure 4.9:** (a) Schematic representation of entropy (architecture) and enthalpy (air surface) effects on the controlled orientation of cylinder-forming  $(PS-b-PDMS)_3$  copolymer after a short air-plasma treatment; (b) Mechanism for plasma-induced random copolymerization to form the capped neutral layer; (c) TEM cross-section images for thin film with air-plasma treatment followed by thermal annealing at 280 °C exhibiting perpendicular orientation.<sup>2,17</sup>

The self-alignment mechanism with respect to the ordered perpendicularly oriented domains was elucidated.<sup>17</sup> Both top and bottom interfaces served as nucleation substrates for the formation of perpendicular cylinders. In the middle of the film, cylinders with mixed orientation were observed for short annealing time. The non-correlated domains from the top and bottom surfaces induced major discrepancies regarding the orientation and position of the cylinders. The higher annealing period contributed to the merging of the differently oriented phases in the transition zone

giving rise to perpendicularly deformed cylinders with elliptical texture. Span-thru well-oriented cylinders sandwiched between SiO<sub>2</sub> substrate and capped neutral air surface were fabricated due to the self-alignment process for the highest annealing period (30 minutes at 280 °C) as can be seen through the illustration in Figure 4.10.

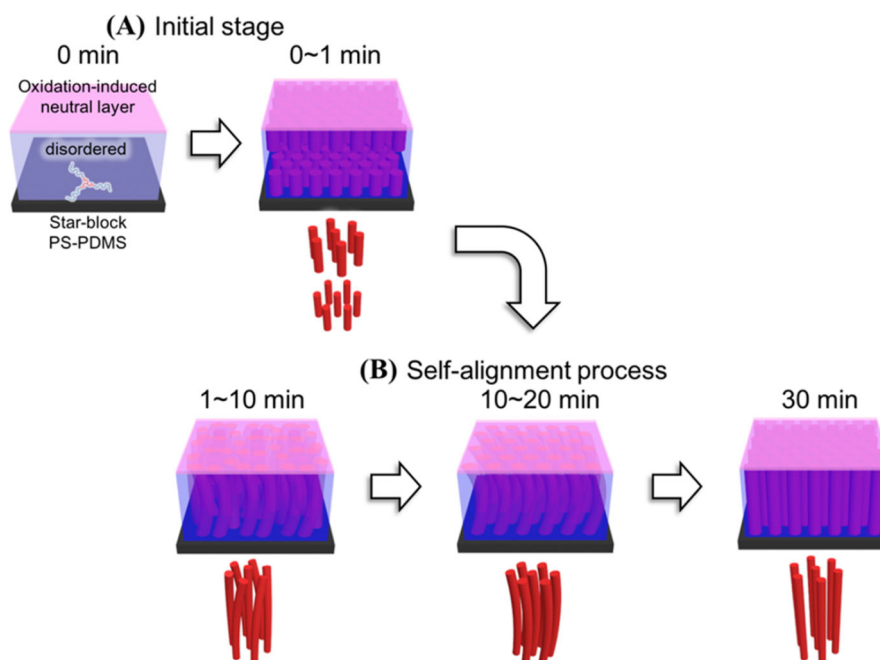


**Figure 4.10:** Self-alignment process for the perpendicular orientation in a cylinder forming  $(PS-b-PDMS)_3$  star block copolymer at different annealing time. (A) The nucleation of perpendicular cylinders from both the top and bottom interfaces during the initial thermal annealing process for short period of time. (B) Span-thru PDMS perpendicular cylinders through the self-alignment process after 30 minutes thermal annealing.<sup>17</sup>

#### 4.4.3 Conclusive Remarks

Can the PS-*b*-PDMS systems to be considered a milestone material? The answer is given from the relative publications in which the versatile character of the specific copolymer led to quite significant findings. It certainly constitutes a thoroughly studied copolymer, yet, the discoveries both in bulk and in thin states are very intriguing to polymer physics and applications. The origins of solid-state assembly are comprehensively elaborated and the formation of novel structures indicates the strong segregation strength between the constituents. The synthesis through the anionic polymerization high standards combined with the meticulous characterization of the copolymers could even allow the construction of an experimental phase-diagram. Note that, only in the highly investigated PS-*b*-PI copolymer a direct correlation between composition and obtained structure in the SSL

exists.<sup>4,5,82</sup> In addition, the ability to synthesize different architecture copolymers<sup>10,16-19,86,154,155,174</sup> consisting of PS and PDMS will lead to a major contribution on the establishment of a clear-cut relationship between structure and properties as conformational asymmetry effects are induced.

Taking into consideration the representative thin film studies presented in a previously, it is straightforward that quite a few research groups have conducted ground-breaking studies to improve the order and to control the orientation of these materials as well as to fabricate masks for subsequent pattern transfer. Advantages such as: nanoscale minimization, low defect density, high etch selectivity as well as edge roughness characteristic and favorable scalability provide an alternative patterning method.<sup>175</sup> Interestingly enough, the concise description involved only studies related to thin film assembly kinetics and fabrication of masks for nanotechnology applications. Besides the development of patterns,<sup>176,177</sup> the PS-*b*-PDMS system has been also utilized as hydrophobic material,<sup>178</sup> in controlled electrospun fibers,<sup>179,180</sup> in the fabrication of metamaterials,<sup>181</sup> photonic nanostructures<sup>182</sup> and in tribology studies.<sup>183</sup>

It is therefore indisputable that the PS-*b*-PDMS systems showcase an outstanding potential in diverse fields due to their exquisite and appealing properties. Overcoming certain limitations related to the PDMS inherent properties could possibly lead to even higher potential applicability of the materials.

## CHAPTER 5

### Experimental Section

In this thesis, linear diblock and triblock copolymers of the PS-*b*-PDMS and (PS-*b*-PDMS)<sub>2</sub> types as well as non-linear star-shaped copolymers, namely (PS-*b*-PDMS)<sub>3</sub>, (PS-*b*-PDMS)<sub>4</sub> and (PS-*b*-PDMS)<sub>6</sub> were synthesized in accordance with the standards of anionic polymerization under high vacuum techniques.<sup>19,23,30</sup> All manipulations took place in rinsed vacuum-sealed glass apparatuses constructed through scientific glassblowing techniques. The diblock copolymer precursors were synthesized through sequential addition of the two monomers under high vacuum conditions. Subsequently, chlorosilane chemistry was employed for the synthesis of (PS-*b*-PDMS)<sub>*n*</sub> (*n*=2, 3, 4 and 6) utilizing dichlorodimethylsilane [(CH<sub>3</sub>)<sub>2</sub>SiCl<sub>2</sub>], trichloromethylsilane (CH<sub>3</sub>SiCl<sub>3</sub>), tetrachlorosilane (SiCl<sub>4</sub>) and 1,2-bis(trichlorosilyl)ethane (Cl<sub>3</sub>Si-CH<sub>2</sub>-CH<sub>2</sub>-SiCl<sub>3</sub>) respectively, as the linking reagents to the living diblock chains precursors.

#### 5.1 High Vacuum Technique

High vacuum technique holds a significant role for the successful synthesis of all linear and non-linear block copolymers prepared in this thesis. To remove all undesired impurities such as oxygen, carbon dioxide and moisture from all reagents (monomers, solvents, linking and termination reagents) involved in the polymerization procedure, high vacuum techniques are always employed. The presence of the above mentioned impurities in the polymerization reactors leads to undesirable termination and/or transfer reactions due to their rapid reaction with the initiator or the living anionic sites (Scheme 2.2). Additional precaution should be given in the linking reagents since the presence of atmospheric traces would result in their deactivation.

The high vacuum conditions are accomplished through a high vacuum line which is constructed from Pyrex (or Kimax) glass and mounted securely to a stainless steel frame (Figure 5.1). The main parts of a high vacuum line are: the mechanical vacuum pump, the mercury or siloxane-oil diffusion pump, the liquid nitrogen trap, the upper and lower glass tube parts and the high vacuum stopcocks.

Silicone oil or mercury, are the fluids of choice inside a diffusion pump. Mercury diffusion pumps demonstrate certain limitations due to the great toxicity of

Hg that may pose a health threat. However, mercury is a heavy metal (low vapor pressure) and a stream of its vapor has a large momentum creating high vacuum conditions and is inert to most organic compounds. Silicone-oil diffusion pumps have also been developed exhibiting similar characteristics.

All the manipulations require extreme precaution and special safety features. The construction of the high vacuum line as well as all of the apparatuses involved in the polymerization takes place through scientific glass-blowing. Pyrex or Kimax glasses are used due to the outstanding resistance in heat and thermal shocks, the chemical durability and low coefficients of thermal expansion.

The length of a high vacuum line is approximately 1.5-2.0 meters, because it becomes more difficult to work if the vacuum ports are spaced more than 30 cm apart especially in the case of non-volatile reagents, since the distillation from one port to another could be a rather challenging task.

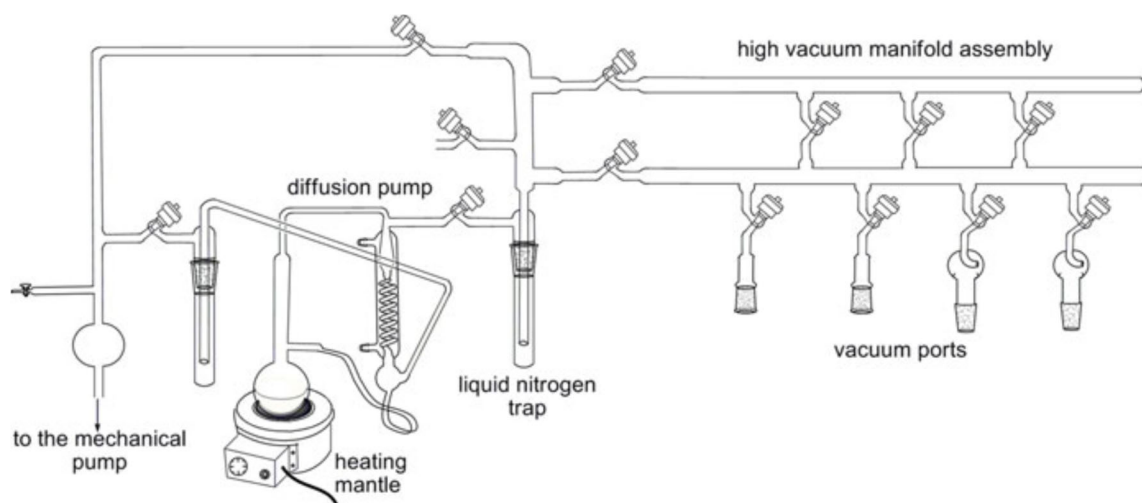


**Figure 5.1:** Schematic illustration of a high-vacuum line.<sup>23</sup>

The mechanical pump is used to reduce the pressure in the system at approximately  $10^{-2}$  mmHg and the mercury in the diffusion pump starts to evaporate by heating with a heating mantle. After mercury distillation is accomplished, the mercury diffusion pump brings the pressure down to  $10^{-6}$  mmHg according to Bernoulli's principle in which particles in flow employ a lower pressure than particles in a stationary state. Specifically, the velocity of an incompressible fluid which flows through a pipe with variable dimensions changes. When a part of the incompressible fluid is accelerated, its movement should be performed from a high pressure area to a

low pressure area to create the total force which accelerates the fluid. Consequently, for variable pipe dimensions, the pressure changes independently of the corresponding height difference.

The diffusion pump introduces a stream of Hg vapor. When the volatile gases diffuse from the manifold into the diffusion pump, they come across the stream of diffusion pump fluid, in its vapor state and gases are swept towards the mechanical pump. During the contact of mercury with the condenser walls, it condenses and returns in the heating glass vessel where the procedure is repeated.

The mercury diffusion pump is connected to the vacuum line through a liquid nitrogen trap that condenses any volatile substances incorporated in the system, and prevents both mechanical and diffusion pump from potential contamination by undesired substances. The upper part of the vacuum line is separated from the lower one by special grade high-vacuum Teflon stopcocks enabling the isolation of smaller parts of the lower part to perform different procedures (e.g., distillations, degassing) simultaneously. All apparatuses are joined to the lower part of the vacuum line through stopcocks equipped with well-suited ground joints through scientific glassblowing.

The use of high vacuum grease of extreme purity is critical to avoid friction between ground joints and apparatuses, since both are constructed from Pyrex or Kimax glass and also vacuum seal joints are attached to all the flasks and apparatuses to further prevent any introduction of environmental impurities.

A Tesla coil is a necessary and convenient tool for the manipulations in the vacuum line, since the quality of vacuum as well as the absence of any pinholes in any apparatus involved in purification and/or polymerization can be easily verified. The sound of the Tesla coil in a properly evacuated vacuum line becomes minimal when it is attached next to the glass. In contrast, the Tesla coil is very noisy when pinholes are evident in an apparatus or volatile compounds are still present in the vacuum line. The confinement of noise after short time indicates gradual high vacuum in the line and the apparatus involved during degassing.

Since the introduction of reagents during anionic polymerization should be taken place under high vacuum conditions, the apparatuses used are equipped with *break-seals*. The thin glass tip can be easily ruptured with a cylindrical magnet encapsulated in a Pyrex or Kimax glass tube and is called *breaker* (Figure 5.2 left).

For the removal of an apparatus or an ampule from the vacuum line, constrictions (seal-offs) are utilized and are heat sealed by an oxidative flame coming from a propane/oxygen torch (Figure 5.2 right).

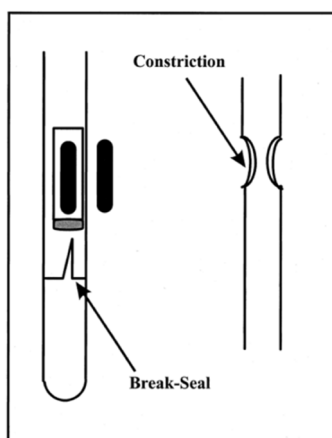


**Figure 5.2:** Schematic representation of breaker with break-seal (left) and a constriction prior the heat sealing (right).

## 5.2 Purification of Reagents

### *Benzene (C<sub>6</sub>H<sub>6</sub>)*

Proper amount of commercially available benzene (free of thiophenes and substituted phenyl-derivatives) is transferred into a round bottom flask containing finely grounded calcium hydride (CaH<sub>2</sub>) and a magnetic stirrer. Then it is attached to the vacuum line, degassed to remove O<sub>2</sub>, CO<sub>2</sub> and CO and left under stirring overnight. The reaction of the CaH<sub>2</sub> drying agent with the moisture is described in the following Scheme (Scheme 5.1).



**Scheme 5.1:** Reaction of CaH<sub>2</sub> with moisture.

The next day, two additional degassing procedures take place to remove all remaining gases from the flask and then the solvent is distilled in a calibrated cylinder containing PS<sup>(-)</sup>Li<sup>(+)</sup> living ends, which are made from the reaction between *n*-BuLi and styrene in a 7:1 ratio. The characteristic orange-yellow color indicates the high purity level of benzene and the complete absence of air. The purified solvent remains stored on the vacuum line and the appropriate quantity is distilled into the polymerization or initiator or other apparatuses when necessary.

### ***Hexane (C<sub>6</sub>H<sub>14</sub>)***

Specific amount of the volatile organic compound is transferred to a round bottom flask containing finely grounded CaH<sub>2</sub> and a magnetic stirrer, attached to the vacuum line and degassed. Similar to the aromatic solvent benzene, the relative mixture (hexane and CaH<sub>2</sub>) is left for reaction of CaH<sub>2</sub> with moisture overnight and the following day, two more degassing steps take place. Finally, the alkene is stored in a calibrated flask containing *n*-BuLi and is distilled to other apparatuses when required.

### ***Tetrahydrofuran (C<sub>4</sub>H<sub>8</sub>O)***

Tetrahydrofuran is refluxed over small sodium (Na) pieces for four hours before being collected in a round-bottom flask containing fresh finely grounded CaH<sub>2</sub> and a magnetic stirrer. The flask is attached to the high vacuum line, degassed and left under stirring overnight. The next day the solvent is degassed at least two times and then is distilled to a calibrated flask containing sodium/potassium (Na/K in a 1/3 ratio) reactive alloy. The bright blue colour developed after the vigorous stirring indicates the high purity of the solvent and is attributed to the free movement of electrons between potassium according to the following reaction:



### ***Terminating Agents***

To avoid the air contamination of the desired polymer with the double molecular weight polymer, properly degassed deactivation agents are utilized. Methanol (CH<sub>3</sub>OH) or chlorotrimethylsilane (CH<sub>3</sub>)<sub>3</sub>SiCl is used as a termination reagent in the linear diblock copolymers, while (CH<sub>3</sub>)<sub>3</sub>SiCl is employed to deactivate any remaining uncoupled active sites after the complete polymerization of copolymers with various arm numbers.

Methanol is transferred in a round bottom flask containing fresh finely grounded CaH<sub>2</sub>, attached in the vacuum line, degassed and left under stirring overnight. The following day the compound is degassed several times and small quantities (~ 1mL) are collected into the desired ampoules equipped with break-seals.

Chlorotrimethylsilane is purified by adopting a similar procedure to the one employed for methanol.

### ***Coupling Agents***

To perform the coupling reactions chlorosilane linking reagents are the compounds of choice. The low molecular weight, being liquid at ambient conditions, volatile reagents such as dichlorodimethylsilane, trichloromethylsilane and

tetrachlorosilane follow an identical purification procedure. An appropriate amount of each silane is transferred into a round bottom flask with finely grounded  $\text{CaH}_2$  and a stirrer, attached on the vacuum line and left overnight under continuous stirring. The following day, at least three more degassing procedures take place and a small amount of the silane is distilled in a newly attached apparatus containing the calibrated ampoules in order to react with any possible impurities. This process is known as silanization and is conducted to deactivate any glass contaminants including Si-OH which are harmful to the Si-Cl bond. The amount that has reacted is distilled in the nitrogen trap through the vacuum line and after high vacuum is achieved specific amount of silane is distilled in the desired ampoules equipped with break-seals.

The necessary ampoule is then attached to a new apparatus for the dilution of each chlorosilane with an appropriate amount of solvent benzene. Initially, the apparatus is rinsed with a proper silane through the silanization process and then the contents are pumped off. When high vacuum is achieved, an appropriate amount of purified benzene is distilled and the apparatus is removed from the vacuum line by heat sealing. Finally, the ampoule is ruptured and the amount of silane is introduced to the benzene for dilution until the desired concentration is reached.

In the case of 1,2-bis(trichlorosilyl)ethane a different process is adopted due to the low volatility of the compound, being a solid at ambient conditions and the increased melting point compared to the aforementioned chlorosilanes. Appropriate quantity of the solid silane is transferred in a round bottom flask equipped with a filter under inert atmosphere, attached in the vacuum line and degassed. Proper quantity of purified hexane is distilled in the apparatus and three partial crystallizations at  $-20\text{ }^\circ\text{C}$  are performed. After the removal of the upper phase through the filter, an appropriate quantity of hexane is distilled in the ampoule which is then transferred to a new rinsed apparatus with desired calibrated ampoules equipped with break-seals.

### ***Initiator***

*Sec*-BuLi is utilized in all polymerizations without performing any purification procedure. Although a dilute solution of the initiator (since desired concentration is needed with accuracy of at least three decimal points) is prepared due to the high concentration of the commercially available product (1.4 M in cyclohexane). Appropriate quantity of the initiator solution is introduced through a septum via a syringe to a suitable apparatus with pre-calibrated ampoules under vacuum and the side arm is removed through heat sealing of the insertion constriction. After the

removal of the cyclohexane in the vacuum line and the reaching of the desired high vacuum, the necessary amount of solvent (benzene or hexane) is distilled in the apparatus. The mixture is degassed and removed from the vacuum line through sealing at the proper constriction. The amount of solvent needed for the desirable concentration of the solution is calculated through the following equation:

$$C_1 \cdot V_1 = C_2 \cdot V_2 \quad (5.1)$$

where  $C_1$  corresponds to the initial concentration of *sec*-BuLi,  $V_1$  is the initial amount of *sec*-BuLi injected in the apparatus,  $C_2$  stands for the final desired concentration and  $V_2$  represents the appropriate amount of solvent in order to achieve the desired concentration.

### ***Monomers***

#### ***Styrene (C<sub>8</sub>H<sub>8</sub>)***

A proper quantity of styrene is attached to a short path distillation apparatus, degassed and left to be dried overnight due to the reaction of moisture with the drying agent (CaH<sub>2</sub>). The low volatility attributed to the high boiling point of the monomer necessitates the use of specialized short path distillation techniques. The following day, is degassed twice and distilled in a different round bottom flask with the appropriate amount of dibutylmagnesium (Bu<sub>2</sub>Mg) (dissolved in heptane since it is commercially available in 1M solution diluted in heptane) which has been introduced via a side arm through an elastic septum and the arm is sealed off with an oxidative torch flame. The concentration of the monomer towards that of the Bu<sub>2</sub>Mg for appropriate purification of the styrene should follow the equation: [monomer]/[Bu<sub>2</sub>Mg] = 20/1. The heptane is removed in the line and the styrene is distilled in the new apparatus containing the organomagnesium compound and is left to react for three hours at low temperature (~0°C–10°C). The polymerization of styrene with dibutylmagnesium is possible as indicated by a bright yellow-greenish colour developed when the pure monomer starts to polymerize, but it proceeds very slowly especially when the temperature is set below ambient conditions. Organolithium compounds are severely restricted to be used as purifying reagents since they rapidly polymerize the monomer and also the reaction is highly exothermic. Finally, the purified monomer is distilled in pre-calibrated ampoules and kept at -20°C. A schematic with all the apparatuses and the steps followed for the purification of styrene is presented in the Figure 5.3.

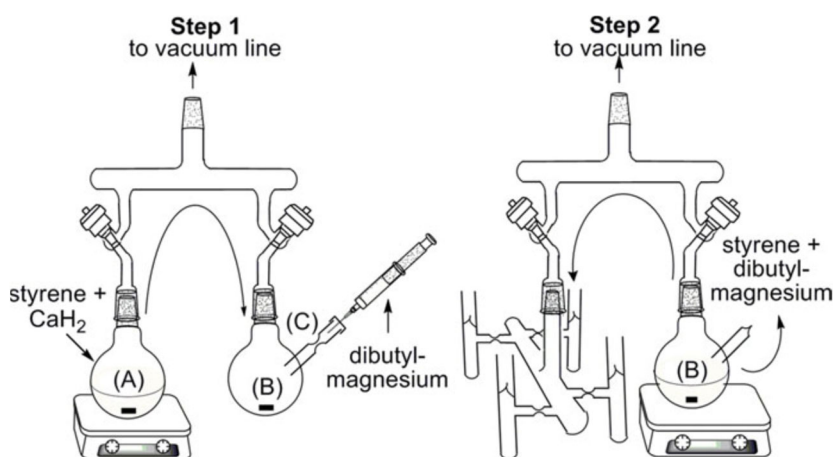


**Figure 5.3:** Schematic representation of purification procedure of the styrene monomer.<sup>23</sup>

### *Hexamethylcyclotrisiloxane [(CH<sub>3</sub>)<sub>2</sub>SiO]<sub>3</sub>*

Hexamethylcyclotrisiloxane (D<sub>3</sub>) is a solid monomer having melting point at 70 °C and special manipulations as well as short path distillation apparatuses are demanded for the effective purification of the compound. Appropriate quantity of solid D<sub>3</sub> is transferred to a round bottom flask with finely grounded CaH<sub>2</sub> and attached on the properly designed apparatus (Figure 5.4a). The quantity is diluted with purified benzene and stirred over the drying agent overnight. The following day the solution is degassed twice and by heating at approximately 40 °C, the benzene is distilled and D<sub>3</sub> is sublimed in the empty flask attached in the short path distillation apparatus. The flask is heat sealed and adjusted in a new short path distillation apparatus (Figure 5.4b). The break seals corresponding to the D<sub>3</sub>/benzene solution and the living polystyryllithium solution are ruptured, and the monomer is allowed to remain in contact with the PS<sup>(-)</sup>Li<sup>(+)</sup> for at least two hours at ambient conditions. The colour of the mixture (yellow-orange), remaining unchanged during the predetermined duration, indicates the absence of any impurities. Then, the solvent is distilled and the monomer is sublimed to a second flask where a new PS<sup>(-)</sup>Li<sup>(+)</sup> is introduced and the procedure is repeated at least one more time. Note that, this step is repeated as many times needed, until the yellow-orange colour remains completely unchanged, to verify the high purity of the monomer. Finally, the solvent is distilled and the monomer is sublimed to a calibrated flask in order to be adjusted to a different dilution apparatus. The concentration of the solution (D<sub>3</sub>/benzene) can be accurately determined by synthesizing a PDMS homopolymer.

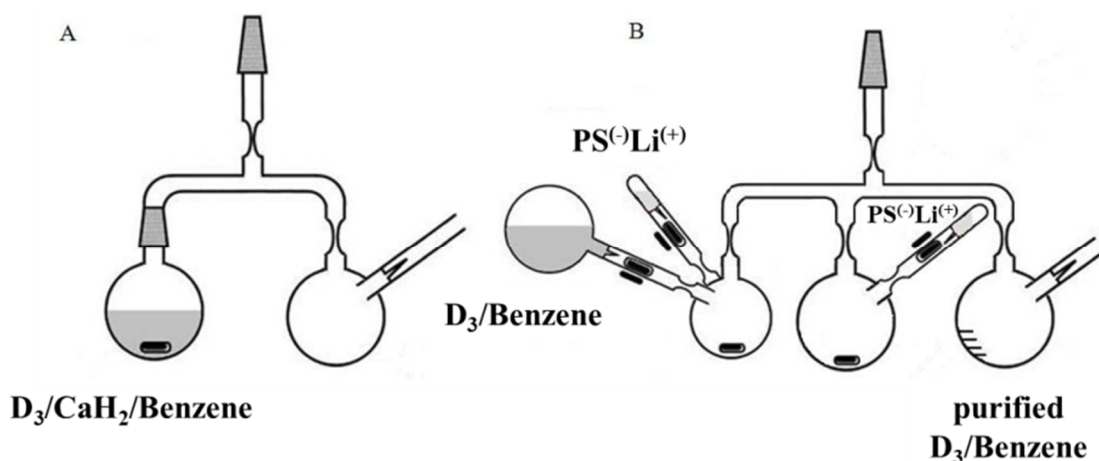


**Figure 5.4:** Schematic representation of apparatuses involved in the purification of  $D_3$  monomer.

### 5.3 Synthetic Protocols

The synthetic procedures with respect to the linear diblock PS-*b*-PDMS and triblock PS-*b*-PDMS-*b*-PS [or (PS-*b*-PDMS)<sub>2</sub>] copolymers and non-linear symmetric star block copolymers of the (PS-*b*-PDMS)<sub>*n*</sub> (*n*=3, 4 and 6) type will be thoroughly described in the following subchapters. Anionic sequential polymerization is employed for all diblock copolymer precursors while the combination with chlorosilane chemistry via coupling reactions with the appropriate multifunctional agents leads to the synthesis of the desired star block copolymers.

#### 5.3.1 Synthesis of Linear Diblock Copolymers

Well-defined linear diblock copolymers are synthesized by sequentially adding styrene with *sec*-BuLi in benzene at 25 °C, followed by the addition of hexamethylcyclotrisiloxane and polar THF solvent (approximately 1:1 ratio with benzene) prior to the termination with methanol. This synthetic route is well-established<sup>10,19</sup> and leads to narrow dispersed copolymers with high molecular and compositional homogeneity. An important aspect which should be mentioned, for the case of linear and non-linear star block copolymers, is that after the complete polymerization of the second monomer the living diblock copolymer precursors react with the appropriate linking reagent and are not terminated with methanol.

After conducting the appropriate scientific glass blowing to prepare the necessary polymerization reactor all the different ampoules containing the two monomers, the initiator, the THF and the termination reagent are attached on the

apparatus (Figure 5.5i). Through a ground joint (A) the apparatus is subsequently attached to the vacuum line and checked for pinholes with the Tesla coil before pumped for sufficient time to remove any volatile species. During this step, the flame drying technique using a hand torch with reducing flame (more propane and less oxygen) is applied (2-3 times) to accelerate degassing and remove any humidity traces. The existence of high vacuum is verified with the Tesla coil. Then, a proper amount of purging agent (concentrated *n*-BuLi in hexane) is injected via a syringe through the elastic septum (b). Afterwards, the constriction that includes the elastic septum is rinsed and detached with a torch oxidative flame and hexane is removed to the nitrogen trap through the vacuum line. Appropriate amount of purified benzene is distilled through the vacuum line into the spherical flask or purge section (B) using liquid nitrogen. Note that, the amount of solvent is chosen in order to obtain a final polymer concentration of approximately less than 5% w/v depending on the molecular weights of the desired segments. After the distillation, the mixture is degassed and the apparatus is detached from the vacuum line by heat sealing in the appropriate constriction (a). The inner walls of the glass apparatus are washed by transferring the solution (*n*-BuLi/Benzene) to the whole reactor. The procedure is repeated three times to ensure that all impurities have reacted with the *n*-BuLi and the solution is collected in the purge section (B). The remaining traces of *n*-BuLi in the inner walls are rinsed by placing the purge section in a warm bath (50 °C) which induces the benzene to reflux and condensate due to the high vacuum conditions. In this way, the solvent is collected in the main polymerization reactor (C) and poured back into the purge section together with *n*-BuLi and the undesired reaction products with *n*-BuLi, by carefully tilting the apparatus. A towel strip dipped in liquid nitrogen is applied to collect the solvent in any part of the apparatus to facilitate the rinsing procedure. To verify the absence of any reaction impurities and *n*-BuLi that would affect the polymerization, the process is repeated for at least ten (10) times in all parts of the apparatus, consisting the polymerization reactor with the necessary ampoules (monomers, initiator, solvents, terminating reagent and/or chlorosilane reagents). Afterwards, the pure solvent is distilled to the main reactor by immersing the purge section in a water bath at 25 °C and the main flask C in an ice bath (at 0 °C) and when the distillation of the pure solvent from the purge section is completed, this part is detached by heat sealing of constriction (c) (Figure 5.5ii) leaving the main polymerization reactor with the appropriate amount of purified solvent.

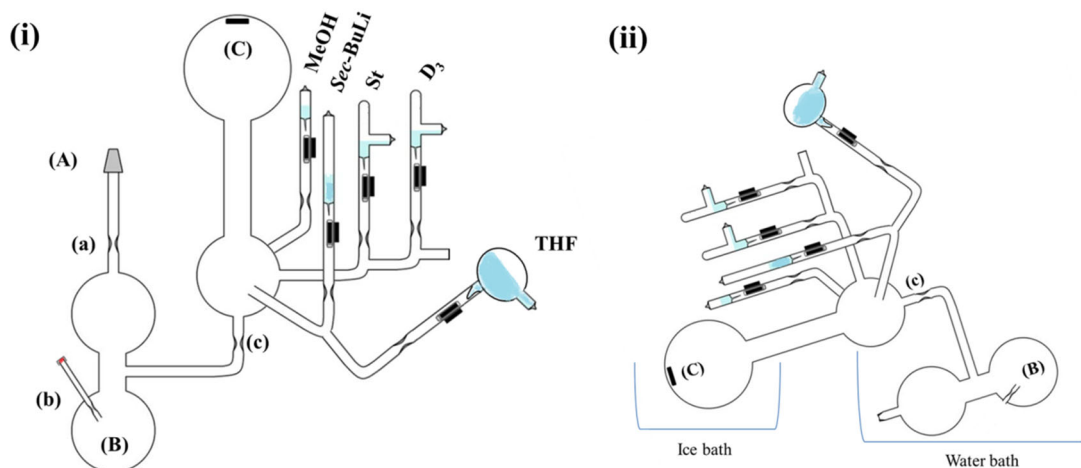


**Figure 5.5:** Schematic representation of apparatuses involved in the polymerization of the linear diblock copolymer.

The clean reactor with the appropriate amount of benzene is left to heat to room temperature before the polymerization takes place. Initially, the break seal of the styrene is ruptured by moving the outside magnetic rod of the breaker and the monomer is poured in the solvent. The break seal of the *sec*-BuLi is then ruptured to initiate the polymerization of styrene which is indicated by the existence of an orange-yellow color (depending on the molecular weight and the concentration of the solution). The polymerization of styrene is left to proceed for 18 h at ambient conditions to ensure that all monomer quantity has been consumed and a small aliquot is retrieved to determine the molecular characteristics of the first block through size exclusion chromatography and vapor or membrane osmometry. It should be noted that the completion of the styrene polymerization is accomplished within approximately 90 minutes (according to kinetic studies) since the  $t_{1/2}$  for this procedure is 15 minutes. The overnight left over is taking place due to increased time duration of the whole purification procedure and the  $D_3$  polymerization involves many steps. The addition of the  $D_3$  monomer is performed to the solution containing the living polystyryllithium chain ends and the ring opening of the monomer in approximately 18 h is indicated by the gradual discoloration. To propagate the polymerization of  $D_3$  an equal volume of THF (compared to the benzene, ratio between the two solvents being 1:1) is added to the solution. The polymerization of  $D_3$  is promoted due to the soft donor character of the THF that allows the polymerization to proceed with the minimum side reactions.<sup>57</sup> After the introduction of the THF in the solution the polymerization is allowed to proceed until 50% conversion at room temperature for

approximately 4 hours and then is placed in a constant temperature freezer ( $-20^{\circ}\text{C}$ ) for one week until completion. The low temperature is critical to avoid any back-biting and redistribution reactions of PDMS by decreasing the reaction kinetics (Figure 2.1). For the completion of the polymerization, a small amount of trimethylchlorosilane or methanol is added to the solution to deactivate the living anions under vacuum. The synthesized sample is precipitated in a large excess of methanol stabilized with a proper antioxidant reagent (2,6-di-tert-butyl-p-cresol) and the obtained diblock copolymer is dried under vacuum for at least 24 h in a drying oven.

According to the method previously described various diblock copolymers with total number average molecular weights, ranging from 5,000-140,000 g/mol and different volume fraction ratios were synthesized by manipulating the feeding ratio of the respective monomers. The quantity of the final diblock sample in each case was at least 10 grams in order to conduct all the necessary molecular, thermal and morphological characterizations in the framework of this thesis. The amount of benzene and therefore of the THF used for the polymerization reactions varied from 250 mL (for the lower molecular weights samples) up to 500 mL (for the higher molecular weights ones) respectively. In all cases, the concentration of the different solutions was kept lower than 5% w/v.

Note that for the star block copolymers, following the completion of the two-stage sequential polymerization of styrene and the hexamethylcyclotrisiloxane a small quantity (ca. 1.5 g) is isolated for characterization and comparison (linear *vs.* star block copolymers with various arm numbers) purposes. Then, the appropriate linking agent is added to the remaining living copolymer solution for the formation of star-block copolymers in a process that will be described in the following subchapters. The synthesis reaction, with respect to the diblock copolymer, is presented in Figure 5.6.

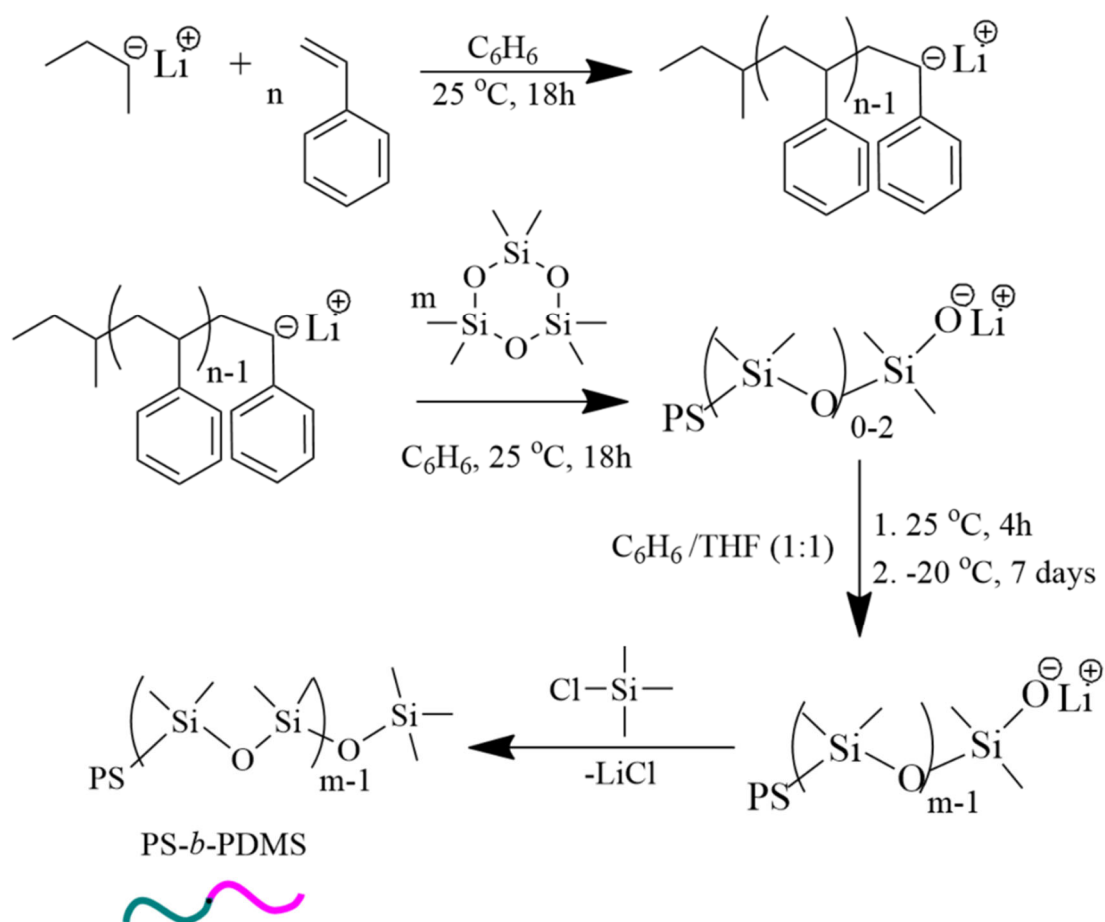


**Figure 5.6:** Synthesis reactions of linear diblock copolymers.

### 5.3.2 Synthesis of Linear Triblock Copolymers

To conduct the coupling and formation of the linear triblock copolymers the use of a difunctional linking reagent is necessary. The dichlorodimethylsilane is added to the already synthesized living diblock copolymer chains instead of methanol and the polymerization is allowed to proceed for approximately one month. The C-Li/Si-Cl ratio is a quite critical parameter for the successful outcome of the reaction and a stoichiometric quantity between the living ends and the chlorosilane is always considered necessary. Specifically, the molar ratio between living chains to active sites is chosen to be 2/1 to verify that all chlorine atoms have been substituted by the desired macromolecular chains without forming any gel-type or high viscosity polymers and to accelerate the reaction kinetics.<sup>10,19,30</sup> Furthermore, to verify the complete reaction of the linking agent, a small excess of the precursor is added (approximately 10%). To monitor the progress of the reaction small aliquots are removed from the solution at frequent intervals (7, 14 and 28 days) and studied



### 5.3.4 Synthesis of Four-Arm Star Block Copolymers

To synthesize four arm star block copolymers, the reaction of living precursor with a tetrafunctional silicon chloride (four chlorine atoms), namely silicon tetrachloride is necessary. The reaction is possible to yield stars with various functionalities, such as three- and four- arm copolymers, especially during the preparation of higher molecular weight polymers due to the lower coupling kinetics of the fourth unit. Thus, the molar ratio between living polymer and coupling agent is of paramount importance to obtain a relatively pure product with low degree of by-products. The C-Li/Si-Cl ratio in this case equals to 4/1. The small excess of the deblock precursor being approximately 10% is also necessary for reasons described previously. The coupling reaction is monitored at frequent time intervals similar to the previously described procedure. Narrow dispersed polymers containing a predetermined number of arms are afforded by consecutive fractionations. The reaction is illustrated in Figure 5.9.

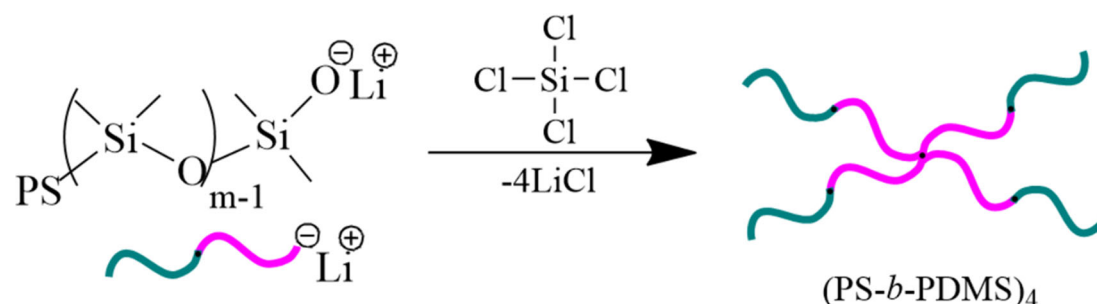


**Figure 5.9:** Synthesis reactions of four arm star block copolymers.

### 5.3.5 Synthesis of Six-Arm Star Block Copolymers

The synthesis of six-arm star block copolymers containing PS and PDMS blocks has never been reported in the literature. The role of star block copolymers in polymer chemistry and physics is quite significant and is expected to be further developed. Anionic polymerization in combination with chlorosilane chemistry provides the ability to synthesize well-defined star block copolymers with precise functionality even when the arm number is increased. A key contributor to the successful outcome of the reaction, as well as the complete coupling between the reactants, is the selection of a less stereo-chemically hindered coupling agent. To avoid any side reactions, the compound of choice is 1,2-bis(trichlorosilyl)ethane because it contains three chlorine atoms per silicon and the two Si groups are divided

by an ethylene spacer.<sup>72</sup> The excess of living arms over Si-Cl is substantially increased and equals to a 6/1 ratio to avoid the production of stars with less arms. Also, it is well-elaborated that the higher the number of incorporated arms, the slower the reaction kinetics. The coupling is left to proceed for sufficient time (at least 45 days) to ensure that all arms have been successfully incorporated and the course of the reaction is monitored with SEC. Fractionation is also carried out to the crude product to remove the unwanted species and to receive a pure material with the desired arm number. The synthetic route employed is presented in Figure 5.10. Again, a small excess of approximately 10% of the diblock precursor is added to eventually control the linking reaction without any unnecessary side products.

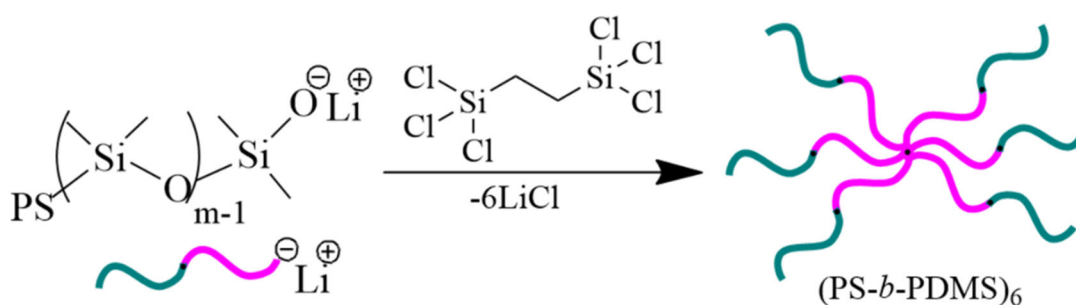


**Figure 5.10:** *Synthesis reactions of six arm star block copolymers.*

### 5.3.6 Fractionation

The excess of diblock precursor used during the coupling reaction leads to a mixture of copolymers (desired star block copolymer and unreacted diblock copolymer) that necessitates the fractionation procedure. In addition, a non-appropriate molar ratio between C-Li and Si-Cl induces the formation of stars with less than the desired functionality. To isolate the pure products by partitioning the different polymer species between two liquid phases, the separation process should be conducted using a specific solvent/non solvent pair which is directly associated with the solubility parameters of the macromolecular chains. The variations in the molecular characteristics including molecular weight and composition favor the separation process.

The fractionation is performed in a proper separation flask equipped with a high vacuum stopcock (to avoid any leakage of the viscous solutions). The sample is diluted in a solvent (toluene) under stirring, forming a solution of 1% w/v or less, while the separation flask is placed in an annealing oven at approximately 70 °C. The non-solvent (methanol) is introduced gradually to the diluted polymer mixture until

the solution becomes cloudy without any evident precipitation. The mixture is subsequently warmed up until it becomes transparent and is transferred to the warm separation flask which has already been removed from the annealing oven. The introduction into the flask should be conducted carefully to avoid any evaporation of the solvents and the temperatures of the mixture and the separation flask should be similar. The system is left to cool down slowly to room temperature and two distinctive phases are subsequently formed. After cooling down, the temperature should remain constant to further promote the separation of the two phases.

The above mentioned procedure contributes to the precipitation of the higher molecular weight macromolecules forming a lower layer of a more concentrated phase, while the lower molecular weight ones form an overlying phase. The successful outcome of the procedure is monitored via SEC by extracting small aliquots of both the lower and upper phases. The lower phase is collected and fractionated until the complete elimination of the undesirable products is confirmed.

### **5.3.7 Additional Synthesis Information**

To synthesize the aforementioned copolymer sequences specific apparatuses are designed to host both the sequential addition of the two monomers and the coupling reactions. In one case, the living copolymers are utilized as precursors for the synthesis of three- as well as the four- arm star block copolymers while in the second case the diblocks are chosen as the precursors for the preparation of the linear triblock and the six-arm star block copolymers. The reason for choosing to synthesize the samples combined is to study the effect of the additional number of arms on the solution and solid state properties compared to the initial linear diblock copolymer. The synthesis of all copolymers sequences employing the same precursor is severely restricted by several factors. Firstly, anionic polymerization requires the reactions to be conducted at relatively low concentrations, less than 5% w/v of the total polymer weight and secondly the chlorosilane chemistry necessitates the use of fractionation to isolate the desired materials which results in desired sample quantity loss. In addition, the coupling reaction takes place using exact quantities between the moles of living copolymers and active sites. Taking these restrictive parameters into consideration, the synthesis of well-defined, narrow dispersed copolymers with the desired functionality obligates the utilization of dilute solutions and precise stoichiometry between the C-Li and Si-Cl molar ratio.

The apparatus used for the synthesis of the parent material and the linking reactions is demonstrated in Figure 5.11. It is straightforward that, the solution is equally divided into two separate reactors in which the appropriate ampoules containing the coupling and termination reagents are adjusted. A small quantity of the diblock precursor is kept in all cases as already described for characterization reasons. The flasks are placed at a constant temperature and the course of the coupling reaction is monitored through SEC by timely taken aliquots.

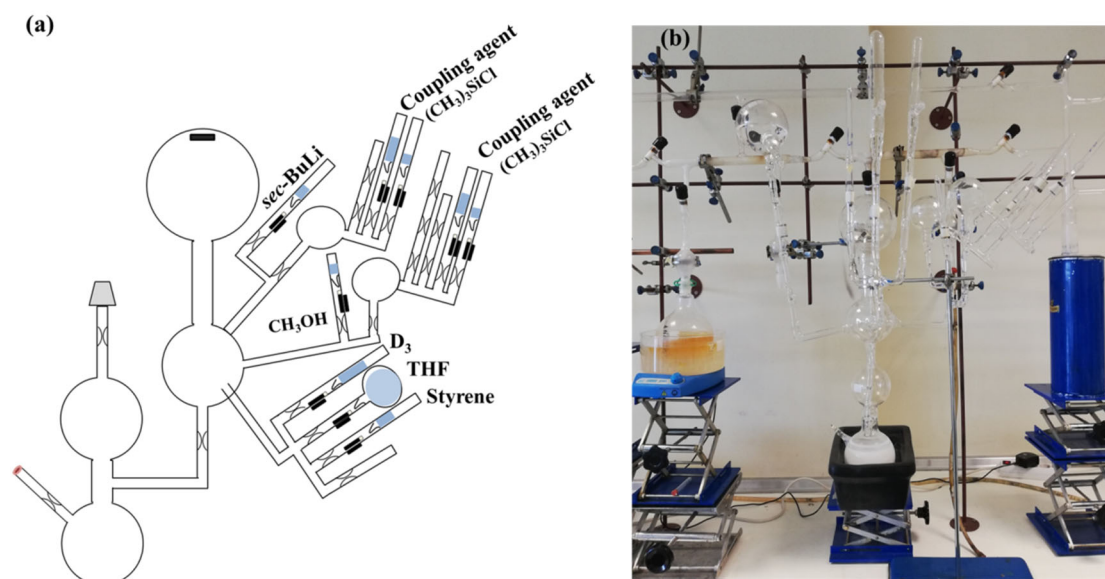


**Figure 5.11:** Apparatus involved in the synthesis of linear and non-linear diblock copolymers. In all cases the main ampoules are attached in every synthesis experiment using the appropriate quantities of the reagents based on the desired final molecular characteristics and functionality of star block copolymers. The ampoules with respect to coupling agents can either be the combination of dichlorodimethylsilane and 1,2-bis(trichlorosilyl)ethane or trichloromethylsilane and silicon tetrachloride.

The synthetic procedures involved in this thesis have been already thoroughly documented. The precise quantities with respect to specific samples characteristic to each copolymer sequence are listed below. In all cases the subscript next to PS and PDMS correspond to the number average molecular weight per segment (as calculated by MO or VPO). The subscript next to the parentheses corresponds to the total number of arms (1, 2, 3, 4, 6).

**PS<sub>51</sub>-*b*-PDMS<sub>35</sub>:** 9.0 g of styrene (0.086 mol) were reacted with 0.176 mmol *sec*-BuLi in 250 ml benzene and were left overnight. 6.0 g of hexamethylcyclotrisiloxane (0.027 mol) were introduced to the solution and afterwards 250 ml of THF were added to propagate the reaction as described above in subchapter 5.3.1.

**(PS<sub>4.2</sub>-*b*-PDMS<sub>5.6</sub>)<sub>1,3,4</sub>**: 10.0 g of styrene (0.096 mol) were reacted with 2.40 mmol *sec*-BuLi in 400 ml benzene and were left overnight. 13.0 g of hexamethylcyclotrisiloxane (0.17 mol) were introduced to the solution followed by the addition of 400 ml of THF to propagate the reaction for the synthesis of the PS<sub>4.2</sub>-*b*-PDMS<sub>5.6</sub> diblock precursor. In the case of (PS-*b*-PDMS)<sub>3</sub> as well as (PS-*b*-PDMS)<sub>4</sub> 0.40 mmol of CH<sub>3</sub>SiCl<sub>3</sub> and 0.30 mmol of SiCl<sub>4</sub> were used, respectively (leading to small excess of the diblock and complete consumption of the linking reagent).

**(PS<sub>5.0</sub>-*b*-PDMS<sub>5.0</sub>)<sub>1,2,6</sub>**: 14.0 g of styrene (0.135 mol) were reacted with 2.80 mmol *sec*-BuLi in 450 ml benzene and were left overnight. 14.0 g of hexamethylcyclotrisiloxane (0.190 mol) were introduced to the solution and afterwards 450 ml of THF were added to propagate the reaction for the synthesis of the PS<sub>5.0</sub>-*b*-PDMS<sub>5.0</sub> diblock precursor. In the case of (PS-*b*-PDMS)<sub>2</sub> as well as (PS-*b*-PDMS)<sub>6</sub> 0.70 mmol of (CH<sub>3</sub>)<sub>2</sub>SiCl<sub>2</sub> and 0.23 mmol of Cl<sub>3</sub>SiCH<sub>2</sub>CH<sub>2</sub>SiCl<sub>3</sub> were used, respectively (leading to small excess of the diblock and complete consumption of the linking reagent).

## 5.4 Molecular Characterization

### 5.4.1 Size Exclusion Chromatography (SEC)

A PL-GPC 50 integrated GPC system from Agilent Technologies equipped with an isocratic pump (SpectraSystem P1000) (1.0 mL/min), a column oven (LabAlliance) (heated at 30 °C), three columns in series (PLgel 5 mm Mixed-C, 3007.5 mm) to hold the stationary phase, detectors including a refractive index detector (RI, Shodex RI-101) and an ultraviolet absorbance detector (UV, SpectraSystem UV1000) to detect the components were utilized using THF as the mobile phase. Calibration with PS standards [eight PS standards (Mp: 4.300 to 3.000.000 g/mol)] has been performed prior to any measurement to verify the accuracy of the measurements. The specific instrumentation was employed to measure polymer molecular-weight distributions (such as  $\bar{M}_n$ ,  $\bar{M}_w$  and dispersity  $\bar{D}$ ), to monitor the coupling reactions and verify the successful fraction in all synthesized samples. All SEC experiments were performed at the Polymers Laboratory, Department of Materials Science Engineering, University of Ioannina.

#### **5.4.2 Membrane and Vapor Pressure Osmometry**

Through membrane osmometry (MO) using a Gonotec Osmomat 090 in 35 °C the accurate  $\bar{M}_n$  values of all synthesized materials were determined. The solvent of choice was dried toluene and the membrane was from regenerated cellulose. Vapor pressure osmometry (VPO) was performed at a Gonotec Osmomat 070 at 45 °C using dried toluene. The practical use is directly correlated to its ability to determine the  $\bar{M}_n$  values of low molecular weight samples ( $<10^4$  g mol<sup>-1</sup>) with high accuracy. All measurements were conducted at the Polymers Laboratory, Department of Materials Science Engineering, University of Ioannina.

#### **5.4.3 Proton Nuclear Magnetic Resonance (<sup>1</sup>H-NMR) Spectroscopy**

To quantify the chemical composition of all synthesized copolymers proton nuclear magnetic resonance spectroscopy was used. The measurements were carried out in CDCl<sub>3</sub> at 25 °C using a Bruker AVANCE II 400 MHz spectrometer, located at the Chemistry Department in the University of Ioannina. Data were processed using UXNMR (Bruker) software.

### **5.5 Thermal Analysis**

#### **5.5.1 Differential Scanning Calorimetry (DSC)**

The differential scanning calorimetry analytical technique was employed to determine the glass transition temperature values of both segments in all synthesized copolymers and to evaluate possible melting and crystallization enthalpies in the PDMS. The measurements were conducted in a Q20 TA instrument. The heating ramp was 10 K/min and the temperature range from 113K to 423K. A small amount of approximately 5-7 mg from each sample was placed in an aluminium pan, which was sealed properly and introduced into the sample holder of the instrument together with a relative reference pan. Changes in composition and physical phases induce a difference in heat flow as a function of temperature between the two pans, which is related to the specific heat of the sample. Two heating and one cooling cycles were employed and the second heating results were reported and analysed using Advantage v5.4.0 (TA instruments) software. All measurements were performed at the Polymers Laboratory, Department of Materials Science Engineering, University of Ioannina.

## 5.6 Morphological Characterization

### 5.6.1 Sample Preparation

A 10 w/v % solution in cyclohexane that demonstrates no preferential affinity towards PS and PDMS segments was prepared for all (PS-*b*-PDMS)<sub>*n*</sub> (*n*= 1, 2, 3, 4 or 6) samples. The solution casting was accomplished within seven days under ambient conditions to promote equilibrium morphologies and subsequently, a bulk portion for all samples was sealed in quartz tubes under vacuum to be thermally annealed. After the completion of the annealing process the bulk portions immediately immersed in liquid nitrogen for a few seconds (quenching). This procedure was adopted to avoid any alternation of the formed morphology which could be induced if a sample was allowed to cool slowly to room temperature due to low molecular weight values (WSL regime). Furthermore, toluene and chloroform were also utilized in some cases to prompt the formation of non-equilibrium phases following a similar procedure to the one previously described. Sample preparation is the most critical parameter to ensure enhanced self-assembly of the copolymers, leading eventually to distinguishable microphase separation. The preparation of samples took place in the Department of Materials Science Engineering, University of Ioannina and in the Chemical Engineering Department, National Tsing Hua University, Hsinchu, Taiwan.

Regarding the thin film preparation specific samples were spin coated onto (3000 rpm) silicon wafers with an intrinsic silicon oxide layer from cyclohexane solution (3 wt%). Due to the PDMS preferential segregation at the air/polymer interface oxygen reactive ion etching (RIE) treatment was implemented to remove the formed wetting layer and to oxidize the polysiloxane domains. RIE treatment for oxidation was carried out by a RF power of 60 W at the pressure of 60 mTorr for 60 s. The CF<sub>4</sub>/O<sub>2</sub> RIE for etching PDMS was generated by RF power of 50 W for 10 s, at which the involving gas of CF<sub>4</sub> and O<sub>2</sub> was in a ratio of 2:1 and the pressure was 150 mTorr. The preparation of thin films as well as the RIE treatment were conducted in the Chemical Engineering Department, National Tsing Hua University, Hsinchu, Taiwan.

### 5.6.2 Transmission Electron Microscopy (TEM)

A classic method for characterizing the structural properties of the synthesized materials is transmission electron microscopy which was performed in a JEOL JEM-2100 (TEM) microscope operating at an accelerating voltage of 200 kV in bright field

mode equipped with a LaB<sub>6</sub> filament. Real-space images were acquired from the ultrathin micro-sections without staining due to intrinsic mass-thickness contrast from PDMS towards PS microdomains. The cryo-ultramicrotoming, for receiving the desired thin sections of the initial bulk films, was performed in a Leica EM UC7 Ultramicrotome or in an EM UC6 microtome with Cryochamber EM FC7. Cryogenic conditions (-140 °C) were employed to increase the toughening of all samples, since the procedure was accomplished below the lowest T<sub>g</sub> of both PDMS and PS (-127 °C and >60 °C respectively), The microtomed sections were picked up on 600 mesh copper grids.

The preparation of the samples and the subsequent observation via TEM were performed in the Department of Materials Science Engineering, University of Ioannina at the Electron Microscopy Unit and in the Chemical Engineering Department, National Tsing Hua University, Hsinchu, Taiwan.

### 5.6.3 Electron Tomography (3D TEM)

In specific samples, electron tomography was conducted to further study the adopted morphologies. To fabricate the PS templates from the self-assembled copolymers a sol-gel reaction was utilized. To avoid the deformation of PS-*b*-PDMS caused by microsectioning during sample preparation, the PDMS block with the extremely low T<sub>g</sub> was degenerated through acid etching. The wet etching process was realized under ambient conditions for 5 days using highly concentrated hydrofluoric acid (HF).<sup>184,185</sup> After rinsing with methanol, a nanoporous PS template with well-defined nanochannels was exploited as a template for templated sol-gel reaction of SiO<sub>2</sub> to give PS-*b*-PDMS/SiO<sub>2</sub> nanohybrids. The nanoporous PS template was immersed in an acid-catalytic tetraethylsiloxane [Si(OC<sub>2</sub>H<sub>5</sub>)<sub>4</sub>] solution diluted by methanol with traces of 1M hydrochloric acid aqueous solution for templated sol-gel reaction.

Microsections of PS/SiO<sub>2</sub> with thickness from 140nm to 180nm were obtained by microtoming at room temperature using Leica UC6 Ultramicrotome, and then transferred to carbon-coated polyvinyl formal copper grids (100 mesh). After a short-time air plasma treatment, fiducial gold markers with diameter of approximately 5 nm (Polysciences, Inc.) were homogeneously distributed onto the microsections for the image alignment to reconstruct 3D imaging. Subsequently, continual images of 71 TEM S3 projection series at an angular interval of 1° were collected from -65° to +65°

tilting angles along x and y axes on a JEOL JEM-2100 TEM operated at 200 kV. Bright-field images were recorded on a Gatan CCD camera. IMOD software was used to perform alignment of the tilting series and 3D reconstruction. A median filter in ImageJ was applied to the reconstructed volume for noise reduction. Finally, visualization of the volume of interest and further 3D analysis for binarization, segmentation were achieved by using Avizo.<sup>186</sup>

The fabrication of templates and the morphological observation were accomplished in the Chemical Engineering Department, National Tsing Hua University, Hsinchu, Taiwan.

#### **5.6.4 Small Angle X-Ray Scattering**

The synchrotron beam source from the beamline BL23A of the National Synchrotron Radiations Research Center (NSRRC) was employed for the SAXS experiments at which a mirror and monochromatic to the energy of 10 keV by a germanium (111) double-crystal monochromator was used to vertically focus the incident X-ray beam. The wavelength of the X-ray beam was 1.24 Å. The beam stop was a round tantalum disk 4 mm in diameter. A MAR CCD X-ray detector (MAR USA) was utilized to collect the two-dimensional (2D) SAXS patterns.

Temperature-resolved SAXS experiments (in-situ SAXS) were performed using step heating from 30 to 230°C for specific samples after casting solution. The corresponding SAXS profiles were recorded every 5 min.

In some cases the X-ray scattering experiments were carried out using a Xenocs Xeuss SAXS/WAXS system equipped with a GeniX3D copper microfocus tube operating at 60 kV and 0.59 mA. The samples were placed in an evacuated chamber in order to be illuminated with monochromatic X-rays in a transmission geometry. The scattered intensity was recorded using a Dectris Pilatus 300k detector located 2.2 m downstream the sample position. The measurements were conducted by Professor Ivanov and his research group.

#### **5.6.5 Additional Characterization Techniques**

Field emission scanning electron microscopy (FE-SEM) observations were performed on a JEOL JSM-7401F using accelerating voltages of 5 keV. The samples were mounted to brass shims using carbon adhesive and then sputter-coated with 2–3 nm of platinum.

Tapping-mode SPM images of thin-film samples were also obtained. A Seiko SPA-400 AFM with a Seiko SPI-3800N probe station was utilized at room temperature. A silicon tip was used in dynamic force mode experiments with a spring force of 5 N/m and a scan rate of 1 Hz. The preparation of samples was carried out in the Department of Materials Science Engineering, University of Ioannina and in the Chemical Engineering Department, National Tsing Hua University, Hsinchu, Taiwan.

In a Hysitron Ti950 tribo-indenter the nanoindentation tests using a spherical indenter with a 2  $\mu\text{m}$  diameter were carried out. The indentation measurements were performed on a microtome film sample with 5  $\mu\text{m}$  thickness in a silicon wafer as a substrate at room temperature. The load-displacement curve was recorded at the same rate of loading and unloading (60  $\mu\text{N/s}$ ) with a maximum load of 500  $\mu\text{N}$  applied. The load-displacement data were recorded continuously, while the tip was driven into the composite materials, and then smoothly removed. The load-displacement (L-D) curves were then used to calculate the mechanical energy dissipation of the fabricated materials at the same rate of loading and unloading (60  $\mu\text{N/s}$ ). The reduced elastic modulus ( $E_r$ ) was determined from the P-h curve, using the Sneddon formula for spherical indenter frictionless punch:

$$E_r = \frac{\sqrt{\pi}}{2} \frac{S}{\sqrt{A_t}} \quad (5.2)$$

The reduced elastic modulus  $E_r$  (indentation modulus) represents the elastic deformation that occurs in both the sample and indenter tip.  $S$  corresponds to the stiffness and  $A_t$  to the projected contact area. Since, the deformation in the diamond indenter tip is negligible the reduced elastic modulus is a representative value with respect to mechanical performance.

## CHAPTER 6

### Experimental Results-Discussion

#### 6.1 Synthesis Discussion

Anionic polymerization enables the synthesis of various types of linear and non-linear copolymers. The diblock copolymer active sites  $[(A-b-B^{(-)}Li^{(+)})]$  can act as precursors and react with relative chlorosilane reagents leading to star copolymers with the desired functionality. Despite the time-consuming reactions and the challenging purification procedures in specialized home-made glass apparatuses constructed through scientific glassblowing, narrow-dispersed linear and complex architecture star block copolymers can be obtained.

In this thesis, it has been demonstrated that by using anionic polymerization and “arm-first” approach as well as the appropriate multifunctional coupling agent, symmetric linear  $(PS-b-PDMS)_2$  and non-linear  $(PS-b-PDMS)_3$ , or 4, or 6 star block copolymers can be synthesized. The fact that the arm number equals the coupling agents’ functional chlorine atoms is determined by the accurate stoichiometry between the living ends and the relative Si-Cl groups in each silane reagent. Furthermore, the precise functionality is enabled by the use of excess of living precursor arms to the respective functional -Cl atoms<sup>30</sup> which is afterwards removed by fractionation procedure.

The use of chlorosilane coupling chemistry to highly segregated living copolymer chains enables the design of well-defined star block copolymers which may be considered a potent alternative to high  $\chi$ /low  $N$  approach for minimizing further the feature sizes in the sub-10 nm regime. The absolute control over the molecular characteristics, the synthesis of copolymers with high homogeneity degree and the relatively adequate quantity (at least 5-10 grams of final purified material) are some of the advantages offered by anionic polymerization and chlorosilane chemistry.

Sequential addition of two monomers led to the synthesis of twenty three (**23**) diblock copolymer samples of the PS-*b*-PDMS type. Specifically eight (**8**) diblock copolymers were synthesized to study their self-assembled properties for targeted applications. The remaining fifteen (**15**) were used as precursors for the synthesis of star block copolymers with various number of arms through chlorosilane chemistry and specifically: six (**6**) samples of the  $(PS-b-PDMS)_2$  sequence, nine (**9**) samples of  $(PS-b-PDMS)_3$ , six (**6**) samples of  $(PS-b-PDMS)_4$  and five (**5**) samples of  $(PS-b-PDMS)_6$  types were prepared. In the subchapters 6.2-6.5 the molecular, thermal and

morphological characterization results of the eight linear diblock copolymers will be presented. The analysis includes also two published manuscripts<sup>97,187</sup> and it should be mentioned that two additional works making use the synthesized linear diblock copolymers are under consideration. In the subchapters 6.6-6.9 the results with respect to the diblock copolymer precursors (15 samples) and their corresponding linear and non-linear star block copolymers [(PS-*b*-PDMS)<sub>2,3,4,6</sub>] (26 samples) are demonstrated including also two published studies.<sup>73,188</sup>

The samples are divided in two distinct categories, due to the fact that their studies were targeting towards different directions. The linear diblock copolymers were synthesized to obtain various structures including lamellae, cylindrical and network phases, as well as to study their self-assembly behavior in bulk and in thin films. The study of the anionically synthesized (PS-*b*-PDMS)<sub>*n*</sub> (where *n* = 1, 2, 3, 4) systems with different number of arms constitutes a relatively new topic as confirmed by recent scientific reports and is expected to provide further insight into the entropy mechanism for self-assembly.<sup>17-19</sup> It is a topic which started from the collaboration between the Avgeropoulos' and Ho's research groups leading already to very significant results concerning the self-assembly mechanism from the thermodynamics point of view. Interestingly enough, the preparation of (PS-*b*-PDMS)<sub>*n*</sub> star block copolymers, where *n*= 6, is a novel synthetic approach that has not been mentioned in the literature yet. In addition, the effect of increasing the number of arms on the solid state properties is also explored.

## **6.2 Molecular Characterization Results of Linear PS-*b*-PDMS Diblock Copolymers**

Anionic polymerization provides high level of molecular control for the individual blocks but precise characterization of the molecular characteristics is mandatory to extract reliable results. The molecular characterization results regarding the eight (8) initial linear diblock copolymers are presented and discussed. It should be mentioned that these copolymers were not used as precursors for the synthesis of the relative non-linear materials with 2, 3, 4 and 6 diblock arms respectively. The molecular characteristics were determined through size exclusion chromatography, membrane osmometry (or vapor pressure osmometry when the  $\bar{M}_n$  values of the constituents were low) and proton nuclear magnetic resonance spectroscopy.

The determination of average molecular weights and distributions as well as interaction between polymers at a given solvent requires the use of dilute solutions with various ranges of concentration. To verify the dispersity indices and to calculate roughly the  $\bar{M}_n$  values, the size exclusion chromatography method is highly applicable especially when the examined sample has similar chemical structure and architecture to the standards used to calibrate the instrument. Through calibration a direct relationship between molecular weights and elution volume or time (isocratic pump conditions: 1 ml/min) is defined. The selective permeation range of the instrumentation is utilized to calculate the average molecular weights of samples with unknown molecular characteristics but in this case SEC constitutes a relative and not an absolute method for determining the average molecular weights. The dependence of polymers' retention volumes on their molecular sizes in solution rather than their molar masses constitutes the intrinsic limitation of SEC.<sup>189</sup>

As a result, the molecular characteristics of the first segment in the linear PS-*b*-PDMS samples can be adequately verified taking into consideration the performed calibration (made with PS standards) but this is not applied in the PDMS 2<sup>nd</sup> block due to the different chemical structure and therefore altered hydrodynamic volume of the block compared to the PS standards. The obtained molecular weight from SEC regarding the PDMS should be divided with an appropriate coefficient (equal to 1.3) to simulate the “real” molecular weight of the segment. For this reason, the absolute determination of  $\bar{M}_n$  values is performed by colligative properties in membrane and/or vapor pressure osmometry that are directly related to the number of the dissolved molecules in solutions with different concentration.

The chemical composition of the individual blocks is precisely quantified by proton nuclear magnetic resonance (<sup>1</sup>H-NMR) spectroscopy. <sup>1</sup>H-NMR provides the ability to calculate the  $\bar{M}_n$  values but only in extremely low molecular weight samples through the molar ratio of integrated peaks corresponding to the end-group moiety and the main chain characteristic groups. The mass fraction of each segment is calculated from the following equations (104 g/mol and 74 g/mol are the molecular weights of the monomeric units for PS and PDMS respectively):

$$f_{\text{PS}} = \frac{\text{integration value}_{6.3-7.2\text{ppm}}}{\text{contributing protons (or 5)}} * \text{monomeric unit molecular weight (or 104)} \quad (6.1)$$

$$f_{\text{PDMS}} = \frac{\text{integration value}_{0.1-0.5\text{ppm}}}{\text{contributing protons (or 6)}} * \text{monomeric unit molecular weight (or 74)} \quad (6.2)$$

The volume fraction of the blocks in the copolymers is also calculated, through <sup>1</sup>H-NMR by the calculated mass fractions, through the use of the following equation:

$$\varphi_{PS} = \frac{f_{PS}\rho_{PDMS}}{f_{PS}\rho_{PDMS} + (1-f_{PS})\rho_{PS}} \quad (6.3)$$

where  $f_{PS}$  is the mass fraction of PS,  $\rho_{PDMS}$  and  $\rho_{PS}$  are the densities of the individual segments ( $\rho_{PDMS}=0.930 \text{ g/cm}^3$ ,  $\rho_{PS}=1.040 \text{ g/cm}^3$ ).

The calculation of  $\varphi$  is quite significant for the prediction of the adopted structures during microphase separation in accordance with the theoretical phase diagram as will be discussed in a following subchapter.

The results concerning the molecular characteristics of the synthesized linear diblock copolymers, as directly calculated from the above mentioned characterization methods are listed in Table 6.1. The eight diblock copolymers demonstrate various molecular characteristics (different molecular weights and volume fractions). For clarification reasons, the PS-*b*-PDMS materials are abbreviated as PS<sub>x</sub>-*b*-PDMS<sub>y</sub>, where x and y represent the number-average molecular weight (kg/mol) of each segment.

**Table 6.1:** Molecular characterization results for linear PS-*b*-PDMS copolymers.

No.	sample	$\bar{M}_n^{PS(a)}$ (g/mol) SEC/MO	$\bar{M}_n^{PDMS(b)}$ (g/mol) MO	$\bar{M}_n^{total(b)}$ (g/mol) MO	$\mathfrak{D}^{(c)}$	$f_{iH-NMR}^{PDMS(d)}$	$\varphi_{PDMS}^{(d)}$
1	PS <sub>14</sub> - <i>b</i> -PDMS <sub>6.4</sub>	14,000	6,400	20,400	1.03	0.28	0.31
2	PS <sub>14</sub> - <i>b</i> -PDMS <sub>9.0</sub>	14,000	9,000	23,000	1.03	0.36	0.39
3	PS <sub>43</sub> - <i>b</i> -PDMS <sub>17</sub>	43,000	17,000	60,000	1.02	0.21	0.24
4	PS <sub>42</sub> - <i>b</i> -PDMS <sub>32</sub>	42,000	32,000	74,200	1.04	0.42	0.45
5	PS <sub>51</sub> - <i>b</i> -PDMS <sub>35</sub>	51,000	35,000	86,000	1.05	0.39	0.42
6	PS <sub>55</sub> - <i>b</i> -PDMS <sub>38</sub>	55,000	38,000	93,000	1.03	0.37	0.40
7	PS <sub>69</sub> - <i>b</i> -PDMS <sub>49</sub>	69,000	49,000	118,000	1.06	0.44	0.47
8	PS <sub>80</sub> - <i>b</i> -PDMS <sub>50</sub>	80,000	50,000	130,000	1.08	0.36	0.39

<sup>(a)</sup>combined SEC (in tetrahydrofuran at 30 °C) and MO (in toluene at 35 °C) results, <sup>(b)</sup>MO in toluene at 35 °C, <sup>(c)</sup>SEC measurements in tetrahydrofuran at 30 °C, <sup>(d)</sup>From <sup>1</sup>H-NMR measurements in CDCl<sub>3</sub> at 25 °C using equation 6.1, 6.2 and 6.3. Note that  $\bar{M}_n^{PDMS}$  was calculated through the equation:  $\bar{M}_n^{PDMS} = \bar{M}_n^{total} - \bar{M}_n^{PS}$  from MO results. Also  $\varphi_{PDMS}=1-\varphi_{PS}$ .

From Table 6.1 it is easily understood that all the linear copolymers exhibit molecular and compositional homogeneity as indicated by the narrow dispersity indices ( $\mathfrak{D} < 1.08$  for all samples). In all cases PS was the first block, due to the fact that it is not possible to synthesize PDMS-*b*-PS copolymers through sequential

monomer addition, taking into account all the necessary requirements to synthesize well-defined block copolymers as already described in Chapter 2 of this thesis. The PDMS segments comprised the minority block and compositions ranging from 0.31 to 0.47 were made and verified to induce the formation of various structures during microphase separation. The total  $\bar{M}_n$  values varied from 20,400-130,000 g/mol to obtain different feature sizes of the adopted nanostructures. The reason for designing different copolymers is to establish the structure/property relationship during self-assembly studies and observe the dependence of increased molecular weight in the microphase separation of this specific diblock copolymer system.

Two representative SEC chromatographs of the PS precursors (green) and the final linear diblock copolymers (purple) concerning the PS<sub>14</sub>-*b*-PDMS<sub>6.4</sub> and PS<sub>55</sub>-*b*-PDMS<sub>38</sub> samples are presented in Figures 6.1 and 6.2. Note that the high percentage of dimer in the PS aliquot (indicated as a shoulder in lower elution time) is attributed to the fact that the termination was conducted in ambient conditions using methanol vapors and not degassed methanol ampules as in the case of the final diblock copolymer.

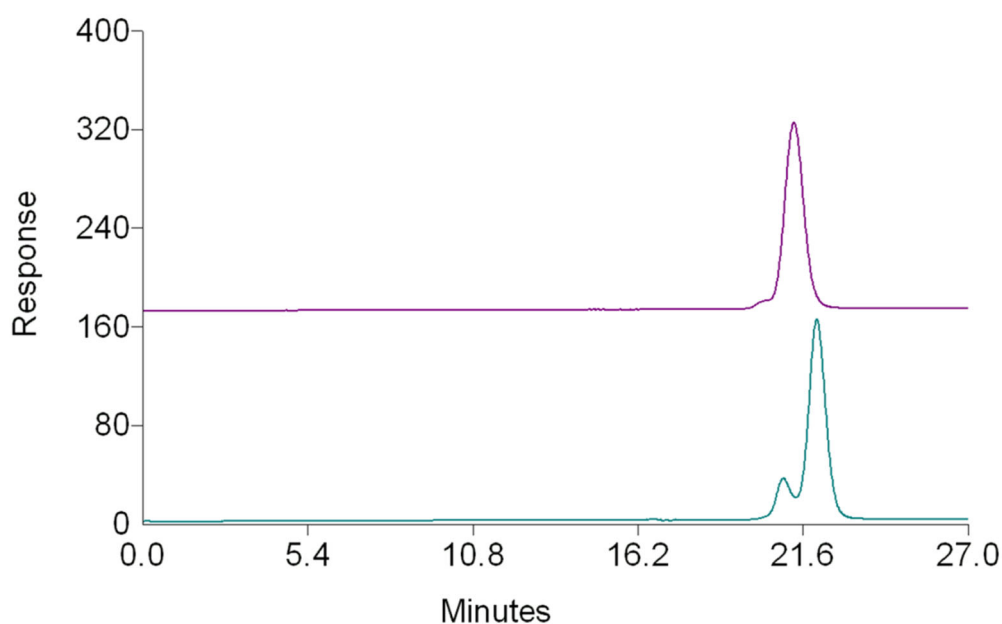


**Figure 6.1:** SEC chromatographs of PS precursor (green) and the final diblock copolymer PS<sub>14</sub>-*b*-PDMS<sub>6.4</sub> (purple).

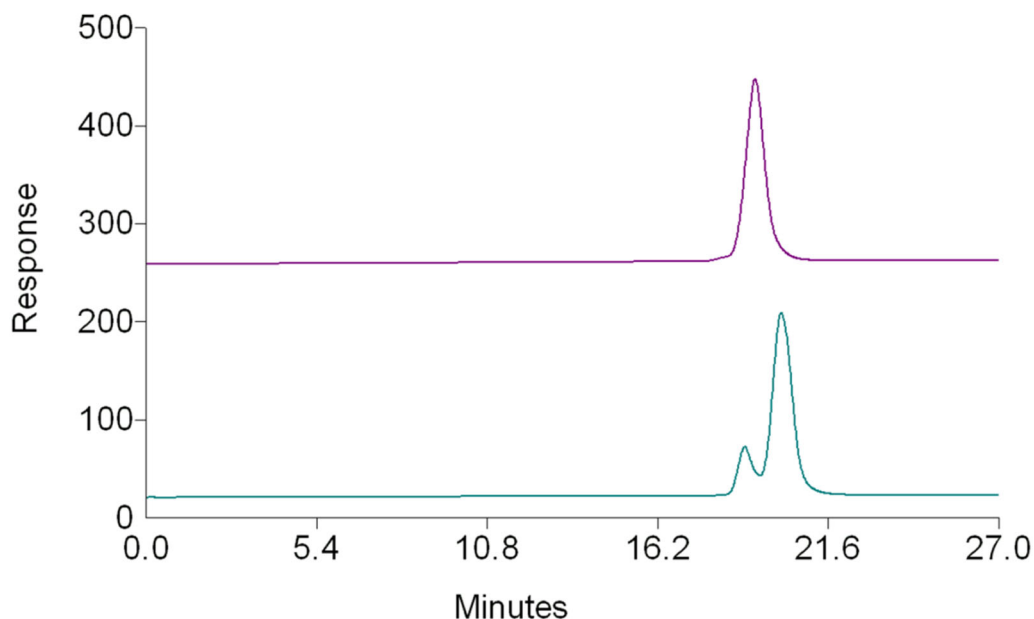


**Figure 6.2:** SEC chromatographs of PS precursor (green) and the final diblock copolymer PS<sub>55</sub>-*b*-PDMS<sub>38</sub> (purple).

From the representative SEC chromatographs it is concluded that the copolymers' molecular weight distributions are monomodal. The absence of any side and/or termination reactions during the polymerization of the D<sub>3</sub> is strongly indicated by the presence of only one peak in the corresponding SEC curves in conjunction with the low Đ values. The narrow dispersed final copolymers are eluted in lower elution times compared to their corresponding PS precursors, demonstrating the higher initiation towards the propagation rate of the second monomer and its complete consumption without any side reactions. As a result, higher average molecular weight values for the diblock copolymers compared to those of the initial PS precursors are produced. Similar results are derived for all synthesized copolymers.

In Figure 6.3 the SEC chromatographs of all eight (8) diblock copolymers of the PS-*b*-PDMS sequence mentioned in Table 5.1 are given for comparison reasons with respect to the total number average molecular weights. It is evident that the lower molecular weights copolymers are eluted in higher elution times and that in all cases narrow dispersed and symmetric Gaussian curves are observed.

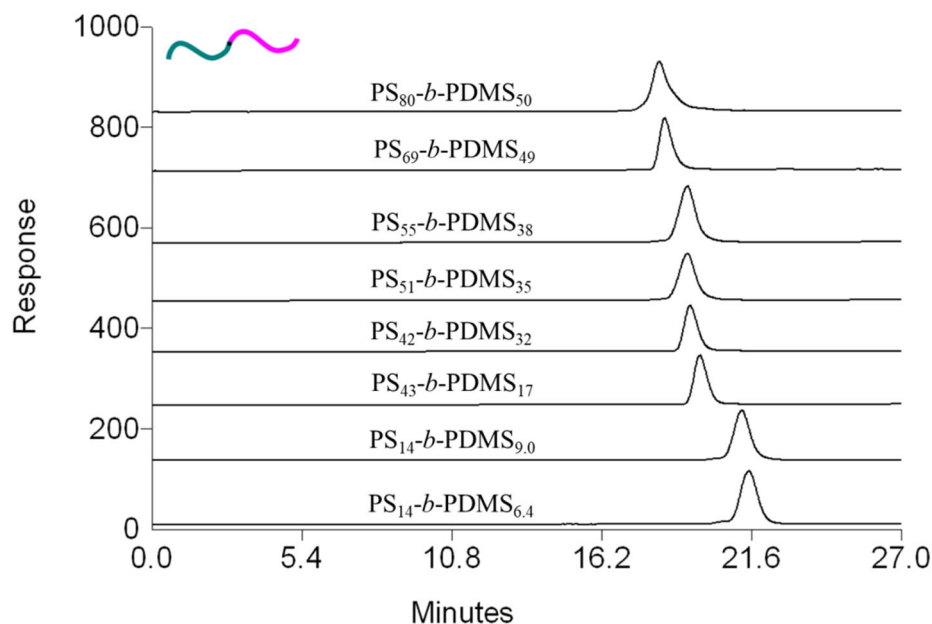


**Figure 6.3:** SEC chromatographs of all final diblock copolymers of the PS-*b*-PDMS sequences.

The molecular characterization via  $^1\text{H-NMR}$  spectroscopy was necessary to verify the composition results as obtained by the average molecular weights of both segments by combining the SEC and MO results. The mass fraction can be directly calculated from  $^1\text{H-NMR}$  spectra through the chemical shifts of the different protons at the monomeric units of the two segments (PS and PDMS). The chemical resonances at 0.1-0.3 ppm are attributed to the six (6) methyl protons (aliphatic protons) of the siloxane monomeric units of PDMS while the ones at 6.7-7.5 ppm to the five (5) protons of the aromatic rings on the monomeric units of PS. The proton chemical shifts appearing at approximately 7.3-7.4 ppm correspond to the deuterated chloroform ( $\text{CDCl}_3$ ) which is used as solvent to dilute the samples.

Two representative  $^1\text{H-NMR}$  spectra corresponding to the  $\text{PS}_{14}\text{-}b\text{-PDMS}_{6,4}$  and  $\text{PS}_{55}\text{-}b\text{-PDMS}_{38}$  samples are presented in Figures 6.4 and 6.5. The intensity of the  $^1\text{H-NMR}$  signals is displayed along the vertical axis of a spectrum and is proportional to the molar concentration of the sample. The integration values of the characteristic protons related to each block are used in equations 6.1 and 6.2 to calculate the mass fractions in all copolymer sequences. Correspondingly, equation 6.3 is employed to extract the volume fraction of PDMS ( $\phi_{\text{PDMS}}$ ), as already displayed in Table 6.1.

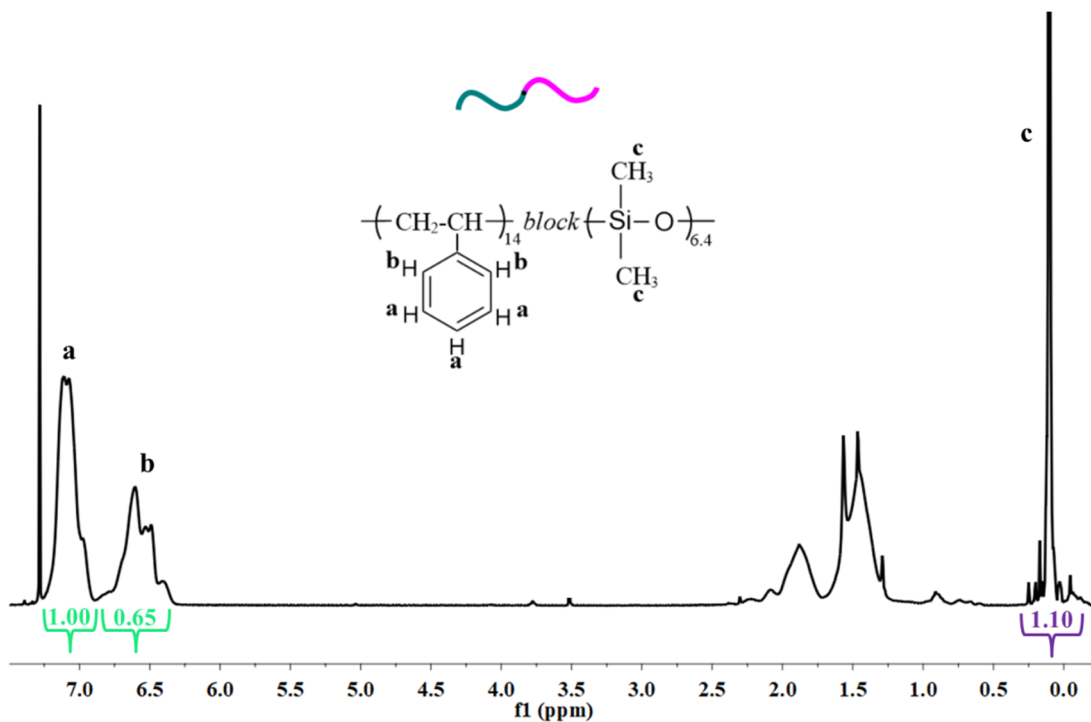


**Figure 6.4:**  $^1\text{H-NMR}$  spectrum of the  $\text{PS}_{14}\text{-}b\text{-PDMS}_{6.4}$  diblock copolymer.

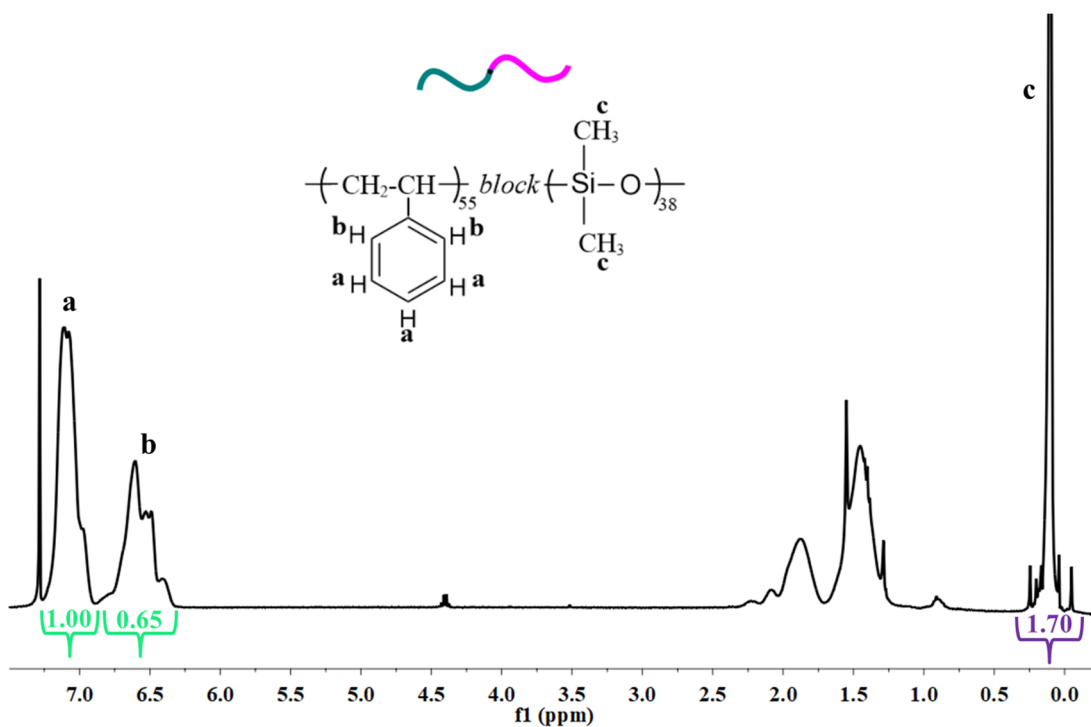


**Figure 6.5:**  $^1\text{H-NMR}$  spectrum of the  $\text{PS}_{55}\text{-}b\text{-PDMS}_{38}$  diblock copolymer.

In Figure 6.6 the  $^1\text{H-NMR}$  spectra corresponding to all eight (8) linear diblock copolymers presented in Table 6.1 are illustrated.

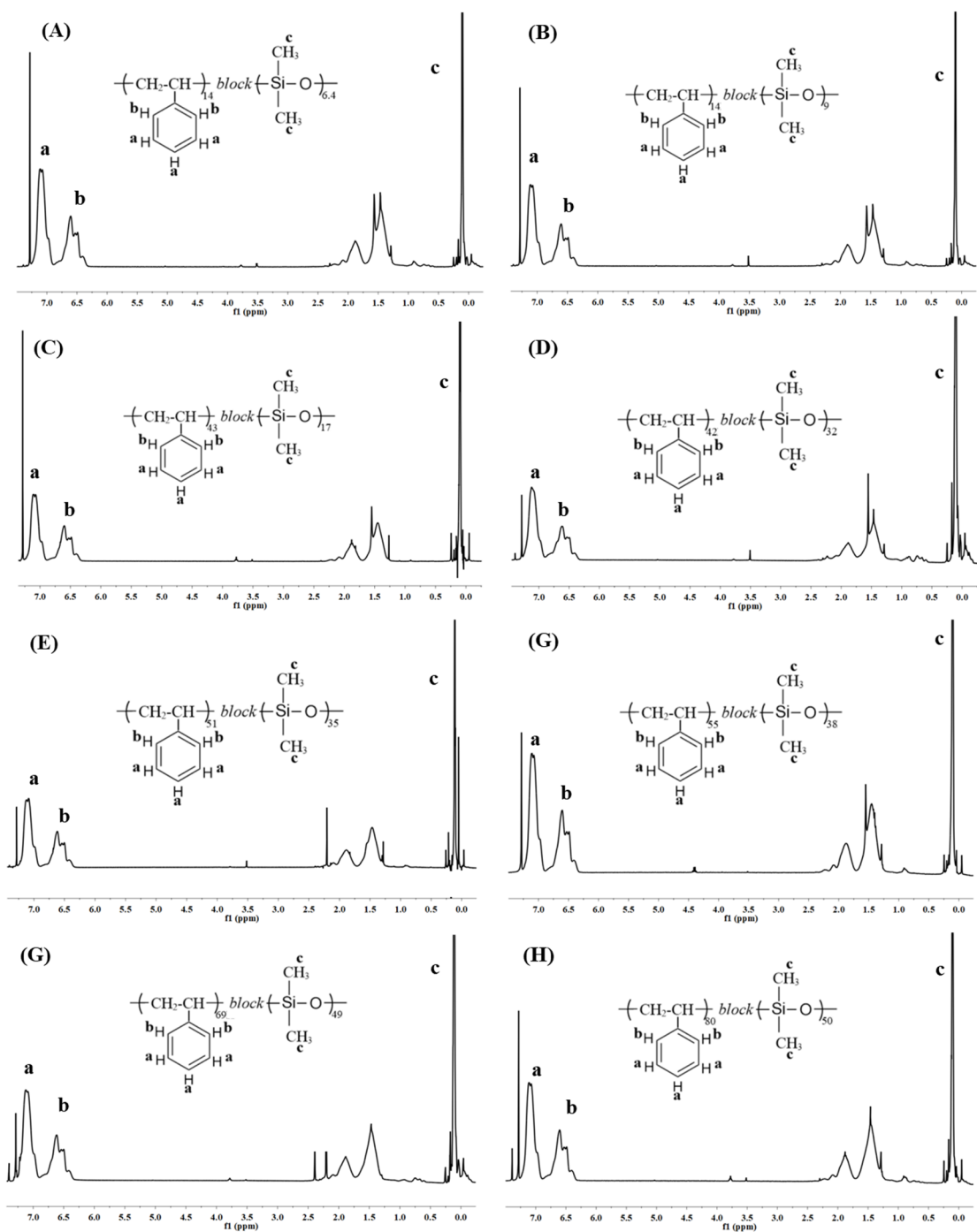


**Figure 6.6:**  $^1\text{H}$ -NMR spectra of: (A)  $\text{PS}_{14}\text{-}b\text{-PDMS}_{6.4}$ , (B)  $\text{PS}_{14}\text{-}b\text{-PDMS}_9$ , (C)  $\text{PS}_{43}\text{-}b\text{-PDMS}_{17}$ , (D)  $\text{PS}_{42}\text{-}b\text{-PDMS}_{32}$ , (E)  $\text{PS}_{51}\text{-}b\text{-PDMS}_{35}$ , (F)  $\text{PS}_{55}\text{-}b\text{-PDMS}_{38}$ , (G)  $\text{PS}_{69}\text{-}b\text{-PDMS}_{49}$  and (H)  $\text{PS}_{80}\text{-}b\text{-PDMS}_{50}$  diblock copolymers.

From the characteristic proton chemical shifts, the high purity and homogeneity degree of the final materials as well as the existence of polystyrene and poly(dimethylsiloxane) units in the respective spectra are verified. The molecular characterization results strongly suggest the synthesis of model diblock copolymers which is in accordance with the high standards of anionic polymerization.

Consequently, all the subsequent morphological characterization results are considered reliable since the structure/property relationship is only dependant to the molecular characteristics of the synthesized copolymers in combination with the strong repulsion between the PS and PDMS segments.

### 6.3 Thermal Characterization Results of Linear PS-*b*-PDMS Diblock Copolymers

The thermal analysis of the synthesized linear copolymers was performed with differential scanning calorimetry (DSC). Useful information including glass transition temperature, melting point and crystallization of a polymeric material can be extracted using DSC. In addition, conclusions regarding the miscibility of the involved segments can be derived. Specifically, in the diblock copolymers, the appearance of two distinct  $T_g$  values, similar to the glass transition temperatures of the corresponding homopolymers (according to the literature), suggest the immiscibility between the blocks and the potential microphase separation during self-assembly studies. On the other hand, the appearance of one  $T_g$  between the glass transition temperature of both blocks indicates a homogenous mixture of the components with no phase separation. Three different  $T_g$  values (two close to the ones of the corresponding homopolymers and one between them), propose at least low miscibility between the two blocks that will lead to weakly separated phases due to partial mixing when studied morphologically in bulk.

As far as polystyrene is concerned, it is an amorphous thermoplastic polymer, able to be heated above its  $T_g$  and to cool down without changing its chemical structure and properties. The pronounced elasticity of poly(dimethylsiloxane) induced by very low  $T_g$  values is attributed to the Si-O-Si bonds. In addition, polysiloxanes are capable of retaining their properties even at substantially increased temperatures without any degradation phenomena, further expanding the temperature range of their potential applicability.

The  $T_g$  and the  $\bar{M}_n$  values of a polymer are highly correlated and specifically beyond a specific  $\bar{M}_n$  value ( $\sim 20,000$  g/mol), the glass transition temperature of a polymer is equal to  $T_g^\infty$  and therefore is no longer dependant on the  $\bar{M}_n$  when it exhibits relatively high values. In Figure 6.7 the dependence of the  $T_g$  value for PS domains versus number average molecular weight is shown based on the literature.<sup>190</sup>

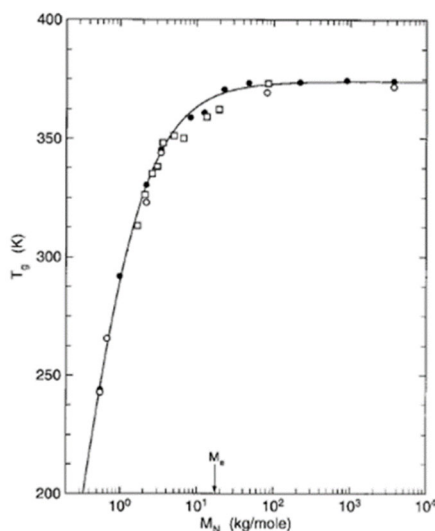


**Figure 6.7:** Diagram including glass transition temperature as a function of molecular weight with respect to the PS segment.<sup>190</sup>

In Figure 6.8 the DSC thermographs of the initial eight linear diblock copolymers synthesized for this thesis are presented. The displayed thermographs correspond to the second heating procedure of each measurement, since the first heating is conducted to erase the thermal history of the sample at a specific rate of 10 K/min.

In each copolymer sequence two separate endothermic transitions are evident, corresponding to the glass transition temperatures of PS and PDMS in the regions of 95 to 109 °C and -121 to -127 °C, respectively. The values of the  $T_g$ s are similar to the ones of the respective homopolymers, indicating the complete immiscibility of the systems. As expected, the temperature in which the polystyrene chains gain mobility is strongly related to the number average molecular weight of the component. Specifically, higher  $\bar{M}_n$  values lead to higher glass transition temperatures for the PS segments (e.g.  $T_g$  of PS in the PS<sub>14</sub>-*b*-PDMS<sub>6.4</sub> ~ 97°C vs.  $T_g$  of PS in the PS<sub>80</sub>-*b*-PDMS<sub>50</sub> ~ 109°C). Concerning the PDMS segment, endothermic processes can be observed in all copolymer sequences, a fact attributed to its semicrystalline nature. The region in which melting temperatures appear varies from -33 to -49 °C. The molecular symmetry and the small methyl side groups of PDMS lead to crystallization behavior. Interestingly enough, the PS<sub>14</sub>-*b*-PDMS<sub>9</sub> sequence also demonstrates an exothermic process upon heating from the glassy phase and before the melting process occurs, corresponding to the cold crystallization temperature. This is attributed to the crystallization of a PDMS part during cooling from melt and on the subsequent heating the nuclei growth is evident.

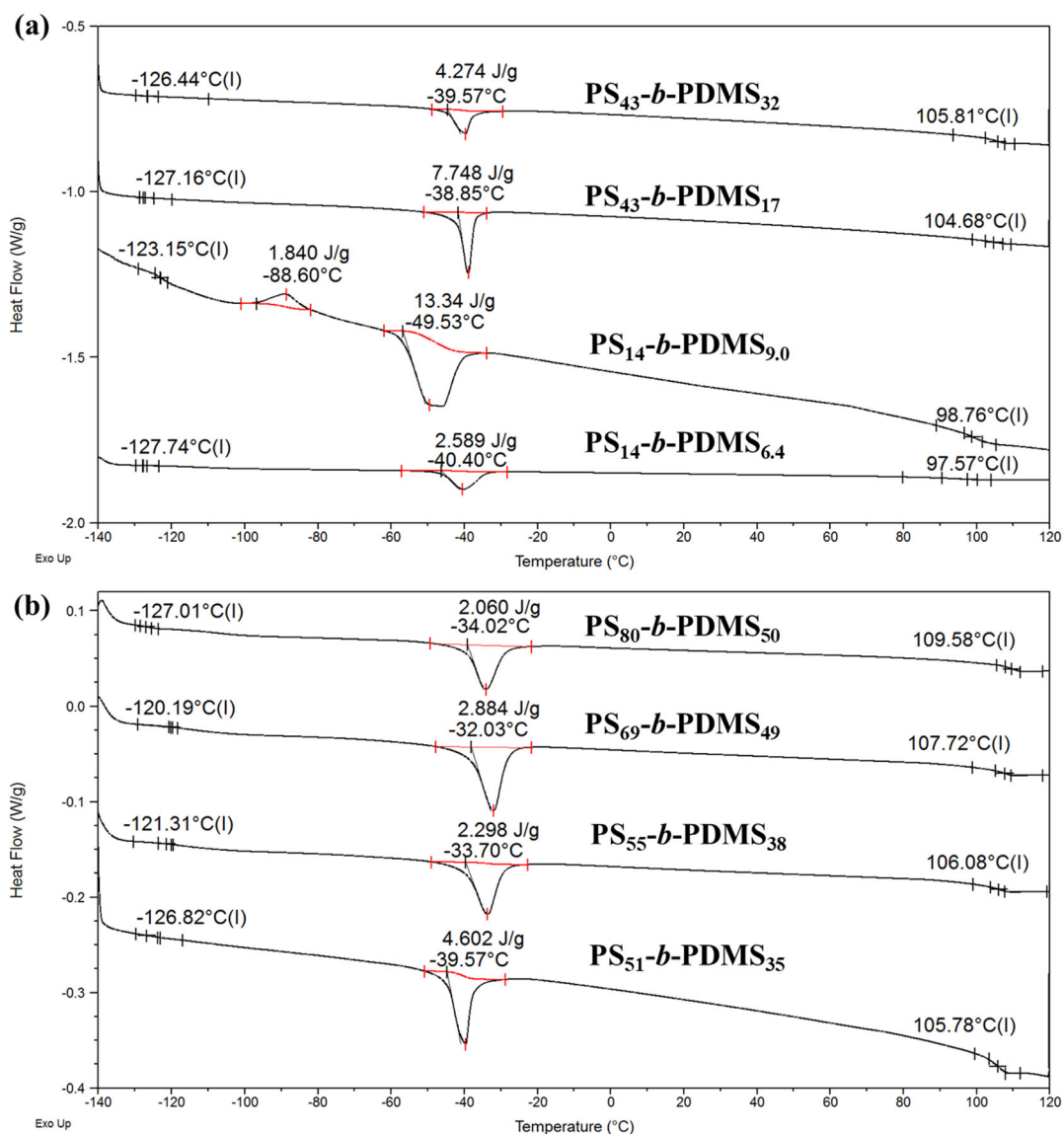


**Figure 6.8:** DSC thermographs corresponding to: (a)  $PS_{14}\text{-}b\text{-}PDMS_{6,4}$ ,  $PS_{14}\text{-}b\text{-}PDMS_9$ ,  $PS_{43}\text{-}b\text{-}PDMS_{17}$  as well as  $PS_{42}\text{-}b\text{-}PDMS_{32}$ , (b)  $PS_{51}\text{-}b\text{-}PDMS_{35}$ ,  $PS_{55}\text{-}b\text{-}PDMS_{38}$ ,  $PS_{69}\text{-}b\text{-}PDMS_{49}$  and  $PS_{80}\text{-}b\text{-}PDMS_{50}$ .

The results obtained from the DSC measurements including the glass transition temperatures of both segments, the crystallization (where evident) as well as melting temperatures along with the corresponding enthalpy values regarding the PDMS are summarized in Table 6.2.

**Table 6.2:** Thermal characterization results for linear PS-*b*-PDMS copolymers.

sample	$T_g^{PS}$ (°C)	$T_g^{PDMS}$ (°C)	$T_m^{PDMS}$ (°C)	enthalpy (J/g)	$T_c^{PDMS}$ (°C)
PS <sub>14</sub> - <i>b</i> -PDMS <sub>6.4</sub>	97.57	-127.74	-40.40	2.589	-
PS <sub>14</sub> - <i>b</i> -PDMS <sub>9.0</sub>	98.76	-123.15	-49.53	13.340	-86.60
PS <sub>43</sub> - <i>b</i> -PDMS <sub>17</sub>	104.68	-127.16	-38.85	7.748	-
PS <sub>42</sub> - <i>b</i> -PDMS <sub>32</sub>	105.81	-126.44	-39.57	4.274	-
PS <sub>51</sub> - <i>b</i> -PDMS <sub>35</sub>	105.78	-126.82	-39.57	4.602	-
PS <sub>55</sub> - <i>b</i> -PDMS <sub>38</sub>	106.08	-121.31	-33.70	2.298	-
PS <sub>69</sub> - <i>b</i> -PDMS <sub>49</sub>	107.72	-120.19	-32.03	2.884	-
PS <sub>80</sub> - <i>b</i> -PDMS <sub>50</sub>	109.58	-127.01	-34.02	2.060	-

#### 6.4 Morphological Characterization Results of Linear PS-*b*-PDMS Diblock Copolymers

The solid state properties, including the identification of the adopted morphology and the calculation of the domains periodicity, of the initial linear diblock copolymers synthesized for this thesis for the microphase separation comparisons were determined by combining transmission electron microscopy (TEM) and small angle X-ray scattering (SAXS) techniques. Both TEM and SAXS constitute the standard characterization techniques in bulk, since they provide unique information of the self-assembled structures. Their contribution to the fundamentals of self-assembly is critical and their role is considered complementary.

SAXS is extensively employed to identify the formed morphologies and to verify the results from TEM studies, taking advantage of the sequence of the observed Bragg reflections. The permitted reflections at specific peak positions for the equilibrium and even in non-common BCP phases are thoroughly elaborated. Strongly segregated systems demonstrate multiple Gaussian ordered reflections, while in weakly segregated samples disordered Lorentzian patterns are evident. In the latter case, the phase verification may be ambiguous due to the lower order peaks. The peak positions with respect to different structures are reported in the following table (Table 6.3) and are based on periodic tables of crystallography as well as space group theory.

**Table 6.3:** Permitted peak positions of Bragg reflections for various structures.

Structure	Ratio q/q*
LAM	1:2:3:4:5:6...
HEX	1: $\sqrt{3}$ : $\sqrt{4}$ : $\sqrt{7}$ : $\sqrt{9}$ : $\sqrt{12}$ ...
BCC	1: $\sqrt{2}$ : $\sqrt{3}$ : $\sqrt{4}$ : $\sqrt{5}$ : $\sqrt{6}$ ...
FCC	$\sqrt{3}$ : $\sqrt{4}$ : $\sqrt{8}$ : $\sqrt{11}$ : $\sqrt{12}$ ...
DG	$\sqrt{6}$ : $\sqrt{8}$ : $\sqrt{16}$ : $\sqrt{20}$ : $\sqrt{22}$ : $\sqrt{38}$ ...
DD	$\sqrt{2}$ : $\sqrt{3}$ : $\sqrt{4}$ : $\sqrt{6}$ : $\sqrt{8}$ : $\sqrt{9}$ ...

The characteristic unit cell distance or domain spacing is calculated from the scattering factor  $q$  evident in the primary reflection through the Bragg's law (equation 6.4):

$$d = \frac{2\pi}{q} \quad (6.4)$$

The sample preparation is a very significant parameter that should be taken into serious consideration prior to morphological characterization studies. The use of a non-selective casting solvent is necessary to promote the formation of equilibrium morphologies. The evaporation of the solvent in the dilute solution (~10% w/v) takes place at a very slow rate in approximately several days (the longer it takes the better it is for achieving equilibrium). Then, the formed film is separated in two parts to study both the unannealed and thermally annealed thin sections. Note that, thermal annealing is conducted to a temperature higher than the  $T_g$  values of both blocks (the higher being the  $T_g$  of PS domains) but due to the irreversible proportional relationship between  $\chi$  and  $T$ , severely increased temperatures are restricted. To choose the proper annealing temperature, all samples are initially studied by DSC to define the  $T_g$  values and especially the glass transition temperature of PS. Any deformation phenomena or alternation of the annealed morphology due to slow cooling to room temperature especially in the low molecular weight samples are avoided by quenching (includes immediate insertion of the film from the annealing temperature directly in liquid nitrogen to freeze the adopted structure during annealing and not during cooling). The thin sections (~40 nm) from the initial films are obtained by ultracryomicrotomy at -140 °C (temperature well below the lowest  $T_g$  between the blocks and is that of PMDS) and the sections are picked up on 600 mesh copper grids. It should be mentioned that, when the under-examination samples

showcase cubic network 3-dimensional morphologies thin sections of at least one unit cell distance should be acquired. Staining procedures are not necessary for the studied diblock copolymers, due to the adequate mass thickness image contrast provided by both blocks. This fact is attributed to the existence of carbon/hydrogen atoms in the PS and silicon/oxygen atoms in the backbone of PDMS providing adequate difference in the electron density between the segments.

The intrinsic stable phase morphology in the PS-*b*-PDMS samples can be modified using solvents with different selectivity towards the segments to induce various structures by a simple composition material. This behaviour is related to the strong segregation of the system and it can be utilized for the design of nanostructures even in cases where the molecular characteristics deviate from the desired ones. In Table 6.4 the solubility parameters with respect to different solvents, PS and PDMS are given.<sup>127</sup>

**Table 6.4:** Solubility parameters for various solvents as well as PS and PDMS segments.

Solvents/Polymers	Solubility Parameters $cal^{1/2}/cm^{3/2}$
1,2-dichloromethane	9.9
chlorobenzene	9.5
tetrahydrofuran	9.3
chloroform	9.3
toluene	8.9
cyclohexane	8.2
polystyrene	9.1
poly(dimethylsiloxane)	7.4

In the case of a non-preferential solvent the evaporation would take place simultaneously for both segments and therefore the components segregate at the same time. When the solvent showcases a relative preference towards one of the blocks the solvent evaporation process differs. Specifically, as the concentration of the solution increases, the least solvated segment exhibits increased self-segment interaction to diminish the less preferred polymer-solvent interactions while minimizing contact with the other block. Consequently, the affinity of PS towards the PS-selective solvents induces a reduction in the PDMS effective volume fraction causing the possible transformation of the morphologies.

To quantify the  $\chi N$  product ( $\chi$ : Flory-Huggins interaction parameter and  $N$ : total degree of polymerization for both blocks), the estimation of total degree of polymerization and  $\chi$  value is required. The degree of polymerization  $N$  for a linear diblock copolymer is calculated from the following equation:

$$N_{PS-b-PDMS} = N_{PS} + N_{PDMS} = \frac{\bar{M}_n^{PS}}{M_0^{St}} + \frac{\bar{M}_n^{PDMS}}{M_0^{Dms}} \quad (6.5)$$

where  $M_0^{St} = 104$  g/mol and  $M_0^{Dms} = 74$  g/mol and correspond to the molecular weight of the monomeric units of each component. In addition, the  $\chi$  value that indicates the enthalpic driving force for microphase separation was estimated  $\sim 0.26^{147}$  at room temperature. To calculate the  $\chi$  value at different temperatures the representative  $\chi = \alpha T^{-1} + \beta$  equation is typically utilized, where  $\alpha = 68.0$  and  $\beta = -0.037$  according to the literature.<sup>57,90</sup> The  $\chi N$  values at room temperature are documented in Table 6.5.

**Table 6.5:** Molecular characteristics, volume fractions of PDMS, total degree of polymerization and  $\chi N$  product for the initial linear diblock copolymers of the PS-*b*-PDMS type used for microphase separation studies.

No.	sample	$\bar{M}_n^{total(a)}$ (g/mol) MO	$\phi_{PDMS}^{(b)}$	$N^{total(c)}$	$\chi N^{(d)}$ (25 °C)
1	PS <sub>14</sub> - <i>b</i> -PDMS <sub>6,4</sub>	20,400	0.31	221	57
2	PS <sub>14</sub> - <i>b</i> -PDMS <sub>9,0</sub>	23,000	0.39	256	66
3	PS <sub>43</sub> - <i>b</i> -PDMS <sub>17</sub>	60,000	0.24	642	167
4	PS <sub>42</sub> - <i>b</i> -PDMS <sub>32</sub>	74,200	0.45	825	217
5	PS <sub>51</sub> - <i>b</i> -PDMS <sub>35</sub>	86,000	0.42	962	250
6	PS <sub>55</sub> - <i>b</i> -PDMS <sub>38</sub>	93,000	0.40	1041	270
7	PS <sub>69</sub> - <i>b</i> -PDMS <sub>49</sub>	118,000	0.47	1325	344
8	PS <sub>80</sub> - <i>b</i> -PDMS <sub>50</sub>	130,000	0.39	1440	375

<sup>(a)</sup>MO in toluene at 35 °C, <sup>(b)</sup>From <sup>1</sup>H-NMR measurements in CDCl<sub>3</sub> at 25 °C, <sup>(c)</sup>From equation 6.5, <sup>(d)</sup>From equation 6.5 and  $\chi = 0.26$  at 25 °C ( $\chi = 68.0T^{-1} - 0.037$ ).

The calculation of  $\chi N$  is important to predict the segregation strength between the chemically dissimilar segments. From the  $\chi N$  values mentioned above it is evident that all copolymers belong either to the intermediate (2 samples of the lower molecular weight values) or in the high segregation (the remaining 6 samples with values well above 100 ranging from 167 up to 375) regimes. In all cases, two distinct homogeneous areas divided by narrow interfaces are expected in which the width is minimal and the junction points (covalent bonds connecting the two chemically different blocks) are located on them. Various composition samples ranging from 20.4-130.0 kg/mol were synthesized to study the alternation on the adopted

morphologies due to the molecular characteristics as well as the solvent used during solution casting. The materials were designed to induce the formation of structures as diverse as cylindrical, lamellar and cubic 3-dimensional networks.

Specifically, samples PS<sub>14</sub>-*b*-PDMS<sub>6.4</sub>, PS<sub>14</sub>-*b*-PDMS<sub>9.0</sub> and PS<sub>43</sub>-*b*-PDMS<sub>17</sub> were synthesized with the specific molecular characteristics to promote the formation of either cylindrical or lamellar structures. A future perspective of this dissertation is to study the above-mentioned samples in thin film state and to improve the ordering kinetics of the systems.

Regarding bulk studies of PS<sub>14</sub>-*b*-PDMS<sub>6.4</sub>, the PDMS domains formed hexagonally close packed (hcp) cylinders in the PS matrix, as expected due to the PDMS volume fraction ( $\phi_{\text{PDMS}}=0.31$ ). In the 1D SAXS pattern both the unannealed (black color line) and the annealed (red color line) for one day at 100 °C ( $\chi=0.14$  at 100 °C) bulk samples are presented for comparison reasons. In the respective SAXS plot seven sharp reflections at the relative  $q$  positions of  $q/q^*=1:\sqrt{3}:2:\sqrt{7}:3:4:5$  (Figure 6.9 a) regarding the annealed sample are very well consistent for a well-ordered cylindrical morphology. Note that in the unannealed sample the reflections at the relative  $q$  positions of  $q/q^*=1:\sqrt{3}:2:3$  are shifted towards relatively higher  $q$  regions due to the less ordered domains (the peaks appear broader compared to those for the annealed sample).

The periodicity of the microphase separated domains was estimated through the primary peak of the annealed sample approximately 21 nm. Two possible projections of the hexagonal packed cylinders can be identified during TEM observations, namely the axial and longitudinal cross-sectional view. To exclude the formation of any other morphology (lamellar or spheres exhibiting hexagonal packing) usually both cylindrical projections are presented. In the micrographs exhibited in Figure 6.9 (b and c) both hexagonal arrangements of round dark PDMS nanodomains in a white PS matrix (axial) and elongated alternating dark and white sheets are demonstrated, completely verifying the hcp cylindrical morphology.

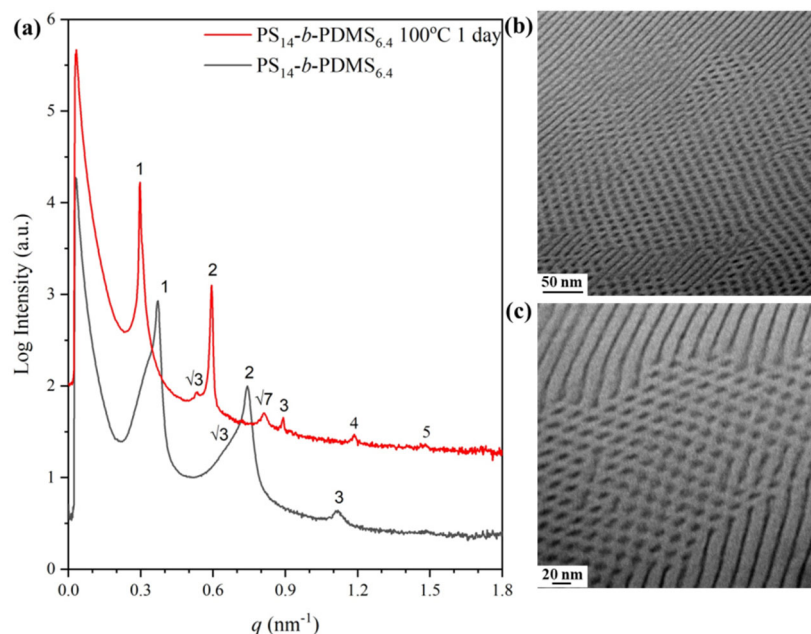


**Figure 6.9:** (a) 1D SAXS plots of the unannealed (black) and annealed (red)  $PS_{14}\text{-}b\text{-}PDMS_{6.4}$ , using cyclohexane for solution casting, indicating the development of cylindrical morphology. (b) TEM micrograph of the thermally annealed sample demonstrating the coexistence of both cylindrical projections (axial and longitudinal cross-sectional view) and (c) TEM micrograph of the thermally annealed sample demonstrating the coexistence of both cylindrical projections in higher magnification.

In the  $PS_{14}\text{-}b\text{-}PDMS_{9.0}$  sample with PDMS volume fraction equal to 0.39, the periodic black PDMS and white PS alternating regions evident in the TEM images in conjunction with the SAXS pattern at the relative scattering peaks of  $q/q^*=1:2:-:4$  confirmed the adaptation of an alternating lamellar structure. The domain spacing was calculated from the first reflection using Bragg's law equal to 19 nm. The combined real-space and scattering results concerning the unannealed sample after casting in cyclohexane are presented in Figure 6.10 (a). A comparison between the previous sample  $PS_{14}\text{-}b\text{-}PDMS_{6.4}$  and  $PS_{14}\text{-}b\text{-}PDMS_{9.0}$  is that, despite the differences in volume fraction, the overall number average molecular weight is approximately similar, and that fact is indicated by the approximately equal values of d-spacing (21 nm vs. 19 nm) even though there is a difference in the adopted morphologies.

The higher molecular weight  $PS_{43}\text{-}b\text{-}PDMS_{17}$  sample was designed to obtain a hexagonal phase during solid state studies. As indicated by the corresponding TEM data the dark PDMS domains arranged in hexagonal symmetry inside the white PS matrix [Figure 6.10 (b)]. In addition, parallel stripes can be also identified corresponding to the longitudinal view of cylinders. 1D SAXS plots further confirmed

the formation of hexagonally close packed cylindrical morphology through the characteristic scattering peaks with a ratio  $q/q^*=1:\sqrt{3}:2:\sqrt{7}:3:\sqrt{13}$  [Figure 6.10 (b)]. A domain periodicity of 48 nm was calculated from the distinct first order peak. As expected, the domain periodicity increases for higher molecular weight samples when compared to values of 21 nm and 19 nm for the two previous samples (PS<sub>14</sub>-*b*-PDMS<sub>6.4</sub> and PS<sub>14</sub>-*b*-PDMS<sub>9.0</sub> respectively).

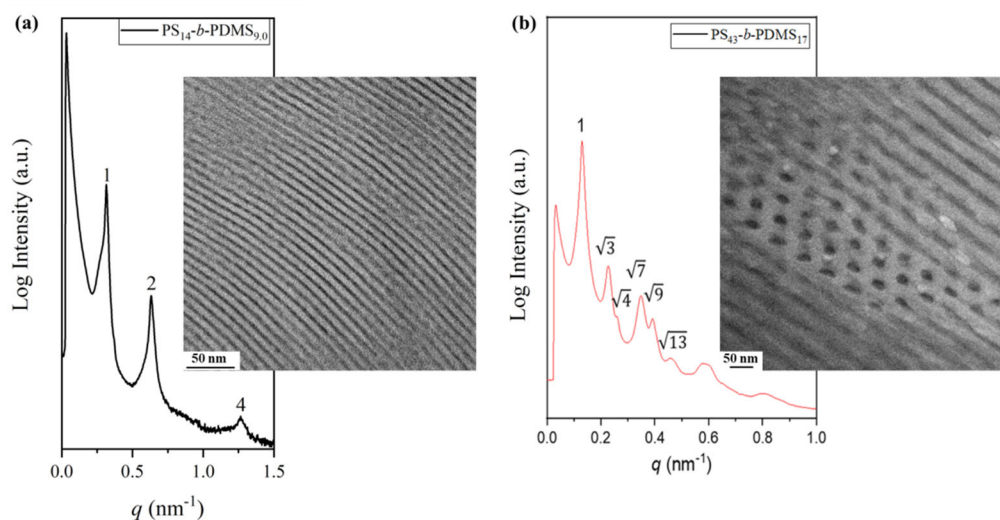


**Figure 6.10:** (a) Combined 1D SAXS plot and TEM micrograph of the unannealed PS<sub>14</sub>-*b*-PDMS<sub>9.0</sub> using cyclohexane for solution casting clearly suggesting the formation of alternating lamellae and (b) combined 1D SAXS plot and TEM micrograph of the unannealed PS<sub>43</sub>-*b*-PDMS<sub>17</sub> using cyclohexane for solution casting indicating the formation of hexagonal cylinders.

The bulk studies for PS<sub>42</sub>-*b*-PDMS<sub>32</sub>, with volume fraction of PDMS equal to 0.45, were performed using TEM to identify the adopted morphology after solution casting in toluene and not cyclohexane (as in the previous three cases). 1D SAXS measurements have not been conducted for the specific sample. The sample was synthesized to give rise to alternating lamellae sheets during self-assembly, as verified by the TEM micrograph (Figure 6.11) in which PS (white) and PDMS (dark) stripes with a layer thickness of approximately 62 nm are observed. The specific molecular characteristics are chosen to confine the entanglements' number across the slip plane at approximately three entanglements per segment taking into consideration that the blocks are in their corresponding homopolymer melts.<sup>190</sup> The use of the PS<sub>42</sub>-*b*-PDMS<sub>32</sub> on ballistic studies constitute a future perspective of the PhD thesis.

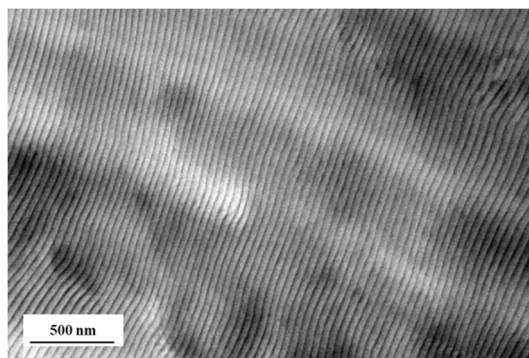


**Figure 6.11:** TEM micrograph of the unannealed PS<sub>42</sub>-*b*-PDMS<sub>32</sub> after casting in toluene.

The formation of 3D cubic network phases constitutes a significant part of this thesis. The remaining four diblock copolymer sequences (PS<sub>51</sub>-*b*-PDMS<sub>35</sub>, PS<sub>55</sub>-*b*-PDMS<sub>38</sub>, PS<sub>69</sub>-*b*-PDMS<sub>49</sub> and PS<sub>80</sub>-*b*-PDMS<sub>50</sub>) were synthesized in an effort to obtain network structures due to their potential applications. It has already been mentioned that double gyroid requires intermediate  $\chi N$  values (ranging from 20-50) and composition (from 0.27-0.34 and 0.66-0.73), according to the phase diagram of  $\chi N$  vs.  $\phi$  for the most studied linear diblock copolymers of the PS-*b*-PI sequence.<sup>82</sup> Thomas and Avgeropoulos research groups<sup>90</sup> established a specific composition range in which DG phase can be adopted for the studied PS-*b*-PDMS systems. More specifically, it has been demonstrated that, PS-*b*-PDMS linear copolymers with  $\phi_{\text{PDMS}} \sim 0.41$ , even for substantially increased  $\chi N$  values, are able to form 3D cubic network phases. This discovery in combination with the research study conducted by Ho and Avgeropoulos groups,<sup>127</sup> in which phase transformations based on different solvents can occur, had a major contribution on determining the desired composition for network phases in PS-*b*-PDMS diblock copolymers.

The PS<sub>51</sub>-*b*-PDMS<sub>35</sub> copolymer with  $\phi_{\text{PDMS}} \sim 0.42$  formed a lamellar morphology after solution casting in cyclohexane under controlled evaporation rate (0.1 ml/day) as evidenced by TEM studies. The SAXS results indicated a well-developed lamellar phase due to the multiple reflections at the relative  $q$  values of 1:2:3:4:5:6:7:8:9:10. The combined results of the equilibrium morphology are presented in Figure 6.12.

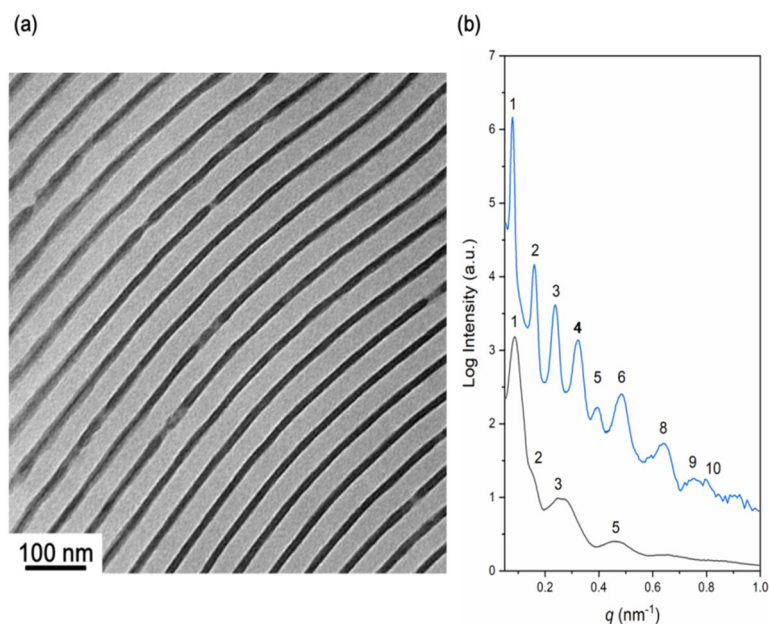


**Figure 6.12:** (a) TEM micrograph of  $PS_{51}\text{-}b\text{-}PDMS_{35}$  after solution casting in cyclohexane. (b) 1D SAXS profile of  $PS_{51}\text{-}b\text{-}PDMS_{35}$  after solution casting using cyclohexane (black line) and followed by thermal annealing at  $180\text{ }^{\circ}\text{C}$  for 24 hours (blue line).<sup>97</sup>

Chloroform was then used for solution casting and the solvent was allowed to slowly evaporate with similar rate as in cyclohexane (0.1 ml/day). The exploitation of a PS selective solvent induced the formation of a network phase with a tetrapod unit. TEM images at various projections including [100], [111], [311] and [321] and the relative  $q$  values at  $\sqrt{2}:\sqrt{3}:\sqrt{4}:\sqrt{6}:\sqrt{10}:\sqrt{12}:\sqrt{14}:\sqrt{18}:\sqrt{21}$  evident in the 1D SAXS plot (red line) strongly suggested the formation of the double diamond (DD) phase relative to  $Pn\bar{3}m$  space group symmetry (Figure 6.13). The results were further supported by 3D-TEM experiments. Based on the value of the primary peak the domain spacing is calculated to be equal to 61.8 nm.

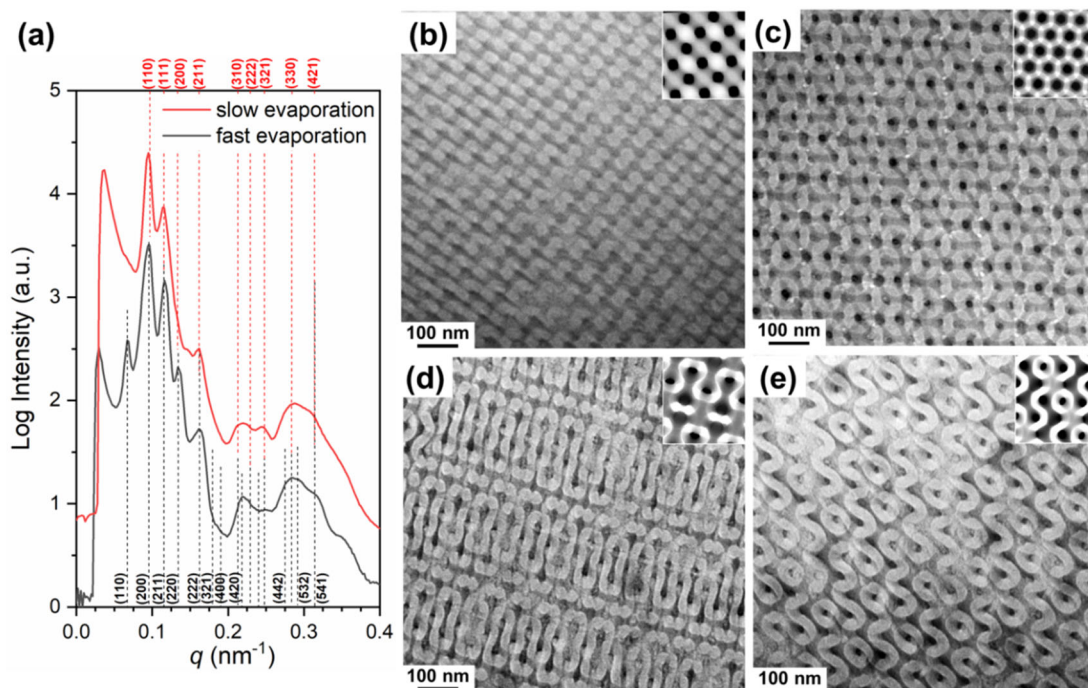


**Figure 6.13:** (A) 1D SAXS plots of  $PS_{51}\text{-}b\text{-}PDMS_{35}$  after solution casting in chloroform under slow and fast evaporation rates. The red dashed lines correspond to the reflection planes of the  $Pn\bar{3}m$  (DD) space group at which two additional peaks in the low- $q$  region are observed. The black dashed lines are attributed to the reflection planes of DP phase with  $Im\bar{3}m$  space group, giving the additional (110) and (220) reflections. TEM micrographs of  $PS_{51}\text{-}b\text{-}PDMS_{35}$  along various projection directions: (B) [100]; (C) [111]; (D) [311]; and (E) [321] for DD phase. (Insets) The corresponding images from simulation based on DD phase.<sup>97</sup>

Two additional peaks [ $\sqrt{2}$  and  $\sqrt{8}$  corresponding to the (110) and (220) planes respectively] at the low  $q$  region were emerged using chloroform as a casting solvent in a significantly increased evaporation rate (0.1 ml/h instead of 0.1 ml/day). The combined TEM, SAXS and 3D-TEM results indicated the formation of a double primitive (DP) phase with a hexapod texture. The permitted reflections of DD and the relative  $q$  values at a peak ratio of  $\sqrt{2}:\sqrt{4}:\sqrt{6}:\sqrt{8}:\sqrt{12}:\sqrt{14}:\sqrt{16}:\sqrt{20}:\sqrt{24}:\sqrt{38}:\sqrt{42}$  (black line) are presented in a joint SAXS plot for comparison reasons. Representative projection directions of the DP phase such as [100], [111] and [321] are demonstrated in the following TEM micrographs (Figure 6.14) together with the 3-D reconstruction along [111] that clearly indicates the formation of a hexapod. The domain spacing is estimated through the Bragg's law equal to 89.3 nm. In addition, the coexistence of both phases is further verified by the 2D SAXS patterns in which the direct correlation of the [111] DP zonal diffraction (black) and the [110] DD zonal diffraction (orange) is straightforward, suggesting an OOT from the DP to DD phase.

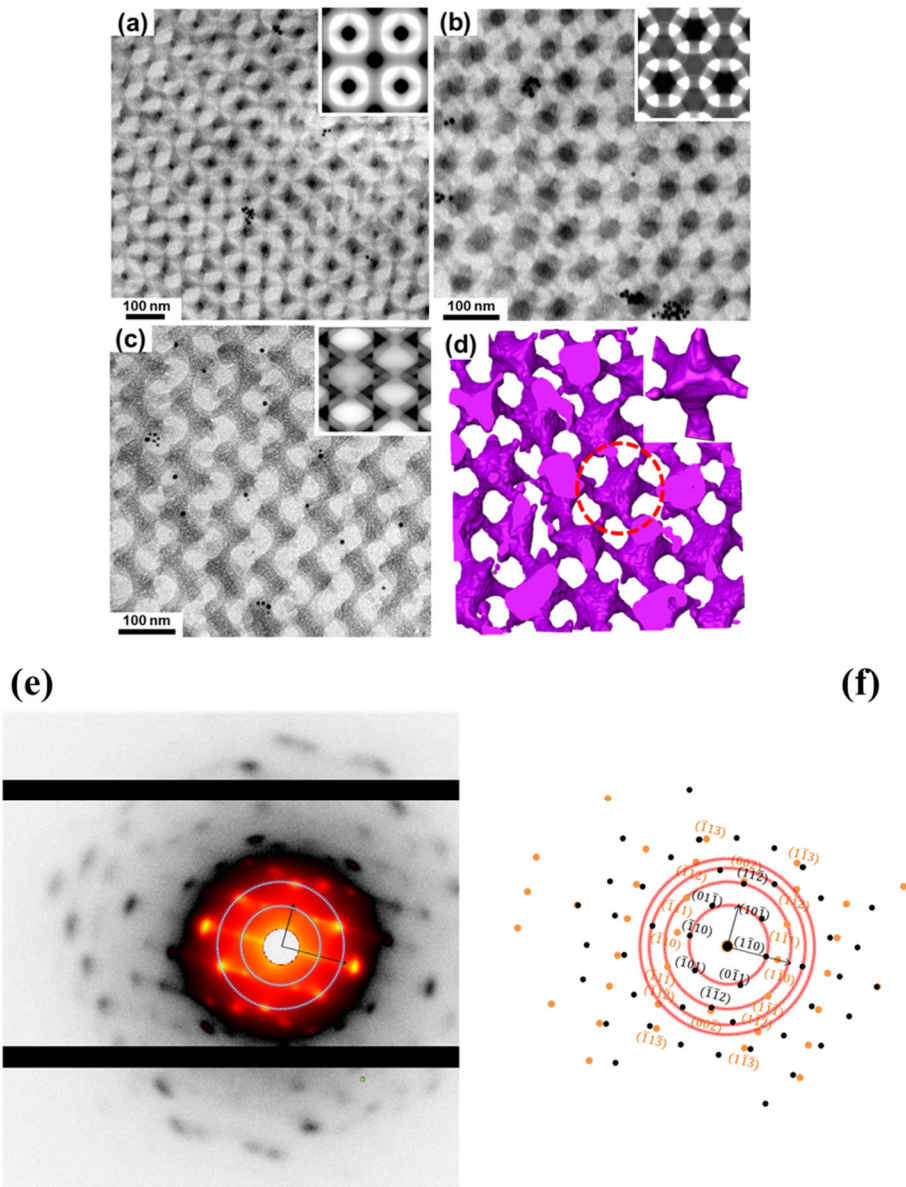


**Figure 6.14:** TEM images with respect to the fast-evaporated  $PS_{51}$ - $b$ - $PDMS_{35}$  along various projection directions: (a)  $[100]$ ; (b)  $[111]$ ; and (c)  $[321]$  for DP phase. (Insets) The respective simulation images based on DP phase. (d) Three-dimensional reconstruction images of the kinetically arrested DP phase from  $PS_{51}$ - $b$ - $PDMS_{35}/SiO_2$  along the  $[111]$  direction. (Inset) The building unit of the DP phase. (e) 2D SAXS pattern of the microphase separated  $PS_{51}$ - $b$ - $PDMS_{35}$  obtained after fast evaporation; (f) the corresponding illustration of the coexistence of the  $[111]$  zonal diffraction of the DP phase (black dots) and the  $[110]$  zonal diffraction of the DD phase (orange dots).<sup>97</sup>

The stability of the formed network phases was further examined through temperature resolved in situ SAXS experiments. Initially, the characteristic reflections with respect to the DP and DD phase are clearly demonstrated. When the temperature reaches 100 °C, an increase on the respective reflections, namely  $(110)_{DP}$  and  $(110)_{DD}$  attributed to the long-range ordering, is evident due to the de-vitrification of the PS

domains. At 130 °C an order-order transition from the DP to the DD phase is observed as indicated by the intensity drop of the  $(110)_{DP}$ . The broadening and merging of the reflections from  $(110)_{DP}$  and  $(110)_{DD}$  occurs at 150 °C designating the emergence of a new phase which is completely transformed once the temperature approaches 160 °C. The new phase corresponds to the double gyroid (DG) as indicated by the reflection from  $(211)_{DG}$  as well as  $(220)_{DG}$ , and the characteristic reflections at the relative  $q$  values of  $\sqrt{6}:\sqrt{8}:\sqrt{14}:\sqrt{18}:\sqrt{22}:\sqrt{32}$ . The planes regarding the DG phase are marked as the red dashed lines. The primary reflection is used for the calculation of the domain spacing which is equal to 100.4 nm. The subsequent TEM studies further verified the formation of DG structure and the combined results are demonstrated in Figure 6.15.

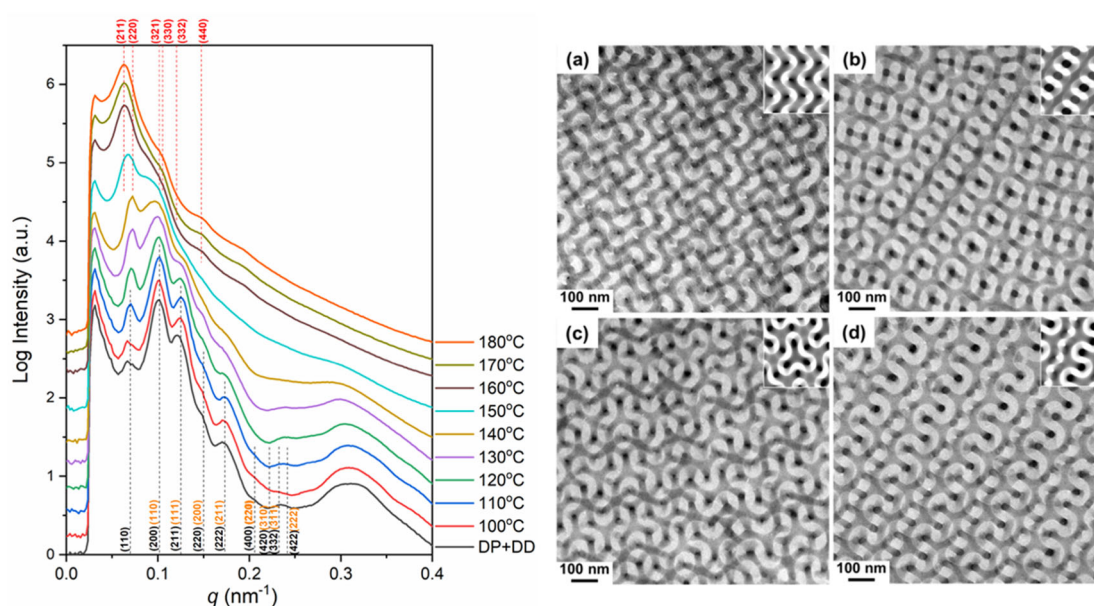


**Figure 6.15:** (left) Temperature-resolved in situ 1D SAXS profiles of  $PS_{51}$ - $b$ - $PDMS_{35}$  after fast solution casting. The red dashed lines are the reflection planes referred to  $Ia\bar{3}d$  space group of DG. The orange brackets are the reflection planes of  $Pn\bar{3}m$  space group of DD phase at which an additional peak is identified in the low- $q$  region. The black dashed lines are the reflection planes based on DP phase with  $Im\bar{3}m$  space group. (right) TEM images of  $PS_{51}$ - $b$ - $PDMS_{35}$  after thermal annealing from various projection directions along (a)  $[100]$ ; (b)  $[110]$ ; (c)  $[111]$ ; and (d)  $[211]$  for DG phase. The insets on the TEM images are the corresponding simulation images based on the DG phase.<sup>97</sup>

The significance of the study is multifaceted due to the ability to form network phases with controlled strut number simply by tuning the processing parameters during solution casting and type of solvent (cyclohexane vs. chloroform).<sup>97</sup> The higher the strut number the higher the packing frustration would be, as a result the minority PDMS segments should stretched out more to fill the space in the more frustrated phase. This fact justifies the inability to obtain exclusively the DP phase which is the

more frustrated network phase evident in this study. The strongly segregated PS-*b*-PDMS samples provide the ability to tune the morphology which is very important for numerous studies.

A similar sample to that discussed above (PS<sub>51</sub>-*b*-PDMS<sub>35</sub>) regarding the overall molecular characteristics, is the PS<sub>55</sub>-*b*-PDMS<sub>38</sub>, which was synthesized to explore the self-assembled structures after casting into various solvents. In the following 1D SAXS profiles (Figure 6.16) the obtained nanostructures of the PS<sub>55</sub>-*b*-PDMS<sub>38</sub> using 1,2-dichloromethane (DCM), chlorobenzene (CB), tetrahydrofuran (THF) and toluene as casting solvents are presented. DCM and CB induced the formation of hexagonal phases as indicated by the reflections at the relative  $q$  positions of  $q/q^*=1:\sqrt{3}:2:\sqrt{7}:\sqrt{13}$  with a domain spacing approximately equal to 70 nm. In contrast, THF and toluene gave rise to DG morphology as verified by the relative  $q$  positions at  $\sqrt{6}:\sqrt{8}:\sqrt{14}:\sqrt{20}$  respectively.

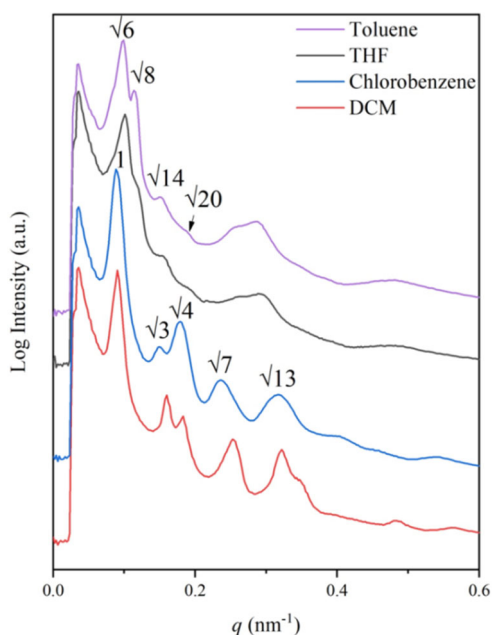


**Figure 6.16:** Different self-assembled structures of the PS<sub>55</sub>-*b*-PDMS<sub>38</sub> obtained from 1,2-dichloromethane (red line), chlorobenzene (blue line), tetrahydrofuran (black line) and toluene (purple line).

Chloroform enabled the formation of a DG phase in opposition to the PS<sub>51</sub>-*b*-PDMS<sub>35</sub> sample that demonstrated a different behavior strongly dependent on the evaporation rate of the solvent adopting either a DD or a mixed DD/DP phase. This discrepancy may be attributed to the volume fraction differentiation between the two samples ( $\phi_{\text{PDMS}} \sim 0.42$  for PS<sub>51</sub>-*b*-PDMS<sub>35</sub> vs.  $\phi_{\text{PDMS}} \sim 0.40$  for PS<sub>55</sub>-*b*-PDMS<sub>38</sub>). It is of

significant importance to mention that, by tuning the composition or conformational asymmetry of the BCP chains, it is possible to promote the formation of uncommon phases even at very narrow regions in the phase diagram. Also, the stabilization of the complex phases is also quite challenging due to packing frustration that hinders the formation of tetrapod or hexapod domains. The combined TEM and SAXS results with respect to the microphase separated domains using chloroform are presented in Figure 6.17.

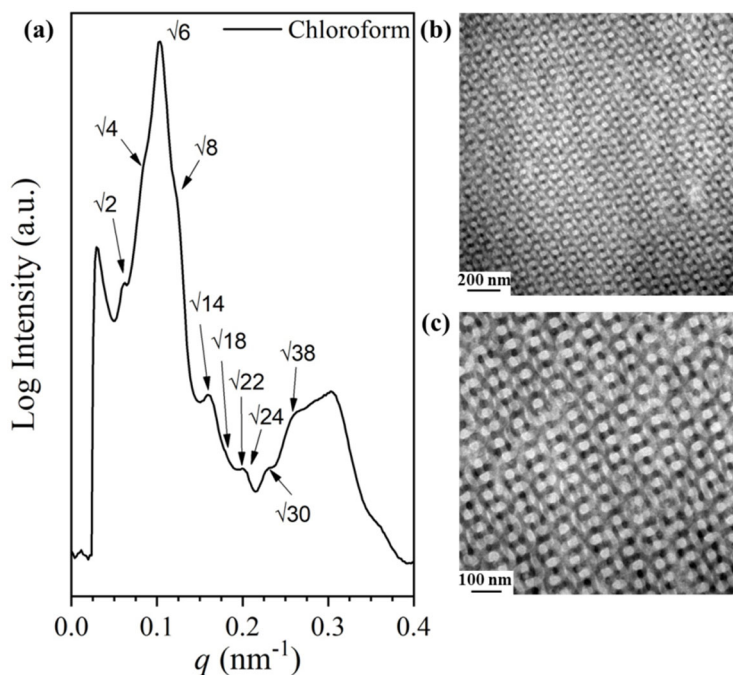


**Figure 6.17:** Self-assembled structure of the  $PS_{55}\text{-}b\text{-}PDMS_{38}$  obtained when solution cast from chloroform, which is consistent with the DG phase.

A higher molecular weight sample was also synthesized to study the formation of the self-assembled structures using cyclohexane, toluene and chloroform under different evaporation rates. The  $PS_{69}\text{-}b\text{-}PDMS_{49}$  with volume fraction of PDMS equal to 0.47, after solution casting in a non-selective solvent (cyclohexane), exhibited alternating dark PDMS and white PS periodicities and the corresponding 1D SAXS plot further confirmed the specific morphology (Figure 6.18). The several reflections at the relative  $q$  values of 1:2:3:4:5:6:7 after annealing at 120 °C ( $\chi=0.135$ ) for 1 day indicated a highly ordered morphology with d-spacing being approximately 90 nm.

The use of chloroform and toluene under controlled evaporation rates led to a DG phase as can be clearly observed in the corresponding 1D SAXS profiles (Figure 6.18). The predicted reflections for the DG morphology took place at the relative  $q$

values of  $\sqrt{6}:\sqrt{8}:\sqrt{14}:\sqrt{22}:\sqrt{32}:\sqrt{40}:\sqrt{50}$  for both toluene (evaporation rate 0.35 ml/day, red line) and chloroform (evaporation rate 1.35 ml/day, blue line and 0.07 ml/day, green line) and the domain spacing was calculated from the primary peak approximately 80 nm. It should be noted that for chloroform, as evident, two different evaporation rates were used, one faster and one slower, in order to report any discrepancies in behavior. The appearance of an additional peak at the low  $q$  region ( $\sqrt{4}$ ) is caused by the distortion or deformation of the lattice since the 2D SAXS pattern has not revealed any different network phase as in the case of the PS<sub>51</sub>-*b*-PDMS<sub>35</sub>. Also, in the specific sequence the adaptation of a pure DD or the coexistence of DD/DP phases has not been possible due to the increased volume fraction of PDMS in combination with the higher total molecular weight. Note that the region where more complex network phases can appear is considerably narrow, rendering the DG structure the most stable for pure (devoid of homopolymer or additives) BCPs.<sup>194</sup> In the TEM images presented in Figure 6.18 (b and c) the adopted morphologies with respect to the solution casted sample in cyclohexane and toluene are demonstrated. The alternating black and white lamellae stripes correspond to the equilibrium morphology, while the [211] direction for the DG phase indicates the formation of a network phase promoted by the PS affinity towards toluene.

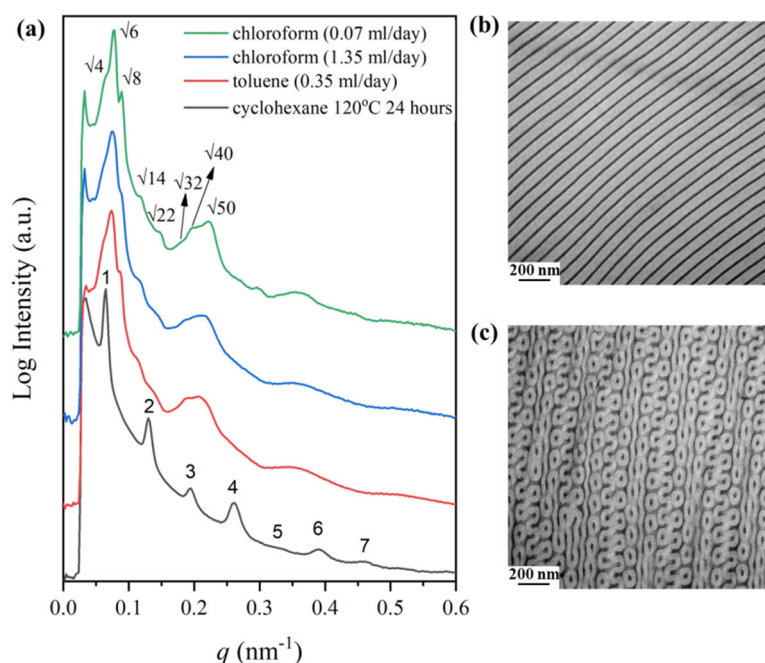


**Figure 6.18:** (a) 1D SAXS plots of the PS<sub>69</sub>-*b*-PDMS<sub>49</sub> using different solvents as well as evaporation rates. Alternating lamellae was obtained using cyclohexane (black line) and DG was adopted when toluene (red line) and chloroform were employed (blue and green lines respectively). (b) TEM micrograph after casting in a non-selective solvent (cyclohexane) (c) TEM micrograph showing [211] projection of DG after casting in a selective solvent (toluene).

The last sample to be discussed is PS<sub>80</sub>-*b*-PDMS<sub>50</sub>. Accordingly, the higher molecular weight sample with  $\phi_{\text{PDMS}}=0.39$  was synthesized in an effort to again obtain cubic network phases. Even though, the casting solvent affects the microphase separation of BCPs and the structure periods, the slightly lower volume fraction (0.39 instead of 0.40-0.41) has not allowed the formation of cubic network structures. The 1D SAXS profile using chloroform during solution casting exhibited a hexagonal phase with the reflection peaks at the relative  $q$  positions of 1:2: $\sqrt{7}$ : $\sqrt{13}$  and an interdomain spacing between neighboring cylinders ( $L_0=\frac{4\pi}{\sqrt{3}q}$ ) equal to 110 nm (larger compared to all other samples due to the highest total number average molecular weight of the sample). It should also be noted that the low  $q$  values are attributed to the high total  $\bar{M}_n$  of the sample and therefore to the increased dimensions of the unit cell, a fact that could possibly lead to overlapping of some of the permitted reflection peaks which are close together. Furthermore, the morphology was also verified in real space measurements, as evidenced by the TEM micrograph (Figure 6.19), where dark hexagonally closed cylinders of PDMS in PS matrix are showcased.

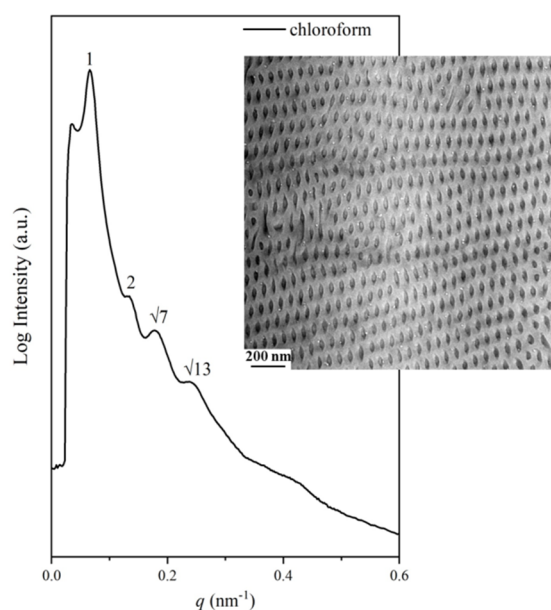


**Figure 6.19:** Combined 1D SAXS plot and TEM results regarding the PS<sub>80</sub>-*b*-PDMS<sub>50</sub> sample after casting in chloroform.

## 6.5 Utilizing Linear Block Copolymers for Superior Mechanical Properties<sup>187</sup>

The linear diblock copolymer of the PS<sub>51</sub>-*b*-PDMS<sub>35</sub> sequence was further studied due to its inherent solid-state properties.

It has already been thoroughly analyzed that when the PS<sub>51</sub>-*b*-PDMS<sub>35</sub> is cast from PS selective solvents, including toluene and chloroform, under controlled evaporation rates, double gyroid and double diamond structures are formed respectively.<sup>97</sup> The PDMS chains are expanded instead of looping due to the higher elasticity and free stretching energy and in combination with the higher swollen ratio of PDMS in chloroform the formation of kinetically trapped phases is enabled. Avgeropoulos and Ho research groups in a very recent publication<sup>187</sup> used the PS<sub>51</sub>-*b*-PDMS<sub>35</sub> sample for the fabrication of nanonetwork epoxy resins. The schematics with respect to the templated synthesis of epoxy resin modified by PBA-*b*-PMMA are presented in the following figure (Figure 6.20).

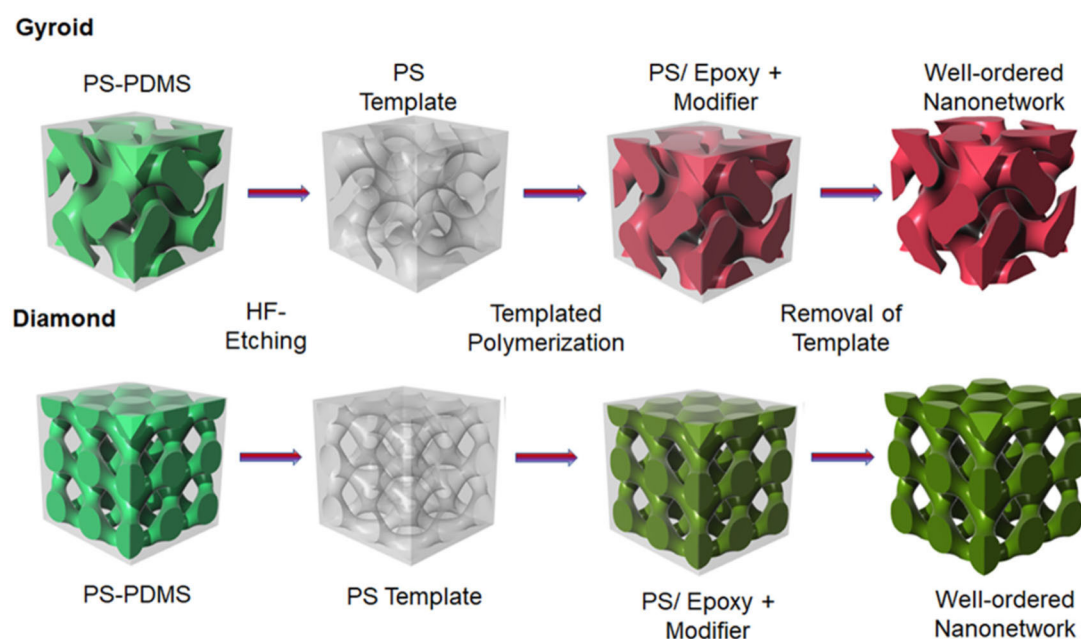


**Figure 6.20:** Schematic illustration of templated synthesis of epoxy resin modified by PBA-*b*-PMMA.<sup>187</sup>

Specifically, after the network phases are adopted through solution casting procedure, selective etching using HF solution (HF/H<sub>2</sub>O/methanol = 0.5/1/1 by volume) is carried out to remove the PDMS segment. Well-ordered nanoporous PS templates with gyroid- and diamond structures having nanochannels of approximate porosity are obtained.

The pore filling for the following templated polymerization of epoxy resin can be accomplished using methanol which is the simplest alcohol and an epoxy resin precursor to provide sufficient wetting ability. The successful pore filling of the hydrophobic PS template should be always confirmed prior to the templated polymerization of the epoxy resin due to the potential blocking of the template which would eventually lead to incomplete networks.

Following, the preparation of a mixture containing epoxy resin (Bisphenol-A type epoxy) with 5% w/w of well soluble PBA-*b*-PMMA [poly(butyl acrylate)-*b*-poly(methyl methacrylate)] and triethylenetetramine took place. To promote the adequate pore filling and to reduce the polymerization reaction, the PS templates were immersed into the precursor solution at low temperature (10°C) for five hours. The pore filling of the epoxy resin into the channels of the template with nanometer sizes is achieved by capillary force. Multistep curing including step heating to 150°C was then conducted to obtain the desired template texture with sufficient cross-linking of the resin.

By dissolving the PS template in an organic solvent such as styrene (monomer of PS) for 12 hours the removal of the template can be sufficiently carried out. The nanoporous resins were vacuum dried overnight to remove any residual styrene.

The aim of this study was to further enhance the energy dissipation through the addition of a BCP-based modifier (PBA-*b*-PMMA) containing both epoxy phobic and epoxy philic blocks, due to the synergic effect of deliberate structuring in the nanoscale and the toughening provided by the modifier at molecular level.

The TEM analysis of the dispersed PBA-*b*-PMMA in the epoxy matrix indicated a spherical micelle structure, where PBA constituted the core and the PMMA the shell, dispersed in the epoxy matrix. As a result, the reinforcement of interfacial strength is provided by the dispersion of the incompatible epoxy-phobic PBA core and the epoxy-philic PMMA shell in the epoxy resin matrix.

The TEM image presented in Figure 6.21 (a) demonstrates the bright PS matrix and the dark epoxy network after staining with vapors of OsO<sub>4</sub> aqueous solution to provide adequate mass thickness, further verifying the formation of a gyroid-structured PS/epoxy nanocomposite. The well-ordered gyroid-structured epoxy resin is revealed after the removal of PS template by FESEM experiments Figure 6.21 (b). The scattering results involving the PS template, the PS/epoxy nanocomposites, and nanoporous epoxy resin with gyroid texture are demonstrated in

Figure 6.21 (c). The characteristic to the double gyroid reflections at the relative  $q$  values of  $\sqrt{6}$ ,  $\sqrt{8}$ ,  $\sqrt{16}$ ,  $\sqrt{20}$ ,  $\sqrt{30}$ , and  $\sqrt{38}$  (blue arrows) and an additional deformation peak at  $\sqrt{4}$  (red arrow) can be clearly identified for the PS template [Figure 6.21 (c) (i)]. The emergence of an additional peak in the lower  $q$  region with a value of  $\sqrt{2}$  (dark blue arrow) for the PS/epoxy nanocomposite is attributed to the shifting of the gyroid nanonetworks during templated polymerization [Figure 6.21 (c) (ii)].<sup>114</sup> The removal of the PS template led to an even more significant shifting as indicated in Figure 6.21 (c) (iii).

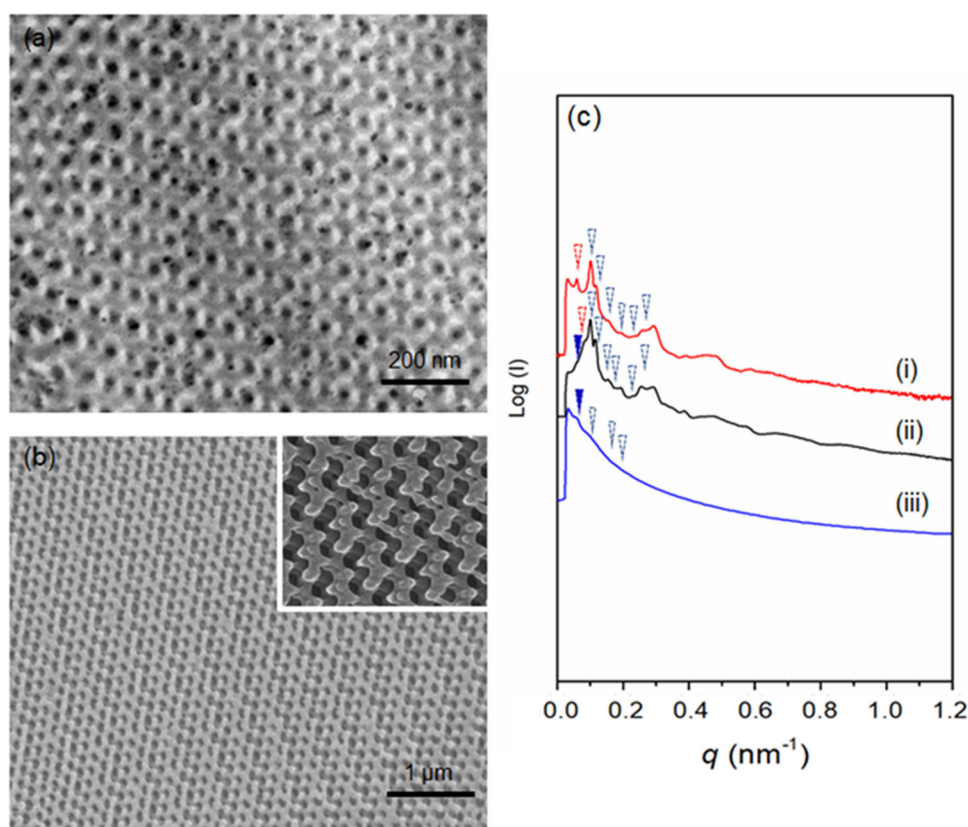


**Figure 6.21:** (a) TEM image of PS/epoxy nanocomposite in gyroid structure. (b) FE-SEM image of well-ordered gyroid epoxy resins, inset shows the magnified image. (c) 1D SAXS profiles of (i) PS template, (ii) PS/epoxy nanocomposites and (iii) nanoporous epoxy resins with gyroid texture.<sup>187</sup>

The results with respect to the diamond-structured epoxy resins after following the same experimental procedure are presented in Figure 6.22. The TEM micrograph of the PS/epoxy nanocomposites [Figure 6.22 (a)] clearly verified the formation of a network phase. FE-SEM results [Figure 6.22 (b)] after the PS removal suggested the formation of a nanonetwork-structured epoxy. The formation of double diamond was also confirmed through the 1D SAXS plots, in which the characteristic reflections at

the relative  $q$  values of  $\sqrt{2}$ ,  $\sqrt{3}$ ,  $\sqrt{4}$ ,  $\sqrt{6}$ ,  $\sqrt{8}$ , and  $\sqrt{10}$  can be observed for the PS template and PS/epoxy nanocomposites [Figures 6.22 (c) (i) and (ii)]. An additional reflection [Figure 6.22 (c) (iii)] at the relative  $q$  value of  $\sqrt{3}$  due to the network shifting was evident again in the nanoporous epoxy.

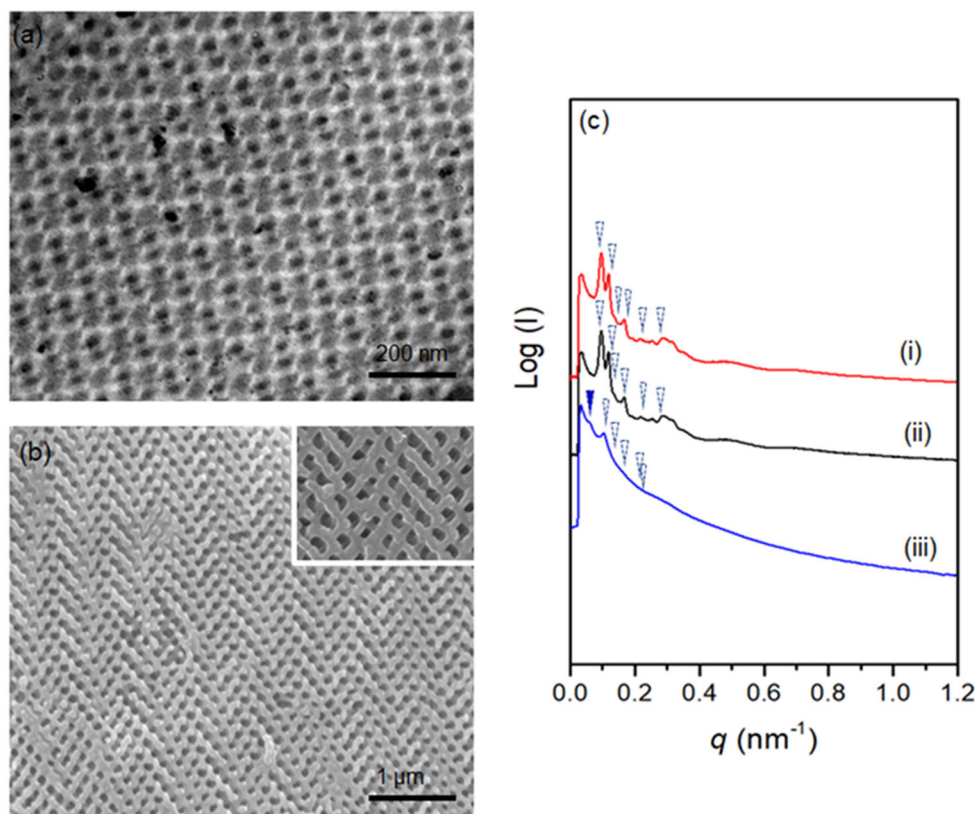


**Figure 6.22:** (a) TEM image of PS/epoxy nanocomposite in diamond structure. (b) FESEM image of well-ordered diamond epoxy resins, inset shows the magnified image. (c) 1D SAXS profiles of (i) PS template, (ii) PS/epoxy nanocomposites and (iii) nanoporous epoxy resins with diamond structure.<sup>187</sup>

The mechanical properties were further studied by nanoindentation analysis and the results concerning a typical load-displacement curve for intrinsic epoxy resins, as well as gyroid- and diamond-structured epoxy resins modified with PBA-*b*-PMMA are depicted in Figure 6.23. Based on the unloading curve, by using the Oliver-Pharr model the reduced elastic modulus ( $E_r$ ) of 4.2 GPa was calculated for the intrinsic epoxy resins based on the unloading curve. The addition of the PBA-*b*-PMMA modifier in the epoxy resins did not induce any substantial change on the modulus which was calculated approximately 3.8 GPa. The porous texture of the gyroid-structured nanonetwork induced a significant decrease on the modulus to 0.9 GPa, while the diamond-structured one showcased a lower modulus value of 0.8 GPa.

The analysis of the energy dissipation capability from plastic deformation was conducted through the enclosed area by loading and unloading curves. The energy with respect to the homogeneous non-structured epoxy resins was calculated by the area under the load-displacement curve equal to  $0.02 \pm 0.002$  nJ. High crosslinking density of the epoxy resins at a given load ( $500\mu\text{N}$ ) leads to 90% elastic behavior. The addition of 5% w/w of the PBA-*b*-PMMA modifier resulted in a five times higher energy dissipation and specifically equal to  $0.09 \pm 0.004$  nJ due to the plastic mode of deformation.

Interestingly enough, the use of artificially engineered network structures such as gyroid- and diamond-structured epoxy resins enabled significant higher energy dissipation from brittle to the plastic deformation with values equal to  $0.36 \pm 0.02$  nJ and  $0.43 \pm 0.03$  nJ respectively. The higher energy dissipation at a given loading with minimum retracting from unloading exhibited in the diamond-structured resin is justified by the higher struts number when compared to the triangular planar gyroid network (Figure 6.30). These findings strongly suggest that the enhancement on the energy dissipation is attributed to the synergic effect of the deliberate structuring of network texture in the nanoscale and the toughening of self-assembled modifiers (BCPs) in the epoxy matrix at the molecular level.

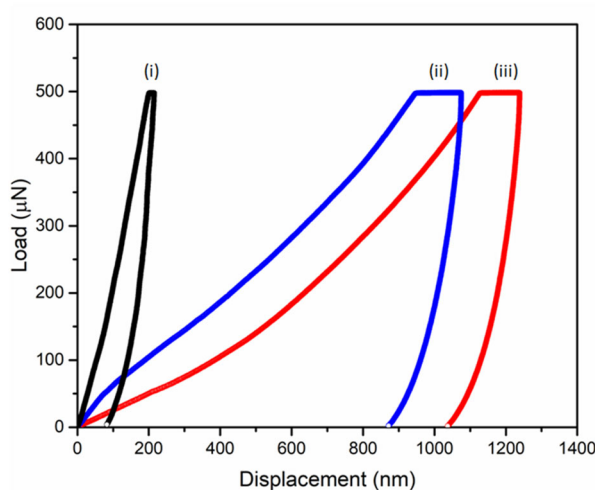


**Figure 6.23:** Load-displacement tests involving (i) non-structured epoxy without modifier, (ii) gyroid-structured epoxy and (iii) diamond-structured epoxy resins with PBA-*b*-PMMA under  $500\mu\text{N}$ .<sup>187</sup>

## 6.6 Molecular Characterization Results of Linear and Non-Linear (PS-*b*-PDMS)<sub>n</sub> Block Copolymers (Where n = 1 or 2 or 3 or 4 or 6)

Various set of samples were synthesized by varying the initial monomer quantities to obtain linear and non-linear copolymers with diverse molecular characteristics and therefore different structures during self-assembly studies. Low and average total  $\bar{M}_n$  values ranging from 7,000–37,000 g/mol were chosen for the respective copolymer precursors. Note that, the star block copolymers despite their increased total  $\bar{M}_n$  values showcase similar domain spacing to the analogous precursors, but enhanced properties due to the significantly higher degree of polymerization. All synthesized materials are summarized in Table 6.6 and are grouped into different sets [overall fifteen (15) sets] to demonstrate the molecular characteristics of the linear (triblock copolymers) and non-linear (star block copolymers) sequences together with their corresponding diblock precursors. The molecular characteristics of the linear triblock and non-linear star block copolymers were calculated after fractionation procedure in order to remove the excess of the diblock precursor (the excess is required to secure the substitution of all chlorine atoms of the linking reagent from diblock chains, as already discussed in the relative synthesis subchapter). The PS-*b*-PDMS precursors are abbreviated again as PS<sub>x</sub>-*b*-PDMS<sub>y</sub>, where x and y represent the number-average molecular weight (kg/mol) of each segment. Correspondingly, the star block copolymers are abbreviated as (PS<sub>x</sub>-*b*-PDMS<sub>y</sub>)<sub>n</sub> where n = 2, 3, 4 or 6.

**Table 6.6:** Molecular characterization results for the linear PS-*b*-PDMS diblock copolymer precursors, linear triblock copolymers (PS-*b*-PDMS)<sub>2</sub> and their corresponding star block copolymers (PS-*b*-PDMS)<sub>3, 4, 6</sub>.

Set	sample	$\bar{M}_n^{PS(a)}$ (g/mol) SEC/VPO /MO	$\bar{M}_n^{PDMS(b)}$ (g/mol) VPO/MO	$\bar{M}_n^{total(b)}$ (g/mol) VPO/MO	$\mathcal{D}^{(c)}$	$f_{PDMS}^{(d)}$ <sup>1</sup> H-NMR	$\varphi_{PDMS}^{(d)}$
1	PS <sub>3</sub> - <i>b</i> -PDMS <sub>5,5</sub>	3,500	4,500	8,000	1.03	0.56	0.59
	(PS <sub>3</sub> - <i>b</i> -PDMS <sub>5,5</sub> ) <sub>2</sub>	7,000	9,000	16,000	1.05	0.56	0.59
2	PS <sub>3,6</sub> - <i>b</i> -PDMS <sub>3,6</sub>	3,600	3,600	7,200	1.04	0.47	0.50
	(PS <sub>3,6</sub> - <i>b</i> -PDMS <sub>3,6</sub> ) <sub>3</sub>	10,800	10,800	21,600	1.07	0.47	0.50
3	PS <sub>3,9</sub> - <i>b</i> -PDMS <sub>4,1</sub>	3,900	4,100	8,000	1.07	0.49	0.52
	(PS <sub>3,9</sub> - <i>b</i> -PDMS <sub>4,1</sub> ) <sub>4</sub>	15,600	16,400	32,000	1.07	0.49	0.52
4	PS <sub>3,9</sub> - <i>b</i> -PDMS <sub>4,2</sub>	3,900	4,200	8,100	1.05	0.52	0.55
	(PS <sub>3,9</sub> - <i>b</i> -PDMS <sub>4,2</sub> ) <sub>3</sub>	11,700	12,600	24,300	1.08	0.52	0.55
5	PS <sub>4,1</sub> - <i>b</i> -PDMS <sub>4,0</sub>	4,100	4,000	8,100	1.04	0.50	0.53
	(PS <sub>4,1</sub> - <i>b</i> -PDMS <sub>4,0</sub> ) <sub>3</sub>	12,300	12,000	24,300	1.07	0.50	0.53
6	PS <sub>15</sub> - <i>b</i> -PDMS <sub>10</sub>	15,000	10,000	25,000	1.03	0.36	0.39
	(PS <sub>15</sub> - <i>b</i> -PDMS <sub>10</sub> ) <sub>3</sub>	45,000	30,000	75,000	1.07	0.36	0.39
7	PS <sub>5</sub> - <i>b</i> -PDMS <sub>3,4</sub>	5,000	3,400	8,400	1.05	0.37	0.40
	(PS <sub>5</sub> - <i>b</i> -PDMS <sub>3,4</sub> ) <sub>3</sub>	15,000	10,200	25,200	1.06	0.37	0.40
	(PS <sub>5</sub> - <i>b</i> -PDMS <sub>3,4</sub> ) <sub>4</sub>	20,000	13,600	33,600	1.08	0.37	0.40
8	PS <sub>4,2</sub> - <i>b</i> -PDMS <sub>5,6</sub>	4,200	5,600	9,800	1.05	0.57	0.60
	(PS <sub>4,2</sub> - <i>b</i> -PDMS <sub>5,6</sub> ) <sub>3</sub>	12,600	16,800	29,400	1.05	0.57	0.60
	(PS <sub>4,2</sub> - <i>b</i> -PDMS <sub>5,6</sub> ) <sub>4</sub>	16,800	22,400	39,200	1.06	0.57	0.60
9	PS <sub>3</sub> - <i>b</i> -PDMS <sub>3,5</sub>	3,000	3,500	6,500	1.05	0.50	0.53
	(PS <sub>3</sub> - <i>b</i> -PDMS <sub>3,5</sub> ) <sub>3</sub>	9,000	10,500	19,500	1.07	0.50	0.53
	(PS <sub>3</sub> - <i>b</i> -PDMS <sub>3,5</sub> ) <sub>4</sub>	12,000	14,000	26,000	1.07	0.50	0.53
10	PS <sub>12,8</sub> - <i>b</i> -PDMS <sub>10,3</sub>	12,800	10,300	23,100	1.04	0.44	0.47
	(PS <sub>12,8</sub> - <i>b</i> -PDMS <sub>10,3</sub> ) <sub>3</sub>	38,400	30,900	69,300	1.06	0.44	0.47
	(PS <sub>12,8</sub> - <i>b</i> -PDMS <sub>10,3</sub> ) <sub>4</sub>	51,200	41,200	92,400	1.07	0.44	0.47
11	PS <sub>4,2</sub> - <i>b</i> -PDMS <sub>2,8</sub>	4,600	2,800	7,200	1.04	0.37	0.40
	(PS <sub>4,2</sub> - <i>b</i> -PDMS <sub>2,8</sub> ) <sub>2</sub>	9,200	5,600	14,400	1.04	0.37	0.40
	(PS <sub>4,2</sub> - <i>b</i> -PDMS <sub>2,8</sub> ) <sub>6</sub>	27,600	16,800	44,400	1.05	0.37	0.40
12	PS <sub>5</sub> - <i>b</i> -PDMS <sub>5</sub>	5,000	5,000	10,000	1.05	0.47	0.50
	(PS <sub>5</sub> - <i>b</i> -PDMS <sub>5</sub> ) <sub>2</sub>	10,000	10,000	20,000	1.07	0.47	0.50
	(PS <sub>5</sub> - <i>b</i> -PDMS <sub>5</sub> ) <sub>6</sub>	30,000	30,000	60,000	1.07	0.47	0.50
13	PS <sub>15,7</sub> - <i>b</i> -PDMS <sub>11,1</sub>	15,700	11,100	26,800	1.03	0.41	0.44
	(PS <sub>15,7</sub> - <i>b</i> -PDMS <sub>11,1</sub> ) <sub>2</sub>	31,400	22,200	53,600	1.05	0.41	0.44
	(PS <sub>15,7</sub> - <i>b</i> -PDMS <sub>11,1</sub> ) <sub>6</sub>	94,200	66,600	160,800	1.07	0.41	0.44
14	PS <sub>22</sub> - <i>b</i> -PDMS <sub>15</sub>	22,000	15,000	37,000	1.05	0.44	0.47
	(PS <sub>22</sub> - <i>b</i> -PDMS <sub>15</sub> ) <sub>2</sub>	44,000	30,000	74,000	1.08	0.44	0.47
	(PS <sub>22</sub> - <i>b</i> -PDMS <sub>15</sub> ) <sub>6</sub>	132,000	90,000	222,000	1.09	0.44	0.47
15	PS <sub>14</sub> - <i>b</i> -PDMS <sub>6</sub>	14,000	6,400	20,400	1.03	0.31	0.34
	(PS <sub>14</sub> - <i>b</i> -PDMS <sub>6</sub> ) <sub>2</sub>	28,000	12,800	40,800	1.03	0.31	0.34
	(PS <sub>14</sub> - <i>b</i> -PDMS <sub>6</sub> ) <sub>3</sub>	42,000	19,200	61,200	1.07	0.31	0.34
	(PS <sub>14</sub> - <i>b</i> -PDMS <sub>6</sub> ) <sub>4</sub>	56,000	25,600	81,600	1.07	0.31	0.34
	(PS <sub>14</sub> - <i>b</i> -PDMS <sub>6</sub> ) <sub>6</sub>	84,000	38,400	122,400	1.05	0.31	0.34

<sup>(a)</sup>combined SEC (in tetrahydrofuran at 30 °C) and MO or VPO (in toluene at 35 °C and 45 °C respectively) results, <sup>(b)</sup> MO or VPO in toluene at 35 °C and 45 °C respectively, <sup>(c)</sup>SEC measurements in tetrahydrofuran at 30 °C, <sup>(d)</sup>From <sup>1</sup>H-NMR measurements in CDCl<sub>3</sub> at 25 °C using equation 6.1, 6.2 and 6.3. Note that  $\bar{M}_n^{PDMS}$  was calculated through the equation:  $\bar{M}_n^{PDMS} = \bar{M}_n^{total} - \bar{M}_n^{PS}$ . Also  $\varphi_{PDMS} = 1 - \varphi_{PS}$ .

The accurate  $\bar{M}_n$  values of the copolymer presursors, triblock copolymers, 3-, 4- and 6-arm star block copolymers were calculated through VPO and/or MO. In the case of non-linear star shaped materials the use of osmometry is imperative, since SEC demonstrates limited sensitivity in resolving stars with three, four, five or six arms. The hydrodynamic volume of star-block copolymers during SEC measurements does not alter significantly when compared to corresponding linear counterparts, causing misinterpretation of the results. The more complex the architecture, the higher the variation on molecular weight values will be during SEC measurements.

In a (A-*b*-B)<sub>3</sub> sequence the real molecular weight is higher and proportional to the star functionality than the phenomenon molecular weight as directly estimated by SEC. The phenomenon molecular weight is (2.5-2.6)\* $\bar{M}_n^{diblock}$  instead of (3.0)\* $\bar{M}_n^{diblock}$ . For the case of the (A-*b*-B)<sub>4</sub> the phenomenon molecular weight is even lower and approximately equal to (3.0-3.1)\* $\bar{M}_n^{diblock}$  instead of (4.0)\* $\bar{M}_n^{diblock}$ . Finally, (A-*b*-B)<sub>6</sub> showcase the higher discrepancy since the phenomenon molecular weight calculated from SEC is (4.0-4.1)\* $\bar{M}_n^{diblock}$  instead of (6.0)\* $\bar{M}_n^{diblock}$ . The total  $\bar{M}_n$  for each sample given in the table corresponds to the real values directly calculated by osmometry experiments. A representative example regarding the variation on the hydrodynamic volume as the architecture varies is given in the following SEC chromatograph (Figure 6.24) which corresponds to samples for set 15 as given in Table 6.6.

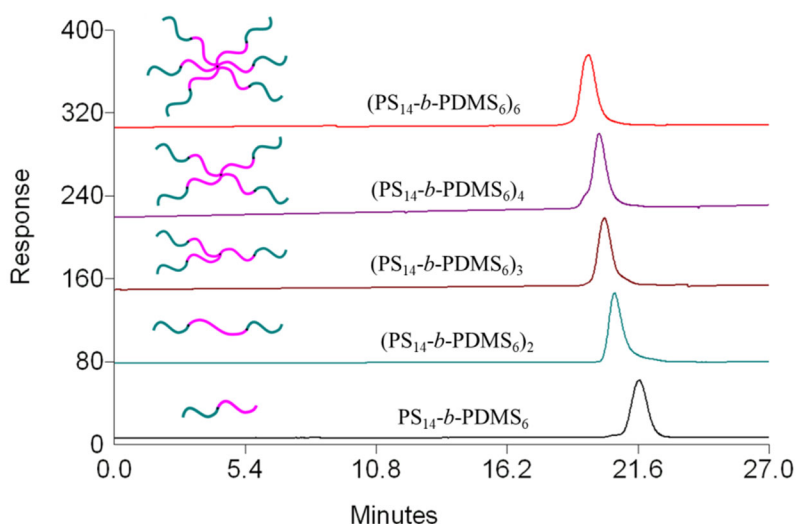


**Figure 6.24:** SEC chromatographs of samples for set 15 corresponding to the  $PS_{14}$ -*b*- $PDMS_6$  (black),  $(PS_{14}$ -*b*- $PDMS_6$ )<sub>2</sub> (green),  $(PS_{14}$ -*b*- $PDMS_6$ )<sub>3</sub> (brown),  $(PS_{14}$ -*b*- $PDMS_6$ )<sub>4</sub> (purple) and  $(PS_{14}$ -*b*- $PDMS_6$ )<sub>6</sub> (red).

The chromatograph demonstrates the linear diblock copolymer which is eluted in higher elution times followed by the fractionated triblock, 3-, 4- and 6-arm star copolymers in lower elution times respectively.

Despite the inability to calculate the real molecular weight values, SEC constitutes a reliable tool for quality control over the linking reactions progress as well as for the determination of the dispersity indices and the evaluation of the successful fractionation of the unpurified products. All samples, evident in Table 6.6, exhibited narrow dispersity indices (varying from 1.03 up to 1.09) further indicating the ability to obtain linear and non-linear copolymers of the specific sequence with high homogeneity degree. In the following chromatograms all final synthesized samples are presented. In addition, two characteristic examples from each linear and non-linear sequence including the unfractionated materials are given for clarification reasons.

#### **Linear Triblock PS-*b*-PDMS-*b*-PS or (PS-*b*-PDMS)<sub>2</sub> Copolymers**

In Figure 6.25 (a) and (b) two representative SEC chromatographs involving the PS homopolymers, the diblock copolymer precursors, the unpurified products after the complete coupling reactions and the final fractionated linear triblock copolymers are presented. It should be noted that, due to the chlorosilane linking chemistry, which demands a precise molar ratio between the living copolymer chains and coupling agents, the produced samples are a mixture of the desired triblock copolymer and unwanted byproducts (small excess of the diblock copolymer precursor). This fact leads to the necessity of extracting all byproducts (excess of the precursors) through a mass fractionation procedure. Repeated fractionations are often required to obtain a completely pure copolymer. To monitor the fractionation, SEC is performed until only one peak corresponding to the desired product is evident. The removal of the unwanted species results also in loss of pure product quantity, since the fractionation yield often ranges from 40-70%. Mass fractionation is a powerful tool due to the necessity of pure products for the self-assembly studies. The appearance of a shoulder (dimer) for the PS homopolymers at lower elution times has already been attributed to the termination at ambient conditions using methanol vapors and by degassed methanol under high vacuum conditions.

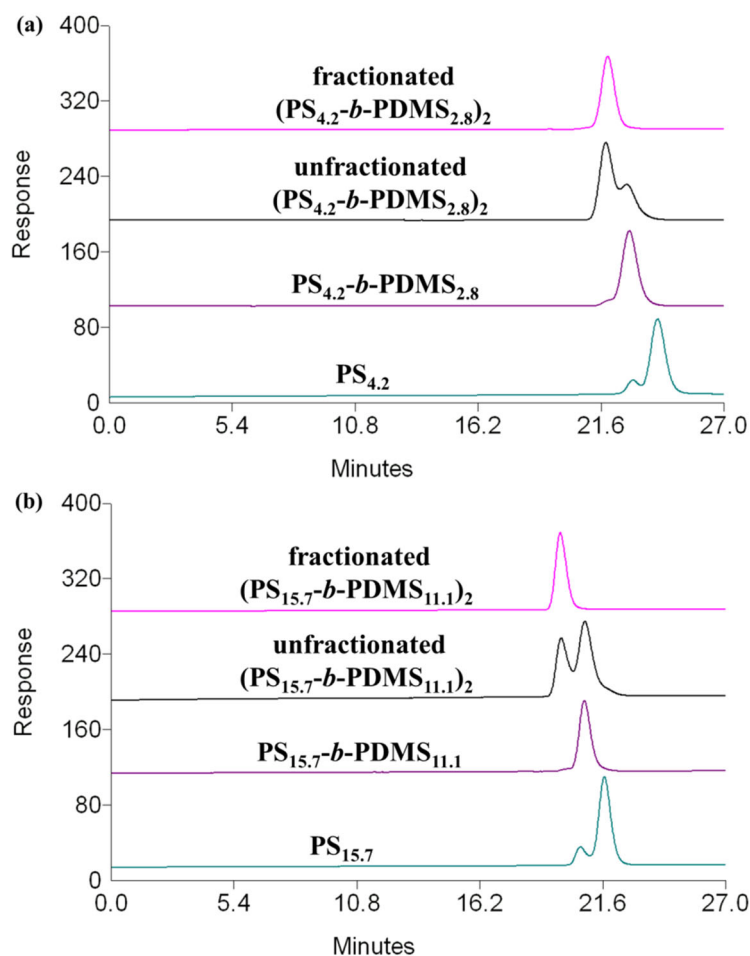


**Figure 6.25:** SEC chromatographs corresponding to (a) PS<sub>4.2</sub> homopolymer (green), PS<sub>4.2</sub>-b-PDMS<sub>2.8</sub> copolymer precursor (purple), unfractionated triblock copolymer (PS<sub>4.2</sub>-b-PDMS<sub>2.8</sub>)<sub>2</sub> (black), fractionated (PS<sub>4.2</sub>-b-PDMS<sub>2.8</sub>)<sub>2</sub> (pink) and (b) PS<sub>15.7</sub> homopolymer (green), PS<sub>15.7</sub>-b-PDMS<sub>11.1</sub> copolymer precursor (purple), unfractionated triblock copolymer (PS<sub>15.7</sub>-b-PDMS<sub>11.1</sub>)<sub>2</sub> (black), fractionated (PS<sub>15.7</sub>-b-PDMS<sub>11.1</sub>)<sub>2</sub> (pink).

All linear diblock precursors along with their purified triblock copolymers synthesized in this thesis are demonstrated in Figure 6.26. The monomodal Gaussian distributions of the SEC chromatographs, further confirmed the successful synthesis and fractionation procedure (where needed). The dispersity indices, in all cases, were lower than 1.1, which is in accordance with the high standards required for anionic polymerization. Also, the low  $\bar{M}_w/\bar{M}_n$  values indicate the complete removal of the undesired species during fractionation. The higher the molecular weight the lower the elution time is, as it can be clearly observed in the relative chromatographs.

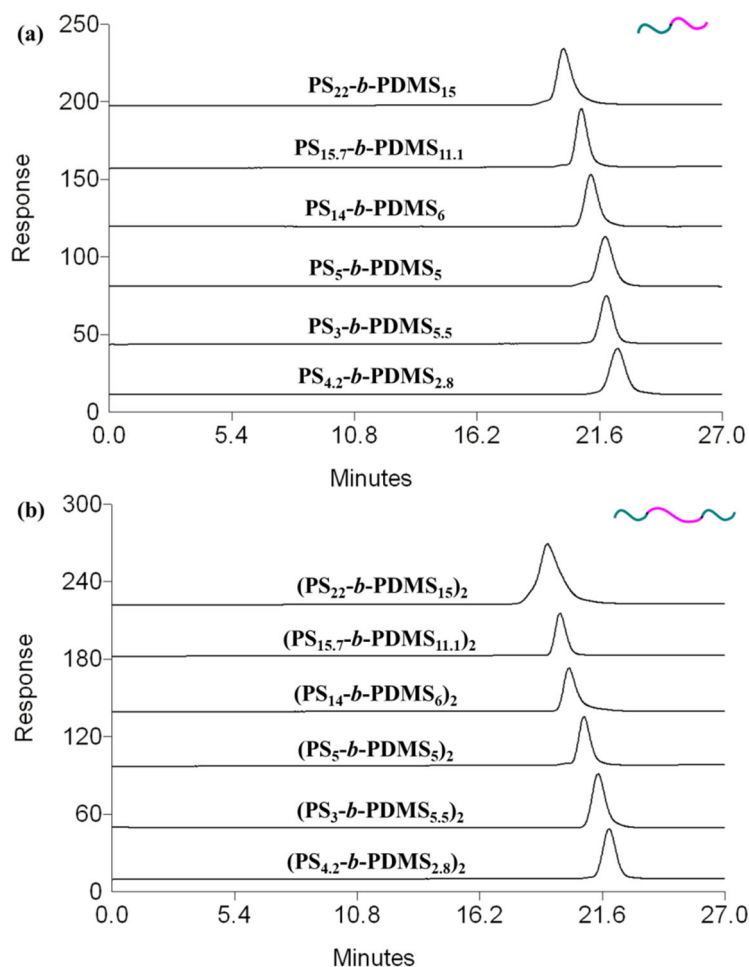


**Figure 6.26:** SEC chromatographs corresponding to (a) all diblock copolymer precursors used for the preparation of triblock copolymers and (b) all fractionated triblock copolymers. For clarification reasons the samples are named after the notations given in Table 6.6.

### Three Arm Star Block Copolymers of the $(PS\text{-}b\text{-}PDMS)_3$ Type

Coherent conclusions can be extracted by observing the SEC chromatographs [Figure 6.27 (a) and (b)] with respect to the PS homopolymers, the diblock copolymer precursors, the unpurified products after the complete coupling reactions (where evident) and the final fractionated non-linear three arm star block copolymers. Notably, in the SEC chromatograph [Figure 6.27 (a)] corresponding to the  $(PS_3\text{-}b\text{-}PDMS_{3.5})_3$  sequence the absence of the unfractionated material is attributed to the precise molar ratio between the living copolymer chains and the trichloromethylsilane during the coupling reaction which led to the direct synthesis of the three arm star block copolymer, without the requirement of mass fractionation. The absolute substitution of all  $-Cl$  atoms without evident byproducts is also allocated to the low total molecular weight of the copolymer precursor that favored the complete substitution of the active sites. In accordance to the SEC principles, higher molecular

weight products are eluted in lower elution times but for non-linear three arm star block copolymers only the phenomenon molecular weight could be calculated as already explained previously.

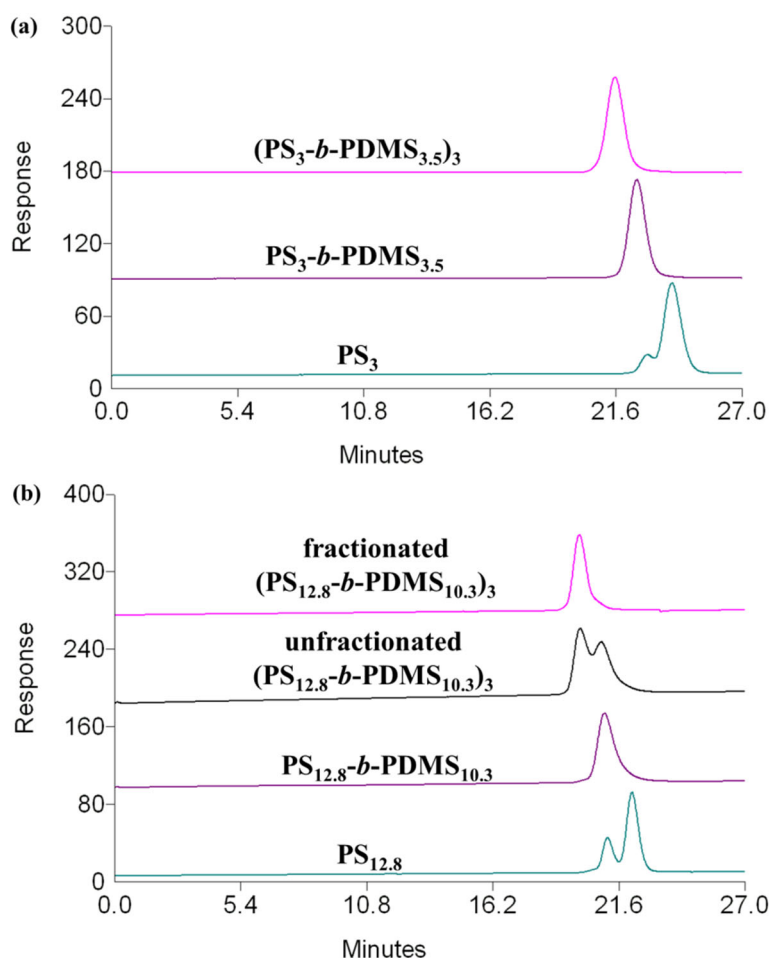


**Figure 6.27:** SEC chromatographs corresponding to (a)  $PS_3$  homopolymer (green),  $PS_3-b-PDMS_{3.5}$  copolymer precursor (purple), tree-arm star block copolymer of the  $(PS_3-b-PDMS_{3.5})_3$  type after the complete coupling reaction (pink) and (b)  $PS_{12.8}$  homopolymer (green),  $PS_{12.8}-b-PDMS_{10.3}$  copolymer precursor (purple), unfractionated three arm star block copolymer  $(PS_{12.8}-b-PDMS_{10.3})_3$  (black), fractionated  $(PS_{12.8}-b-PDMS_{10.3})_2$  (pink).

The diblock precursors and their corresponding three arm star block copolymers can be clearly observed in Figure 6.28. Narrow molecular weight distributions for the intermediate diblock arms and the final star shaped materials indicating no homopolymer or other byproducts, are evident for all synthesized sequences.

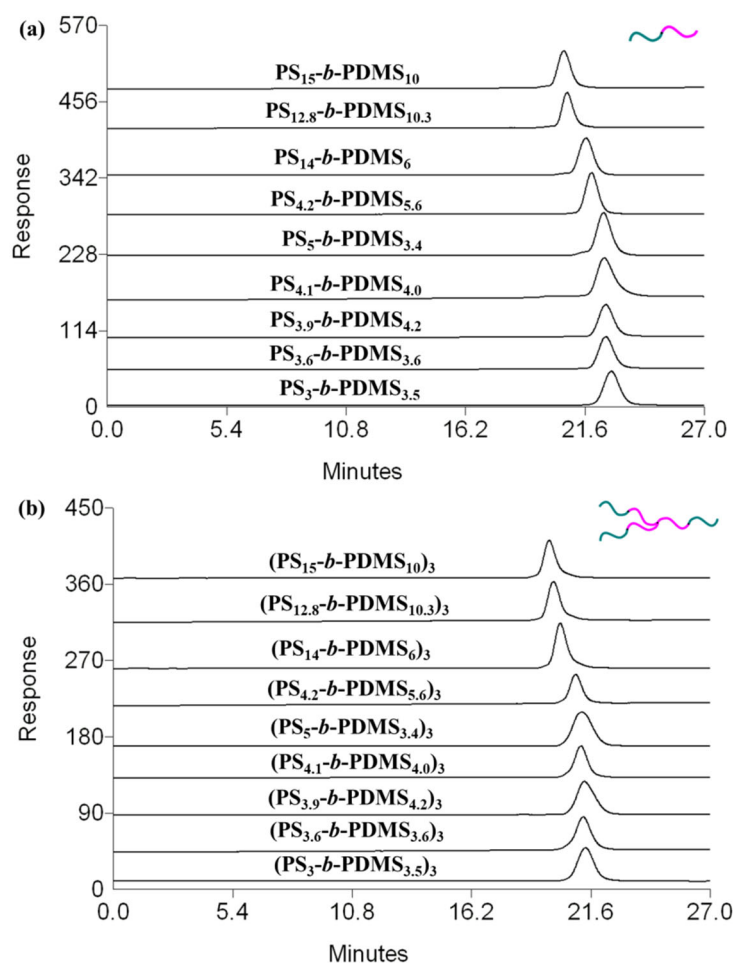


**Figure 6.28:** SEC chromatographs corresponding to (a) all diblock copolymer precursors used for the preparation of three arm star block copolymers and (b) all final three arm star block copolymers. For clarification reasons the samples are named after the notations given in Table 6.6.

#### **Four Arm Star Block Copolymers of the (PS-*b*-PDMS)<sub>4</sub> Type**

In accordance with the aforementioned results, sequential addition of styrene and D<sub>3</sub> using different feeding ratio of the monomers followed by chlorosilane chemistry with the appropriate reagent (silicon tetrachloride) led to the preparation of well-defined four arm star block copolymers. The excess of diblock copolymer precursors after the complete linking reaction afforded a mixture of the desired four arm stars and unwanted species. Note that, as the number of active sites increases and/or the molecular weight of the living copolymer is high enough, steric hindrance phenomena may appear leading to stars with mixed functionality and therefore the isolation of the desired material can be even more challenging. For this reason the appropriate molar ratio between C-Li and Si-Cl is very critical. In the following SEC chromatographs [Figure 6.29 (a) and (b)], two characteristic examples of the PS

homopolymers, the diblock copolymer precursors, the unpurified products after the complete coupling reactions and the final fractionated non-linear four arm star block copolymers are presented.

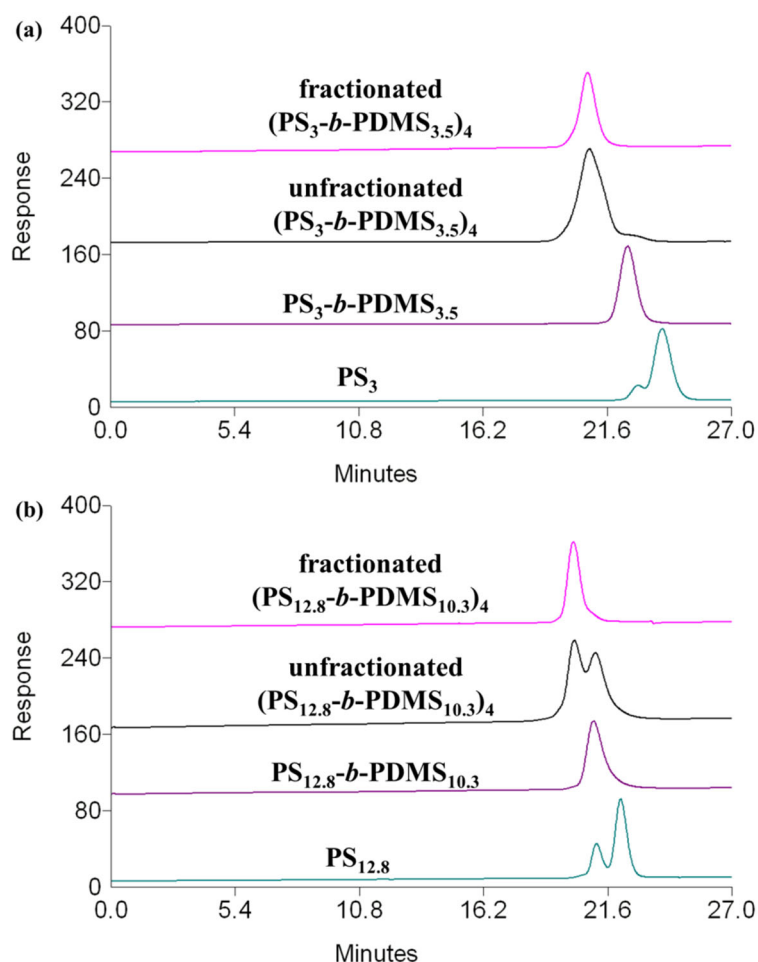


**Figure 6.29:** SEC chromatographs corresponding to (a)  $PS_3$  homopolymer (green),  $PS_3-b-PDMS_{3.5}$  copolymer precursor (purple), unfractionated four arm star block copolymer of the  $(PS_3-b-PDMS_{3.5})_3$  (black), fractionated  $(PS_3-b-PDMS_{3.5})_3$  (pink) and (b)  $PS_{12.8}$  homopolymer (green),  $PS_{12.8}-b-PDMS_{10.3}$  copolymer precursor (purple), unfractionated four arm star block copolymer  $(PS_{12.8}-b-PDMS_{10.3})_3$  (black), fractionated  $(PS_{12.8}-b-PDMS_{10.3})_2$  (pink).

All diblock precursors and their respective four arm star block copolymers are demonstrated in Figure 6.30. Monomodal Gaussian curves are identified for the intermediate diblock arms and the final star copolymers with four arms further verifying the absence of homopolymer and other byproducts including precursor and/or star with different than the desired functionality (e.g. 3 arms). Consequently, the successful synthesis and the fractionation procedure (where needed) can be clearly concluded also for this series of samples from the obtained chromatographs of the final products.

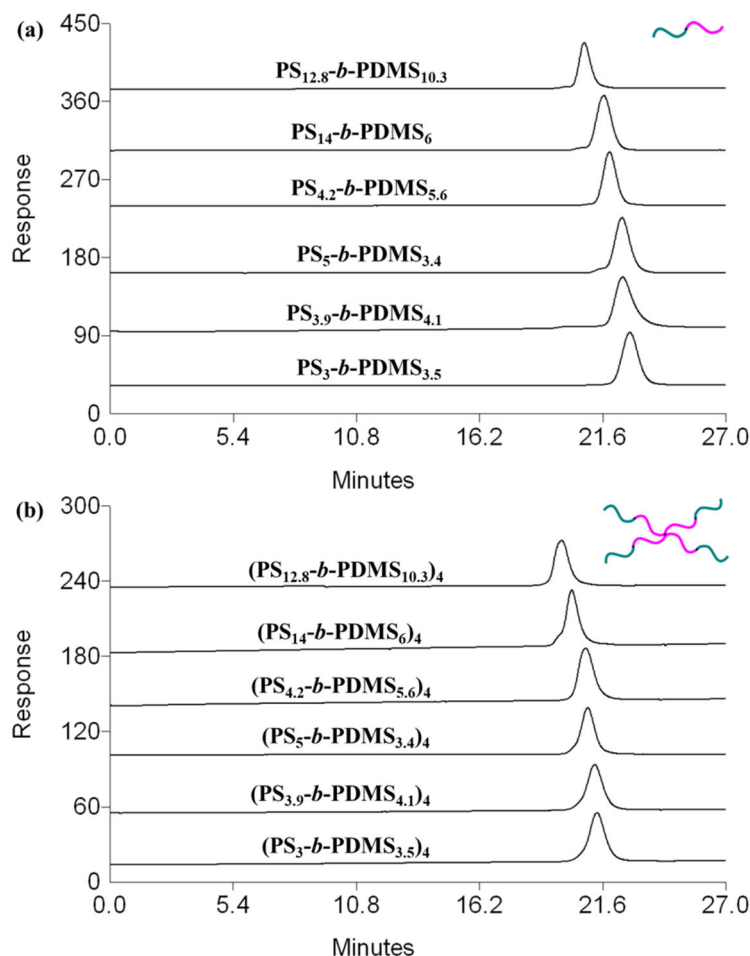


**Figure 6.30:** SEC chromatographs corresponding to (a) all diblock copolymer precursors used for the preparation of four arm star block copolymers and (b) all final four arm star block copolymers. For clarification reasons the samples are named after the notations given in Table 6.6.

### **Six Arm Star Block Copolymers of the (PS-*b*-PDMS)<sub>6</sub> Type**

It has already been mentioned that the synthesis of PDMS-containing star block copolymers with six arms has never been reported in the literature before. SEC experiments had a decisive role on monitoring the coupling reaction, the incorporation rate of the arms in the active sites of 1,2-bis(trichlorosilyl)ethane reagent and has been also used to evaluate the successful mass fractionation. Two representative SEC chromatographs regarding the PS homopolymers, the diblock copolymer precursors, the unpurified products after the complete coupling reactions and the final fractionated six arm star block copolymers are given in Figure 6.31 (a) and (b). It should be mentioned that the molar ratio between C-Li and Si-Cl is of major importance to receive a final product as pure as possible. The fractionation of an unpurified product involving only unwanted diblock copolymer arms as byproducts is rendered a rather easy task due to the high difference in elution time between the

molecular weight of the desired star and the linear precursor. On the other hand, unpurified products containing star with various functionalities (if any) have to be removed by repeated mass fractionations to obtain a pure material.

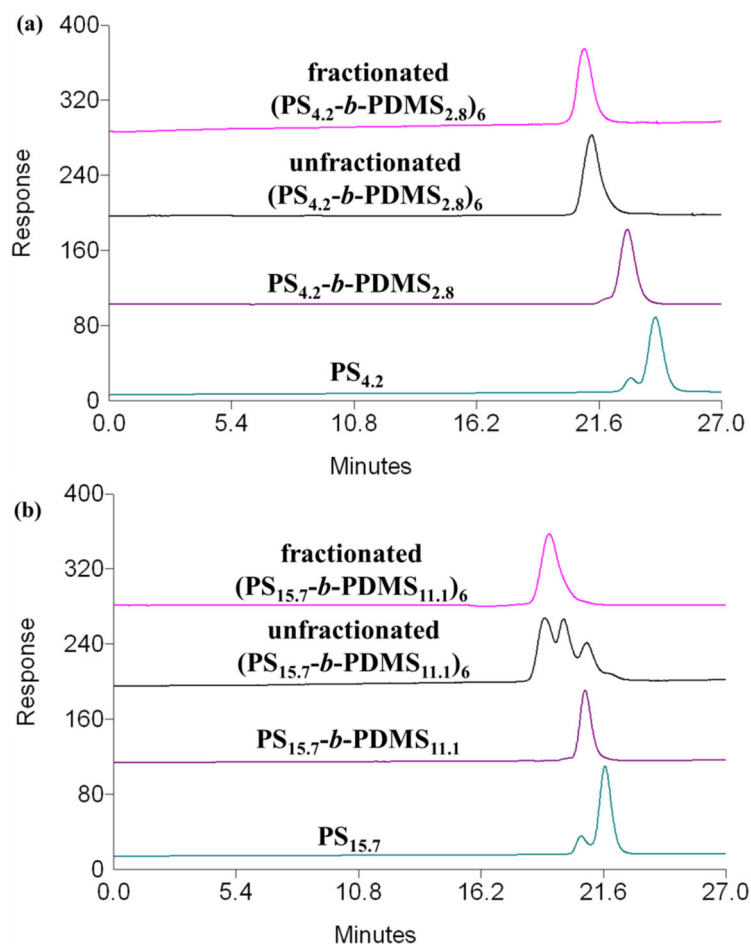


**Figure 6.31:** SEC chromatographs corresponding to (a)  $PS_{4.2}$  homopolymer (green),  $PS_{4.2}\text{-}b\text{-}PDMS_{2.8}$  copolymer precursor (purple), unfractionated six-arm star block copolymer  $(PS_{4.2}\text{-}b\text{-}PDMS_{2.8})_6$  (black), fractionated  $(PS_{4.2}\text{-}b\text{-}PDMS_{2.8})_6$  (pink) and (b)  $PS_{15.7}$  homopolymer (green),  $PS_{15.7}\text{-}b\text{-}PDMS_{11.1}$  copolymer precursor (purple), unfractionated six-arm star block copolymer  $(PS_{15.7}\text{-}b\text{-}PDMS_{11.1})_6$  (black), fractionated  $(PS_{15.7}\text{-}b\text{-}PDMS_{11.1})_6$  (pink).

The five diblock copolymer arms and the corresponding six-arm star block copolymers are summarized in Figure 6.32. The highest variation on the hydrodynamic volume between the synthesized copolymers can be realized in the star block copolymers consist of six arms. Yet, the phenomenon molecular weight differs substantially from the real one as evident from the osmometry experiments presented already in Table 6.6. From SEC measurements it is concluded that the complex architecture copolymers have been successfully synthesized and fractionated and that the dispersity indices are below 1.1 indicating high compositional and molecular homogeneity.

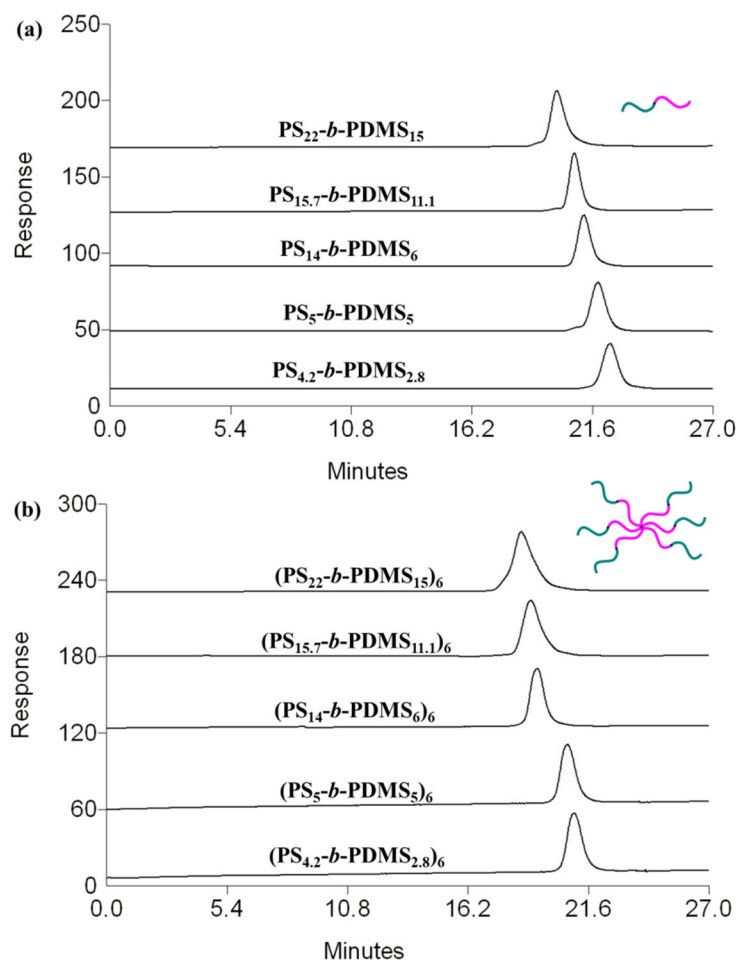


**Figure 6.32:** SEC chromatographs corresponding to (a) all diblock copolymer precursors used for the preparation of six arm star block copolymers and (b) all purified six arm star block copolymers. For clarification reasons the samples are named after the notations given in Table 6.6.

After the meticulous characterization through SEC and MO/VPO to determine the  $\bar{D}$  as well as  $\bar{M}_n$  values with high accuracy,  $^1\text{H-NMR}$  studies were conducted to calculate mass and eventually volume fractions. The identification of the characteristic chemical shifts assigned to specific proton atoms along the monomeric units of the two blocks was critical to determine the molecular composition by  $^1\text{H-NMR}$  measurements. It should be noted that, only the completely purified samples were submitted to these experiments to avoid any mistake on the calculation of the blocks' composition due to the presence of impurities. The chemical shifts ratio and consequently the mass and volume fractions between the diblock copolymer precursors and linear and non-linear stars remained identical for all sample. This behavior is attributed to the fact that every arm corresponds to a diblock copolymer linked to each coupling agent's chlorine group. The experimental coherency

confirmed the high uniformity degree of all synthesized materials. The chemical shifts of the six protons in the siloxane methyl groups at the monomeric unit of PDMS ( $\delta$ : 0.1-0.5 ppm, C-H<sub>3</sub>) and the five protons of the aromatic ring in the monomeric unit of PS ( $\delta$ : 6.3-7.2 ppm, Ar-H) are presented in Figures 6.33-6.36. Note that, the series of samples already given in the respective SEC chromatographs corresponding to the sets 9, 10, 11 and 13, are also involved in Figure 6.33 together with the integration values for consistency reasons.

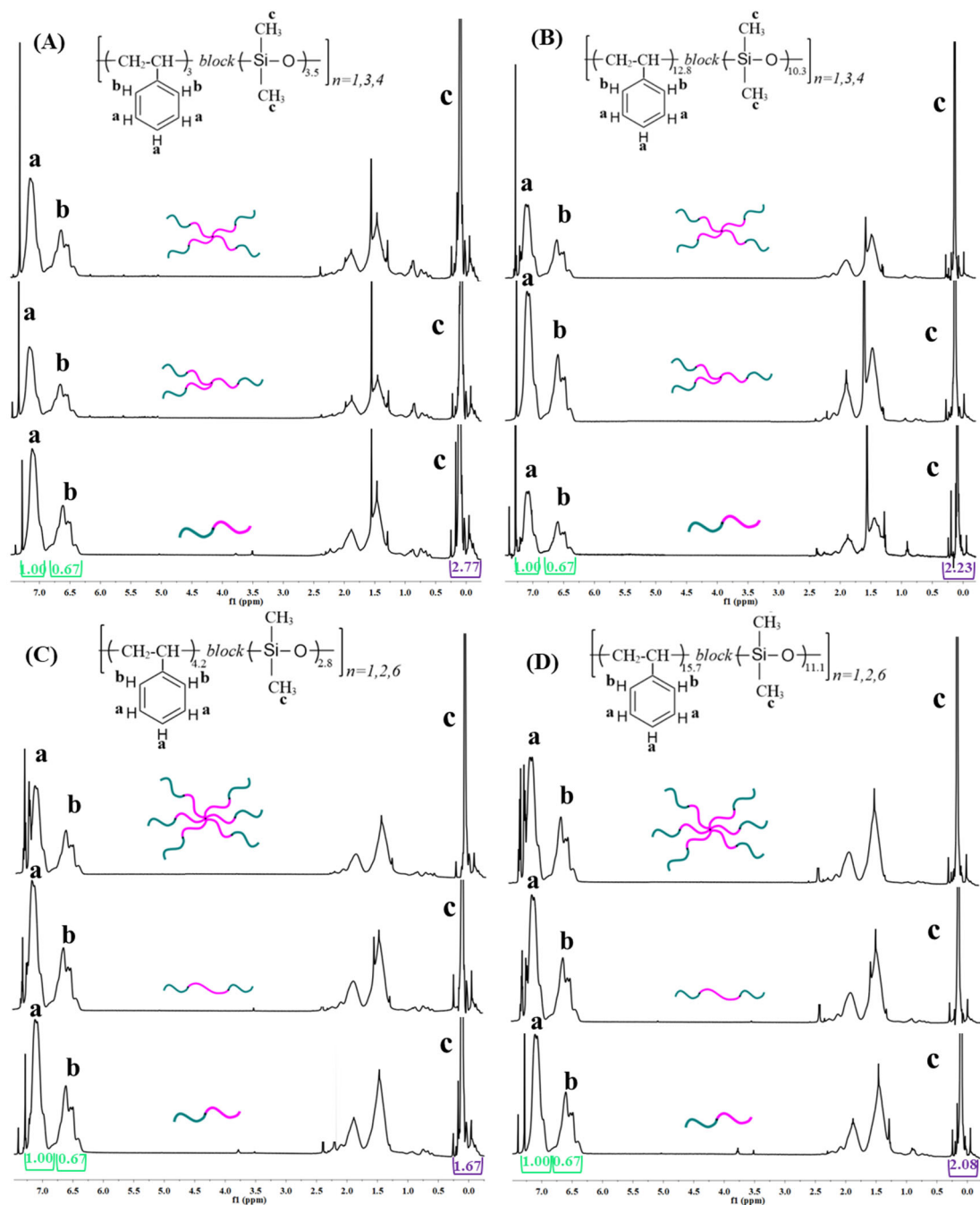


**Figure 6.33:** <sup>1</sup>H-NMR spectra corresponding to the: (A) (PS<sub>3</sub>-b-PDMS<sub>3.5</sub>)<sub>1,3,4</sub>, (B) (PS<sub>12.8</sub>-b-PDMS<sub>10.3</sub>)<sub>1,3,4</sub>, (C) (PS<sub>4.2</sub>-b-PDMS<sub>2.8</sub>)<sub>1,2,6</sub> and (D) (PS<sub>15.7</sub>-b-PDMS<sub>11.1</sub>)<sub>1,2,6</sub>.

In addition, the  $^1\text{H-NMR}$  spectra of set number 15 (Table 6.6) involving the synthesized copolymers with all various arm numbers  $[(\text{PS}_{14}\text{-}b\text{-PDMS}_6)_n]$  where  $n=1, 2, 3, 4, 6$ ] along with their integration values are given in Figure 6.34. It is straightforward that the complex architecture has not any impact on the mass fraction and therefore on the volume fraction ratios.

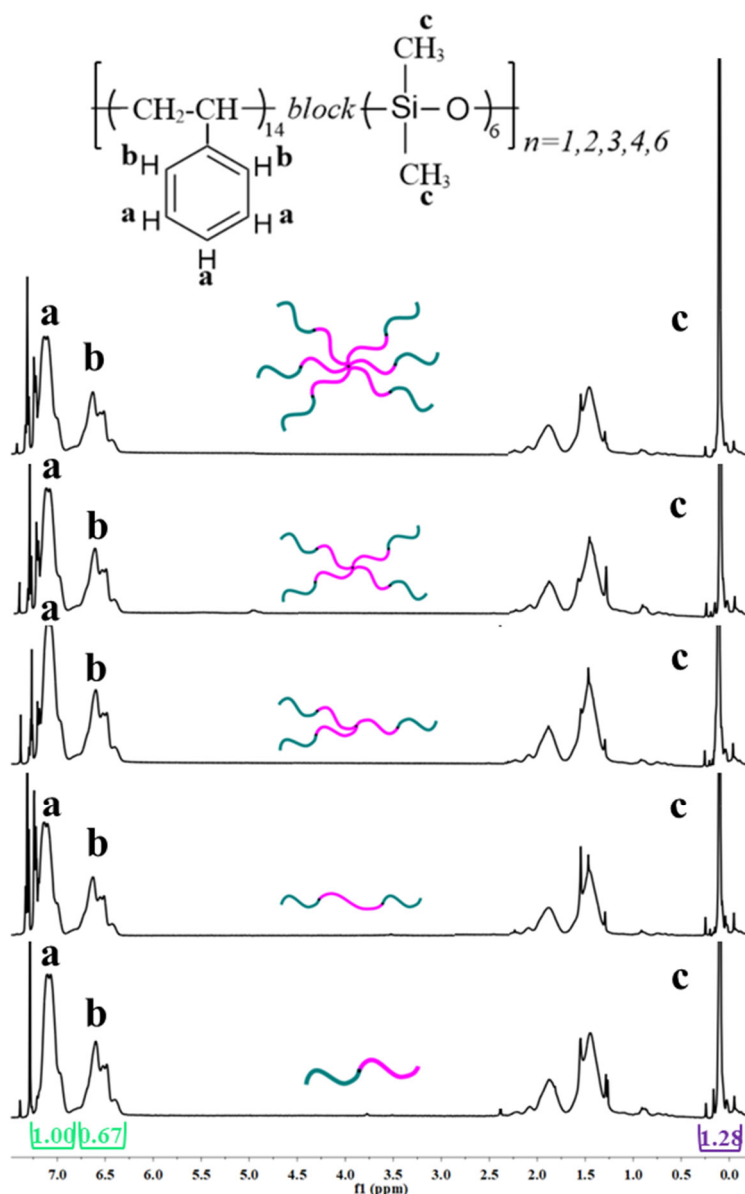


**Figure 6.34:**  $^1\text{H-NMR}$  spectra corresponding to set of  $(\text{PS}_{14}\text{-}b\text{-PDMS}_6)_{1,2,3,4,6}$ .

The remaining  $^1\text{H-NMR}$  spectra are given below (Figures 6.35 and 6.36) for clarification reasons and are divided in groups consisting of the diblock copolymer precursors together with their corresponding linear and non-linear star block copolymers as already presented in Table 6.x. The division in the relative set of samples has been carried out based on the synthetic protocol followed in each set.

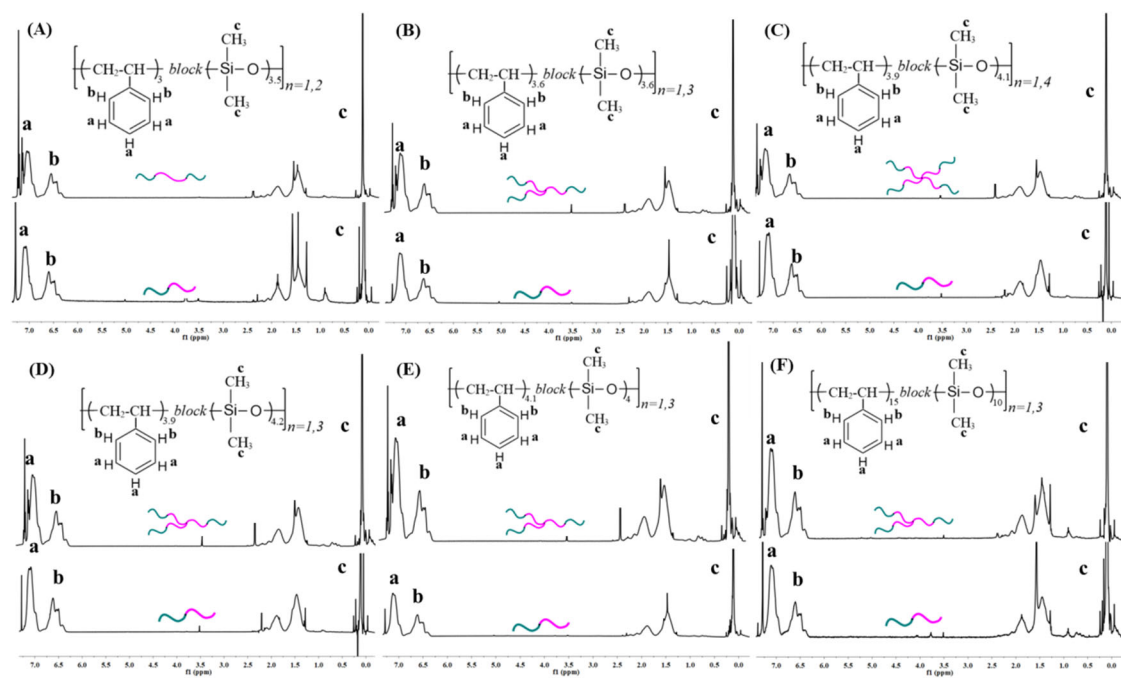


**Figure 6.35:**  $^1\text{H-NMR}$  spectra corresponding to the: (A)  $(\text{PS}_3\text{-}b\text{-PDMS}_{3.5})_{1,2}$ , (B)  $(\text{PS}_{3.6}\text{-}b\text{-PDMS}_{3.6})_{1,3}$ , (C)  $(\text{PS}_{3.9}\text{-}b\text{-PDMS}_{4.1})_{1,4}$ , (D)  $(\text{PS}_{3.9}\text{-}b\text{-PDMS}_{4.2})_{1,3}$ , (E)  $(\text{PS}_{4.1}\text{-}b\text{-PDMS}_4)_{1,3}$  and (F)  $(\text{PS}_{15}\text{-}b\text{-PDMS}_{10})_{1,3}$ .

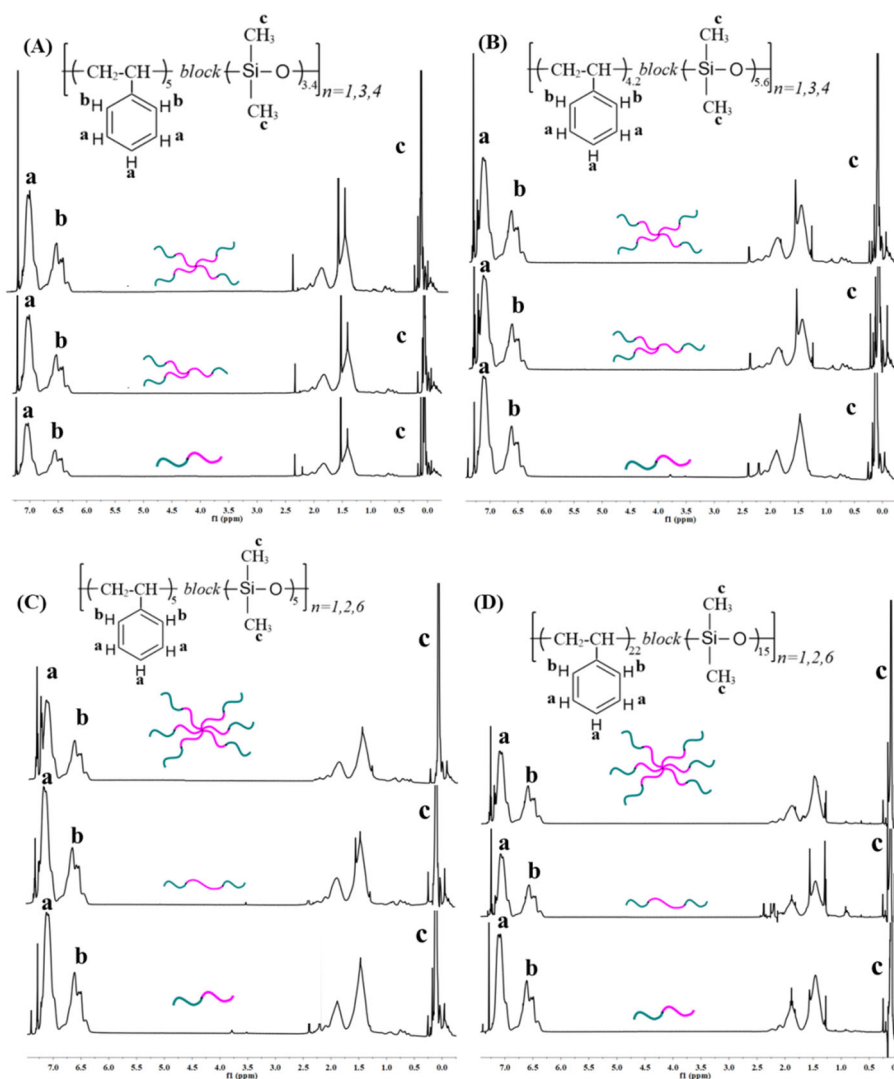
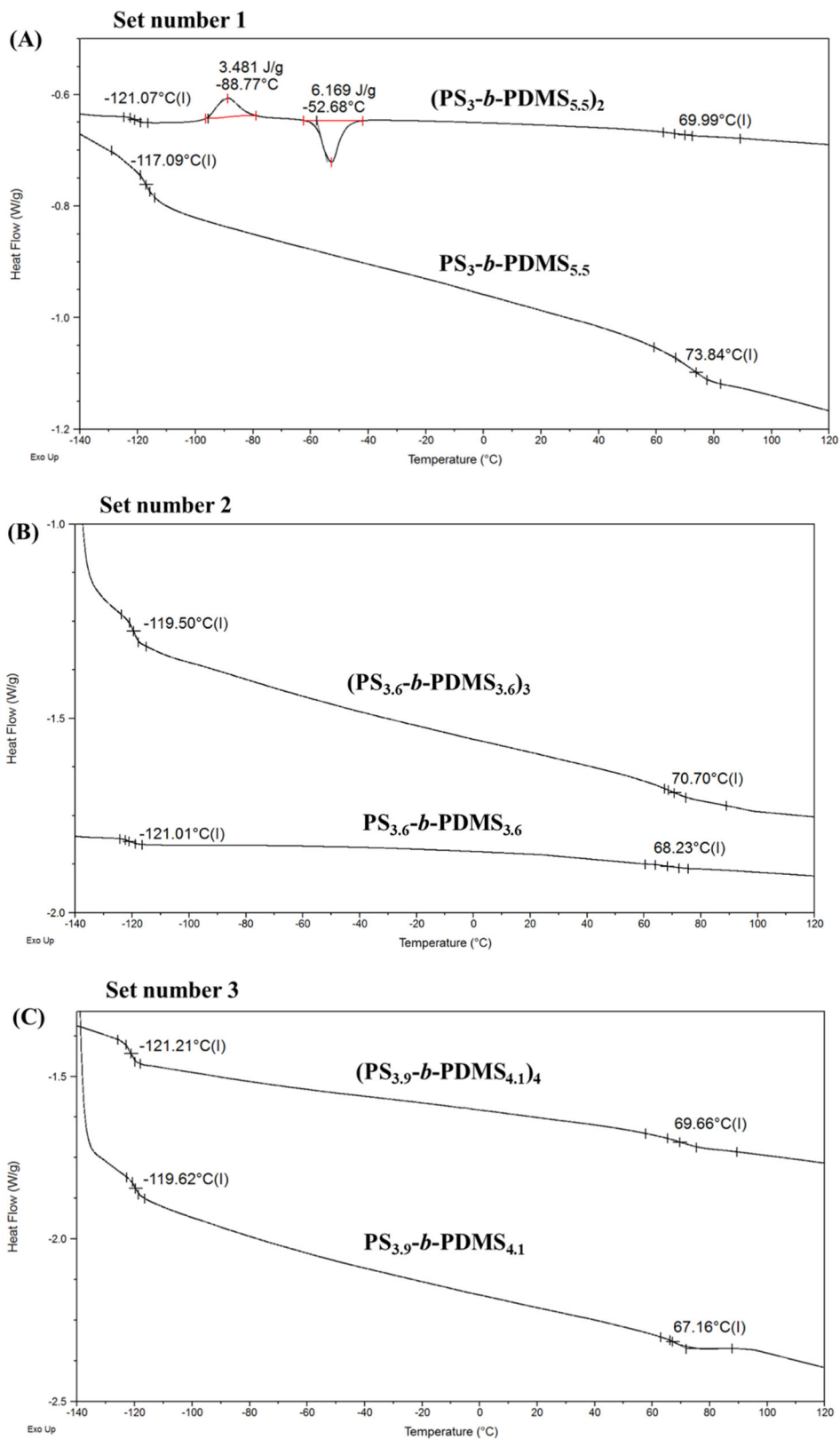


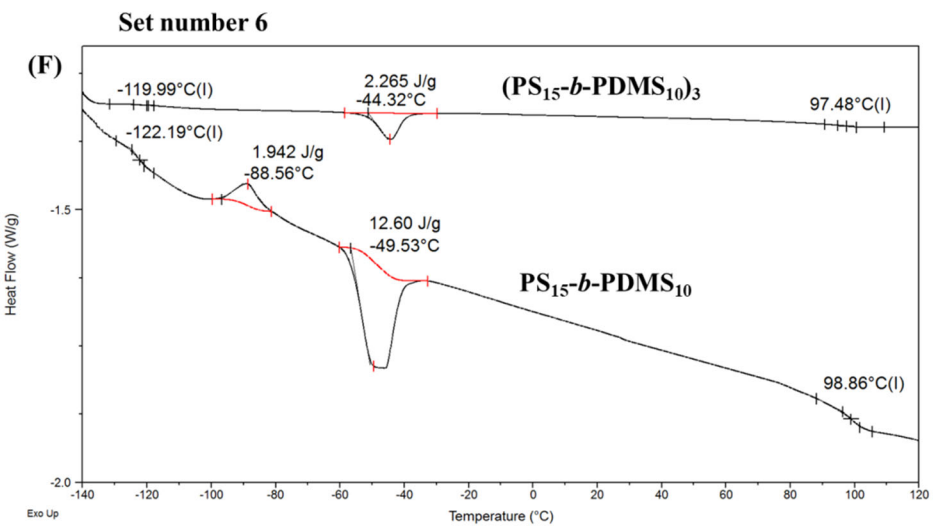
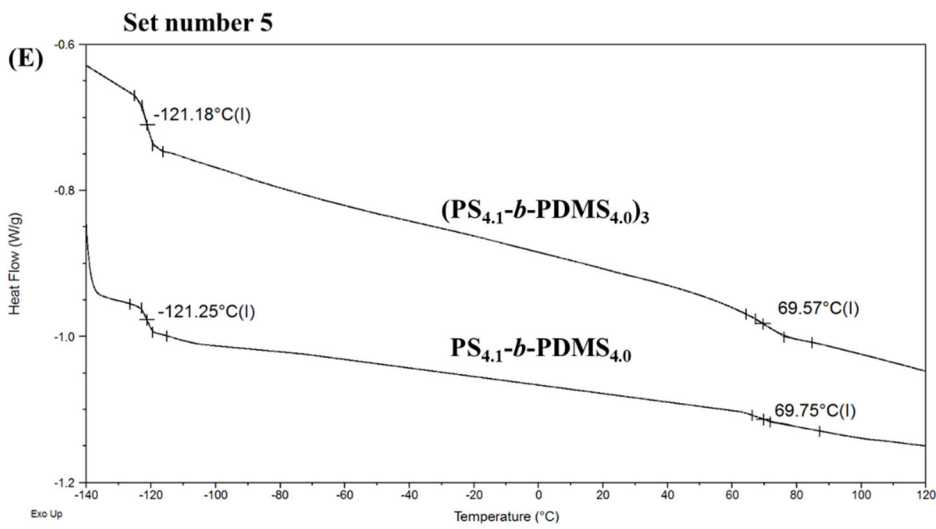
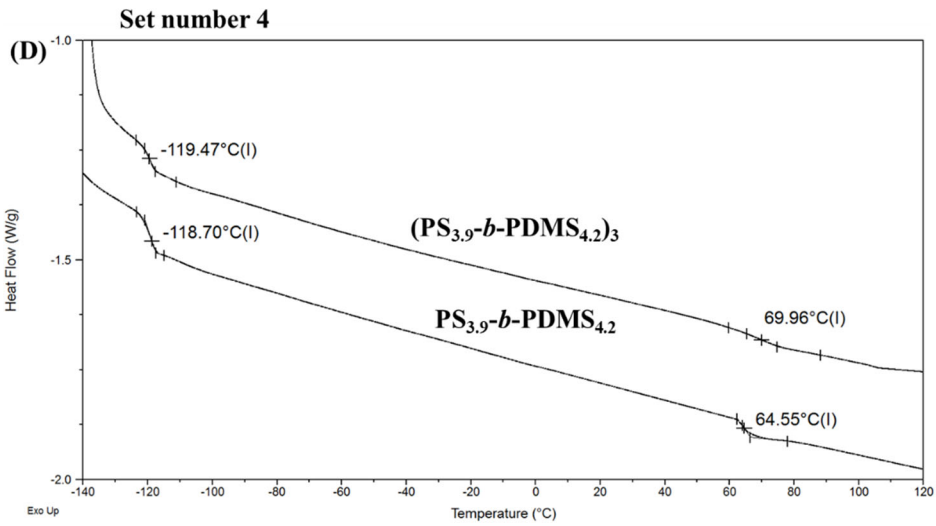
**Figure 6.36:**  $^1\text{H-NMR}$  spectra corresponding to the: (A)  $(\text{PS}_5\text{-}b\text{-PDMS}_{3.4})_{1,3,4}$ , (B)  $(\text{PS}_{4.2}\text{-}b\text{-PDMS}_{5.6})_{1,3,4}$ , (C)  $(\text{PS}_5\text{-}b\text{-PDMS}_5)_{1,2,6}$  and (D)  $(\text{PS}_{22}\text{-}b\text{-PDMS}_{15})_{1,2,6}$ .

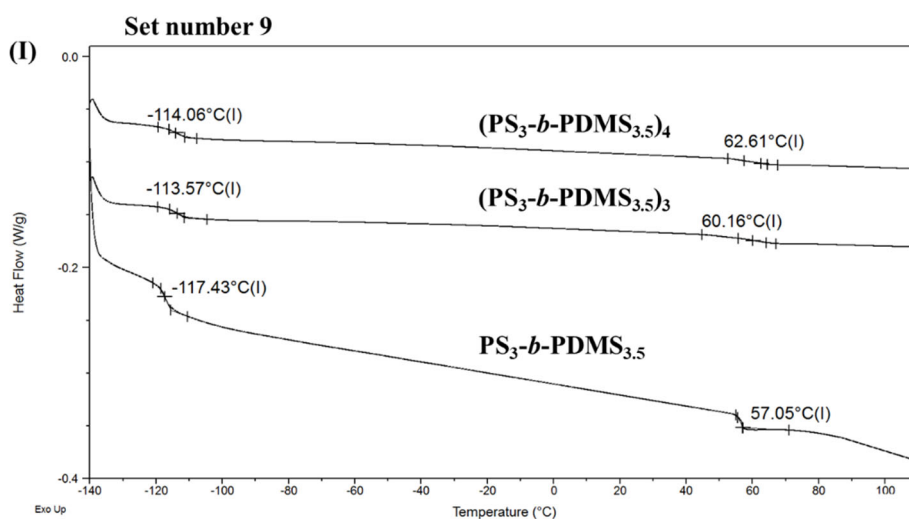
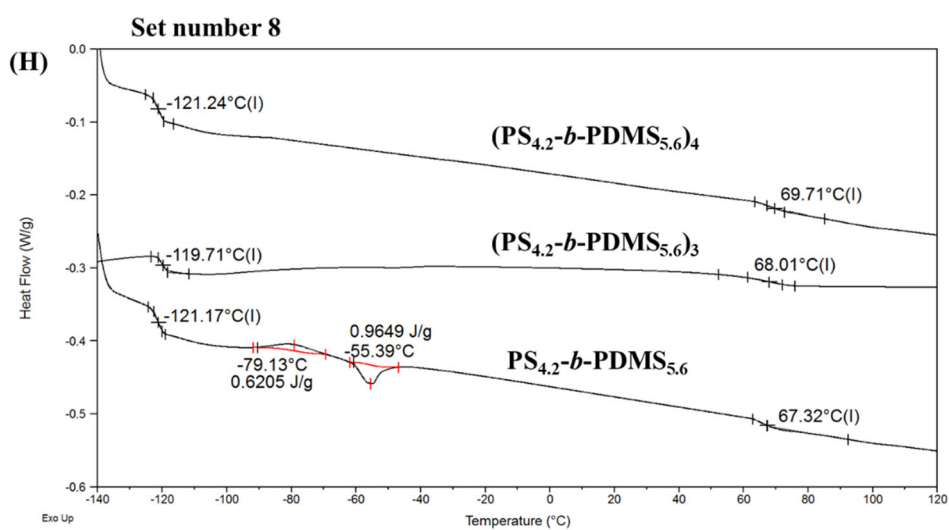
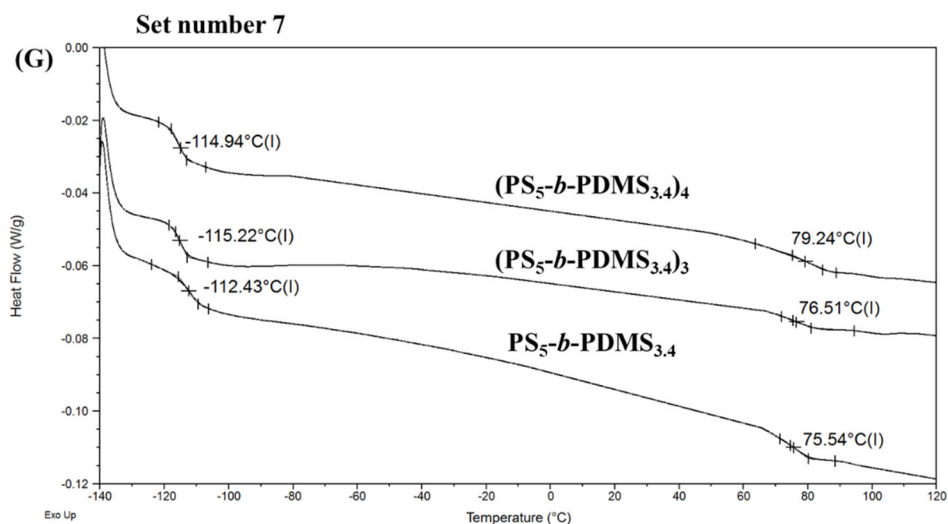
### 6.7 Thermal Characterization Results of Linear and Non-Linear $(\text{PS-}b\text{-PDMS})_n$ Block Copolymers (Where $n = 1$ or $2$ or $3$ or $4$ or $6$ )

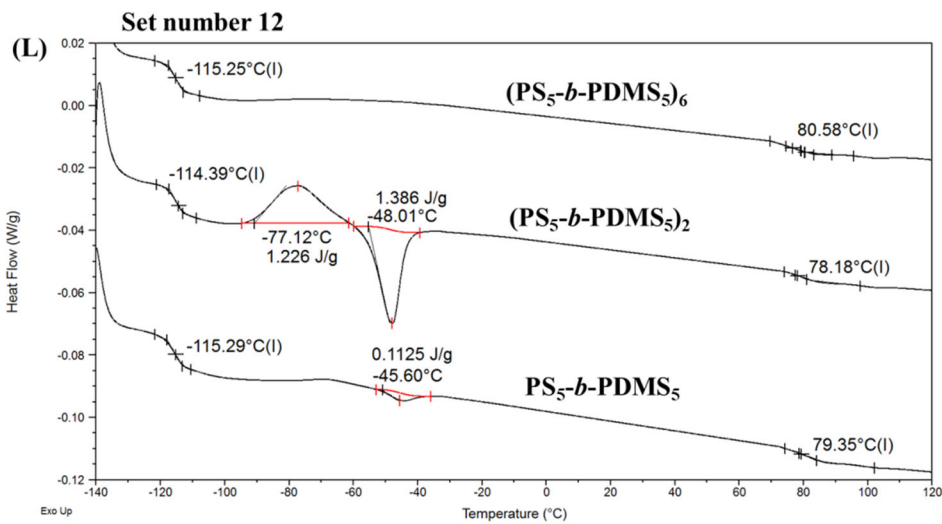
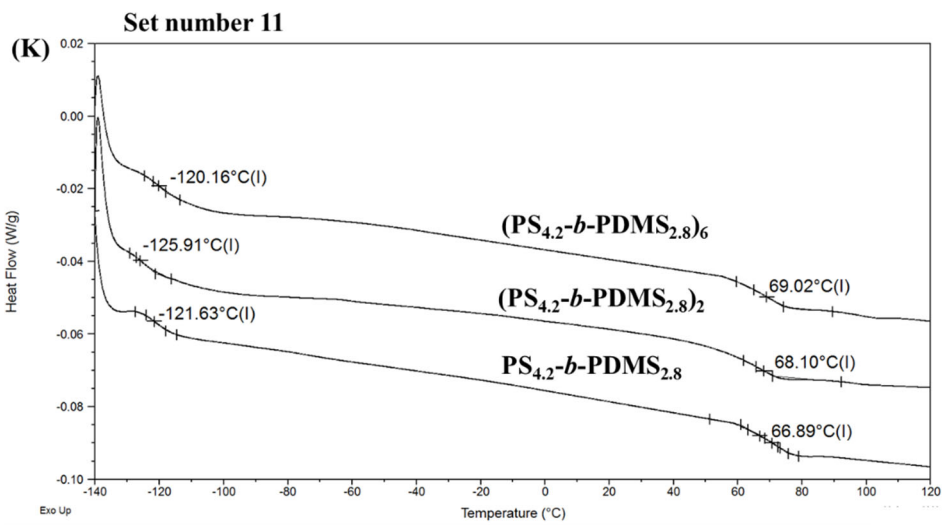
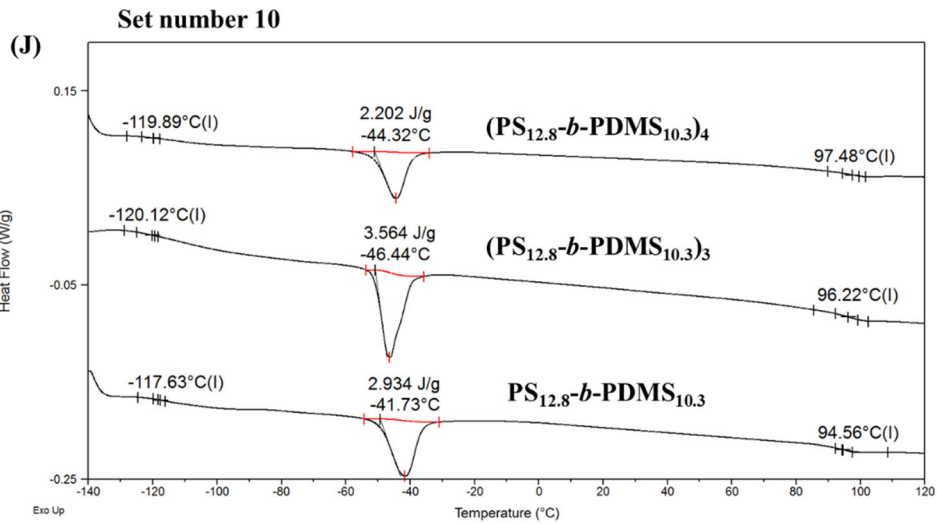
All synthesized materials were thermally characterized through DSC to determine the glass transition temperatures of both segments as well as any other transition evident in the semicrystalline (PDMS) block. The results are divided in groups consisting of the linear precursor along with the corresponding linear triblock and/or non-linear star block copolymers as notated in Table 6.6. In all cases the DSC experiments revealed the strong immiscibility between the components for the linear and non-linear architectures and their potential microphase separation during self-assembly studies. Also, in some cases additional transitions attributed to the crystallization and melting of the PDMS crystallites were evident. It should be noted

that, even if the architecture varies significantly the glass transition temperatures of both PS and PDMS segments have not experienced significant alternations when compared to those observed in their linear precursors. In Figures 6.37 A-O all DSC thermographs corresponding to the different set of samples are presented.









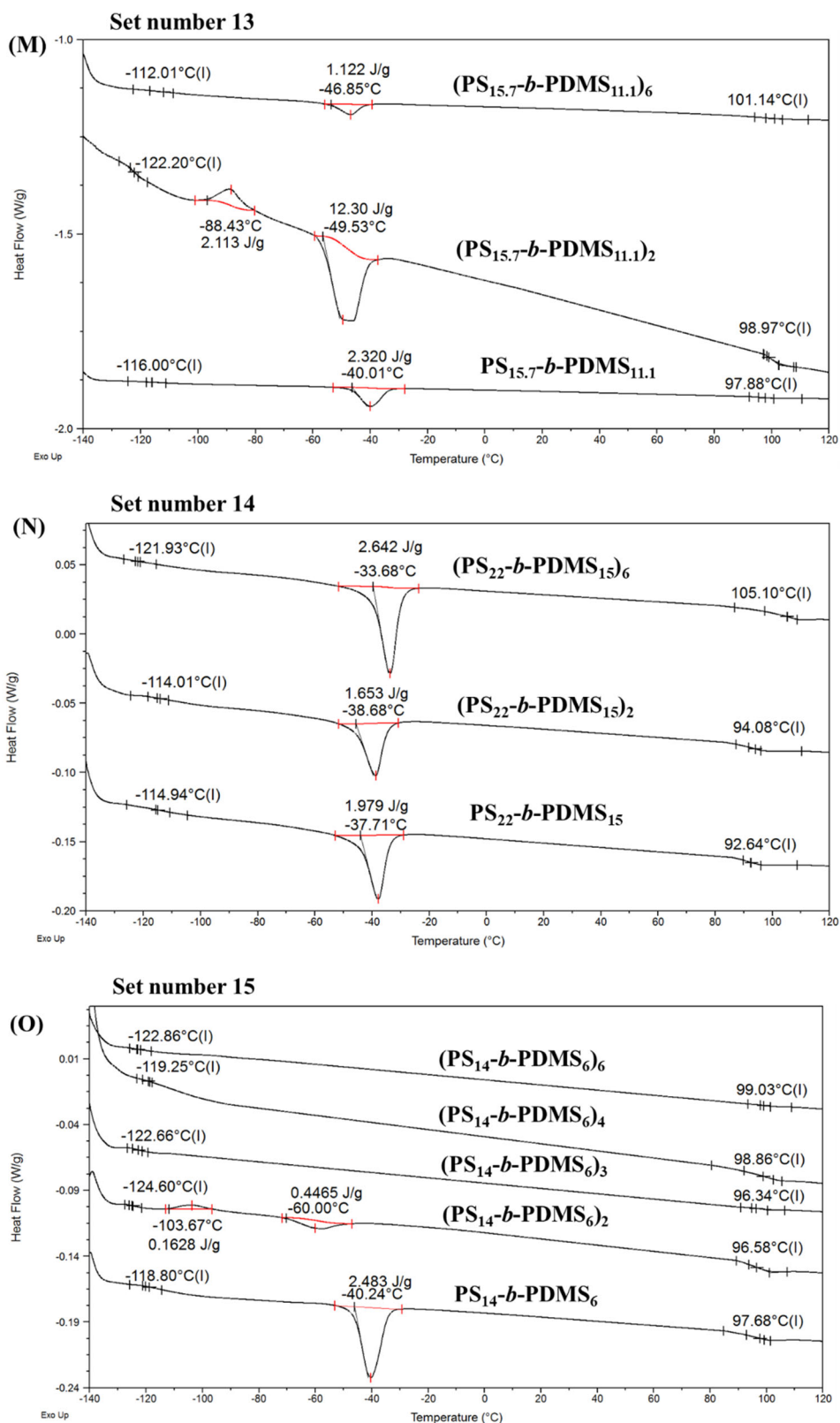


**Figure 6.37:** DSC thermographs corresponding to the: (A)  $(PS_3-b-PDMS_{3.5})_{1,2}$ , (B)  $(PS_{3.6}-b-PDMS_{3.6})_{1,3}$ , (C)  $(PS_{3.9}-b-PDMS_{4.1})_{1,4}$ , (D)  $(PS_{3.9}-b-PDMS_{4.2})_{1,3}$ , (E)  $(PS_{4.1}-b-PDMS_4)_{1,3}$ , (F)  $(PS_{15}-b-PDMS_{10})_{1,3}$ , (G)  $(PS_5-b-PDMS_{3.4})_{1,3,4}$ , (H)  $(PS_{4.2}-b-PDMS_{5.6})_{1,3,4}$ , (I)  $(PS_3-b-PDMS_{3.5})_{1,3,4}$ , (J)  $(PS_{12.8}-b-PDMS_{10.3})_{1,3,4}$ , (K)  $(PS_{4.2}-b-PDMS_{2.8})_{1,2,6}$ , (L)  $(PS_5-b-PDMS_5)_{1,2,6}$ , (M)  $(PS_{15.7}-b-PDMS_{11.1})_{1,2,6}$ , (N)  $(PS_{22}-b-PDMS_{15})_{1,2,6}$  and (O)  $(PS_{14}-b-PDMS_6)_{1,2,3,4,6}$ .

A concise description of the observed transitions in each set of samples is provided below.

### **Set Number 1-6**

The DSC experiments for the first five sets of samples revealed two distinct  $T_g$ s with values similar to the corresponding homopolymers. The  $T_g$  values of the linear triblock copolymers and the non-linear three- and four- arm star block copolymers are not altered significantly despite the more complex architecture and the increased molecular weight of the individual blocks. The  $T_g$  of the PS segments ranged from approximately 69 to 73 °C (due to the low average molecular weight of the block), while for the PDMS varied from -117 to -121 °C.

In the  $(PS_3-b-PDMS_{5.5})_2$  two additional transitions, attributed to the melting and cold crystallization temperature of the PDMS, were observed. In the remaining sequences, the absence of  $T_m$  can be possibly attributed to the low molecular weight of the segments and therefore the PDMS is considered amorphous.

The  $T_g$ s of the PS block in the linear  $PS_{15}-b-PDMS_{10}$  precursor and the corresponding  $(PS_{15}-b-PDMS_{10})_3$  (set number 6) appeared at approximately 98 °C due to the increased average molecular weight of the segment compared to the previous set of samples, while for the PDMS blocks at approximately -120 °C. In both samples a melting temperature was evident, while the cold crystallization of the PDMS crystallites took place only in the linear precursor. The values of all observed transitions are summarized in Table 6.7.

### **Set Number 7-10**

These set of samples involve the non-linear (three- and four- arm star) copolymers with their corresponding linear copolymer precursors. The experiments took place to observe any differences on the thermal transitions due to the complexity of the systems.

The two separate glass transition temperatures at values similar to the corresponding homopolymers for the  $(PS_5-b-PDMS_{3.4})_{1,3,4}$  sequences indicated the immiscibility between the two segments. Furthermore, in this series of samples the  $T_g$ s of the segments did not alter substantially as the architecture varies similar to the previous cases. The absence of any other thermal transitions suggested that the anionically synthesized linear and non-linear copolymers are 100% atactic.

Two distinct  $T_g$ s were also evident in the  $(PS_{4.2}-b-PDMS_{5.6})_{1,3,4}$  sequences indicating the potential microphase separation during self-assembly studies. The glass

transition temperature of the PS in all different architecture copolymers was observed at values less than 70 °C due to the low average molecular weight of the segment, while for the PDMS at  $\sim -121$  °C. For the PS<sub>4.2</sub>-*b*-PDMS<sub>5.6</sub> two additional transitions ( $T_c$  as well as  $T_m$  at -79.13 and -55.39 respectively) were observed.

The lower  $T_g$  values for the PS segments were observed in the (PS<sub>3</sub>-*b*-PDMS<sub>3.5</sub>)<sub>1,3,4</sub> sequences, as expected due to the very low molecular characteristics of the systems. The PDMS segments showcase the  $T_g$  values in the region of -113 to -117 °C while no other thermal transition was evident. The appearance of two separate glass transitions even for low  $\bar{M}_n^{total}$  values is justified by the high segregation strength between the segments.

Higher glass transition temperatures for the PS (from 94 to 97 °C) were demonstrated in the (PS<sub>12.8</sub>-*b*-PDMS<sub>10.3</sub>)<sub>1,3,4</sub> sequences due to the increased molecular weight of the segments. For the PDMS segments two different transitions corresponding to the  $T_g$  and  $T_m$  were observed for the linear and non-linear copolymers.

The relative values as directly calculated by the DSC measurements regarding these sets of samples are presented in Table 6.7.

#### **Set Number 11-14**

The results concerning the linear diblock copolymers and the corresponding triblock and six arm star block copolymers are analyzed as follows:

In the (PS<sub>4.2</sub>-*b*-PDMS<sub>2.8</sub>)<sub>1,2,6</sub> sequences two separate glass transition temperatures were observed strongly suggesting the immiscibility of the components. The extremely low total average molecular weight of the PDMS segment did not allow the appearance of any other transition.

Coherent results regarding the glass transition temperatures of the PS and PDMS are demonstrated in the relative DSC thermographs of the (PS<sub>5</sub>-*b*-PDMS<sub>5</sub>)<sub>1,2,6</sub> copolymers. In the PS<sub>5</sub>-*b*-PDMS<sub>5</sub> an additional transition corresponding to the  $T_m$  of PDMS was evident, while for the (PS<sub>5</sub>-*b*-PDMS<sub>5</sub>)<sub>2</sub> both  $T_c$  and  $T_m$  was observed. In the six arm star no additional transitions were showcased.

In the (PS<sub>15.7</sub>-*b*-PDMS<sub>11.1</sub>)<sub>1,2,6</sub> samples two distinct  $T_g$ s at values similar to the respective homopolymers were observed. In addition the melting temperature regarding the PDMS block appeared in all copolymers involved in this set of samples, while a cold crystallization was evident only in the triblock copolymer.

Two separate  $T_g$  values and one transition corresponding to the melting temperature of PDMS were observed for the  $(PS_{22}-b-PDMS_{15})_{1,2,6}$  copolymers. In this set of samples a discrepancy between the  $T_g$  values of PS as the architecture varies is obvious. Specifically, the  $T_g$  of PS was 92 °C, 94 °C and 105 °C for the diblock, triblock and six-arm respectively. This fact may be attributed to the higher molecular weight in combination with the severe overcrowding effect in the six arm star block copolymer.

All the experimentally observed values with respect to the thermal transitions of these set of samples are presented in Table 6.7.

### **Set Number 15**

A direct comparison between the thermal transitions in all different architectures can be conducted for the  $(PS_{14}-b-PDMS_6)_{1,2,3,4,6}$  sequences. It is straightforward that for the given molecular characteristics the architecture had not any impact on the glass transition temperature of the PS which ranged between 96 to 99 °C. Correspondingly, the PDMS experienced the glass transition at temperatures ranging from -118 to -124 °C. Also, the melting of the PDMS crystallites was obtained only for the linear diblock as well as the triblock copolymers. An additional transition at -103 °C was observed for the  $(PS_{14}-b-PDMS_6)_2$  which is attributed to the cold crystallization.

It should be mentioned that, despite the similar thermal transitions between the components as the architecture varies, a significantly increased thermal stability is expected for the more complex copolymers as already reported in the literature.<sup>19</sup> The experimental coherency of the glass transition temperatures of the individual blocks as the architecture changes is probably attributed to the topology of the copolymers. Specifically, the triblock copolymer and the non-linear star block copolymers are comprised by several arms corresponding to the diblock copolymer precursor, joined to a central junction point. All arms have identical chemical composition and  $\bar{M}_n$  values which leads to very similar thermal transitions between the different architecture copolymers.

**Table 6.7:** Thermal characterization results of linear and non-linear copolymers.

Set	sample	$T_g^{PS}$ (°C)	$T_g^{PDMS}$ (°C)	$T_m^{PDMS}$ (°C)	enthalpy (J/g)	$T_c^{PDMS}$ (°C)
1	PS <sub>3</sub> - <i>b</i> -PDMS <sub>5.5</sub>	73.84	-117.09	-	-	-
	(PS <sub>3</sub> - <i>b</i> -PDMS <sub>5.5</sub> ) <sub>2</sub>	69.99	-121.07	-52.68	6.169	-88.77
2	PS <sub>3.6</sub> - <i>b</i> -PDMS <sub>3.6</sub>	68.23	-121.01	-	-	-
	(PS <sub>3.6</sub> - <i>b</i> -PDMS <sub>3.6</sub> ) <sub>3</sub>	70.70	-119.50	-	-	-
3	PS <sub>3.9</sub> - <i>b</i> -PDMS <sub>4.1</sub>	67.16	-119.62	-	-	-
	(PS <sub>3.9</sub> - <i>b</i> -PDMS <sub>4.1</sub> ) <sub>4</sub>	69.66	-121.21	-	-	-
4	PS <sub>3.9</sub> - <i>b</i> -PDMS <sub>4.2</sub>	64.55	-118.70	-	-	-
	(PS <sub>3.9</sub> - <i>b</i> -PDMS <sub>4.2</sub> ) <sub>3</sub>	69.96	-119.47	-	-	-
5	PS <sub>4.1</sub> - <i>b</i> -PDMS <sub>4.0</sub>	69.75	-121.25	-	-	-
	(PS <sub>4.1</sub> - <i>b</i> -PDMS <sub>4.0</sub> ) <sub>3</sub>	69.57	-121.18	-	-	-
6	PS <sub>15</sub> - <i>b</i> -PDMS <sub>10</sub>	98.86	-122.19	-49.53	12.60	-88.56
	(PS <sub>15</sub> - <i>b</i> -PDMS <sub>10</sub> ) <sub>3</sub>	97.48	-119.99	-44.32	2.265	-
7	PS <sub>5</sub> - <i>b</i> -PDMS <sub>3.4</sub>	75.54	-112.43	-	-	-
	(PS <sub>5</sub> - <i>b</i> -PDMS <sub>3.4</sub> ) <sub>3</sub>	76.51	-115.22	-	-	-
	(PS <sub>5</sub> - <i>b</i> -PDMS <sub>3.4</sub> ) <sub>4</sub>	79.24	-114.94	-	-	-
8	PS <sub>4.2</sub> - <i>b</i> -PDMS <sub>5.6</sub>	67.32	-121.17	-55.39	0.965	-79.13
	(PS <sub>4.2</sub> - <i>b</i> -PDMS <sub>5.6</sub> ) <sub>3</sub>	68.01	-119.71	-	-	-
	(PS <sub>4.2</sub> - <i>b</i> -PDMS <sub>5.6</sub> ) <sub>4</sub>	69.71	-121.24	-	-	-
9	PS <sub>3</sub> - <i>b</i> -PDMS <sub>3.5</sub>	57.05	-117.43	-	-	-
	(PS <sub>3</sub> - <i>b</i> -PDMS <sub>3.5</sub> ) <sub>3</sub>	60.16	-113.57	-	-	-
	(PS <sub>3</sub> - <i>b</i> -PDMS <sub>3.5</sub> ) <sub>4</sub>	62.61	-114.06	-	-	-
10	PS <sub>12.8</sub> - <i>b</i> -PDMS <sub>10.3</sub>	94.56	-117.63	-41.73	2.934	-
	(PS <sub>12.8</sub> - <i>b</i> -PDMS <sub>10.3</sub> ) <sub>3</sub>	96.22	-120.12	-46.44	3.564	-
	(PS <sub>12.8</sub> - <i>b</i> -PDMS <sub>10.3</sub> ) <sub>4</sub>	97.48	-119.89	-44.32	2.202	-
11	PS <sub>4.2</sub> - <i>b</i> -PDMS <sub>2.8</sub>	66.89	-121.63	-	-	-
	(PS <sub>4.2</sub> - <i>b</i> -PDMS <sub>2.8</sub> ) <sub>2</sub>	68.10	-125.91	-	-	-
	(PS <sub>4.2</sub> - <i>b</i> -PDMS <sub>2.8</sub> ) <sub>6</sub>	69.02	-120.16	-	-	-
12	PS <sub>5</sub> - <i>b</i> -PDMS <sub>5</sub>	79.35	-115.29	-45.60	0.113	-
	(PS <sub>5</sub> - <i>b</i> -PDMS <sub>5</sub> ) <sub>2</sub>	78.18	-114.39	-48.01	1.386	-77.12
	(PS <sub>5</sub> - <i>b</i> -PDMS <sub>5</sub> ) <sub>6</sub>	80.58	-115.25	-	-	-
13	PS <sub>15.7</sub> - <i>b</i> -PDMS <sub>11.1</sub>	97.88	-116.00	-40.01	2.320	-
	(PS <sub>15.7</sub> - <i>b</i> -PDMS <sub>11.1</sub> ) <sub>2</sub>	98.97	-122.20	-49.53	12.30	-88.43
	(PS <sub>15.7</sub> - <i>b</i> -PDMS <sub>11.1</sub> ) <sub>6</sub>	101.14	-121.01	-46.85	1.122	-
14	PS <sub>22</sub> - <i>b</i> -PDMS <sub>15</sub>	92.64	-114.94	-37.71	1.979	-
	(PS <sub>22</sub> - <i>b</i> -PDMS <sub>15</sub> ) <sub>2</sub>	94.08	-114.01	-38.68	1.653	-
	(PS <sub>22</sub> - <i>b</i> -PDMS <sub>15</sub> ) <sub>6</sub>	105.10	-121.93	-33.68	2.642	-
15	PS <sub>14</sub> - <i>b</i> -PDMS <sub>6</sub>	97.68	-118.80	-40.24	2.483	-
	(PS <sub>14</sub> - <i>b</i> -PDMS <sub>6</sub> ) <sub>2</sub>	96.58	-124.60	-60.00	0.447	-103.67
	(PS <sub>14</sub> - <i>b</i> -PDMS <sub>6</sub> ) <sub>3</sub>	96.34	-122.66	-	-	-
	(PS <sub>14</sub> - <i>b</i> -PDMS <sub>6</sub> ) <sub>4</sub>	98.86	-119.25	-	-	-
	(PS <sub>14</sub> - <i>b</i> -PDMS <sub>6</sub> ) <sub>6</sub>	99.03	-122.86	-	-	-

## **6.8 Morphological Characterization Results of Linear and Non-Linear (PS-*b*-PDMS)<sub>*n*</sub> Block Copolymers (Where *n* = 1 or 2 or 3 or 4 or 6)**

The morphological characterization results of the synthesized materials will be presented in separate groups which will involve each linear diblock precursor together with its corresponding linear triblock and/or non-linear star block copolymer to compare the structure/properties relationship as the architecture varies. The linear triblock and non-linear star block copolymers showcase equal volume fraction to the diblock precursors and also the total number average molecular weight values are equal to those of the diblock precursors multiplied with the respective functionality (2-fold, 3-fold, 4-fold and 6-fold respectively). Notably, for the triblock and non-linear star block copolymers the domain spacing values remain almost similar to that obtained for the respective diblock precursor and the increased total degree of polymerization gives rise to low-dimensional well-defined morphologies. This fact is evident in Table 6.8 where the total number average molecular weight values, PDMS volume fraction, total degree of polymerization and  $\chi N$  product (at 25°C) for each sample are summarized.

**Table 6.8:** Molecular characteristics, PDMS volume fractions, total degree of polymerization and  $\chi N$  product for all linear and non-linear copolymers.

Set	sample	$\bar{M}_n^{total(a)}$ (g/mol) VPO/MO	$\varphi_{PDMS}^{(b)}$	$N^{total(c)}$	$\chi N^{(d)}$ (25 °C)	$\chi N^{(d)}$ (100 °C)
1	PS <sub>3</sub> - <i>b</i> -PDMS <sub>5.5</sub>	8,000	0.59	94	24	13
	(PS <sub>3</sub> - <i>b</i> -PDMS <sub>5.5</sub> ) <sub>2</sub>	16,000	0.59	188	49	26
2	PS <sub>3.6</sub> - <i>b</i> -PDMS <sub>3.6</sub>	7,200	0.50	82	21	11
	(PS <sub>3.6</sub> - <i>b</i> -PDMS <sub>3.6</sub> ) <sub>3</sub>	21,600	0.50	246	64	34
3	PS <sub>3.9</sub> - <i>b</i> -PDMS <sub>4.1</sub>	8,000	0.52	93	24	13
	(PS <sub>3.9</sub> - <i>b</i> -PDMS <sub>4.1</sub> ) <sub>4</sub>	32,000	0.52	372	71	52
4	PS <sub>3.9</sub> - <i>b</i> -PDMS <sub>4.2</sub>	8,100	0.55	94	24	13
	(PS <sub>3.9</sub> - <i>b</i> -PDMS <sub>4.2</sub> ) <sub>3</sub>	24,300	0.55	282	73	39
5	PS <sub>4.1</sub> - <i>b</i> -PDMS <sub>4.0</sub>	8,100	0.53	93	24	13
	(PS <sub>4.1</sub> - <i>b</i> -PDMS <sub>4.0</sub> ) <sub>3</sub>	24,300	0.53	280	73	39
6	PS <sub>15</sub> - <i>b</i> -PDMS <sub>10</sub>	25,000	0.39	279	72	39
	(PS <sub>15</sub> - <i>b</i> -PDMS <sub>10</sub> ) <sub>3</sub>	75,000	0.39	837	218	117
7	PS <sub>5</sub> - <i>b</i> -PDMS <sub>3.4</sub>	8,400	0.40	94	24	13
	(PS <sub>5</sub> - <i>b</i> -PDMS <sub>3.4</sub> ) <sub>3</sub>	25,200	0.40	282	73	39
	(PS <sub>5</sub> - <i>b</i> -PDMS <sub>3.4</sub> ) <sub>4</sub>	33,600	0.40	376	97	53
8	PS <sub>4.2</sub> - <i>b</i> -PDMS <sub>5.6</sub>	9,800	0.60	115	30	16
	(PS <sub>4.2</sub> - <i>b</i> -PDMS <sub>5.6</sub> ) <sub>3</sub>	29,400	0.60	345	90	48
	(PS <sub>4.2</sub> - <i>b</i> -PDMS <sub>5.6</sub> ) <sub>4</sub>	39,200	0.60	460	120	64
9	PS <sub>3</sub> - <i>b</i> -PDMS <sub>3.5</sub>	6,500	0.53	75	20	10.5
	(PS <sub>3</sub> - <i>b</i> -PDMS <sub>3.5</sub> ) <sub>3</sub>	19,500	0.53	225	59	31.5
	(PS <sub>3</sub> - <i>b</i> -PDMS <sub>3.5</sub> ) <sub>4</sub>	26,000	0.53	300	78	42
10	PS <sub>12.8</sub> - <i>b</i> -PDMS <sub>10.3</sub>	23,100	0.47	262	68	37
	(PS <sub>12.8</sub> - <i>b</i> -PDMS <sub>10.3</sub> ) <sub>3</sub>	69,300	0.47	786	204	110
	(PS <sub>12.8</sub> - <i>b</i> -PDMS <sub>10.3</sub> ) <sub>4</sub>	92,400	0.47	1048	272	147
11	PS <sub>4.2</sub> - <i>b</i> -PDMS <sub>2.8</sub>	7,200	0.40	78	20	11
	(PS <sub>4.2</sub> - <i>b</i> -PDMS <sub>2.8</sub> ) <sub>2</sub>	14,400	0.40	156	41	22
	(PS <sub>4.2</sub> - <i>b</i> -PDMS <sub>2.8</sub> ) <sub>6</sub>	44,400	0.40	468	121	66
12	PS <sub>5</sub> - <i>b</i> -PDMS <sub>5</sub>	10,000	0.50	142	37	20
	(PS <sub>5</sub> - <i>b</i> -PDMS <sub>5</sub> ) <sub>2</sub>	20,000	0.50	284	74	40
	(PS <sub>5</sub> - <i>b</i> -PDMS <sub>5</sub> ) <sub>6</sub>	60,000	0.50	852	221	120
13	PS <sub>15.7</sub> - <i>b</i> -PDMS <sub>11.1</sub>	26,800	0.44	300	78	42
	(PS <sub>15.7</sub> - <i>b</i> -PDMS <sub>11.1</sub> ) <sub>2</sub>	53,600	0.44	600	156	84
	(PS <sub>15.7</sub> - <i>b</i> -PDMS <sub>11.1</sub> ) <sub>6</sub>	160,800	0.44	1800	468	252
14	PS <sub>22</sub> - <i>b</i> -PDMS <sub>15</sub>	37,000	0.47	413	107	58
	(PS <sub>22</sub> - <i>b</i> -PDMS <sub>15</sub> ) <sub>2</sub>	74,000	0.47	826	214	116
	(PS <sub>22</sub> - <i>b</i> -PDMS <sub>15</sub> ) <sub>6</sub>	222,000	0.47	2478	644	347
15	PS <sub>14</sub> - <i>b</i> -PDMS <sub>6</sub>	20,400	0.34	215	65	30
	(PS <sub>14</sub> - <i>b</i> -PDMS <sub>6</sub> ) <sub>2</sub>	40,800	0.34	430	112	60
	(PS <sub>14</sub> - <i>b</i> -PDMS <sub>6</sub> ) <sub>3</sub>	61,200	0.34	645	167	90
	(PS <sub>14</sub> - <i>b</i> -PDMS <sub>6</sub> ) <sub>4</sub>	81,600	0.34	860	223	120
	(PS <sub>14</sub> - <i>b</i> -PDMS <sub>6</sub> ) <sub>6</sub>	122,400	0.34	1290	335	180

<sup>(a)</sup>MO in toluene at 35 °C, <sup>(b)</sup>From <sup>1</sup>H-NMR measurements in CDCl<sub>3</sub> at 25 °C, <sup>(c)</sup>From equation 6.6, <sup>(d)</sup>From equation 6.5 and  $\chi=0.26$  at 25 °C and 0.14 at 100 °C ( $\chi=68.0T^{-1} - 0.037$ ).

## **Morphological Characterization for Set Number 1-5**

The first five set of samples to be discussed, consist of low molecular weight diblock precursors ( $<8,000$  g/mol) and their corresponding triblock, 3- and 4- arm star block copolymers have been synthesized not only to study their self-assembled structures but also to perform measurements with respect to the order-disorder transition. The chemical immiscibility provided by PS and PDMS segments allows the microphase separation even for low  $N$  values. All samples were designed to demonstrate similar number average molecular weights for the diblock arms and the composition values  $\phi_{\text{PDMS}}$  varied from 0.50 up to 0.59. All nearly symmetric copolymers were casted using cyclohexane as a neutral solvent to avoid any kinetically trapped morphology and to obtain alternating lamellae domains in each case. In addition, the results presented below correspond to the thermally annealed samples for 1 day at  $100^\circ\text{C}$ .

The scattering results for the  $\text{PS}_{3.6}\text{-}b\text{-}\text{PDMS}_{5.5}$  and its corresponding  $(\text{PS}_{3.6}\text{-}b\text{-}\text{PDMS}_{5.5})_2$  triblock copolymer (set number 1) confirmed the formation of a lamellar structure. A Gaussian first-order peak and two less obvious additional peaks at a  $q/q^*$  ratio of 1:2:3 (Figure 6.38 A red line) were evident for the linear precursor. The respective triblock copolymer showcased four distinct peaks at a ratio of 1:2:3:4 (Figure 6.38 A black line), indicating an enhanced ordering degree of the lamellae. A domain periodicity of 15 nm was calculated for both copolymers.

The second set of samples (set number 2) involving the  $\text{PS}_{3.6}\text{-}b\text{-}\text{PDMS}_{3.6}$  precursor and the  $(\text{PS}_{3.6}\text{-}b\text{-}\text{PDMS}_{3.6})_3$  three arm star was also studied with SAXS experiments. In both samples the lamellar structure was confirmed through the characteristic reflection peaks at the relative  $q$  values of 1:3 (Figure 6.38 B). The fact that the second-order peak is quite weak or absent can be justified by the nearly symmetric molecular characteristics of the blocks and therefore the symmetric composition as verified by  $^1\text{H-NMR}$  measurements. The structure factor of the compositionally symmetric lamellar-forming copolymers equals to zero and through the equation  $[\sin(n\phi\pi)/n]^2$  it is evident that when  $\phi$  (volume fraction) = 0.5 the complete absence of all odd numbered reflections ( $2^{\text{nd}}$ ,  $4^{\text{th}}$ , etc.) is expected. The  $d$ -spacing was calculated through the primary peak equal to 13.5 nm for the precursor and 14 nm for the complex architecture copolymer.

Coherent results were obtained in the case of the  $\text{PS}_{3.9}\text{-}b\text{-PDMS}_{4.1}$  and its four arm star block copolymer of the  $(\text{PS}_{3.9}\text{-}b\text{-PDMS}_{4.1})_4$  type (set number 3). The formation of the lamellae structure in both cases was evidenced by characteristic reflections at the relative  $q$  values of 1:-:3 suggesting compositionally symmetric copolymers (due to lack of the odd numbered reflections) with domain periodicity equal to 13.7 nm (precursor) and 14.2 nm (4-arm star block copolymer) respectively (Figure 6.48 C).

The fourth and fifth series of samples (set number 4 and 5) including the  $\text{PS}_{3.9}\text{-}b\text{-PDMS}_{4.2}$  and  $(\text{PS}_{3.9}\text{-}b\text{-PDMS}_{4.2})_3$  (set number 4) as well as the  $\text{PS}_{4.1}\text{-}b\text{-PDMS}_{4.0}$  and  $(\text{PS}_{4.1}\text{-}b\text{-PDMS}_{4.0})_3$  (set number 5) are illustrated in Figure 6.38 D and E respectively. The 1D SAXS plots verified the formation of a well-developed lamellar structure in the case of  $(\text{PS}_{3.9}\text{-}b\text{-PDMS}_{4.2})_3$  since four distinct scattering peaks at the relative  $q$  values of 1:2:3:4 can be observed. The linear precursor demonstrated reflections at the relative  $q$  values of 1:-:3. The domain periodicity in both cases was calculated equal to 13.5 nm. A periodicity of 13.0 nm was estimated for the  $\text{PS}_{4.1}\text{-}b\text{-PDMS}_{4.0}$  and the corresponding  $(\text{PS}_{4.1}\text{-}b\text{-PDMS}_{4.0})_3$ . The three arm star exhibited three scattering peaks at the relative  $q$  values of 1:2:3 (Figure 6.38 E black line) and the diblock copolymer precursor showcased a disordered behavior due to the appearance of only one broader peak corresponding to the primary reflection and it may be attributed to the insufficient casting (Figure 6.38 E red line).

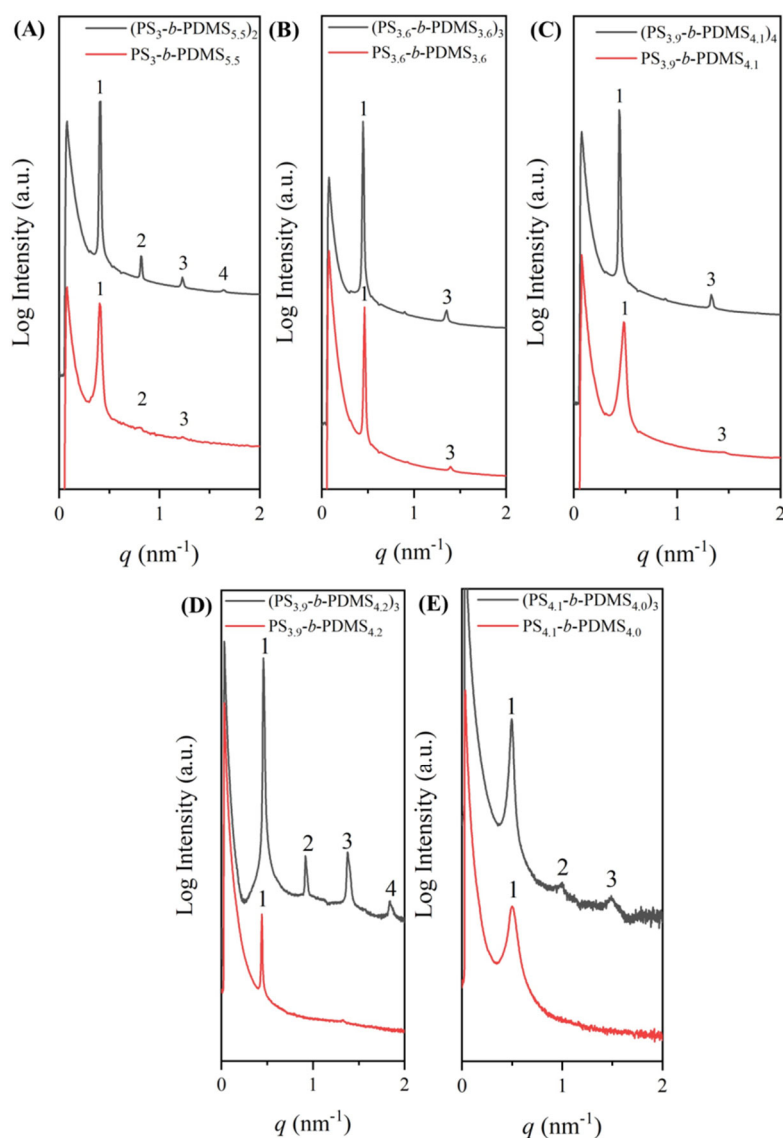


**Figure 6.38:** 1D SAXS profiles of the lamellae-forming  $(PS_x-b-PDMS_y)_n$  samples with different arm numbers ( $n = 1, 3,$  and  $4$ ). (A)  $PS_3-b-PDMS_{5.5}$  (red line) and  $(PS_3-b-PDMS_{5.5})_2$  (black line) corresponding to set number 1, (B)  $PS_{3.6}-b-PDMS_{3.6}$  (red line) and  $(PS_{3.6}-b-PDMS_{3.6})_3$  (black line) corresponding to set number 2, (C)  $PS_{3.9}-b-PDMS_{4.1}$  (red line) and  $(PS_{3.9}-b-PDMS_{4.1})_4$  (black line) corresponding to set number 3, (D)  $PS_{3.9}-b-PDMS_{4.2}$  (red line) and  $(PS_{3.9}-b-PDMS_{4.2})_3$  (black line) corresponding to set number 4 and (E)  $PS_{4.1}-b-PDMS_{4.0}$  (red line) and  $(PS_{4.1}-b-PDMS_{4.0})_3$  (black line) corresponding to set number 5.

Four representative TEM micrographs of the lamellae-forming  $(PS_x-b-PDMS_y)_n$  samples with different arm numbers ( $n = 1, 3,$  and  $4$ ) are given in the following figure involving the solution casted  $PS_{3.6}-b-PDMS_{3.6}$  (Figure 6.39 A) and the  $(PS_{3.6}-b-PDMS_{3.6})_3$  (Figure 6.39 B), as well as the  $PS_{3.9}-b-PDMS_{4.1}$  (Figure 6.39 C) and  $(PS_{3.9}-b-PDMS_{4.1})_4$  (Figure 6.39 D) corresponding to samples from set number 2 and 3 respectively. In all TEM images alternating white PS and dark PDMS sheets

can be clearly observed, further verifying that the complex architecture did not induce any alternation either on the adopted morphology or on the domain periodicity. Similar results were obtained in all remaining sequences.

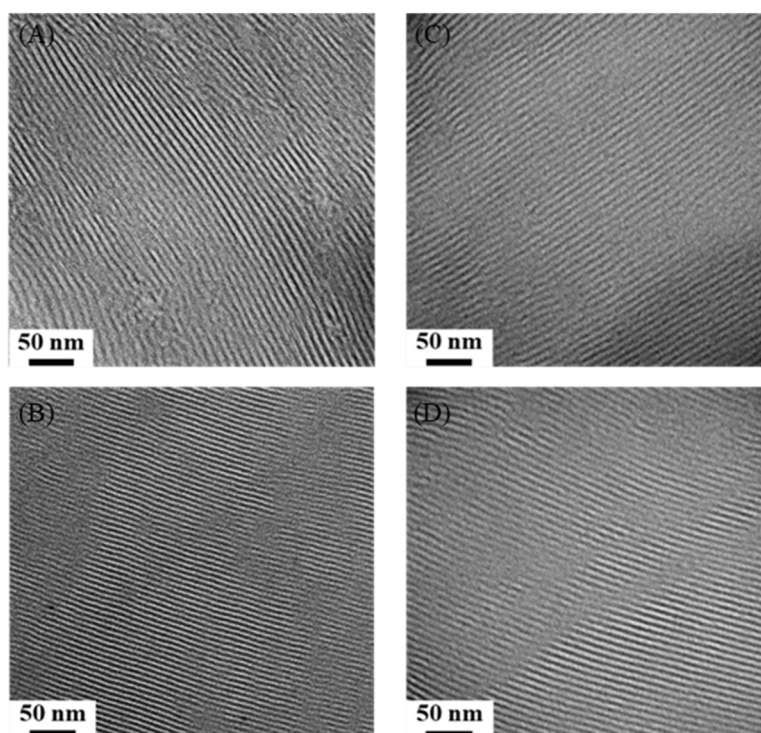


**Figure 6.39:** TEM images with respect to the: (A)  $PS_{3.6}\text{-}b\text{-}PDMS_{3.6}$ , (B)  $(PS_{3.6}\text{-}b\text{-}PDMS_{3.6})_3$ , (C)  $PS_{3.9}\text{-}b\text{-}PDMS_{4.1}$ , and (D)  $(PS_{3.9}\text{-}b\text{-}PDMS_{4.1})_4$ .<sup>73</sup>

In situ SAXS experiments were conducted to some of the above mentioned copolymers [ $PS_{3.6}\text{-}b\text{-}PDMS_{3.6}$  and  $(PS_{3.6}\text{-}b\text{-}PDMS_{3.6})_3$  from set number 2 as well as  $(PS_{3.9}\text{-}b\text{-}PDMS_{4.1})_4$  from set number 3] to study the self-assembly behavior as the temperature increases, to compare the effect of complex architecture on the adopted morphology and to determine any potential order-order and/or order-disorder transition as well. Strikingly, after thermal annealing from room temperature to 180°C using a step heating rate (10°C/10 min) a notable shift of the primary peak to a lower  $q$  region with approximately 50% increase on the domain spacing (from 13.5 to 21.0 nm) was evidenced for sample  $PS_{3.6}\text{-}b\text{-}PDMS_{3.6}$ . A similar behavior for the complex architecture copolymers, meaning  $(PS_{3.6}\text{-}b\text{-}PDMS_{3.6})_3$  and  $(PS_{3.9}\text{-}b\text{-}PDMS_{4.1})_4$  with a profound increase on the domain spacing of the three arm star from 14.0 to 21.0 and from 14.2 to 22.0 nm for the four arm star was observed. Note that, lower segregation strength due to the irreversible relationship between temperature and  $\chi$  should

eventually lead to lower  $d$ -spacing values and not to a 50% increase on the periodicity. In Figure 6.40 the in situ temperature-resolved 1D SAXS profiles for the different sequences recorded from 90 to 180 °C are presented.

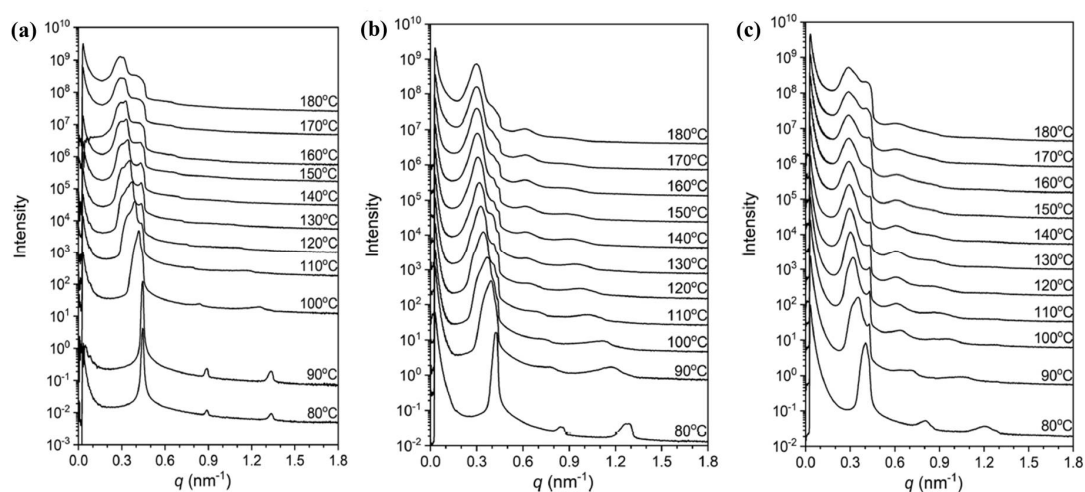


**Figure 6.40:** In situ temperature-resolved 1D SAXS profiles from 90 to 180 °C corresponding to: (a)  $PS_{3.6}\text{-}b\text{-}PDMS_{3.6}$ , (b)  $(PS_{3.6}\text{-}b\text{-}PDMS_{3.6})_3$ , and (c)  $(PS_{3.9}\text{-}b\text{-}PDMS_{4.1})_4$ .<sup>73</sup>

A universal behavior independent from the complexity of the systems was evidenced, which leads to an order-order transition from the interdigitating structure to bilayers in the self-assembled lamellar phase. The wet brush-like form or interdigitating conformation is attributed to the solution casting process. The appearance of a peak at the lower  $q$  region for all copolymers was revealed when the annealing temperature exceeded the  $T_g$  of PS (90°C) due to the enhanced chain mobility which enabled the macromolecular chains to form a bilayer texture. The transition gave rise to high variation on the  $d$ -spacing, a finding that has never been observed in the bulk state for a coil-coil copolymer as in our case. The fact that the copolymers exhibit low  $\chi N$  value allows for free zones at the interface and the formation of the interdigitating conformation after solution casting. The temperature increase induces an enlargement on the excluded volumes of the individual chains. The unfavourable formation of the voids causes the rearrangement of the chains and a transition to a bilayer structure with lower voids to reach the local minimum free energy state. The star block copolymers showcased a coherent behavior with respect to the domain spacing variation due to the uniform and homogenous expansion of the polymeric chains (each arm consist of one diblock copolymer). A hypothetical schematic regarding the chain dispositions of all copolymers is given in Figure 6.41 where the PS chains are illustrated in red color and the PDMS with blue.

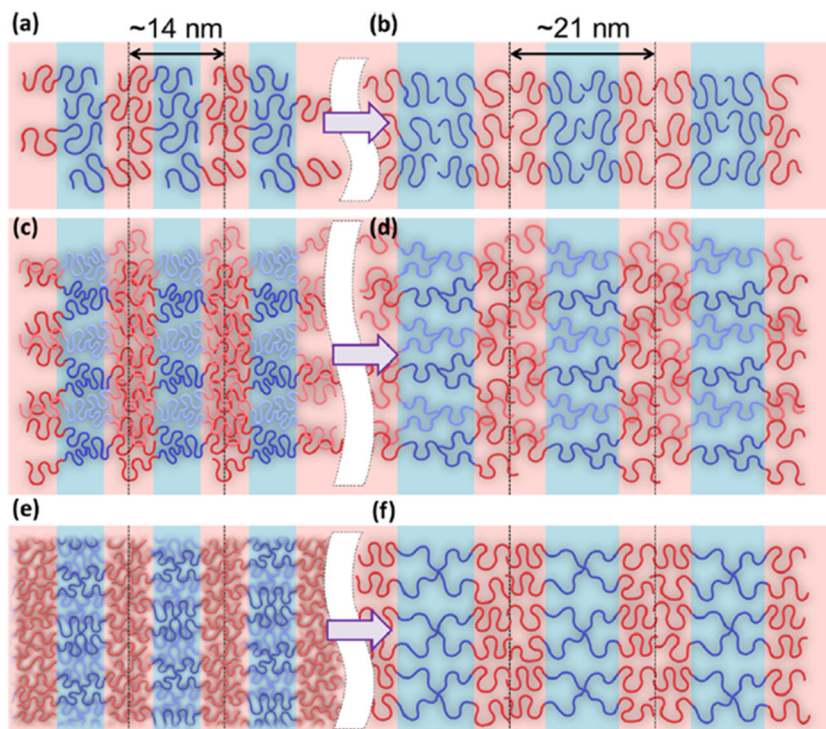


**Figure 6.41:** Schematics regarding the chain dispositions of the self-assembled  $PS_{3,6}$ - $PDMS_{3,6}$ ,  $(PS_{3,6}$ - $b$ - $PDMS_{3,6})_3$ , and  $(PS_{3,9}$ - $b$ - $PDMS_{4,1})_4$  with interdigitating structures (a,c,e) and bilayers (b,d,f) for polymer chain packing in a lamellar phase. Red color corresponds to PS segments and blue to the PDMS.<sup>73</sup>

Furthermore, the complex architecture has a severe impact on the self-assembly of the systems due to the lower degree of wet brushes in the more complex architectures. This behavior is elaborated in Figure 6.42 where the order-order transition initiates at lower annealing temperature and is faster for higher arm numbers. The diagrams show the domain spacing variation (as directly calculated from the primary peaks of both interdigitating and bilayers) as a function of temperature for both structures of all copolymer sequences.

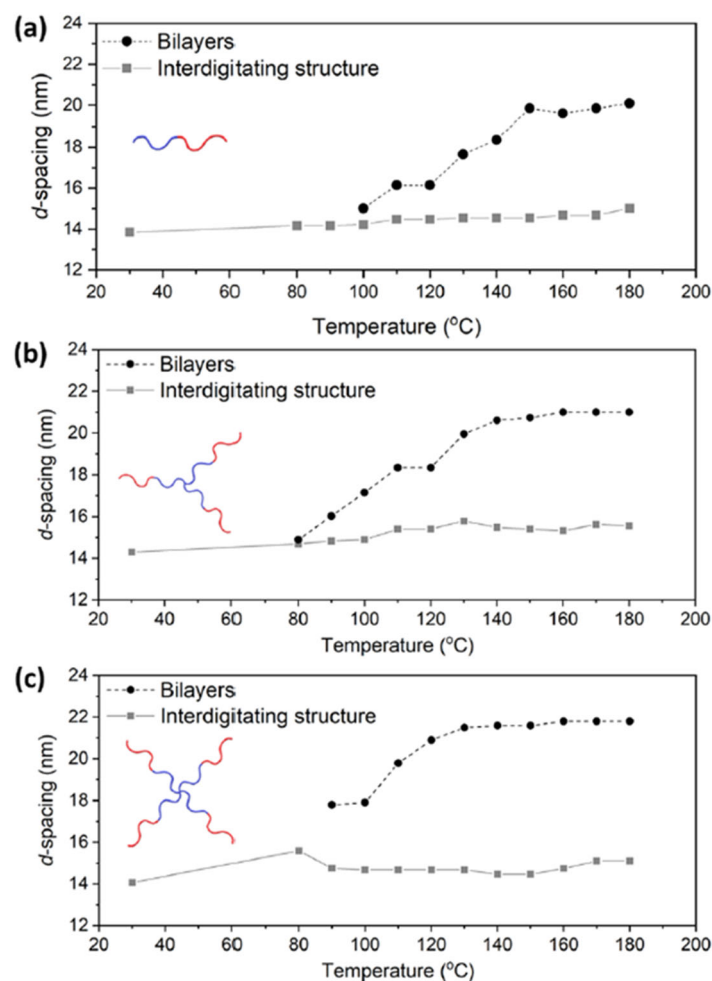


**Figure 6.42:** Domain spacing increase of: (a)  $PS_{3.6}\text{-}b\text{-}PDMS_{3.6}$ , (b)  $(PS_{3.6}\text{-}b\text{-}PDMS_{3.6})_3$ , and (c)  $(PS_{3.9}\text{-}b\text{-}PDMS_{4.1})_4$  after in situ thermal annealing.<sup>73</sup>

In addition, the reversibility of the transition from bilayers to interdigitating was examined with scattering experiments after cooling to ambient conditions for all copolymers. The  $PS_{3.6}\text{-}b\text{-}PDMS_{3.6}$  demonstrated a coexistence of both structures after cooling and remaining 6 hours at ambient conditions (Figure 6.43 below). The star block copolymers exhibited a quick transition back to the solution casted morphology with the approximate  $d$  spacing values due to the architecture complexity which provides higher ordering as the number of arms increases.

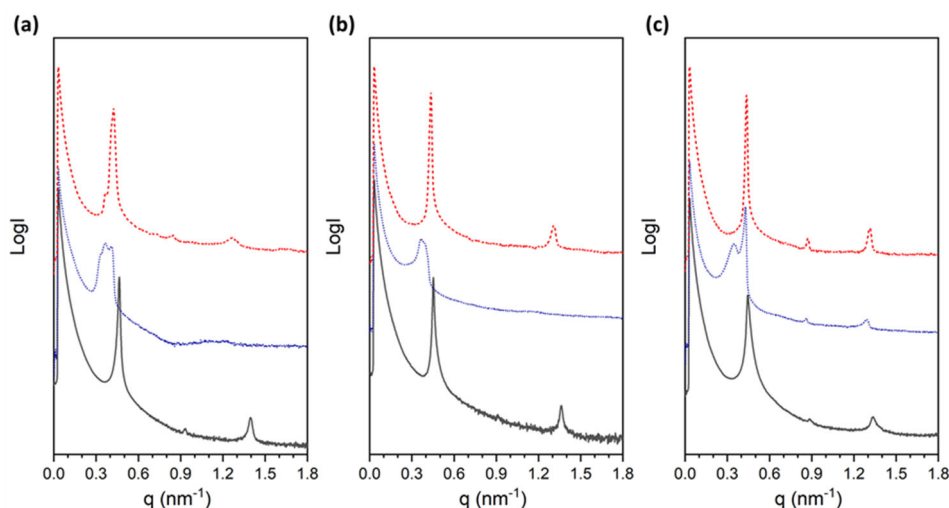


**Figure 6.43:** SAXS profiles of (a)  $PS_{3.6}\text{-}b\text{-}PDMS_{3.6}$ , (b)  $(PS_{3.6}\text{-}b\text{-}PDMS_{3.6})_3$ , and (c)  $(PS_{3.9}\text{-}b\text{-}PDMS_{4.1})_4$  after solution casting (black solid line) followed by thermal treatment (blue dot line) and keeping at room temperature for six hours (red dash line), respectively.<sup>73</sup>

To further examine the metastability of the interdigitating structure, sample  $PS_{3.6}\text{-}b\text{-}PDMS_{3.6}$  was submitted to in-situ temperature-resolved SAXS experiments to a temperature higher than the order-disorder transition temperature ( $310^\circ\text{C}$ ) followed by cooling to ambient conditions. A disassociated self-assembled structure was evident over  $300^\circ\text{C}$  (Figure 6.44), enabling the formation of bilayers with less degree of interdigitating. After cooling to ambient conditions the degree of interdigitating structure is augmented as in the case of thermal annealing below the  $T_{ODT}$ . The complete absence of the double layered structure took place after two weeks as verified by the 1D SAXS plot in which the  $q$  value of the primary peak indicated the shifting back to the initial solution casted morphology.

The specific study is considered very promising and sheds light on the design of nanostructured linear and non-linear coil-coil BCPs with temperature-responsive inter-domain spacing variation. Preliminary results have already been published in the literature through a joined publication by the Avgeropoulos' and Ho's research groups.<sup>73</sup>

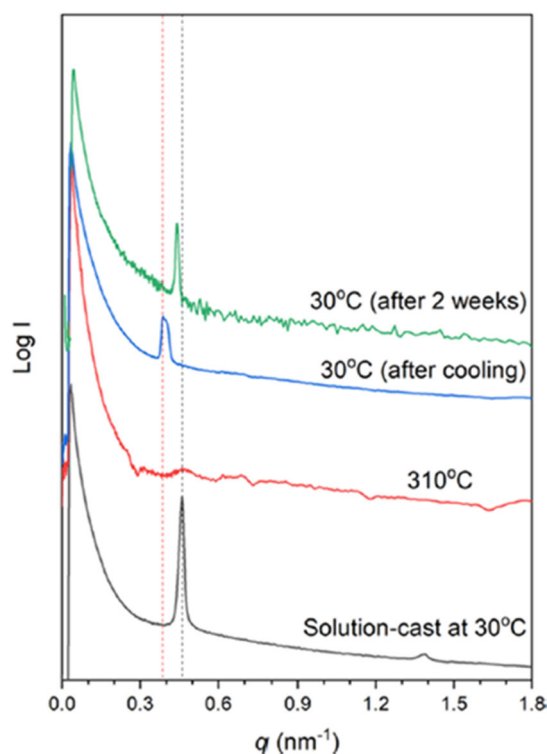


**Figure 6.44:** SAXS profiles of  $PS_{3.6}\text{-}b\text{-}PDMS_{3.6}$  after solution casting (black), followed by thermal treatment over  $T_{ODT}$  (red), cooling to room temperature (blue) and keeping at room temperature for 2 weeks (green), respectively.<sup>73</sup>

### **Set number 6**

The linear  $PS_{15}\text{-}b\text{-}PDMS_{10}$  copolymer and its corresponding  $(PS_{15}\text{-}b\text{-}PDMS_{10})_3$  three arm star were casted in a non-selective solvent (cyclohexane) to promote the formation of equilibrium morphologies. The PDMS constituted the minority component as indicated by the  $\phi_{PDMS}$  which is equal to 0.39 (Table 6.6). Lamellar structures with enlarged domain spacing ( $\sim 25$  nm for both samples) when compared to the previous sequences due to the higher molecular weight of the components were obtained. The 1D SAXS profiles showcased the relative  $q$  values at a ratio of 1:2:3 and in combination with the results obtained from TEM (which as well showed alternating black PDMS and white PS regions), the formation of lamellae was further confirmed. The combined 1D SAXS results and the real space TEM imaging are given in Figure 6.45.

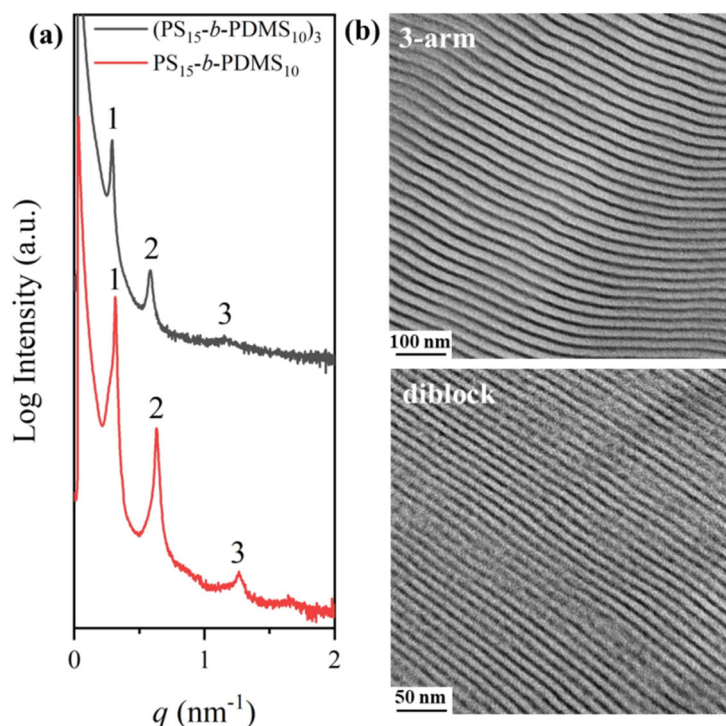


**Figure 6.45:** Combined results of the: (a) 1D SAXS plots corresponding to the  $PS_{15}\text{-}b\text{-}PDMS_{10}$  (red line) and the  $(PS_{15}\text{-}b\text{-}PDMS_{10})_3$  (black line) (b) TEM micrograph of the  $PS_{15}\text{-}b\text{-}PDMS_{10}$  and  $(PS_{15}\text{-}b\text{-}PDMS_{10})_3$ .

### Set number 7

Sample  $PS_5\text{-}b\text{-}PDMS_{3.4}$  was the diblock copolymer precursor for the preparation of  $(PS_5\text{-}b\text{-}PDMS_{3.4})_3$  and  $(PS_5\text{-}b\text{-}PDMS_{3.4})_4$  respectively. The use of a neutral solvent during solution casting (cyclohexane) in combination with the volume fraction of PDMS ( $\phi_{PDMS}=0.40$ ) gave rise to lamellar morphology for all copolymers irrespective to the number of arms. The scattering experiments through the relative  $q$  values at a ratio of 1:2:3 indicated the formation of lamellae [Figure 6.46 (a)]. In Figure 6.46 (b) the TEM images regarding the self-assembled structures for the different sequences after thermal annealing for one day at  $100^\circ\text{C}$  are illustrated. The alternating black (PDMS) and white (PS) domains evident in the TEM micrographs strongly suggest the formation of lamellar morphologies. Using the primary peak, the domain spacing was calculated 12.5 nm, 13 nm as well as 13 nm for the precursor, three arm- and four-arm star block copolymers respectively. The evident variation in lamellar thickness between the copolymers is attributed to the angle which is viewed.

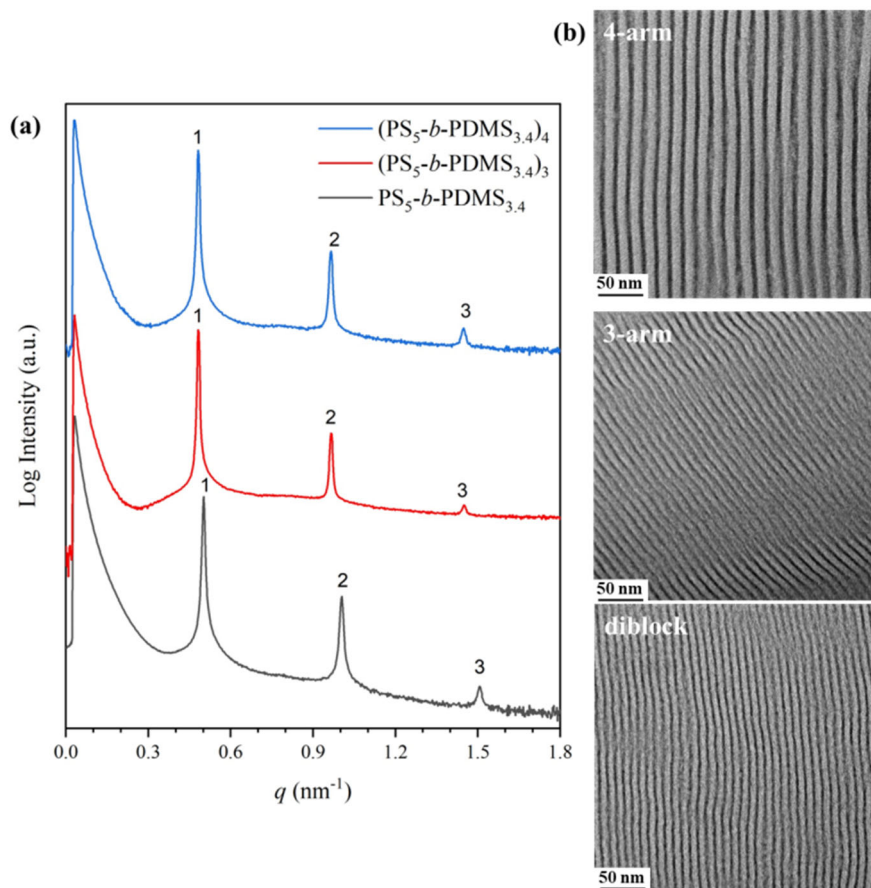


**Figure 6.46:** Combined results with respect to the (a) 1D SAXS plots of the  $\text{PS}_5\text{-}b\text{-PDMS}_{3,4}$  (black line), the  $(\text{PS}_5\text{-}b\text{-PDMS}_{3,4})_3$  (red line) and the  $(\text{PS}_5\text{-}b\text{-PDMS}_{3,4})_4$  (blue line) (b) TEM micrographs of all different architecture copolymers.

### **Set number 8**

The  $(\text{PS}_{4.2}\text{-}b\text{-PDMS}_{5.6})_{1,3,4}$  sequences were morphologically studied using cyclohexane for solution casting and thermal annealing for one day at a temperature near the  $T_g$  of PS ( $>65$  °C). The adequate mass thickness contrast between the individual blocks gave rise to alternating dark PDMS and bright PS layers for all different architecture copolymers [Figure 6.47 (A-C)]. Besides the alternating lamellae in the TEM micrograph of the diblock precursor [Figure 6.47 (A)], local regions with wagging texture in diffused gray tone were evident. After performing scattering experiments the formation of lamellar structures was confirmed through the characteristic reflections at the relative  $q/q^*=1:2:3:4$ . The domain spacing values for the diblock, the three- and four- arm were calculated through the  $q^*$  and were found 14.6, 15.0 and 14.9 nm, respectively. Notably, an additional set of reflections (indicated with arrows in the relative 1D SAXS profiles) was observed in the diblock

copolymer indicating a coexistence of lamellae with another phase. As the number of arms increased, the intensities of the additional reflections decreased, demonstrating the effect of complex architecture on the self-assembly.

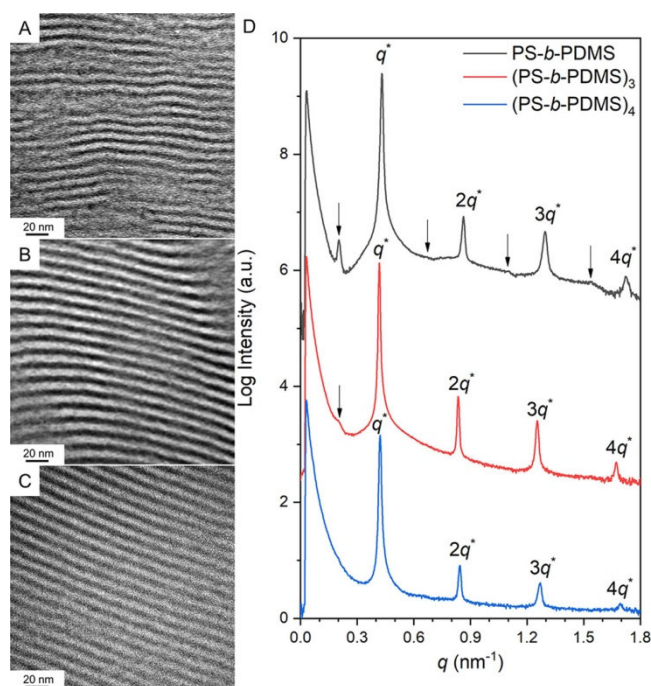


**Figure 6.47:** TEM micrographs of the (A)  $PS_{4.2}\text{-}b\text{-}PDMS_{5.6}$ , (B)  $(PS_{4.2}\text{-}b\text{-}PDMS_{5.6})_3$  and (C)  $(PS_{4.2}\text{-}b\text{-}PDMS_{5.6})_4$ . (D) Corresponding 1D SAXS plots of  $PS_{4.2}\text{-}b\text{-}PDMS_{5.6}$  (black line),  $(PS_{4.2}\text{-}b\text{-}PDMS_{5.6})_3$  (red) and  $(PS_{4.2}\text{-}b\text{-}PDMS_{5.6})_4$  (blue). The primary peaks are denoted as  $q^*$  and the solid arrows mark the additional reflections from the forming lamellar phase. All samples were isothermally annealed at temperature near the  $T_g$  of PS for 1 day.<sup>188</sup>

Closely observing the 1D SAXS profiles of the as cast and after thermal annealing regarding the diblock copolymer, the formation of typical lamellae at the relative  $q$  values of 1:2:3:4 (marked by black solid lines) and the additional peaks at the relative  $q$  values of 0.5:1.5:2.5:3.5 (equal to  $q/q_s = 1:3:5:7$  and marked by red dashed lines) is straightforward. In Figure 6.48 the first-order peak with respect to the typical lamellae is denoted as  $q^*$  and the one observed in the low- $q$  region is denoted as  $q_s$ . As expected, the additional reflection in the lower  $q$  region gives double domain spacing value.

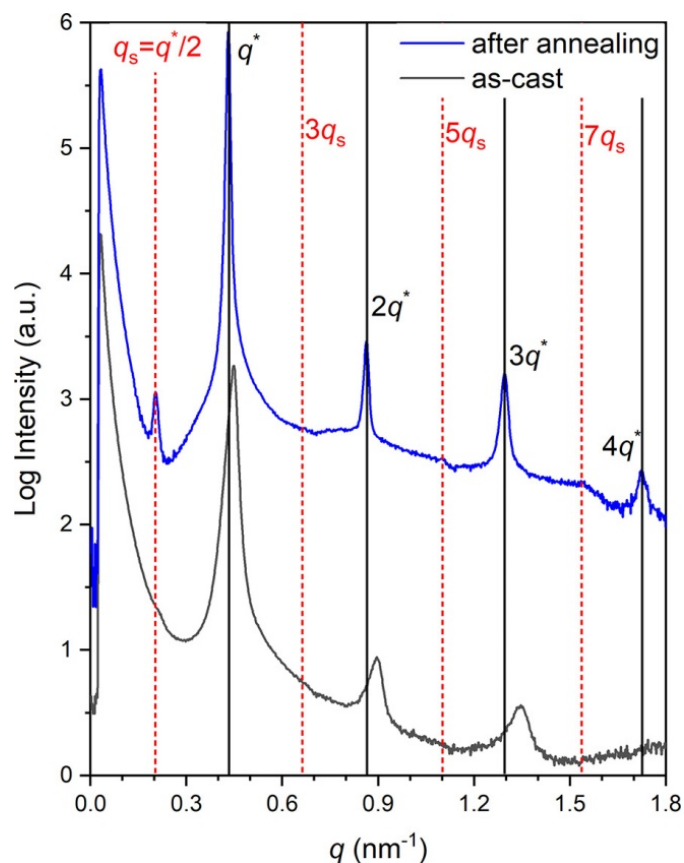


**Figure 6.48:** 1D SAXS profiles of the as-cast and annealed (for one day near the  $T_g$  of PS)  $PS_{4.2}$ - $b$ - $PDMS_{5.6}$ . Solid lines label  $q/q^*$  at integers of 1, 2, 3, and 4. Dashed lines indicate  $q/q_s$  at the intervals of 1, 3, 5 and 7.<sup>188</sup>

Similar self-assembled behavior has been observed by Bates and Lodge et al.<sup>193</sup> for charged block copolymers with symmetric composition. The justification of the superlattice formation on the PS- $b$ -PDMS coil-coil copolymer was conducted based on the two proposed models of the above-mentioned research. In one case the novel structure formation could be allocated to the DSD'SDS stacking due to the different packing densities between the blocks. The soft PDMS segments should be divided in two different domains with higher (D') and lower (D) packing densities and alternately intervene in the hard PS region inducing a double distance from D to D while S to S distance equals to the one of the typical lamellae (Figure 6.49 A). The specific model could not be justified by real-space imaging (TEM) as a result a second one is analysed.

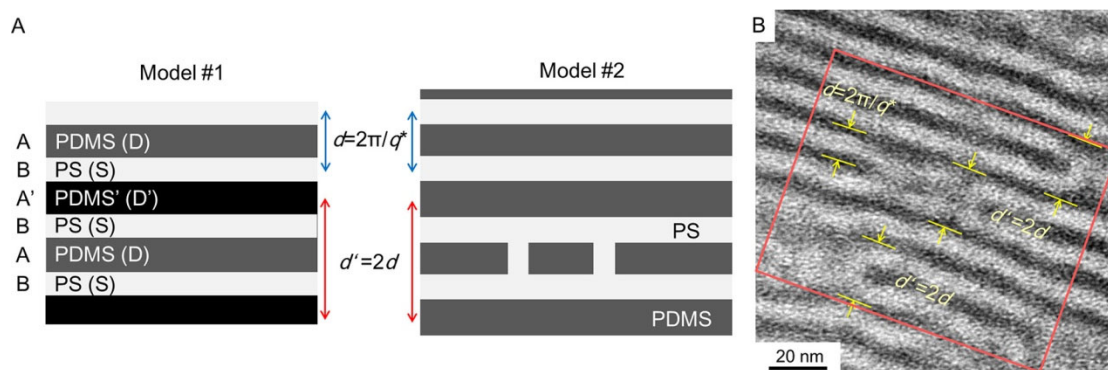


**Figure 6.49:** (A) Possible models regarding superlattice in lamellar morphology based on the literature.<sup>193</sup> (B) TEM micrographs of PS<sub>4.2</sub>-b-PDMS<sub>5.6</sub> after thermal annealing at for 1 day.<sup>188</sup>

In Figure 6.49 A a different model (#2) with ladder-like texture is presented. The formed line defects cause a discontinuity on the PDMS lines (similar to a perforated lamellae structure) allowing bright PS domains to be randomly penetrated. This behavior is evident in the relative TEM micrograph (Figure 6.49 B) in which the PDMS discontinuity induces double domain spacing. Also, disordered-like regions are showcased which is in accordance to Bates and Lodge research work<sup>193</sup> where the superlattice structure is located in an intermediate state between lamellae and disorder.

The stability of the structure was further examined with in-situ temperature resolved SAXS experiments. The heating process has been conducted in two stages and specifically 10°C/ 5 min in the range 30-70°C and 5°C/ 5 min from 70 to ~230°C. The coexistence of typical lamellae and superlattice morphology is evident at 30°C. After exceeding the  $T_g$  of PS, an additional peak (marked by a red arrow) is emerged and a slight shifting of the primary reflection  $q^*$  to the lower  $q$  regions occurs. The  $q_s$  reflection corresponding to the superlattice remains unchanged (same spacing values) until 120°C and disappears at 130°C. The splitting of the first order reflection has already discussed for set number 2 and 3 and is attributed to the order-order transition from interdigitating to bilayers structure. It is also evident that as the temperature increases the intensity of the bilayer structure is also increased. The appearance of chain interdigitation is significantly lower at 140°C (1 order of magnitude compared to the initial stage). The kinetic process for the transformation of interdigitating to bilayers is a slow process and traces of the original lamellae could possibly remain at higher temperatures. The bilayer structure showcases a ~30% expansion which remained until the end of heating.

It is concluded that the superlattice formation is strongly correlated to the interdigitating structure that is subsequently transformed to bilayer as the temperature increases. After three days at ambient conditions the bilayers transform to interdigitating lamellae and the initial reflection of the superlattice structure is emerged suggesting a reversible phase transformation. The in situ scattering data are given in Figure 6.50 A along with the d-spacing values and intensities as a function of temperature (Figure 6.50 B) for the observed lamellar-like morphologies.

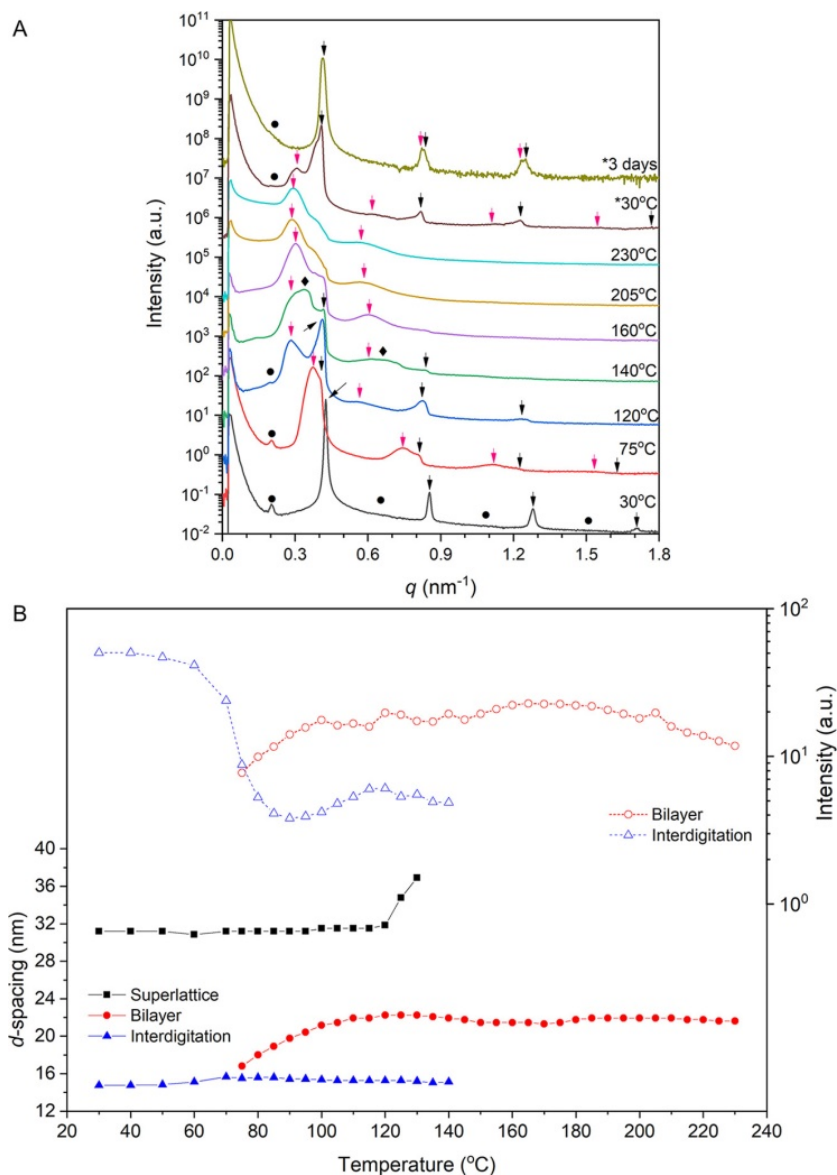


**Figure 6.50:** In situ SAXS profiles with respect to the  $PS_{4.2}\text{-}b\text{-}PDMS_{5.6}$ . The black and red arrows correspond to the  $q/q^*$  at integers of 1, 2, 3, and 4 from lamellae with chain interdigitation and bilayers, respectively. Dots indicate  $q/q^*$  at the intervals of 0.5, 1.5, 2.5, and 3.5 resulting from superlattice structures. (B) Temperature dependent d spacing and intensities for the observed superlattice structure, lamellae with chain interdigitation, and bilayer texture as directly calculated from the in situ temperature resolved SAXS results.<sup>188</sup>

To gain further insight towards the superlattice formation, a different schematic is presented in Figure 6.51. The PS chains are given in black and the PDMS in blue. Also the PDMS domains correspond to the grey area while the PS regions are white. The blue arrows indicate the domain periodicity of the typical lamellae while the red corresponds to the superlattice structure. As shown in Figure 6.51 A the ladder-like structure is stabilized through the chain interdigitation that allows highly dense domains due to the wet-brush like texture. It is evident that superlattice structure could be found in the less populated regions which become more significant after thermal annealing as indicated in Figure 6.51 B giving rise to the lamellae with bilayers.

The architecture effect on the superlattice formation is also discussed. Based on the scattering and TEM results, it is concluded that the superlattice formation is severely restricted for more complex architecture systems. Specifically, only a tiny reflection peak for the three arm star block copolymer and the complete absence of the four arm star  $q_s$  reflection can be observed. The multiple arms due to the overcrowding induce higher vacancy degrees, causing larger overstretching which render them less thermodynamically favourable for packing of polymeric chains (Figure 6.51 C and D).

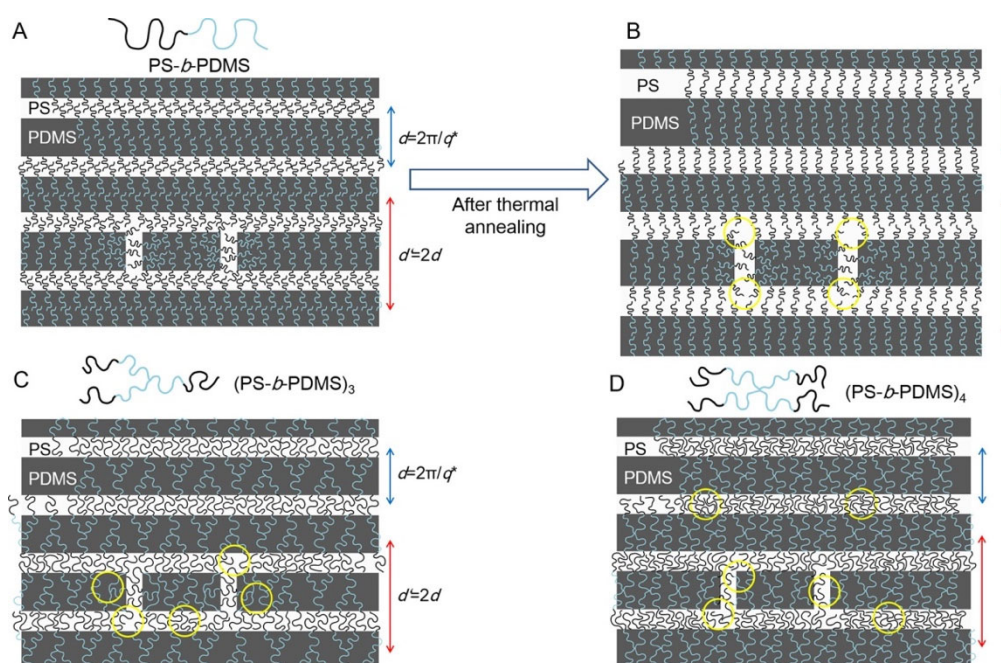


**Figure 6.51:** Hypothetical chain dispositions of superlattice structure with chain interdigitation in self-assembled (A)  $PS_{4.2}-b-PDMS_{5.6}$  and (B) order-order transition to lamellar with bilayer texture, (C)  $(PS_{4.2}-b-PDMS_{5.6})_3$ , and (D)  $(PS_{4.2}-b-PDMS_{5.6})_4$  based on model 2. PDMS segments (blue) occupy the grey area and PS segments (black) reside in the ladder-like regions.<sup>188</sup>

### Set number 9

This set comprises from samples  $\text{PS}_3\text{-}b\text{-PDMS}_{3.5}$ ,  $(\text{PS}_3\text{-}b\text{-PDMS}_{3.5})_3$  and  $(\text{PS}_3\text{-}b\text{-PDMS}_{3.5})_4$  from which the films were prepared using cyclohexane as a casting solvent followed by thermal annealing at  $100^\circ\text{C}$  for one day. The bulk assembly in these samples was studied with scattering experiments and real space imaging (TEM). The 1D SAXS profiles revealed the formation of alternating lamellae based on the characteristic reflection positions at the relative  $q$  values of 1:2:3. As it was expected, the diblock copolymer with the lowest molecular weight enabled the lowest domain spacing values as well as its corresponding non-linear copolymers in bulk state. Specifically, a domain period equal to 10.8 nm was obtained for the diblock precursor and 11.5 nm for the star block copolymers. The TEM micrographs exhibited well-defined black (PDMS) and white (PS) layers indicating the high segregation strength between the blocks. Both scattering experiments and real space imaging are presented in Figure 6.52.

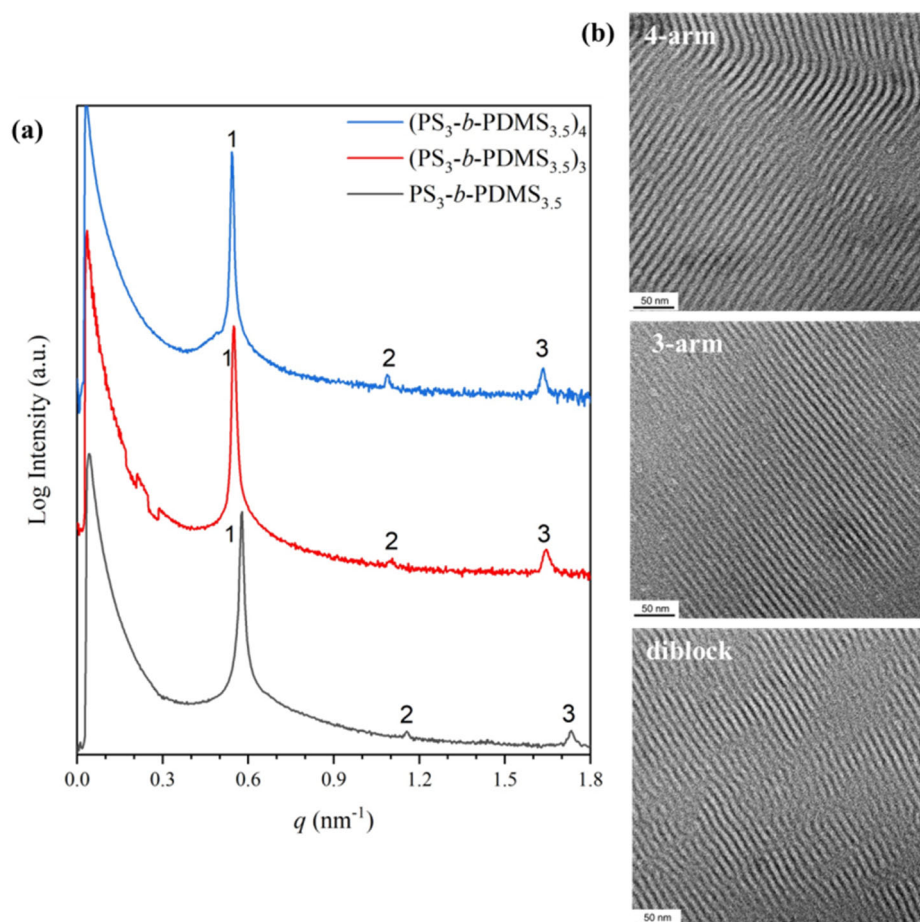


**Figure 6.52:** 1D SAXS plots corresponding to the  $\text{PS}_3\text{-}b\text{-PDMS}_{3.5}$  (black line),  $(\text{PS}_3\text{-}b\text{-PDMS}_{3.5})_3$  (red line) and  $(\text{PS}_3\text{-}b\text{-PDMS}_{3.5})_4$  (blue line).

## Set number 10

A higher molecular weight diblock copolymer precursor along with the 3- and 4- arm star block copolymers, namely  $PS_{12.8}\text{-}b\text{-}PDMS_{10.3}$ ,  $(PS_{12.8}\text{-}b\text{-}PDMS_{10.3})_3$  and  $(PS_{12.8}\text{-}b\text{-}PDMS_{10.3})_4$ , were synthesized. The samples were casted in cyclohexane and submitted to thermal annealing for one day at  $100^\circ\text{C}$  prior to their morphological characterization. As expected, the nearly symmetric composition ( $\phi_{PDMS}=0.47$ ) and the use of a neutral solvent induced the formation of well-developed lamellar morphologies as indicated by the multiple reflections in the corresponding 1D SAXS plots. The diblock copolymer exhibited the reflections in the relative  $q$  values of 1:2:3, while the well-ordered star block copolymers showcased multiple reflections following a 1:2:3:4:5:6 ratio [Figure 6.53 (a)]. Through the position of the primary peak in the SAXS patterns the domain period was calculated 25 nm for the linear copolymer and 25.3 nm for the star block copolymers. The TEM images [Figure 6.53 (b)] confirmed the formation of well-ordered lamellae for all copolymers.

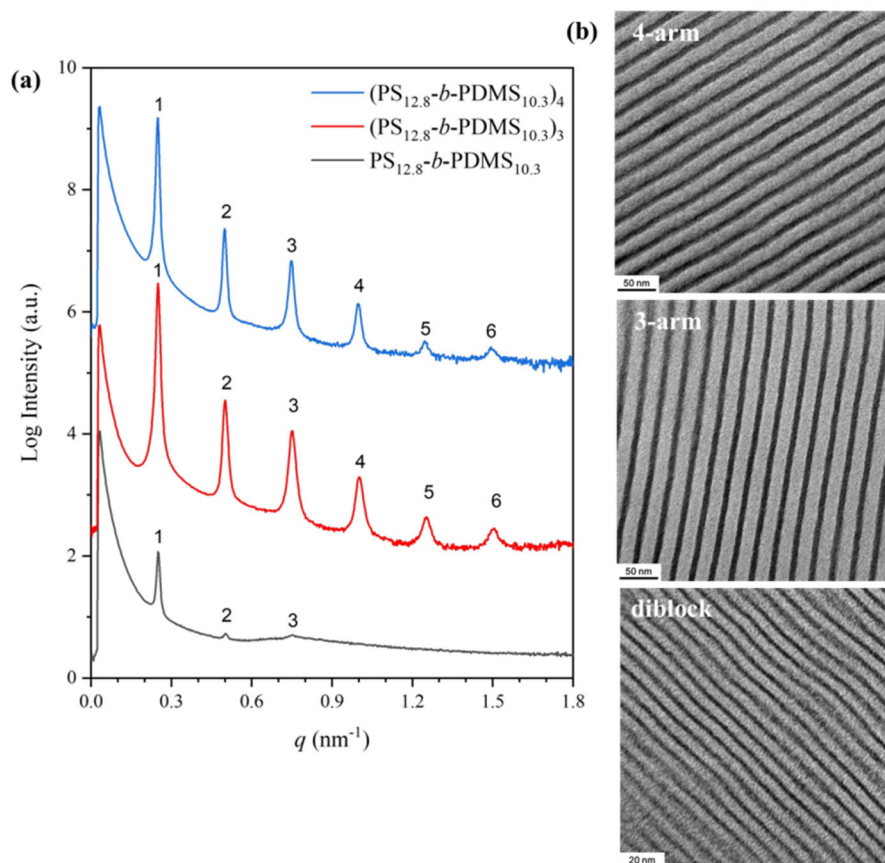


**Figure 6.53:** Combined results with respect to (a) the 1D SAXS plots of the  $PS_{12.8}\text{-}b\text{-}PDMS_{10.3}$  (black line),  $(PS_{12.8}\text{-}b\text{-}PDMS_{10.3})_3$  (red line) and  $(PS_{12.8}\text{-}b\text{-}PDMS_{10.3})_4$  (blue line) and (b) the corresponding TEM micrographs.

It is clear that the equilibrium morphology of the thermally annealed films is lamellar as verified by scattering and real imaging results. To study the evolution of the morphology of the PS<sub>12.8</sub>-*b*-PDMS<sub>10.3</sub> various solvents with different selectivity towards the individual blocks were employed. The use of DCM (9.9 cal<sup>1/2</sup>/cm<sup>3/2</sup>), chloroform (9.3 cal<sup>1/2</sup>/cm<sup>3/2</sup>) and toluene (8.9 cal<sup>1/2</sup>/cm<sup>3/2</sup>) led to the formation of lamellar morphologies despite the selectivity towards the PS segment as evidenced by the 1D SAXS plots with peak positions at the relative  $q$  values of 1:2:3:4. On the other hand, the use of THF (9.3 cal<sup>1/2</sup>/cm<sup>3/2</sup>) induced the formation of square arrays of cylinders (p4mm symmetry) and hexagonal cylinders (p6mm symmetry) due to the distortion of the lattice. The reflections at the relative  $q$  values with a 1: $\sqrt{2}$ :2: $\sqrt{5}$ :3:4 ratio are attributed to the p4mm symmetry while the 1: $\sqrt{3}$ :2: $\sqrt{7}$  to the p6mm symmetry [Figure 6.54 (a)]. The ability to minimize the interfacial area and the packing frustration renders the C<sub>p6mm</sub><sup>6</sup> the most preferable among all cylindrical phases.<sup>194</sup> The more closely packed lattice was favored by the more swollen domains due to the solution casting process. In the relative TEM micrograph the coexistence of the two symmetries and also parallel stripes corresponding to the longitudinal view of cylinders can be observed. The use of chlorobenzene (9.5 cal<sup>1/2</sup>/cm<sup>3/2</sup>) gave rise to DG phase as indicated (Figure 6.54) by the characteristic reflections at the relative  $q$  values of  $\sqrt{6}$ : $\sqrt{8}$ : $\sqrt{14}$ : $\sqrt{20}$ : $\sqrt{22}$ : $\sqrt{46}$ : $\sqrt{50}$  [Figure 6.54 (a)] and the corresponding TEM image [Figure 6.54 (b)] in which the [111] projection is given.

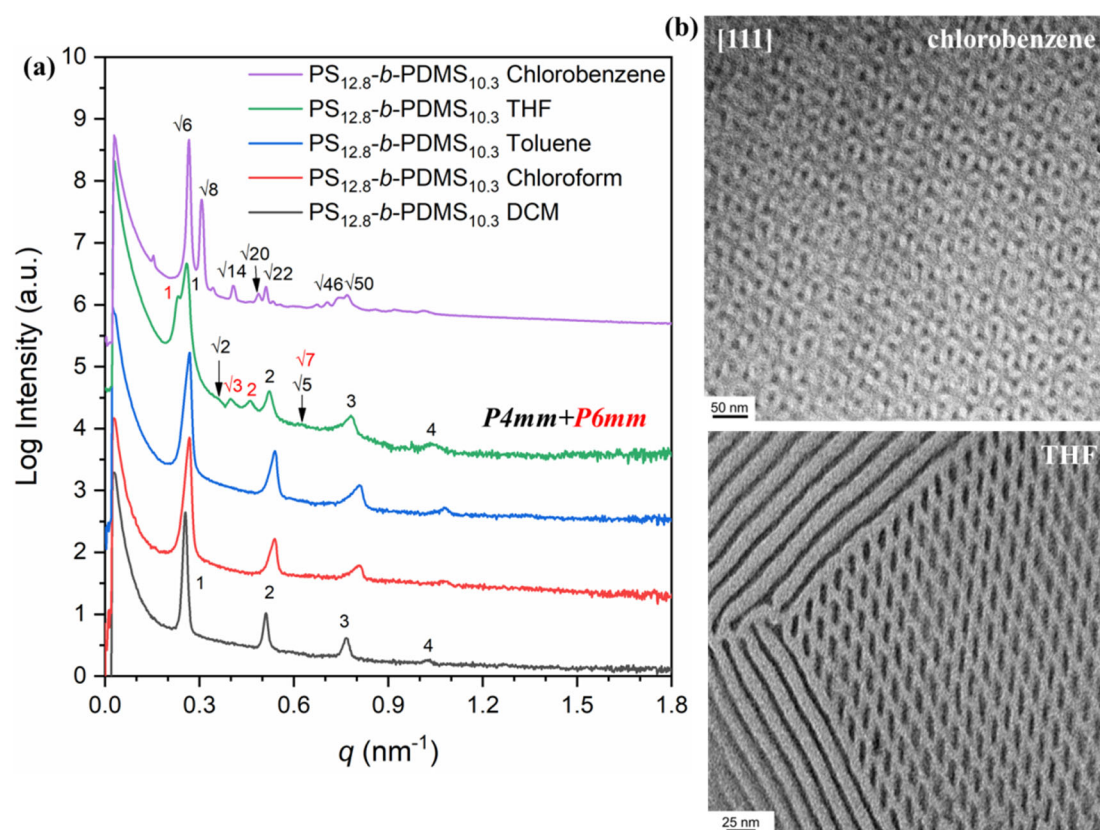


**Figure 6.54:** (a) 1D SAXS plots of the  $PS_{12.8}\text{-}b\text{-}PDMS_{10.3}$  after casting in DCM (black line), chloroform (red line), toluene (blue line), THF (green line) and chlorobenzene (purple line) (b) TEM images with respect to the self-assembled morphologies after casting in chlorobenzene and THF.

The processing parameters as already thoroughly described (including the evaporation rate of each solvent and the duration of thermal annealing) have a great impact on the adopted morphology. The bulk portion of the  $PS_{12.8}\text{-}b\text{-}PDMS_{10.3}$  was prepared using chlorobenzene at a fixed evaporation rate  $< 0.1\text{ml/day}$  and studied as cast, after thermal annealing at  $110^\circ\text{C}$  for 2 hours and for 12 hours respectively. A slight increase on the domain spacing from 23.5 nm to 24.9 was observed for the annealed samples. In Figure 6.55 (below) the 1D and 2D SAXS patterns of the as cast, the thermally annealed for 2 hours and for 12 hours are presented. Besides the slight increase on the domain spacing value, the increase of the annealing duration led to the appearance of additional peaks at higher  $q$  regions as illustrated on the SAXS patterns.

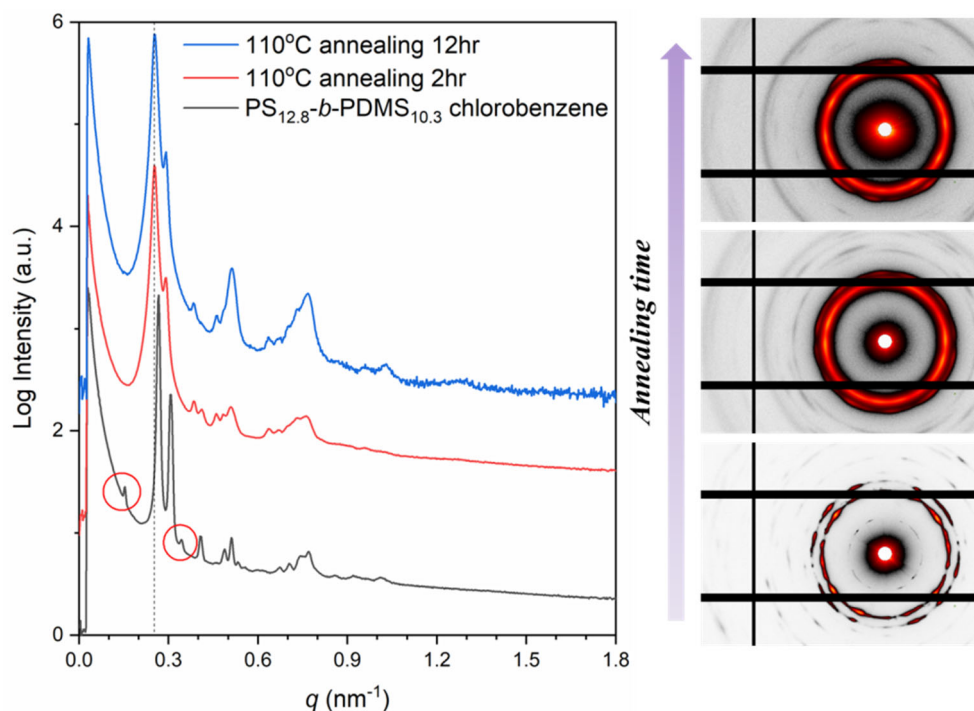


**Figure 6.55:** (left) 1D profiles of the  $PS_{12.8}$ - $b$ - $PDMS_{10.3}$  after casting in chlorobenzene. As-cast (black line), thermally annealed for 2 hours at  $110^\circ\text{C}$  (red line) and thermally annealed for 12 hours at  $110^\circ\text{C}$  (blue line). (right) 2D SAXS images for different annealing duration.

Specifically, the as cast sample demonstrated the characteristic peak positions at the relative  $q$  values of:

$$\sqrt{2}:\sqrt{6}:\sqrt{8}:\sqrt{10}:\sqrt{14}:\sqrt{18}:\sqrt{20}:\sqrt{22}:\sqrt{24}:\sqrt{26}:\sqrt{30}:\sqrt{32}:\sqrt{38}:\sqrt{42}:\sqrt{46}:\sqrt{50}:\sqrt{62}:\sqrt{72}:\sqrt{78}:\sqrt{86}.$$

The thermally annealed for two hours at  $110^\circ\text{C}$  showcased the  $\sqrt{6}:\sqrt{8}:\sqrt{10}:\sqrt{14}:\sqrt{16}:\sqrt{20}:\sqrt{22}:\sqrt{24}:\sqrt{38}:\sqrt{42}:\sqrt{46}:\sqrt{50}:\sqrt{54}:\sqrt{72}:\sqrt{78}:\sqrt{86}:\sqrt{96}$  while the one thermally annealed for twelve hours gave rise to the  $\sqrt{6}:\sqrt{8}:\sqrt{10}:\sqrt{14}:\sqrt{16}:\sqrt{20}:\sqrt{22}:\sqrt{24}:\sqrt{30}:\sqrt{38}:\sqrt{42}:\sqrt{46}:\sqrt{50}:\sqrt{54}:\sqrt{70}:\sqrt{86}:\sqrt{100}$ .

More importantly, it is evident that the annealing temperature is chosen to remove the distortion of the lattice by eliminating the  $\sqrt{2}$  (red circle),  $\sqrt{10}$  (red circle),  $\sqrt{18}$  and  $\sqrt{78}$ . Although the ordering degree is significantly better for the as cast sample (due to the higher  $\chi$  value) as indicated by the discontinuous dots on the respective 2D pattern the appearance of triclinic DG structure which is attributed to the distortion of the lattice and can be eliminated after thermal annealing. For clarification reasons the 1D SAXS profiles were plotted separately and presented in the following Figure 6.56. The SAXS patterns demonstrate a discontinuity on the signal to showcase the signals from the reflections at the higher  $q$  values more clearly. The arrow on the right parts of the images signifies the intensity of the permitted peaks located at the higher  $q$  regions.

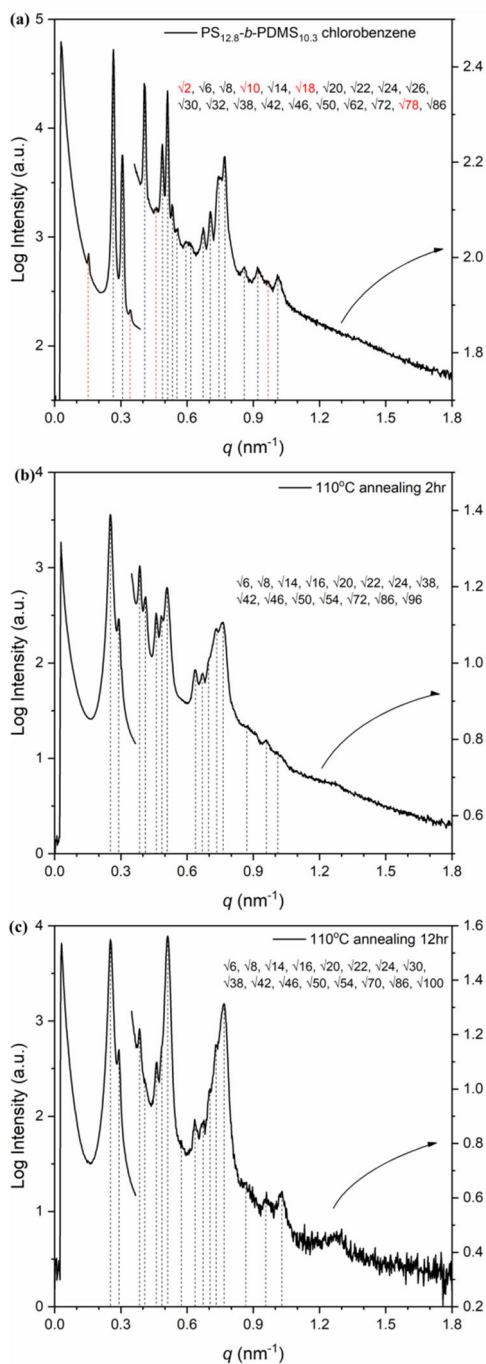


**Figure 6.56:** 1D profiles of the  $PS_{12.8}\text{-}b\text{-}PDMS_{10.3}$  after casting in chlorobenzene for the (a) as-cast, (b) thermally annealed for 2 hours at  $110^\circ\text{C}$  and (c) thermally annealed for 12 hours at  $110^\circ\text{C}$ .

### Set number 11

A low average molecular weight sample, meaning the  $PS_{4.2}\text{-}b\text{-}PDMS_{2.8}$  with PDMS volume fraction equal to 0.40 was synthesized and used as a precursor for the preparation of a triblock copolymer  $[(PS_{4.2}\text{-}b\text{-}PDMS_{2.8})_2]$  and a six-arm star block copolymer  $[(PS_{4.2}\text{-}b\text{-}PDMS_{2.8})_6]$ . Note that, the bulk studies related to the PDMS-

containing six arm star constitute a novel research and have never been reported in the literature before. The copolymers were casted in cyclohexane followed by thermal annealing at 100°C for 4 days. The characteristic reflections at the relative  $q$  values of  $\sqrt{6}:\sqrt{8}:\sqrt{14}:\sqrt{20}:\sqrt{22}:\sqrt{24}:\sqrt{26}:\sqrt{30}:\sqrt{38}:\sqrt{42}:\sqrt{46}:\sqrt{50}$  and  $\sqrt{6}:\sqrt{8}:\sqrt{14}:\sqrt{20}:\sqrt{22}:\sqrt{24}:\sqrt{26}$  observed in the 1D SAXS plots revealed the formation of DG phases with  $d_{(221)}^{DG}$  equal to 12.3 nm and 12.5 nm for the linear diblock precursor and the triblock copolymer, respectively. Interestingly enough, for the six arm star copolymer a lamellar morphology with a domain periodicity equal to 12.3 nm was adopted. Important is to mention that, in the low molecular weight  $(PS_5-b-PDMS_{3.4})_{1,3,4}$  samples with the same PDMS volume fraction (0.40) but slightly increased  $N$ , a lamellar morphology was observed in all copolymer sequences. Even in the four arm star the architecture had not any impact on the adopted morphology.

The formation of a lamellae structure instead of DG for the  $(PS_{4.2}-b-PDMS_{2.8})_6$  may be attributed to the highly symmetric conformation in combination with the overcrowding effect which prevents the minority component from curving. Manipulating the effective volume fraction through the use of a PS selective solvent (toluene) a higher asymmetry is induced leading to the formation of a DG phase with a unit cell length of 12.5 nm. The scattering results are presented in Figure 6.57.

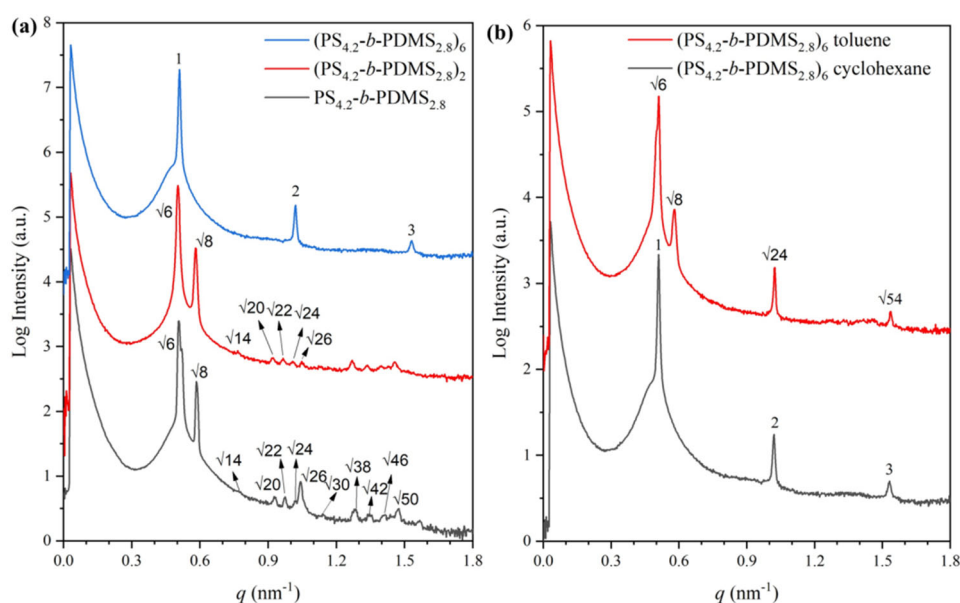


**Figure 6.57:** Combined results with respect to the 1D SAXS plots of the (a)  $PS_{4.2}-b-PDMS_{2.8}$  (black line),  $(PS_{4.2}-b-PDMS_{2.8})_2$  (red line) and  $(PS_{4.2}-b-PDMS_{2.8})_6$  (blue line) after casting in cyclohexane (b)  $(PS_{4.2}-b-PDMS_{2.8})_6$  after casting in cyclohexane (black line) and toluene (red line).

## Set number 12

The solution casted (in cyclohexane) linear and non-linear copolymers of the  $(PS_5-b-PDMS_5)_{1,2,6}$  sequences after thermal annealing at  $100^\circ\text{C}$  for one day were studied through TEM and SAXS (Figure 6.58). The symmetric composition gave rise to lamellar morphologies as indicated by the Bragg peaks at relative positions equal to  $q/q^*=1:2:3$ . The domain spacing was calculated 16.5 nm, 17 nm and 17 nm for the linear diblock, the triblock and six arm star block copolymers respectively. Toluene was also used to prepare bulk films but the symmetric volume fraction of the individual blocks had not allowed any transformation of the phase. The TEM micrographs further verified the formation of black PDMS and white PS domains corresponding to the lamellar phase.

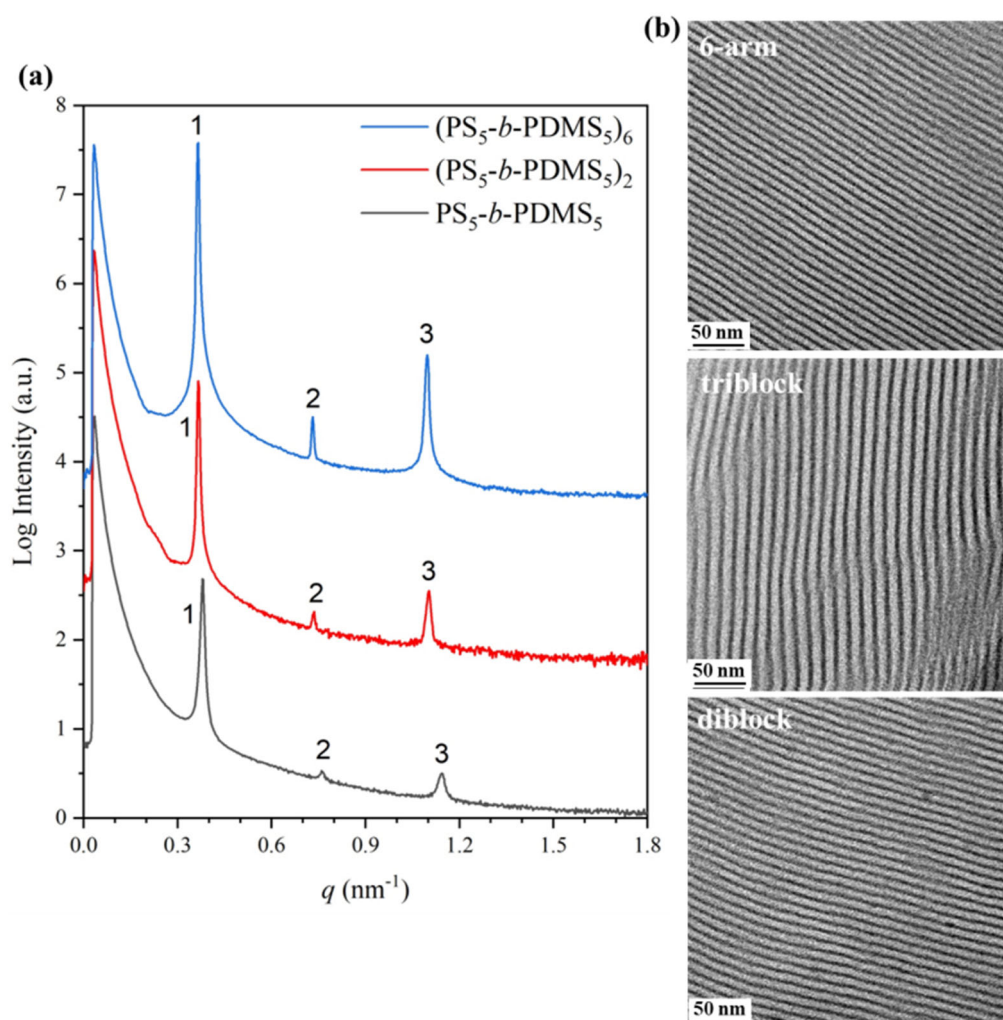


**Figure 6.58:** Combined results with respect to the 1D SAXS plots of (a) the  $PS_5-b-PDMS_5$  (black line),  $(PS_5-b-PDMS_5)_2$  (red line) and  $(PS_5-b-PDMS_5)_6$  (blue line) and (b) the corresponding TEM micrographs.

### Set number 13

A higher molecular weight diblock was used as the precursor for the preparation of one triblock and one six-arm star block copolymer. Specifically the  $(\text{PS}_{15.7}\text{-}b\text{-PDMS}_{11.1})_n$  samples, where  $n=1, 2$  or  $6$ , with  $\phi_{\text{PDMS}}=0.44$  were casted in cyclohexane and thermally annealed for one day at  $100^\circ\text{C}$ . Lamellar structures appeared, as clearly indicated by the multiple peaks at a  $q$  ratio of 1:2:3:4 for the diblock precursor and of 1:2:3:4:5:6 for the remaining samples, in the SAXS patterns [Figure 6.59 (a)]. The domain periodicity was calculated 27.5, 27.8 and 28.0 nm for the  $\text{PS}_{15.7}\text{-}b\text{-PDMS}_{11.1}$ ,  $(\text{PS}_{15.7}\text{-}b\text{-PDMS}_{11.1})_2$  and  $(\text{PS}_{15.7}\text{-}b\text{-PDMS}_{11.1})_6$  respectively. Well-oriented black (PDMS) and white stripes (PS) were also observed in the TEM studies [Figure 6.59 (b)]. For the 6-arm star block copolymer continuous lamellar layers bending in particular boundaries corresponding to a chevron texture was evident. This fact may be attributed to the overcrowding of the PDMS core, thus, the dissimilar elasticity between the two segments (flexible inner chains vs. rigid outer chains) gives rise to the formation of bended lamellar sheets.

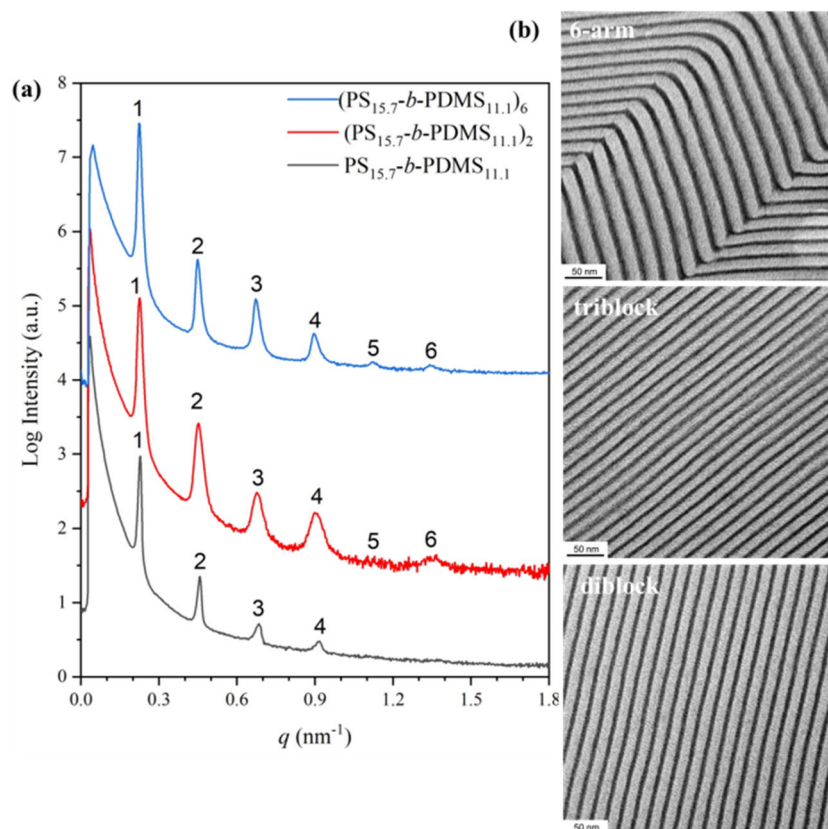


**Figure 6.59:** Combined results with respect to (a) the 1D SAXS plots of the  $\text{PS}_{15.7}\text{-}b\text{-PDMS}_{11.1}$  (black line),  $(\text{PS}_{15.7}\text{-}b\text{-PDMS}_{11.1})_2$  (red line) and  $(\text{PS}_{15.7}\text{-}b\text{-PDMS}_{11.1})_6$  (blue line) and (b) the corresponding TEM micrographs. All samples were casted in cyclohexane and were thermally annealed for one day at  $100^\circ\text{C}$ .

Interestingly enough, a different self-assembled behavior was adopted for the samples after casting in toluene. Note that the solvent was left to evaporate in a five day time period and no thermal annealing was conducted. Significant deviations on the obtained morphologies between the diblock precursor, the triblock and 6-arm star block copolymers were observed. Three different network structures were formed for the three different sequences, a fact that has never been reported for such a series of samples. The reflections evident in the  $PS_{15.7-b-PDMS_{11.1}}$  1D SAXS pattern and the ones in the  $(PS_{15.7-b-PDMS_{11.1}})_2$  are attributed to the formation of  $tDD$  and  $tDG$  ( $t$ : triclinic) phases respectively. The high extent of distortion on the lattices is straightforward due to the splitting of multiple peaks. The network phases were also confirmed by the 2D SAXS patterns. TEM experiments were carried out to determine the adopted morphologies and the results strongly suggested the formation of DD and DG structures. The 1D, 2D SAXS and the TEM images are observed in Figure 6.60.

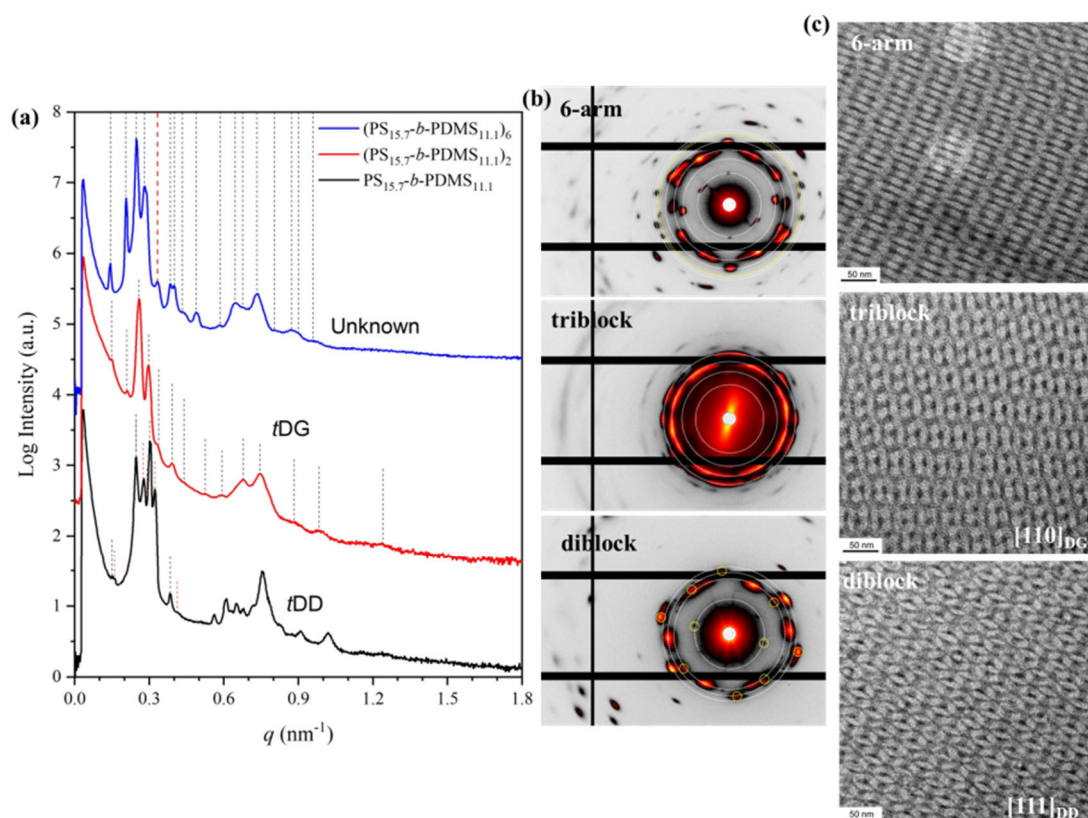


**Figure 6.60:** Combined results with respect to the 1D SAXS plots of the (a)  $PS_{15.7-b-PDMS_{11.1}}$  (black line),  $(PS_{15.7-b-PDMS_{11.1}})_2$  (red line) and  $(PS_{15.7-b-PDMS_{11.1}})_6$  (blue line), (b) 2D SAXS patterns and (c) the corresponding TEM micrographs. All samples were prepared using toluene and studied as cast.

The complex architecture star block copolymer with the 6 arms induced a novel network phase in which the scattering positions could not be allocated to any of the already known structures. The Bragg reflections appeared at the relative  $q$  values of  $\sqrt{2}:\sqrt{4}:\sqrt{6}:\sqrt{8}:\sqrt{11}:\sqrt{14}:\sqrt{16}:\sqrt{18}$ . The additional strong reflection ( $\sqrt{11}$ ) indicates the formation of a new network phase which is also confirmed by the relative TEM micrograph.

To further study the adopted phase on the 6-arm star, the casting procedure was conducted again in toluene and the solvent was left to evaporate for seven days. 1D and 2D scattering experiments were carried out at 30°C and 90°C to clarify the self-assembled structure. The casting procedure gave rise to the reflections at the relative peak positions of  $\sqrt{2}:\sqrt{4}:\sqrt{8}:\sqrt{10}$  (indicated with black dash lines) and additional peaks (red dash lines). In Figure 6.61 the scattering results and a corresponding TEM image are presented.

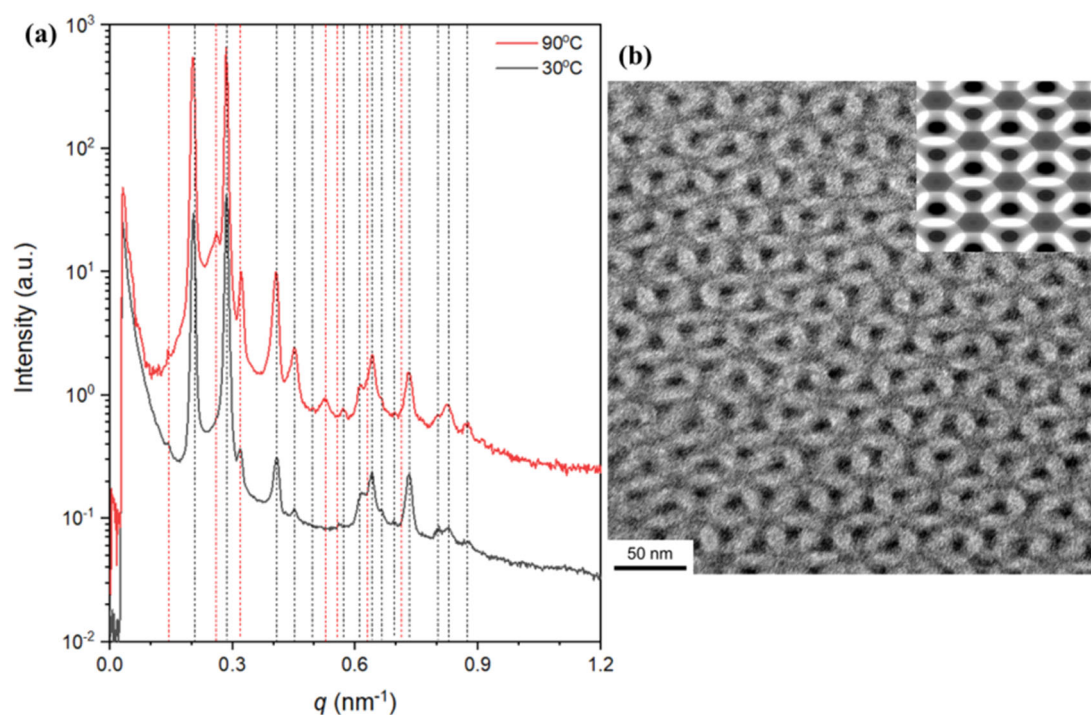


**Figure 6.61:** Combined results with respect to the (a) 1D SAXS profiles of the  $(PS_{15.7}\text{-}b\text{-}PDMS_{11.1})_6$  at 30 °C (black line) and 90 °C (red line) (b) TEM micrograph. (Inset) Corresponding image based on simulation.

The formation of a cubic lattice is confirmed by the 2D SAXS pattern in which the Cartesian coordinates are given in orange (Figure 6.62).

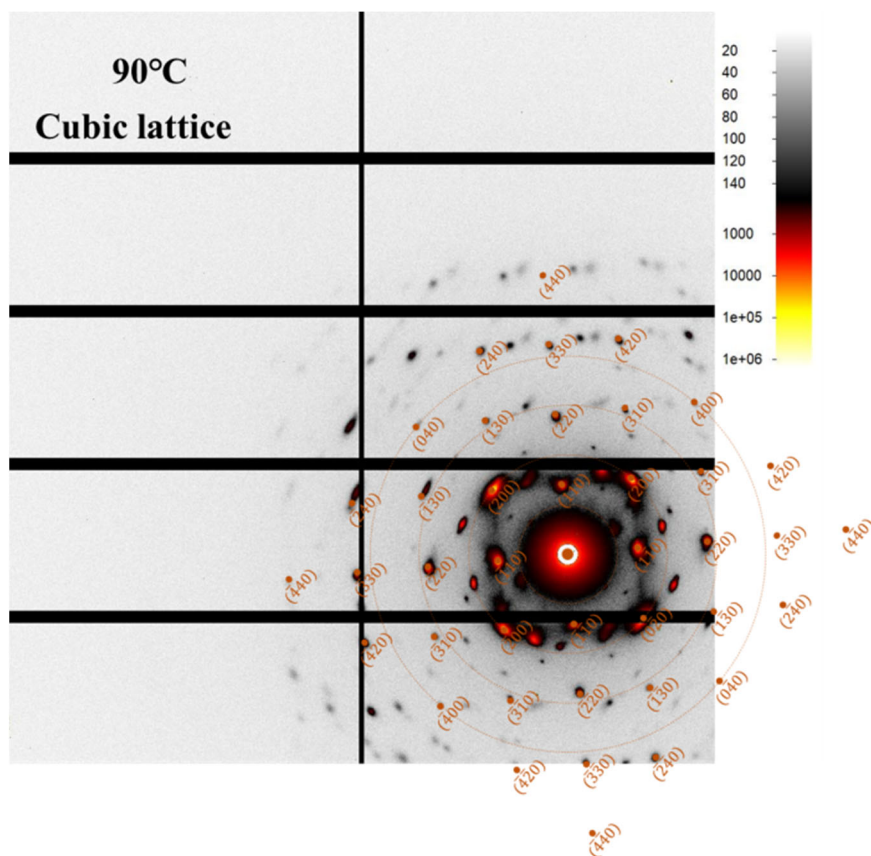


**Figure 6.62:** 2D SAXS pattern of the self-assembled  $(PS_{15.7}\text{-}b\text{-}PDMS_{11.1})_6$  at  $90^\circ\text{C}$ .

#### **Set number 14**

The  $PS_{22}\text{-}b\text{-}PDMS_{15}$  and  $(PS_{22}\text{-}b\text{-}PDMS_{15})_2$  sequences with  $\phi_{PDMS}=0.47$  were casted in cyclohexane and studied through SAXS (Figure 6.63). For the  $PS_{22}\text{-}b\text{-}PDMS_{15}$  the four sharp reflections at the relative  $q$  values of 1:2:3:4 revealed the formation of a lamellar morphology. Similar results were also obtained for the triblock copolymer. Based on the primary peaks the domain spacing values were calculated 37 and 35 nm for the linear diblock and triblock copolymers respectively. Further characterization on the synthesized samples is required and constitutes a future perspective of this thesis. Note that, the major discrepancies on the self-assembly behavior have been observed in the intermediate molecular weight complex architecture copolymers. As a result the meticulous characterization of the samples is considered of major importance.

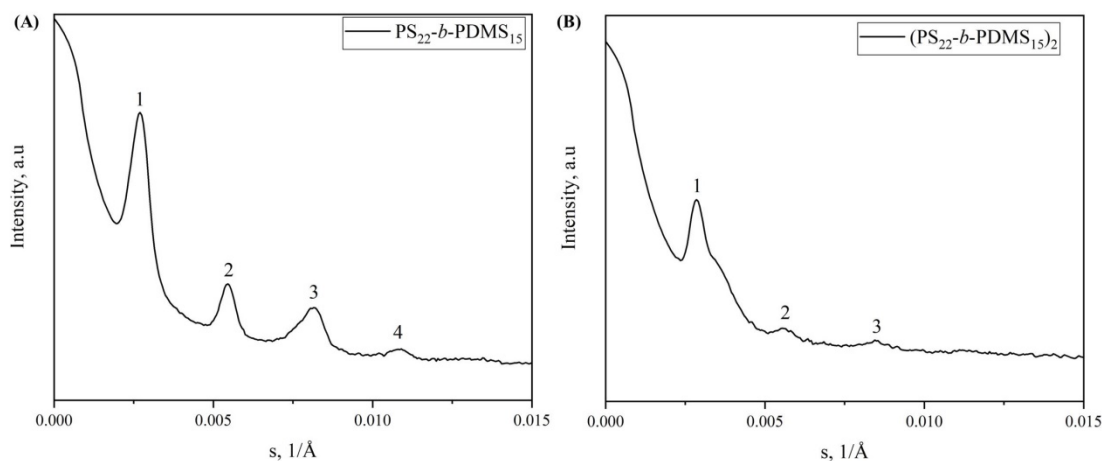


**Figure 6.63:** 1D SAXS profiles of the (a)  $PS_{22}\text{-}b\text{-}PDMS_{15}$  and (b)  $(PS_{15.7}\text{-}b\text{-}PDMS_{11.1})_2$ .

### **Set number 15**

The last set to be discussed is  $(PS_{14}\text{-}b\text{-}PDMS_6)_{1,2,3,4,6}$  which constitutes the only series of samples that the triblock copolymer as well as the three-, four- and six-arm star block copolymers were synthesized using the same diblock copolymer precursor. The specific sequences were prepared to study the structure/properties relationship as the architecture varies and the molecular characteristics of the copolymer arms remained identical. All samples were casted in cyclohexane and subsequently submitted to thermal annealing for 1 day at  $100^\circ\text{C}$ . Note that, the  $\phi_{PDMS}$  equals to 0.34 and based on the theoretical phase diagram<sup>9</sup> cylindrical phases are expected.

Regarding scattering results [Figure 6.64 (a)], it is concluded that the structures are well-defined due to the sharp primary peaks and the adopted morphologies can be identified by the Bragg-reflection sequences. For the diblock and triblock copolymers the seven reflections at the relative  $q$  positions of  $q/q^*=1:\sqrt{3}:2:\sqrt{7}:3:4:5$  are consistent with a well-ordered cylindrical morphology. Similar projections were also obtained for the three-arm star block copolymer at the scattering peak ratio of  $q/q^*=1:\sqrt{3}:2:\sqrt{7}:3:4$ . Bragg's equation led to a domain spacing equal to 21.1 nm ( $q^*=0.297\text{nm}^{-1}$ ) with a corresponding unit cell size ( $\alpha=2d/\sqrt{3}$ ) of 24.3 nm for the diblock precursor. Coherent results concerning neighboring cylinders inter-domain spacing were acquired for the triblock as well as 3-arm star block copolymers.

TEM measurements [Figure 6.64 (b)] on the linear diblock and the three-arm star block copolymers, showcased a hexagonal arrangement of PDMS cylinders in the PS matrices as well as alternating bright and dark regions corresponding to in-plane cylinders further verifying the scattering results. In the TEM image of the triblock copolymer only limited cylinders are evident.

For the 4- and 6-arm star samples a different structure was obtained. Notably, SAXS results demonstrated a different scattering pattern with the relative peaks at a ratio of  $q/q^*=1:2:3:4:5$ , typical for the lamellar phase and the domain spacing values calculated from the distinct first order peaks were approximately 21.9 nm. It should be mentioned that, TEM imaging is limited to selective areas while SAXS is related to overall ordering of the examined sample. In the related TEM images alternating lamellae domains could be clearly observed especially for the 4-arm star, while the grain boundary regions in which vertical cylinders appear are quite limited for the more complex architecture copolymer (6-arm). One possible explanation regarding the cylinders-like domains in the TEM images of the 6-arm star may be attributed to the formation of broken chevron tilt grain boundaries that had been reported for a miktoarm star block copolymer of the  $I_5S$  type [I: poly(isoprene), S: polystyrene].<sup>195</sup> The overcrowding effect due to the multiple PDMS chains and the difference on the elasticity between PS and PDMS caused the interfacial bending and the discontinuity in the chevron texture.

The major discrepancy on the adopted morphology could not be attributed to the solution casting process due to the use of a non-selective solvent which is not able to promote any non-equilibrium kinetically trapped morphology. Two plausible explanations can be provided with respect to the formation of a lamellar morphology in the 4- and 6- arm stars. In one case, the cylinders during solution casting were predominantly allocated horizontally due to the existence of multiple arms that cause overcrowding effect and favor the parallel orientation. To further explore this argument 2D SAXS patterns were acquired, which could not support the formation of longitudinal oriented cylinders. A different elucidation of the adopted structure involves the effect of complex architecture systems on the phase diagram. Even though the volume fraction of PDMS does not justify the formation of alternating lamellae structure, the phase boundaries on star block copolymers according to self-consistent field theory<sup>9</sup> demonstrate significant shifts when compared to the ones of the respective diblock copolymers.

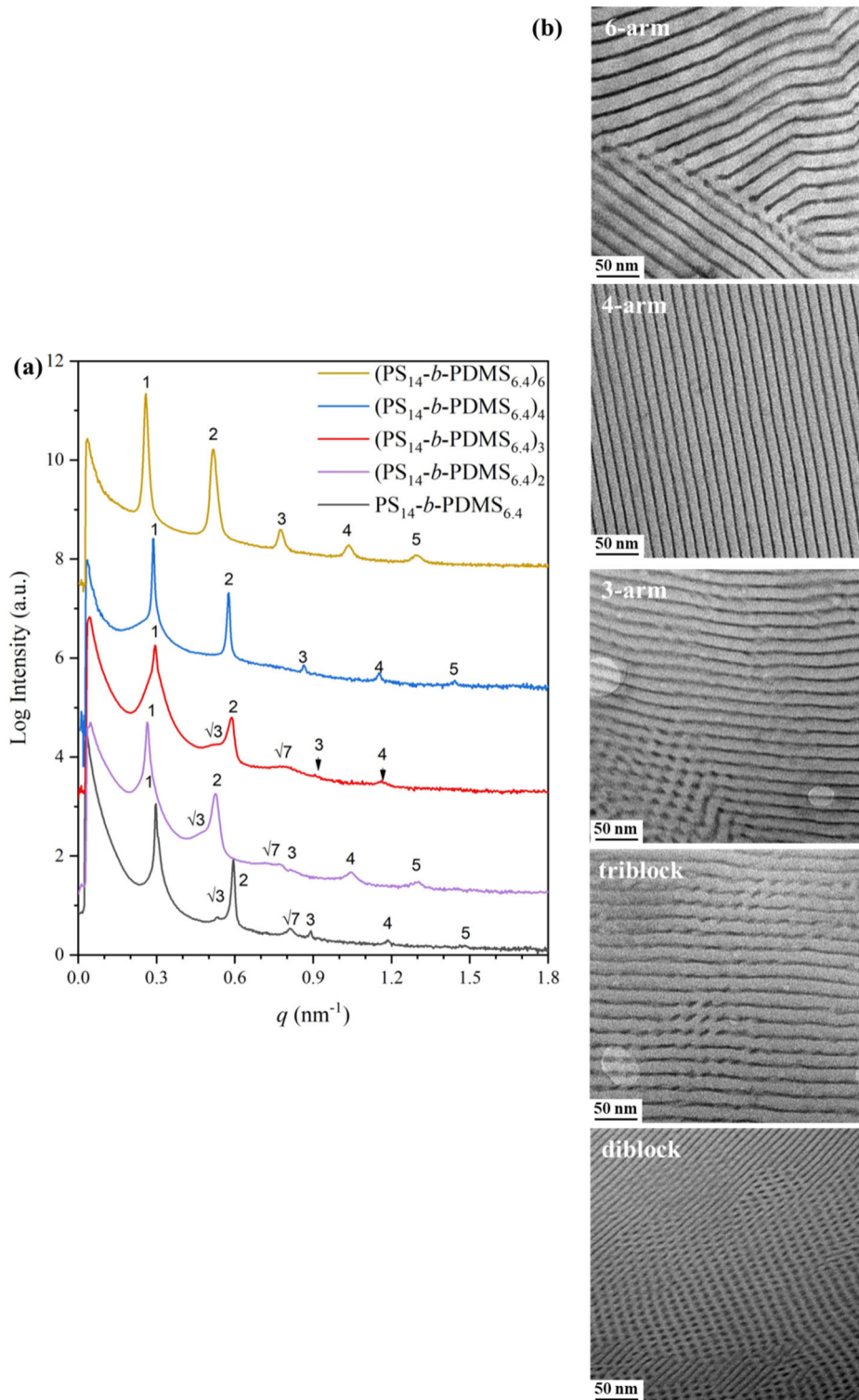


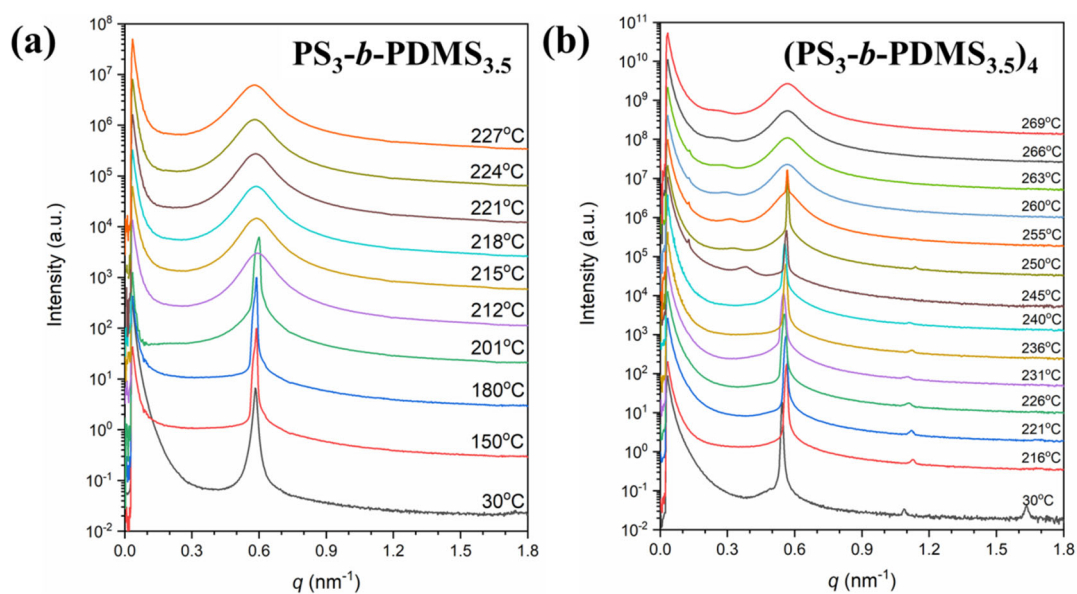
**Figure 6.64:** Combined results with respect to (a) the 1D SAXS plots of the  $PS_{14}$ - $b$ - $PDMS_6$  (black line),  $(PS_{14}$ - $b$ - $PDMS_6$ )<sub>2</sub> (purple line),  $(PS_{14}$ - $b$ - $PDMS_6$ )<sub>3</sub> (red line),  $(PS_{14}$ - $b$ - $PDMS_6$ )<sub>4</sub> (blue line) and  $(PS_{14}$ - $b$ - $PDMS_6$ )<sub>6</sub> (yellow line) (b) the corresponding TEM micrographs. All samples were casted in cyclohexane and were thermally annealed for one day at 100 °C.

## 6.9 Topological Effect on Order-Disorder Transition

The high incompatibility between the individual blocks in a PS-*b*-PDMS system has led to a  $\chi$  value equal to 0.27 at room temperature based on the equation  $\chi=68.0T^{-1} - 0.037$ .<sup>147</sup> In the related study, the homopolymer binary blends of the PS and PDMS were used for the calculation of  $\alpha$  and  $\beta$  values used in the  $\chi=\alpha T^{-1} + \beta$  equation. In a comprehensive study conducted by Fredrickson et al.<sup>196</sup> it has been demonstrated that binary systems and block copolymers should not share a common  $\chi$  parameter.

Hillmyer et al.<sup>197</sup> reported a different equation and specifically  $\chi=33.6T^{-1} + 0.033$  that concluded to a lower  $\chi$  value (0.15 at room temperature), using a volume reference of 118 Å<sup>3</sup> and two different PS-*b*-PDMS samples<sup>198</sup> which have been used in a different publication.

In the framework of this dissertation the order-disorder transition temperatures for specific copolymer sequences were estimated through in situ temperature resolved scattering experiments. In situ SAXS studies were carried out in samples: PS<sub>3</sub>-*b*-PDMS<sub>3.5</sub>, (PS<sub>3</sub>-*b*-PDMS<sub>3.5</sub>)<sub>3</sub>, (PS<sub>3</sub>-*b*-PDMS<sub>3.5</sub>)<sub>4</sub>, PS<sub>5</sub>-*b*-PDMS<sub>3.4</sub>, (PS<sub>5</sub>-*b*-PDMS<sub>3.4</sub>)<sub>3</sub>, PS<sub>3.9</sub>-*b*-PDMS<sub>4.1</sub>, (PS<sub>3.9</sub>-*b*-PDMS<sub>4.1</sub>)<sub>3</sub> and PS<sub>5</sub>-*b*-PDMS<sub>5</sub>. Some representative 1D SAXS profiles demonstrating the ODT temperature are presented in Figures 6.65 a-f.



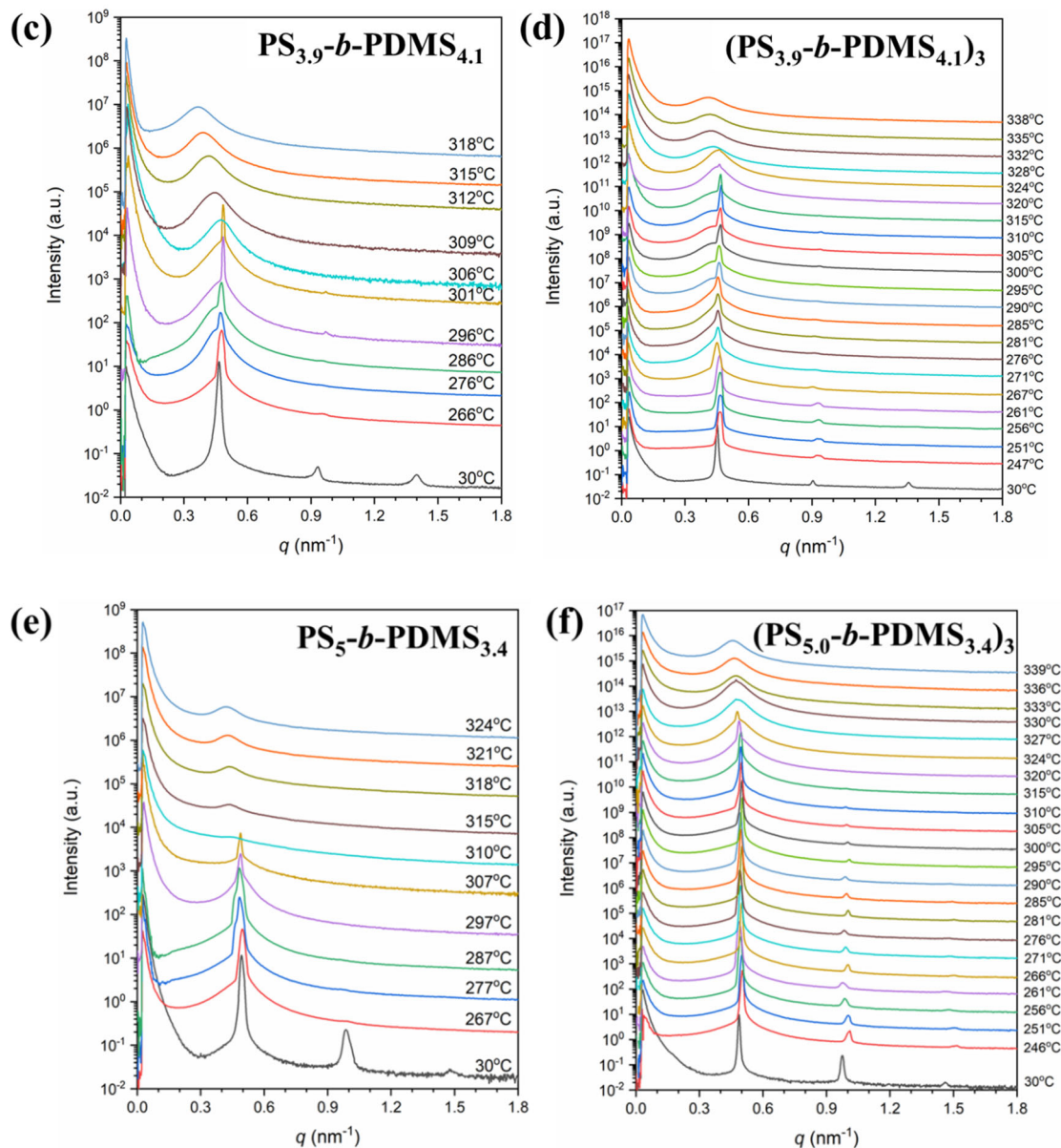


**Figure 6.65:** In-situ SAXS profiles indicating the ODT temperatures with respect to the: (a)  $\text{PS}_3\text{-}b\text{-PDMS}_{3.5}$ , (b)  $(\text{PS}_3\text{-}b\text{-PDMS}_{3.5})_4$ , (c)  $\text{PS}_{3.9}\text{-}b\text{-PDMS}_{4.1}$ , (d)  $(\text{PS}_{3.9}\text{-}b\text{-PDMS}_{4.1})_3$ , (e)  $\text{PS}_5\text{-}b\text{-PDMS}_{3.4}$  and (f)  $(\text{PS}_5\text{-}b\text{-PDMS}_{3.4})_3$ .

As the temperature increases the intensity of the primary peaks becomes weaker and shifts to lower  $q$  regions indicating the transition from order to disorder for all copolymer sequences. In addition, the complex architecture copolymers experienced an ODT at higher temperatures comparing to their linear precursors as clearly evidenced in Figure 6.66, indicating a severe topological effect due to the multiple arms. Also, the higher molecular weight linear diblock copolymers showcase a substantially increased ODT (for example  $\sim 350$  °C for  $\text{PS}_5\text{-}b\text{-PDMS}_5$  vs.  $\sim 212$  °C

for PS<sub>3</sub>-*b*-PDMS<sub>3.5</sub>) when compared to the lower molecular weight ones. Important is to mention that, in all cases a lamellar morphology was adopted and an order-order transition had not taken place in any copolymer sequence.

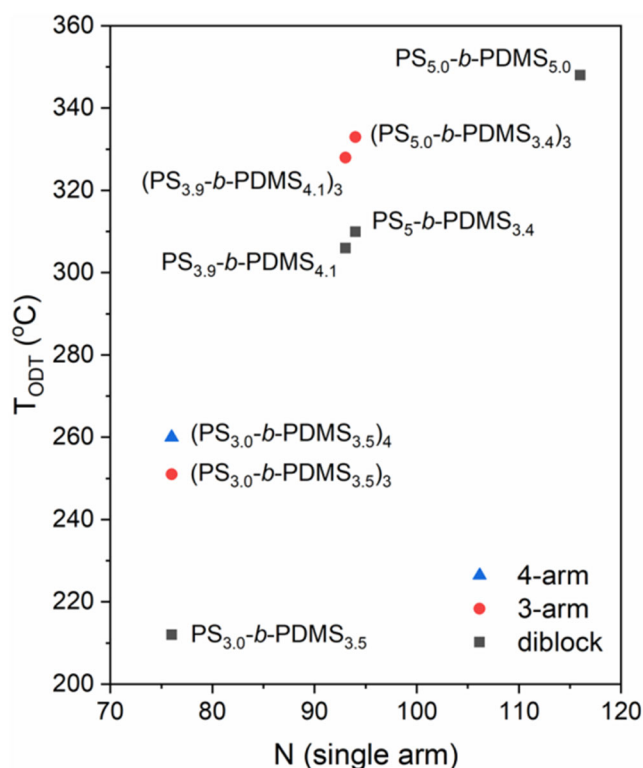


**Figure 6.66:** ODT temperatures as a function of  $N$  with respect to the: PS<sub>3</sub>-*b*-PDMS<sub>3.5</sub>, (PS<sub>3</sub>-*b*-PDMS<sub>3.5</sub>)<sub>4</sub>, PS<sub>3.9</sub>-*b*-PDMS<sub>4.1</sub>, (PS<sub>3.9</sub>-*b*-PDMS<sub>4.1</sub>)<sub>3</sub>, PS<sub>5</sub>-*b*-PDMS<sub>3.4</sub>, (PS<sub>5</sub>-*b*-PDMS<sub>3.4</sub>)<sub>3</sub> and PS<sub>5</sub>-*b*-PDMS<sub>5</sub>.

Using the Fredrickson-Helfand<sup>77</sup> Theory:

$$(\chi N)_{\text{ODT}} = 10.495 + 41.022\bar{N}^{-\frac{1}{3}} + 123.0\bar{N}^{-0.56} \quad (6.7)$$

$$\text{where } b_{AB} = \sqrt{f_A^v l_A^2 + f_B^v l_B^2}, \bar{N} = \frac{N b_{AB}^6}{v_0^2}, v_0 = 0.108 \text{ \AA}^3$$

and based on the experimentally observed results, a diagram of  $\chi$  as a function of the inversed ODT temperature was plotted and presented in Figure 6.67. All different copolymer sequences studied are included in the diagram and a linear regression is evident demonstrating that higher  $N$  values lead to higher  $\chi$  values. Important is to mention, that star block copolymers showcase higher  $\chi$  value than their respective linear precursors.

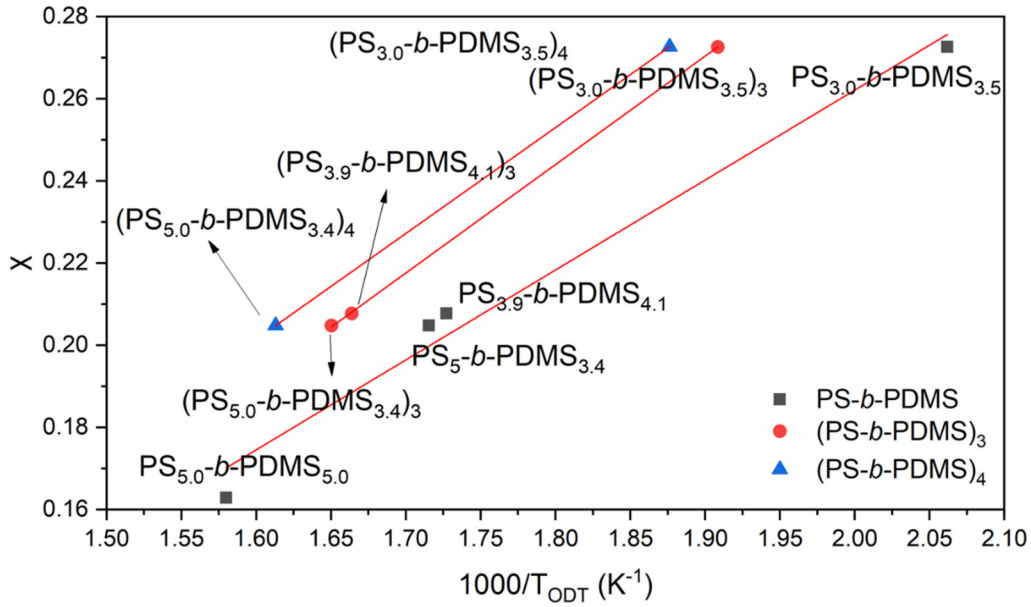


**Figure 6.67:** Parameter  $\chi$  as a function of the inversed ODT temperature for the various copolymer sequences. Black symbols correspond to the linear copolymers, red and blue symbols to the 3- and 4-arm star block copolymers respectively.

For the linear diblock copolymers the following relationship is established:

$$\chi(T) = \frac{218.9}{T} - 0.176 \quad (6.8)$$

for the three-arm star block copolymers the equation is expressed as follows:

$$\chi(T) = \frac{264.0}{T} - 0.231 \quad (6.9)$$

for the four-arm star block copolymers the  $\chi$  value can be calculated through the equation:

$$\chi(T) = \frac{257.7}{T} - 0.210 \quad (6.10)$$

The above mentioned results indicate a substantially increased  $\chi$  value compared to the one already been thoroughly used for the PS-*b*-PDMS system. Specifically for the linear diblock copolymers a  $\chi$  parameter of 0.55 at 25 °C is calculated from equation 6.8, strongly suggesting the highly segregated character of the individual blocks.

This study is considered of major significance because it includes experimental results of various copolymers systems and also it clearly demonstrates the effect of complex architecture on the self-assembly behavior. Note that, the structure/property relationship of star block copolymers is limited due to the time-consuming experimental procedures in combination with the living polymerization techniques required, rendering their synthesis quite demanding. Their self-assembled

behavior is based mainly on theoretical calculations. The specific study further verifies the potential use of the  $(\text{PS-}b\text{-PDMS})_n$  (where  $n=1, 2, 3, 4$  or  $6$ ) in physics-related studies. The ability to synthesize different copolymer sequences with various molecular characteristics would probably contribute to the construction of an experimental phase diagram based exclusively on the highly segregated PS-*b*-PDMS copolymers.

### 6.10 Morphological Characterization of Block Copolymers in Thin Film State

The  $\text{PS}_{15}\text{-}b\text{-PDMS}_{10}$  and the  $(\text{PS}_{15}\text{-}b\text{-PDMS}_{10})_3$  sequences were further studied to justify any discrepancies with respect to the self-assembly in thin film state between the linear and non-linear architecture.

Thin films with thickness of approximately 100 nm were prepared through spin coating onto silicon wafers from 3 wt % dilute solutions of the copolymers in cyclohexane at 2500 rpm. The films were thermally annealed at 120°C in a hot stage for 1 hour and then immersed in liquid nitrogen. Scanning probe microscopy (SPM) experiments were conducted on the as-spun thermally annealed films.

As expected, the lower surface energy of the PDMS segments induced the formation of a silicon oxide layer in the top surface of the films due to the preferential segregation at the air/polymer interface. A representative example of the PDMS layer at the top air-film surface is presented in Figure 6.68 a (height) and b (phase) in which a smooth surface is evident. A short  $\text{CF}_4/\text{O}_2$  plasma treatment (in a 2:1 ratio) is required to etch the PDMS surface layer followed by oxygen plasma to remove the PS and oxidize the PDMS for adequate contrast. In the  $\text{PS}_{15}\text{-}b\text{-PDMS}_{10}$  precursor, lamellae domains without long range order was observed after RIE [Figure 6.68 c (height) and d (phase)]. The lack of well-ordered domains may be attributed to the processing parameters. Higher annealing temperature for shorter annealing times may lead to improved order due to the higher diffusivity of the chains.

The three arm star block copolymer of the  $(\text{PS}_{15}\text{-}b\text{-PDMS}_{10})_3$  type exhibited improved order as shown in Figure 6.68 e (height) and f (phase). This fact is probably allocated to the complex architecture in combination with the significantly high  $N$  value. A future perspective of this PhD thesis is to study the self-assembled morphology at the interface of the copolymers and the  $\text{SiO}_2$  substrate to determine the entropy effect of the star architecture.

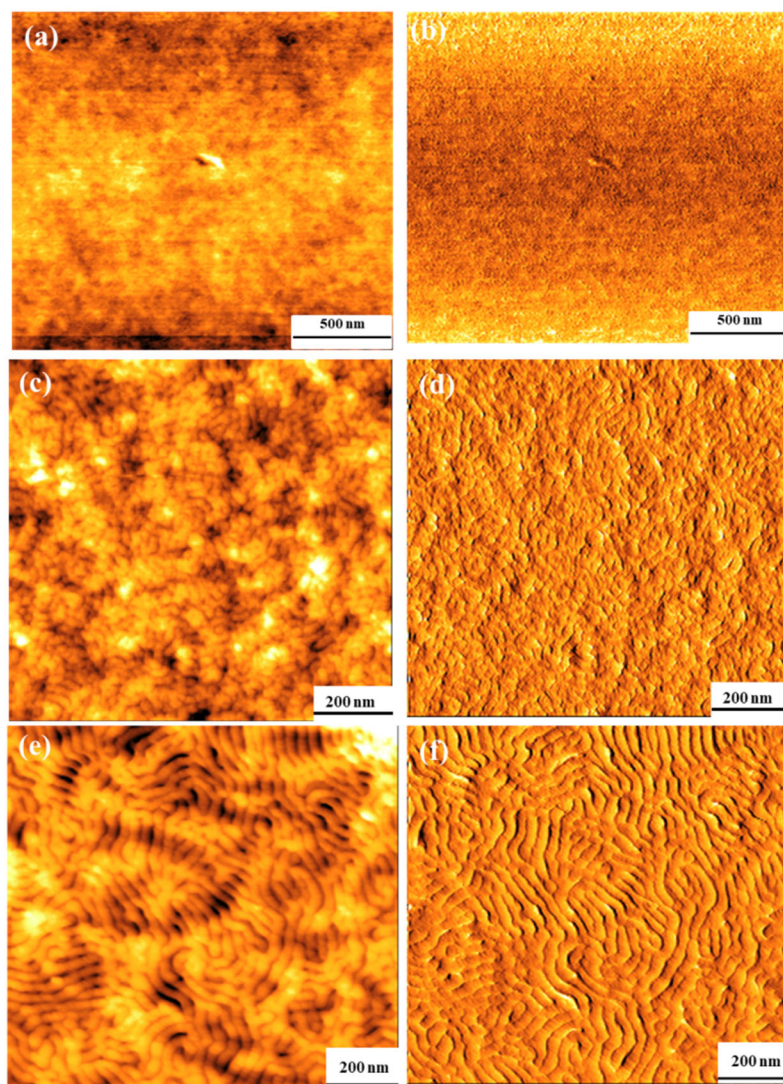


**Figure 6.68:** SPM top-view height (a,c,e) and phase images (b,d,f) of set number 6 corresponding to the  $(PS_{15}\text{-}b\text{-}PDMS_{10})_{1,3}$  copolymers. Specifically: (a)-(b) corresponds to the thermally annealed  $(PS_{15}\text{-}b\text{-}PDMS_{10})_3$  without RIE, (c)-(d) to the thermally annealed  $PS_{15}\text{-}b\text{-}PDMS_{10}$  after RIE and (e)-(f) to the thermally annealed  $(PS_{15}\text{-}b\text{-}PDMS_{10})_3$  after RIE.

## CHAPTER 7

### Conclusions-Future Work

#### 7.1 Conclusions

Even though anionic polymerization requires time-consuming reactions, meticulous purification procedures of all compounds involved in the polymerization and the knowledge of scientific glassblowing in order to construct the necessary apparatuses, well defined narrow-dispersed linear and complex architecture star block copolymers consisting of PS and PDMS can be synthesized. The ability to synthesize various architecture copolymers with different molecular characteristics (molecular weights and composition) enables the extensive use of the systems for several studies related to polymer physics and potential applications.

The samples were divided in two categories to provide the conclusions from the molecular, thermal and morphological characterizations and specifically:

- (a) Linear diblock copolymers of the PS-*b*-PDMS type
- (b) Linear and non-linear copolymers of the (PS-*b*-PDMS)<sub>*n*</sub> sequences, where *n* = 1 or 2 or 3 or 4 or 6.

Size exclusion chromatography, membrane osmometry or vapor pressure osmometry and proton nuclear magnetic resonance spectroscopy were performed to determine the molecular characteristics of the synthesized copolymers and to verify the high molecular and compositional homogeneity. Differential scanning calorimetry was conducted to determine the thermal transitions and their variations as the molecular weight and/or the architecture changes. To study the self-assembly behavior of the synthesized materials and to establish the structure/property relationship between the linear and non-linear copolymers, morphological characterization techniques including small angle X-ray scattering and transmission electron microscopy were carried out. Additionally, 3D-TEM and FESEM, were employed in certain cases to further characterize the samples.

Important is to mention that the majority of the aforementioned morphological characterization methods were carried out in the Chemical Engineering Department at National Tsing Hua University located in Hsinchu, Taiwan, through the collaboration with Professor Rong-Ming Ho and his research group.

### ***Linear diblock copolymers of the PS-*b*-PDMS type***

The samples were synthesized through sequential anionic polymerization under high vacuum techniques, using rinsed vessels and purified reagents. Depending on the aimed molecular characteristics the appropriate quantities of the reagents were employed.

The conclusions drawn from the molecular characterization are concisely presented as follows:

- ✓ The  $\bar{M}_n$  values of the eight linear diblock copolymers were calculated through SEC and MO. Different molecular weights (ranging from 20,000 to 130,000 g/mol) and volume fraction ratios between the individual blocks were chosen to induce diverse structures during microphase separation.
- ✓ Monomodal distributions were obtained in all sequences and the dispersity indices varied from 1.02 to 1.08, which in accordance with the high standards of anionic polymerization.
- ✓ The mass as well volume fractions of the individual blocks were calculated through  $^1\text{H-NMR}$  which further indicated the successful synthesis and the high molecular and compositional homogeneity degree.

The thermal analysis was performed through DSC and the glass transition temperatures as well as any evident crystallization and/or melting temperatures were measured for all synthesized linear diblock copolymers. More specifically:

- ✓ The existence of two separate  $T_g$  at values similar to those already reported for the respective homopolymers verified the immiscibility between the constituent segments indicating the potential microphase separation during self-assembly studies.
- ✓ The  $T_g$  values with respect to the PS segments were evident in the region of 97 °C to 109 °C while for the PDMS in the region of -120 °C to -127 °C.
- ✓ In all copolymer sequences an additional transition corresponding to the melting temperature of the PDMS crystallites was observed in the region of -32 °C to 49 °C.
- ✓ In the case of PS<sub>14</sub>-*b*-PDMS<sub>9.0</sub> a transition at approximately -86 °C is attributed to the cold crystallization of PDMS. This behavior is witnessed during heating due to the presence of nuclei grown in the previous cooling cycle.

The morphological characterization results through TEM and SAXS indicated the formation of various structures directly associated to the solvent used during solution casting. In all cases well-defined domains separated by narrow IMDS were observed. The conclusions are summarized as follows:

- ✓ Diverse structures exhibiting long-range order ranging from hexagonally close packed cylinders, alternating lamellae and cubic network phases were obtained depending on the molecular characteristics and the use of a selective or a non-selective solvent.
- ✓ PS<sub>55</sub>-*b*-PDMS<sub>31</sub> with  $\phi_{\text{PDMS}}=0.42$  showcased a lamellar morphology after casting in a non-selective solvent (cyclohexane). The use of a selective solvent (chloroform) induced the formation of network phases strongly related to the evaporation rate of the solvent as verified by TEM, 3D-TEM and 2D SAXS measurements.
- ✓ The solution casting led to the formation of a novel kinetically trapped double primitive phase, while order-order transitions from hexapod to tetrapod and finally to tripod networks were experienced by tuning the temperature during in situ SAXS experiments.
- ✓ The ability to adopt either double diamond or double gyroid phases taking advantage of the same diblock copolymer led to the fabrication of well-ordered nanonetwork epoxy resins modified with poly(butyl acrylate)-*b*-poly(methyl methacrylate) block copolymer for enhanced energy dissipation.
- ✓ The samples with close molecular characteristics adopted double gyroid morphologies after solution casting to selective solvents due to the volume fraction differentiation when compared to the PS<sub>55</sub>-*b*-PDMS<sub>31</sub> sequence.

***Linear and non-linear diblock copolymers of the (PS-*b*-PDMS)<sub>n</sub> type where n=1 or 2 or 3 or 4 or 6***

The linear diblock precursors were synthesized using anionic polymerization through sequential addition of the two monomers. The diblock copolymer active sites were coupled with the appropriate chlorosilane reagents to obtain star block copolymers with the desired functionality. In all cases a small quantity of the precursors was kept to perform all the necessary molecular, thermal and morphological characterizations and to evaluate the effect of complex architecture on the solution and solid state properties.

*The synthesis of six arm star block copolymers consisting of PS and PDMS is of major importance and has not been mentioned in the literature yet. In addition, the morphological characterization of the star shaped materials with six equivalent arms is considered quite novel and would potentially lead to better understanding of the self-assembly mechanism when the complexity of the systems is increased.*

The conclusions from the molecular characterization concerning the linear diblock precursors and the corresponding linear and non-linear star block copolymers are listed below:

- ✓ The accurate  $\bar{M}_n$  values of all linear and non-linear diblock copolymers were calculated through MO or VPO due to the inability of SEC to resolve more complex architecture copolymers. Thus, SEC constitutes a reliable tool to monitor the course of the coupling reactions, the successful fractionation procedure and the dispersity indices in the linear triblock and non-linear three, four and six arm star block copolymers.
- ✓ Of particular importance is the effective fractionation of the triblock and star block copolymers through a proper solvent/ non-solvent pair in order to remove any unreacted species and/or star with undesired functionality.
- ✓ Narrow-dispersed copolymers with dispersity indices lower than 1.09 were obtained in all cases.
- ✓ The mass as well as volume fractions of the individual blocks were calculated through  $^1\text{H-NMR}$  experiments. The  $\phi_{\text{PDMS}}$  varied from 0.34 to 0.60 to induce different structures during self-assembly studies.

DSC experiments were carried out to specify the thermal transitions of the components in the different architecture copolymers. The conclusions are summarized as follows:

- ✓ Two distinct glass transition temperatures at values similar to those already reported for the corresponding homopolymers were observed in all copolymer sequences verifying the immiscibility of the two different blocks. Furthermore, in some cases additional transitions corresponding to the melting and crystallization temperatures of the PDMS crystallites were evidenced.

- ✓ The complexity of the system had not any significant impact on the glass transition temperatures of the segments when compared to the linear precursors, even though the triblock and star block copolymers showcase increased molecular weight values. This behavior is probably allocated to the fact that the linear and non-linear star block copolymers are constituted by multiple linear diblock copolymer chains (arms) connected to a central junction point (core) and the arms exhibit identical chemical composition and total number average molecular weight.

The characterization of all different architecture copolymers in bulk was performed using TEM and SAXS. The main objective was to study the structure/properties relationship and to compare the effect of the conformational asymmetry on the microphase separation as the architecture varies. The conclusions are listed below:

- ✓ Well-ordered structures were obtained even in samples with extremely low  $\bar{M}_n$  values. Although, the more complex architecture copolymers exhibit enhanced ordering due to the significantly increased molecular weights. Similar domain spacing values were obtained for the more complex architecture copolymers and their corresponding linear precursors. Various structures including lamellar, cylindrical and cubic network phases were obtained.
- ✓ The (PS<sub>3</sub>-*b*-PDMS<sub>3.5</sub>)<sub>1,3,4</sub> sequences showcased the lower domain spacing values reported in bulk for the specific samples. Domain periodicities equal to 10.8 and 11.5 nm for the precursor and the three as well as four arm star block copolymers were obtained, respectively.
- ✓ The PS<sub>3.6</sub>-*b*-PDMS<sub>3.6</sub> linear precursor and the corresponding (PS<sub>3.6</sub>-*b*-PDMS<sub>3.6</sub>)<sub>3</sub> three arm star as well as the four arm star of the (PS<sub>3.9</sub>-*b*-PDMS<sub>4.1</sub>)<sub>4</sub> type were studied with in situ SAXS experiments. In all three cases an interdigitating structure was obtained during solution casting irrespective of the number of arms. An order-order transition from the interdigitating structure to bilayers with 50% increase on the d-spacing was observed as the temperature was raised above the glass transition temperature of the PS. The transition was found to be reversible after

cooling down to room temperature and the star block copolymers experienced an even more profound transition due to the topological effect of complex architecture on the self-assembly.

- ✓ For PS<sub>4.2</sub>-*b*-PDMS<sub>5.6</sub> the wet-brush-like chain packing led to the formation of a superlattice lamellae structure, which was severely restricted in the more complex architecture copolymers. The in-situ SAXS experiments indicated that when temperature increased a transition to the bilayer structure was experienced and after cooling down to room temperature the original morphology was adopted.
- ✓ The major discrepancies concerning the structure/properties relationship were observed in the six-arm star block copolymers. Specifically, in most cases the overcrowding effect and the symmetric topology of the six-arm star induced different morphologies when compared to the linear copolymer precursors and the triblock copolymers.
- ✓ The solution casting in a non-selective solvent indicated that the six arm star block copolymers demonstrate an enlarged regime in which lamellar morphology is formed. This fact is attributed to the complexity of the system that prohibits the curvature of the minority component.
- ✓ A cubic network structure which could not be assigned to one already established in the literature was obtained for the (PS<sub>15.7</sub>-*b*-PDMS<sub>11.1</sub>)<sub>6</sub> after casting in a PS selective solvent.
- ✓ The profound impact of complex architecture on the self-assembly was evidenced in the (PS<sub>14</sub>-*b*-PDMS<sub>6</sub>)<sub>1,2,3,4,6</sub> sequences in which for *n* values higher than 3 a lamellar morphology instead of cylindrical was adopted.
- ✓ The order-disorder temperature with respect to some linear as well as three and four arm star block copolymers was determined through in-situ SAXS experiments.
- ✓ Through the linear fit of the experimental results the following relationships were established:

$$\chi^{\text{diblock}}(T) = \frac{218.9}{T} - 0.176$$

$$\chi^{\text{3-arm}}(T) = \frac{264.0}{T} - 0.231$$

$$\chi^{\text{4-arm}}(T) = \frac{257.7}{T} - 0.210$$

- ✓ A substantially increased  $\chi$  value (0.55 at 25 °C) for the linear diblock copolymers compared to the one reported in the literature was determined.
- ✓ A linear diblock precursor and the respective three-arm star block copolymer were further studied in thin film state to determine the architecture effect on the self-assembly. Even though, the star-block copolymer showcased improved ordered additional studies are required.

## 7.2 Future Work

The immediate future work of this thesis involves:

- (a) The stabilization of double primitive morphology in PS-*b*-PDMS copolymer melts by introducing architectural asymmetry without incorporating additives such as homopolymers.
- (b) Further investigation of the PS<sub>14</sub>-*b*-PDMS<sub>6.4</sub>, PS<sub>14</sub>-*b*-PDMS<sub>9.0</sub> and PS<sub>43</sub>-*b*-PDMS<sub>17</sub> samples in thin film state. Tuning of parameters in order to induce the desired orientation of the domains is of primary importance.
- (c) The study of the complex architecture copolymers in thin film state to gain further insight into the entropy effect.
- (d) Ballistic studies to transfer a thin copolymer layer onto rigid substrates using various incident velocity rates as well as angles.
- (e) The morphological characterization of (PS<sub>4.2</sub>-*b*-PDMS<sub>2.8</sub>)<sub>1,2,6</sub> and (PS<sub>22</sub>-*b*-PDMS<sub>15</sub>)<sub>1,2,6</sub> sequences via TEM.
- (f) Additional study through 3D TEM experiments for the (PS<sub>15.1</sub>-*b*-PDMS<sub>11.7</sub>)<sub>6</sub> to justify the cubic network structure observed in the scattering and real space imaging.
- (g) The submission of one manuscript in a peer reviewed journal related to the novel synthesis and solid state properties of the six-arm star block copolymers as well as the comparison with the respective copolymers with different functionalities.
- (h) The submission of one manuscript in a peer reviewed journal in which a detailed analysis regarding the estimation of  $\chi$  values for the different architecture (PS-*b*-PDMS)<sub>n</sub> (where n= 1, 3 or 4) copolymers will be provided.



## References

1. Cummins C., Ghoshal T., Holmes J. D., Morris M. A., *Adv. Mater.* **2016**, *28*, 5586–5618.
2. Lo T. Y., Krishnan M. R., Lu K. Y., Ho R. M., *Prog. Polym. Sci.* **2018**, *77*, 19–68.
3. Park C., Yoon J., Thomas E. L., *Polymer* **2003**, *44*, 6725–6760.
4. Bates F. S., Fredrickson G. H., *Annu. Rev. Phys. Chem.* **1990**, *41*, 525–557.
5. Bates F. S., Fredrickson G. H., *Phys. Today* **1999**, *52*, 32–38.
6. Sinturel C., Bates F. S., Hillmyer M. A., *ACS Macro Lett.* **2015**, *4*, 1044–1050.
7. Grubbs R. B., Grubbs R. H., *Macromolecules* **2017**, *50*, 6979–6997.
8. Polymeropoulos G., Zapsas G., Ntetsikas K., Bilalis P., Gnanou Y., Hadjichristidis N., *Macromolecules* **2017**, *50*, 1253–1290.
9. Matsen M. W., *Macromolecules* **2012**, *45*, 2161–2165.
10. Bellas V., Iatrou H., Hadjichristidis N., *Macromolecules* **2000**, *33*, 6993–6997.
11. Jung Y. S., Ross C. A., *Nano Lett.* **2007**, *7*, 2046–2050.
12. Choi P., Fu P. F., Guo L. J., *Adv. Funct. Mater.* **2007**, *17*, 65–70.
13. Giammaria T. J., Laus M., Perego M., *Adv. Phys. X* **2018**, *3*, 391–411.
14. Chao C. C., Ho R. M., Georgopoulos P., Avgeropoulos A., Thomas E. L., *Soft Matter* **2010**, *6*, 3582–3587.
15. Sinturel C., Vayer M., Morris M., Hillmyer M. A., *Macromolecules* **2013**, *46*, 5399–5415.
16. Lo T. Y., Dehghan A., Georgopoulos P., Avgeropoulos A., Shi A. C., Ho R. M., *Macromolecules* **2016**, *49*, 624–633.
17. Lu K. Y., Lo T. Y., Georgopoulos P., Avgeropoulos A., Shi A. C., Ho R. M., *Macromolecules* **2017**, *50*, 9403–9410.
18. Lu K. Y., Wang H. F., Lin J. W., Chuang W. T., *Macromolecules* **2018**, *51*, 7656–7665.
19. Georgopoulos P., Lo T. Y., Ho R. M., Avgeropoulos A., *Polym. Chem.* **2017**, *8*, 843–850.
20. Feng, H., Lu, X., Wang, W., Kang, N. G., Mays, J. W. *Polymers* **2017**, *9*.
21. Szwarc M., *Nature* **1956**, *178*, 1168.
22. Fetters L. J., *J. Polym. Sci. Part C Polym. Symp.* **2007**, *26*, 1–35.
23. Hadjichristidis N., Hirao A., *Anionic Polymerization: Principles, Practice, Strength, Consequences and Applications*. 2015.
24. Webster O. W., *Science* **1991**, *251*, 887–893.
25. Noro A., Iinuma M., Suzuki J., Takano A., Matsushita Y., *Macromolecules* **2004**, *37*, 3804–3808.
26. Lynd N. A., Hillmyer M. A., *Macromolecules* **2005**, *38*, 8803–8810.
27. Baskaran D., Müller A. H. E., *Anionic Vinyl Polymerization*, 2010.
28. Stefik M., Guldin S., Vignolini S., Wiesner U., Steiner U., *Chem. Soc. Rev.* **2015**, *44*, 5076–5091.
29. Dolan J. A., Wilts B. D., Vignolini S., Baumberg J. J., Steiner U., Wilkinson T. D., *Adv. Opt. Mater.* **2015**, *3*, 12–32.
30. Hadjichristidis N., Iatrou H., Pispas S., Pitsikalis M., *J. Polym. Sci. Part A Polym. Chem.* **2000**, *38*, 3211–3234.
31. Rundle R. E. J., *Phys. Chem.* **1957**, *61*, 45–50.
32. Lambert C., von Ragué Schleyer P., *Angew. Chemie Int. Ed. English* **1994**, *33*, 1129–1140.
33. Schade C., von Ragué Schleyer P., *Adv. Organomet. Chem.* **1987**, *27*, 169–278.
34. Hsieh H. L., *J. Polym. Sci. Part A Gen. Pap.* **1965**, *3*, 153–161.
35. Treybig N. M., Anthony G. R., **1979**, *14*, 295–326.
36. Welch, F. J., *J. Am. Chem. Soc.* **1960**, *82*, 6000–6005.
37. Bywater S., Worsfold D. J., *Canadian Journal of Chemistry* **1962**, *40*, 1564–1570.
38. Fetters L. J., Morton M., *Macromolecules* **1969**, *2*, 453–458.

39. Mays J. W., Hadjichristidis N., *Polym. Bull.* **1989**, *22*, 471–474.
40. Conlon D. A., Crivello J. V., Lee J. L., O' Brien M. J., *Macromolecules* **1989**, *22*, 509–516.
41. Hatada K., Kitayama T., Ute K., *Prog. Polym. Sci.* **1988**, *13*, 189–276.
42. Yuki H., Hatada K., *Adv. Polym. Sci.* **1979**, *31*, 1–45.
43. Hirao A., Hiraiishi Y., Nakahama S., Takenaka K., *Macromolecules* **1998**, *31*, 281–287.
44. Kennemur J. G., *Macromolecules* **2019**, *52*, 1354–1370.
45. Zhongde X., Mays J., Xuexin C., Hadjichristidis N., Schilling F. C., Bair H. E., Pearson D. S., Fetters L. J., *Macromolecules* **1985**, *18*, 2560–2566.
46. Tsoukatos T., Avgeropoulos A., Hadjichristidis N., Hong K., Mays J. W., *Macromolecules* **2002**, *35*, 7928–7935.
47. Francois, B., Fu, X., *Makromol. Chem.* **1990**, *191*, 2743–2753.
48. Mavroudis A., Avgeropoulos A., Hadjichristidis N., Thomas E. L., Lohse D. J., *Chem. Mater.* **2003**, *15*, 1976–1983.
49. Esswein B., Moiler., *Angew. Chemie Int. Ed. English* **1996**, *35*, 623–625.
50. Kricheldorf H. R., Berl M., Scharnagl N., *Macromolecules* **1988**, *21*, 286–293.
51. Uhrig D., Mays J., *Polym. Chem.* **2011**, *2*, 69–76.
52. Chalari I., Hadjichristidis N., *J. Polym. Sci. Part A Polym. Chem.* **2002**, *40*, 1519–1526.
53. Szwarc M., Levy M., Milkovich R., *J. Am. Chem. Soc.* **1956**, *78*, 2656.
54. Tsvetanov Ch. B., Dimov D. K., Petrova E. B., Dotcheva D. T., *Makromol. Chem., Macromol. Symp.* **1992** *60*, 297–313.
55. Nagasaki Y., Sato Y., Kato M., *Macromol. Rapid Commun.* **1997**, *18*, 827–835.
56. Stolarzewicz A., Czaja M., Neugebauer D., *Polymer* **2000**, *41*, 7865–7869.
57. Zilliox J. G., Hoovers J. E. L., Bywater S., *Macromolecules* **1975**, *8*, 573–578.
58. Schulte L., Grydgaard A., Jakobsen M. R., Szweczykowski P. P., Guo F., Vigild M. E., Berg R. H., Ndoni S., *Polymer* **2011**, *52*, 422–429.
59. Cavicchi K. A., Lodge T. P., *Macromolecules* **2003**, *36*, 7158–7164.
60. Cavicchi, K. A., Zalusky, A. S., Hillmyer, M. A., Lodge, T. P., *Macromol. Rapid Commun.* **2004**, *25*, 704–709.
61. Zavin B. G., Zhdanov A. A., Ścibiorek M., Chojnowski J., *Eur. Polym. J.* **1985**, *21*, 135–140.
62. Chojnowski J., Fortuniak W., Kowalewska A., *Makromol. Chem., Macromol. Symp.* **1993** *73*, 183–201.
63. Haddleton D. M., Bon S. A. F., Robinson K. L., Emery N. J., Moss I., *Macromol. Chem. Phys.* **2000**, *201*, 694–698.
64. Maschke, U., Wagner, T., Coqueret, X., *Makromol. Chemie* **1992**, *193*, 2453–2466.
65. Chao C. C., Wang T. C., Ho R. M., Georgopoulos P., Avgeropoulos A., Thomas E. L., *ACS Nano* **2010**, *4*, 2088–2094.
66. Avgeropoulos A., Chan V. Z. H., Lee V. Y., Ngo D., Miller R. D., Hadjichristidis N., Thomas E. L., *Chem. Mater.* **1998**, *10*, 2109–2115.
67. Khanna V., Cochran E. W., Hexemer A., Stein G. E., Fredrickson G. H., Kramer E. J., Li X., Wang J., Hahn S. F., *Macromolecules* **2006**, *39*, 9346–9356.
68. Lee S., Cheng L. C., Gadelrab K. R., Ntetsikas K., Moschovas D., Yager K. G., Avgeropoulos A., Alexander-Katz A., Ross C. A., *ACS Nano* **2018**, *12*, 6193–6202.
69. Sun J., Lee C., Osuji C. O., Gopalan P., *Macromolecules* **2021**, *54*, 9542–9550.
70. Hadjichristidis N., Pispas S., Iatrou H., Pitsikalis M., *Curr. Org. Chem.* **2005**, *6*, 155–176.
71. Alward D. B., Kinning D. J., Thomas E. L., Fetters L. J., *Macromolecules* **1986**, *19*, 215–224.
72. Roovers J., Zhou L. L., Toporowski P. M., van der Zwan M., Iatrou H., Hadjichristidis N., *Macromolecules* **1993**, *26*, 4324–4331.

73. Manesi G. M., Chang C. Y., Avgeropoulos A., Ho R. M., *ACS Appl. Polym. Mater.* **2020**, *2*, 3685–3695.
74. Bates F. S., *Science* **1991**, *251*, 898-904.
75. Kennemur J. G., Yao L., Bates F. S., Hillmyer M. A., *Macromolecules* **2014**, *47*, 1411–1418.
76. Leibler L., *Macromolecules* **1980**, *13*, 1602-1617.
77. Glaser, J., Medapuram, P., Beardsley, T. M., Matsen, M. W., Morse, D. C., *Phys. Rev. Lett.* **2014**, *113*, 1–5.
78. Helfand E., *Macromolecules* **1975**, *8*, 552-556.
79. Helfand E., Wasserman Z. R., *Macromolecules* **1976**, *9*, 879-887.
80. Helfand E., Wasserman Z. R., *Macromolecules* **1978**, *11*, 960-966.
81. Semenov, A. N., *J. Exper. Theor. Phys.* **1985**, *61*, 733-742.
82. Matsen M. W., Bates F. S., *Macromolecules* **1996**, *29*, 1091-1098.
83. Khandpur A. K., Förster S., Bates F. S., Hamley I. W., Ryan A. J., Bras W., Almdal K., Mortensen K., *Macromolecules* **1995**, *28*, 8796–8806.
84. Bates C. M., Bates F. S., *Macromolecules* **2017**, *50*, 3–22.
85. Matsen M. W., Bates F. S., *J. Chem. Phys.* **1997**, *106*, 2436–2448.
86. Shan W., Zhang W., Huang M., Ji Y., Zhang R., Zhang R., Su Z., Liu H., Feng X., Guo D., Huang J., Liu T., Li T., Mao J., Wesdemiotis C., Shi A. C., Cheng S. Z. D., *Giant* **2020**, *1*, 100002.
87. Matsen, M. W., *J. Phys. Condens. Matter* **2002**, *14*, 21-47.
88. Hofman A. H., ten Brinke G., Loos K., *Polymer* **2016**, *107*, 343–356.
89. Matsen M. W., Schick M., *Phys. Rev. Lett.* **1994**, *72*, 2660–2663.
90. Politakos N., Ntoukas E., Avgeropoulos A., Krikorian V., Pate B. D., Thomas E. L., Hill R. M., *J. Polym. Sci., Part B: Polym. Phys.* **2009**, *47*, 2419–2427.
91. Hajduk D. A., Takenouchi H., Hillmyer M. A., Bates F. S., Vigild M. E., Almdal K., *Macromolecules* **1997**, *30*, 3788–3795.
92. Matsen M. W., Bates F. S., *J. Polym. Sci. Part B Polym. Phys.* **1997**, *35*, 945–952.
93. Almdal K., Hillmyer M. A., Bates F. S., *Macromolecules* **2002**, *35*, 7685–7691.
94. Li W., Duan C., Shi A. C., *ACS Macro Lett.* **2017**, *6*, 1257–1262.
95. Zhu L., Huang P., Chen W. Y., Weng X., Cheng S. Z. D., Ge Q., Quirk R. P., Senador T., Shaw M. T., Thomas E. L., Lotz B., Hsiao B. S., Yeh F., Liu L., *Macromolecules* **2003**, *36*, 3180–3188.
96. Pester C. W., Schmidt K., Ruppel M., Schoberth H. G., Böker A., *Macromolecules* **2015**, *48*, 6206–6213.
97. Chang C. Y., Manesi G. M., Yang C. Y., Hung Y. C., Yang K. C., Chiu P. T., Avgeropoulos A., Ho R. M., *Proc. Natl. Acad. Sci. U. S. A.* **2021**, *118*, e2022275118.
98. Grason G. M., DiDonna B. A., Kamien R. D., *Phys. Rev. Lett.* **2003**, *91*, 1–4.
99. Grason G. M., Kamien R. D., *Macromolecules* **2004**, *37*, 7371–7380.
100. Xie N., Li W., Qiu F., Shi A. C., *ACS Macro Lett.* **2014**, *3*, 909–910.
101. Takenaka M., Wakada T., Akasaka S., Nishitsuji S., Saijo K., Shimizu H., Kim M. I., Hasegawa H., *Macromolecules* **2007**, *40*, 4399–4402.
102. Yue K., Huang M., Marson R. L., Hec J., Huang J., Zhou Z., Wang J., Liu C., Yan X., Wu K., Guo Z., Liu H., Zhang W., Ni P., Wesdemiotis C., Zhang W. Bin Glotzer S. C., Cheng S. Z. D., *Proc. Natl. Acad. Sci. U. S. A.* **2016**, *113*, 14195–14200.
103. Lewis R. M., Arora A., Beech H. K., Lee B., Lindsay A. P., Lodge T. P., Dorfman K. D., Bates F. S., *Phys. Rev. Lett.* **2018**, *121*, 208002.
104. Peterca M., Percec V., *Science* **2010**, *330*, 333–334.
105. Bates M. W., Lequieu J., Barbon S. M., Lewis R. M., Delaney K. T., Anastasaki A., Hawker C. J., Fredrickson G. H., Bates C. M., *Proc. Natl. Acad. Sci. U. S. A.* **2019**, *116*, 13194–13199.

106. Kim K., Schulze M. W., Arora A., Lewis R. M., Marc A., Dorfman K. D., Bates F. S., *Science* **2017**, *356*, 520–523.
107. Lodge T. P., *Macromolecules* **2020**, *53*, 2–4.
108. Jeon S., Jun T., Jeon H. Il, Ahn H., Lee S., Lee B., Ryu D. Y., *Macromolecules* **2021**, *54*, 9351–9360.
109. Jeon S., Jun T., Jo S., Ahn H., Lee S., Lee B., Ryu D. Y., *Macromol. Rapid Commun.* **2019**, *40*, 1–6.
110. Gillard T. M., Lee S., Bates F. S., *Proc. Natl. Acad. Sci. U. S. A.* **2016**, *113*, 5167–5172.
111. Park H., Jo S., Kang, B., Hur K., Oh S. S., Ryu D. Y., Lee S., *Nanophotonics* **2022**, 1–33.
112. Avgeropoulos A., Dair J. B., Hadjichristidis N., Thomas L. E., *Macromolecules* **1997**, *30*, 5634–5642.
113. Reddy A., Feng X., Thomas E. L., Grason G. M., *Macromolecules* **2021**, *54*, 9223–9257.
114. Feng X., Burke C. J., Zhuo M., Guo H., Yang K., Reddy A., Prasad I., Ho R. M., Avgeropoulos A., Grason G. M., Thomas E. L., *Nature* **2019**, *575*, 175–179.
115. Matsushita Y., Nomura M., Watanabe J., Mogi Y., Noda I., Imai M., *Macromolecules* **1995**, *28*, 6007–6013.
116. Mayes A. M., Olvera De La Cruz M., *J. Chem. Phys.* **1989**, *91*, 7228–7235.
117. Matsen M. W., Thompson R. B., *J. Chem. Phys.* **1999**, *111*, 7139–7146.
118. Park J., Jang S., Kim J. K., *J. Polym. Sci. Part B Polym. Phys.* **2015**, *53*, 1–21.
119. Olvera de la Cruz M., Sanchez C., *Macromolecules* **1986**, *19*, 2501–2508.
120. Matsen M. W., Schick M., *Macromolecules* **1994**, *27*, 6761–6767.
121. Herman D. S., Kinning D. J., Thomas E. L., *Macromolecules* **1987**, *20*, 2940–2942.
122. Matsushita Y., Takasu T., Yagi K., Tomioka K., Noda I., *Polymer* **1994**, *35*, 2862–2866.
123. Jang S., Moon C. H., Kwak J., Bae, D., Lee, Y., Kim K. J., Lee W. B., *Macromolecules* **2014**, *47*, 5295–5302.
124. Seo Y., Jang S., Ahn S., Mishra A. K., Kim J. K., Lee W. B., *Macromolecules* **2018**, *51*, 2750–2755.
125. Sun Z., Zhang W., Hong S., Chen Z., Liu X., Xiao S., *Polymer* **2017**, *121*, 297–303.
126. Isono T., Kawakami N., Watanabe K., Yoshida K., Otsuka I., Mamiya H., Ito H., Yamamoto T., Tajima K., Borsali R., Satoh T., *Polym. Chem.* **2019**, *10*, 1119–1129.
127. Lo T. Y., Chao C. C., Ho R. M., Georgopoulos P., Avgeropoulos A., Thomas E. L., *Macromolecules* **2013**, *46*, 7513–7524.
128. Li W., Liu M., Qiu F., Shi A. C., *J. Phys. Chem. B* **2013**, *117*, 5280–5288.
129. Huang C., Zhu Y., Man X., *Phys. Rep.* **2021**, *932*, 1–36.
130. Segalman R. A., *Mater. Sci. Eng. R Reports* **2005**, *48*, 191–226.
131. Knoll A., Horvat A., Lyakhova K. S., Krausch G., Sevink G. J. A., Zvelindovsky A. V., Magerle R., *Phys. Rev. Lett.* **2002**, *89*, 355011–355014.
132. Brassat K., Kool D., Nallet C. G. A., Lindner J. K. N., *Adv. Mater. Interfaces* **2020**, *7*, 1–10.
133. Griffiths R. A., Williams A., Oakland C., Roberts J., Vijayaraghavan A., Thomson T., *J. Phys. D. Appl. Phys.* **2013**, *46*.
134. Hu H., Gopinadhan M., Osuji C. O., *Soft Matter* **2014**, *10*, 3867–3889.
135. Koo K., Ahn H., Kim S. W., Ryu D. Y., Russell T. P., *Soft Matter* **2013**, *9*, 9059–9071.
136. Nunns A., Gwyther J., Manners I., *Polymer* **2013**, *54*, 1269–1284.
137. Bang J., Jeong U., Ryu D. Y., Russell T. P., Hawker J. C., *Adv. Mater.* **2009**, *21*, 4769–4792.
138. Bates M. C., Maher J. M., Janes W. D., Ellison J. C., Willson C. G., *Macromolecules* **2014**, *47*, 2–12.
139. Russell T. P., Hjelm P. R., Seeger A. P., *Macromolecules* **1990**, *23*, 890–893.

140. Yue Z., Sivaniah E., Hashimoto T., *Macromolecules* **2008**, *41*, 9948–9951.
141. Jeong J. W., Park W. I., Kim M. J., Ross C. A., Jung Y. S., *Nano Lett.* **2011**, *11*, 4095–4101.
142. Kim J. M., Hur Y. H., Jeong J. W., Nam T. W., Lee J. H., Jeon K., Kim Y., Jung Y. S., *Chem. Mater.* **2016**, *28*, 5680–5688.
143. Pitet L. M., Wuister S. F., Peeters E., Kramer E. J., Hawker C. J., Meijer E. W., *Macromolecules* **2013**, *46*, 8289–8295.
144. Luo Y., Montarnal D., Kim S., Shi W., Barteau K. P., Pester C. W., Hustad P. D., Christianson M. D., Fredrickson G. H., Kramer E. J., Hawker C. J., *Macromolecules* **2015**, *48*, 3422–3430.
145. Cushen J. D., Otsuka I., Bates C. M., Halila S., Fort S., Rochas C., Easley J. A., Rausch E. L., Thio A., Borsali R., Willson C. G., Ellison C. J., *ACS Nano* **2012**, *6*, 3424–3433.
146. Bates C. M., Seshimo T., Maher M. J., Durand W. J., Cushen J. D., Dean L. M., Blachut G., Ellison C. J., Willson C. G., *Science* **2012**, *338*, 775–779.
147. Nose T., *Polymer* **1995**, *36*, 2243–2248.
148. Azuma K., Sun J., Choo Y., Rokhlenko Y., Dwyer J. H., Schweitzer B., Hayakawa T., Osuji C. O., Gopalan P., *Macromolecules* **2018**, *51*, 6460–6467.
149. Luo Y., Kim B., Montarnal D., Mester Z., Pester C. W., McGrath A. J., Hill G., Kramer E. J., Fredrickson G. H., Hawker C. J., *J. Polym. Sci. Part A Polym. Chem.* **2016**, *54*, 2200–2208.
150. Matsen M. W., *Macromolecules* **2010**, *43*, 1671–1674.
151. Xiong S., Wan L., Ishida Y., Chapuis Y. A., Craig G. S. W., Ruiz R., Nealey P. F., *ACS Nano* **2016**, *10*, 7855–7865.
152. Matsen M. W., *Eur. Phys. J. E* **2013**, *36*.
153. Park S. M., Liang X., Harteneck B. D., Pick T. E., Hiroshiba N., Wu Y., Helms B. A., Olynick D. L., *ACS Nano* **2011**, *5*, 8523–8531.
154. Lontos G., Manesi G. M., Moutsios I., Moschovas D., Piryazev A. A., Bersenev E. A., Ivanov D. A., Avgeropoulos A., *Macromolecules* **2022**, *55*, 88–99.
155. Kawamoto K., Zhong M., Gadelrab K. R., Cheng L. C., Ross C. A., Alexander-Katz A., Johnson J. A., *J. Am. Chem. Soc.* **2016**, *138*, 11501–11504.
156. Cheng L. C., Gadelrab K. R., Kawamoto K., Yager K. G., Johnson J. A., Alexander-Katz A., Ross C. A., *Nano Lett.* **2018**, *18*, 4360–4369.
157. Puliyalil H., Cvelbar U., *Nanomaterials* **2016**, *6*.
158. Jung Y. S., Chang J. B., Verploegen E., Berggren K. K., Ross C. A., *Nano Lett.* **2010**, *10*, 1000–1005.
159. Jung Y. S., Lee J. H., Lee J. Y., Ross C. A., *Nano Lett.* **2010**, *10*, 3722–3726.
160. Bai W., Hannon A. F., Gotrik K. W., Choi H. K., Aissou K., Lontos G., Ntetsikas K., Alexander-Katz A., Avgeropoulos A., Ross C. A., *Macromolecules* **2014**, *47*, 6000–6008.
161. O’Driscoll B. M. D., Kelly R. A., Shaw M., Mokarian-Tabari P., Lontos G., Ntetsikas K., Avgeropoulos A., Petkov N., Morris M. A., *Eur. Polym. J.* **2013**, *49*, 3445–3454.
162. Son J. G., Gotrik K. W., Ross C. A., *ACS Macro Lett.* **2012**, *1*, 1279–1284.
163. Gu W., Xu J., Kim J. K., Hong S. W., Wei X., Yang X., Lee K. Y., Kuo D. S., Xiao S., Russell T. P., *Adv. Mater.* **2013**, *25*, 3677–3682.
164. Kim E., Kim W., Lee K. H., Ross C. A., Son J. G., *Adv. Funct. Mater.* **2014**, *24*, 6981–6988.
165. Jeong J., Ha J. S., Lee S. S., Son J. G., *Macromol. Rapid Commun.* **2015**, *36*, 1261–1266.
166. Borah D., Rasappa S., Salaun M., Zellsman M., Lorret O., Lontos G., Ntetsikas K., Avgeropoulos A., Morris M. A., *Adv. Funct. Mater.* **2015**, *25*, 3425–3432.
167. Giammaria T. J., Ferrarese Lupi F., Seguini G., Perego M., Vita F., Francescangeli O., Wenning B., Ober C. K., Sparnacci K., Antonioli D., Gianotti V., Laus M., *ACS Appl. Mater. Interfaces* **2016**, *8*, 9897–9908.

168. Borah D., Shaw M. T., Holmes J. D., Morris M. A., *ACS Appl. Mater. Interfaces* **2013**, *5*, 2004–2012.
169. Lee J. H., Kim Y. J., Cho J. Y., Yang S. R., Kim J. M., Yim S., Lee H., Jung Y. S., *Adv. Mater.* **2015**, *27*, 4814–4822.
170. Jeong J. W., Hur Y. H., Kim H. J., Kim J. M., Park W. I., Kim M. J., Kim B. J., Jung Y. S., *ACS Nano* **2013**, *7*, 6747–6757.
171. Oh J., Suh H. S., Ko Y., Nah Y., Lee J. C., Yeom B., Char K., Ross C. A., Son J. G., *Nat. Commun.* **2019**, *10*, (8pp)
172. Park W. I., You B. K., Mun B. H., Seo H. K., Lee J. Y., Hosaka S., Yin Y., Ross C. A., Lee K. J., Jung Y. S., *ACS Nano* **2013**, *7*, 2651–2658.
173. You B. K., Park W. I., Kim J. M., Park K. Il, Seo H. K., Lee J. Y., Jung Y. S., Lee K. J., *ACS Nano* **2014**, *8*, 9492–9502.
174. Fei H. F., Yavitt B. M., Hu X., Kopanati G., Ribbe A., Watkins J. J., *Macromolecules* **2019**, *52*, 6449–6457.
175. Oh J., Oh J. S., Sung D., Yim S., Song S., Yeom G., *Adv. Etch Technol. Nanopatterning VI* **2017**, *10149*, 101490U.
176. Arias-Zapata J., Cordeiro J., Böhme S., Girardot C., Garnier J., Bézard P., Ntetsikas K., Lontos G., Avgeropoulos A., Peyrade, D., Zelsmann M., *Microelectron. Eng.* **2015**, *141*, 155–159.
177. Cheng L.-C., Bai W., Fernandez Martin E., Tu K.-H., Ntetsikas K., Lontos G., Avgeropoulos A., Ross C. A., *Nanotechnology* **2017**, *28*, 145301
178. Ma M., Hill R. M., Lowery J. L., Fridrikh S. V., Rutledge G. C., *Langmuir* **2005**, *21*, 5549–5554.
179. Ma M., Titievsky K., Thomas E. L., Rutledge G. C., *Nano Lett.* **2009**, *9*, 1678–1683.
180. Ma M., Thomas E. L., Rutledge G. C., Yu B., Li B., Jin Q., Ding D., Shi A. C., *Macromolecules* **2010**, *43*, 3061–3071.
181. Ito K., Yamada Y., Miura A., Iizuka H., *RSC Adv.* **2019**, *9*, 16431–16438.
182. Rasappa S., Hulkkonen H., Schulte L., Ndoni S., Reuna J., Salminen T., Niemi T., *J. Colloid Interface Sci.* **2019**, *534*, 420–429.
183. Kim A., Müftü S., Thomas E. L., Lee J. H., *ACS Appl. Polym. Mater.* **2021**, *3*, 4413–4418.
184. Ndoni S., Vigild M. E., Berg R. H., *J Am Chem Soc* **2003**, *125*, 13366–13367.
185. Lin T.-C., Yang K.-C., Georgopoulos P., Avgeropoulos A., Ho R.-M., *Polymer* **2017**, *126*, 360–367.
186. Wang X.-B., Lo T.-Y., Hsueh H.-Y., Ho R.-M., *Macromolecules* **2013**, *46*, 2997–3004.
187. Siddique S. K., Sadek H., Lee T.-L., Tsai C.-Y., Chang S.-Y., Tsai H.-H., Lin T.-S., Manesi G.-M., Avgeropoulos A., Ho R.-M., *Polymers* **2022**, *14*, 1891.
188. Chang C.-Y., Manesi G.-M., Avgeropoulos A., Ho R.-M., *Macromolecules* **2022**, *55*, 3449–3457.
189. Berek D., *J. Sep. Sci.* **2010**, *33*, 315–335.
190. Fox G. T., Flory P. J., *J. Polym. Sci.* **1954**, *75*, 315.
191. Fetters L. J., Lohse D. J., Richter D., Witten T. A., Zirkel A., *Macromolecules* **1994**, *27*, 4639–4647.
192. Martinez-Veracoechea J. F., Fernando Escobedo A. F., *Macromolecules* **2009**, *42*, 9058–9062.
193. Shim J., Bates F. S., Lodge T. P., *Nat. Commun.* **2019**, *10*, 2108.
194. Gao Y., Deng H., Li W., Qiu F., Shi A.-C., *Phys. Rev. Lett.* **2016**, *116*, 068304.
195. Yang L., Hong S., Gido P. S., Velis G., Hadjichristidis N., *Macromolecules* **2001**, *34*, 9069–9073.
196. Maurer W. W., Bates S. F., Lodge P. T., Almdal K., Mortensen K., Fredrickson H. G., *J. Chem. Phys.* **1998**, *108*, 2989.

197. Kennemur G. J., Yao L., Bates S. F., Hillmyer A. M., *Macromolecules* **2014**, *47*, 1411–1418.
198. Andersen T. H., Tougaard, S., Larsen, N. B., Almdal, K., Johannsen, I., *J. Electron Spectrosc.* **2001**, *121*, 93-110.